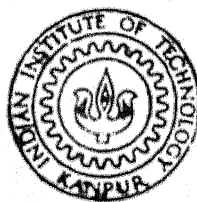


RECRYSTALLISATION BEHAVIOUR AND DEVELOPMENT OF TEXTURE IN A FEW DUAL-PHASE STEELS

DIPAK KUMAR MONDAL



DEPARTMENT OF METALLURGICAL ENGINEERING
INDIAN INSTITUTE OF TECHNOLOGY, KANPUR

AUGUST, 1987

Acc. No. A.108232

ME-1987-D-MON-REC

RECRYSTALLISATION BEHAVIOUR AND DEVELOPMENT OF TEXTURE IN A FEW DUAL-PHASE STEELS

**A Thesis Submitted
in Partial Fulfilment of the Requirements
for the Degree of
DOCTOR OF PHILOSOPHY**

**by
DIPAK KUMAR MONDAL**

**to the
DEPARTMENT OF METALLURGICAL ENGINEERING
INDIAN INSTITUTE OF TECHNOLOGY, KANPUR
AUGUST, 1987**

Certificate

Certified that the work reported in this thesis
entitled 'RECRYSTALLISATION BEHAVIOUR AND DEVELOPMENT OF
TEXTURE IN A FEW DUAL-PHASE STEELS' by SHRI D. K. MONDAL
has been carried out under my supervision and has not
been submitted elsewhere for the award of a degree.

August, 1987.



(R. K. Ray)
Professor

Department of metallurgical Engineering
Indian Institute of Technology
Kanpur

Acknowledgement

I take this opportunity to express my sincere gratitude and indebtedness to my supervisor, Professor R.K. Ray for brilliant guidance and active co-operation throughout the course of this work.

I would like to thank M/s K.P. Mukherjee, M.N. Mungole, H.C. Srivastava, P.K. Pal and S. Das for assisting me at various stages of this work. Special thanks are due to Mr. G.S. Thapa and Mr. B.K. Jain for tracing the figures and Mr. R.N. Srivastava for the excellent typing.

I am also grateful to Dr. U.V. Schlippenbach of the Institut für Metallkunde in R.W.T.H. Aachen, West Germany for generating the O.D.F.'s from my texture samples using a Lücke texture goniometer. Thanks are also extended to the Electron-Microscope Division, National Metallurgical Laboratory, Jamshedpur where some of the transmission electron microscopy work was carried out.

Synopsis

The present investigation deals with a systematic study of the recrystallisation behaviour and texture formation in three dual-phase steel compositions. Such a study was considered useful for providing an insight into the response of these steels to thermo-mechanical processing with particular reference to their deep-drawing characteristics.

The steels, designated A1, A4 and A5 have the following nominal compositions (in weight per cent): A1-0.10 C, 1.50 Si, 0.1 V; A4-0.10 C, 1.50 Si, 1.50 Mn, 0.1 V; and A5-0.10 C, 1.50 Mn, 0.1 V.

Dual-phase structures were produced in all the three alloys in two different ways, namely, (a) by air-cooling from the austenitising temperature (910°C) and then intercritically annealing the ferrite-pearlite structure at 750°C and 810°C followed by water-quenching; and (b) by water-quenching from the same austenitising temperature and then intercritically annealing the martensitic structure again at 750°C and 810°C followed by final water-quenching. These two treatments will henceforward be referred to as AC/WQ and WQ/WQ respectively. These initial heat-treatments produced four different dual-phase structures for each alloy. A total of twelve such different dual-phase distributions for the three alloys were obtained. These have been characterised by optical and electron metallography and by measurement of some of the mechanical properties. These studies have revealed that for a particular initial heat-treatment, the volume percent of martensite is maximum in alloy A4 and this is nearly twice the

value obtained for the alloys A1 and A5. Although the amount of martensite in alloy A1 is somewhat lower than that in alloy A5, the overall strength of alloy A1 is higher than that of alloy A5 due possibly to the significant solid solution hardening of the ferritic matrix caused by silicon. Alloy A4 has been found to have the highest strength amongst the three alloys. The martensite in all the alloys has been found to consist mostly of dislocated laths. The ferrite phase present in the alloys A1 and A4 have formed in two different ways: (i) before and/or during the intercritical annealing ('old' ferrite) and (ii) during the cooling of the alloys from the intercritical annealing temperature (transformed or 'new' ferrite). The amount of new ferrite has been found to be larger in alloy A1 as compared to alloy A4. Alloy A5 did not show any measurable amount of new ferrite. Hardly any significant difference in microstructure could be found in any of the alloys as a result of the two treatments, namely, AC/WQ and WQ/WQ.

Steel samples having the twelve different distributions of ferrite-martensite structures in the three alloys, as mentioned above, have been subjected to cold-deformation upto ~60% by rolling. Each one out of these twelve deformed structures was subjected to recrystallisation anneals at temperatures, namely, 650°C, 700°C, 750°C, 800°C and 850°C for various lengths of time till full recrystallisation was achieved. The structures of the cold-deformed, partially recrystallised and fully recrystallised materials were characterised by both optical and electron microscopy. In all cases these observations were carried out on the transverse sections of the specimens. In any one alloy, optical as well as electron microstructures obtained from the cold-deformed

materials were found to be practically the same irrespective of the different initial heat-treatments. All the three cold-worked alloys showed elongated cell-like structures, sometimes showing a number of deformation bands in some of the deformed grains. The structural features were found to be coarsest for the alloy A1, rather coarse for alloy A5 and finest in alloy A4. Selected area diffraction (S.A.D.) patterns taken systematically over large number of ferritic areas in thin foils from all the three alloys showed, in general, the following common crystallographic orientations, namely, $\{112\} \langle 111 \rangle$, $\{110\} \langle 111 \rangle$, $\{310\} \langle 001 \rangle$, $\{147\} \langle 311 \rangle$ in addition to a host of other orientations. In contrast to the alloys A1 and A4, many areas in a number of thin foils from the cold-worked alloy A5 showed distinct signs of recovery at places leading to the formation of subgrains.

Transmission electron microscopic (T.E.M.) studies of the partially and fully recrystallised materials were confined to those samples only which were annealed at the temperatures 650°C and 800°C for various lengths of time. At the lower temperature of 650°C , the cold-worked ferritic areas started recrystallising, whereas at the higher temperature of 800°C re-austenitisation of martensite and recrystallisation of cold-worked ferrite took place simultaneously. The end-product in both the cases, however, consisted of islands of martensite embedded in a recrystallised ferrite matrix. During the recrystallisation anneal strain-free ferrite grains were found to nucleate at both the deformed ferrite-martensite interfaces as well as inside the deformed ferrite grains, presumably in the deformation band regions. At the higher temperature of anneal, the austenite grains appeared to form both at

the deformed ferrite-martensite interfaces as well as within the martensitic areas.

Extensive studies on any of the three alloys with the help of the T.E.M. showed no perceptible difference in the microstructure as a function of the initial dual-phase heat-treatment. Almost invariably, the recrystallised ferrite grains have been found to nucleate at or near cold-worked regions of the same or nearly the same orientation. Thus the process of recrystallisation in all the three alloys, irrespective of the initial heat-treatment as well as annealing temperature, can be best described as an in-situ process.

The kinetics of primary recrystallisation of ferrite in the cold-rolled dual-phase steels were analysed from the relevant microhardness data using an Avrami-type relationship. In general, the Avrami plots showed straightline segments with two distinct slopes indicating two distinct processes during recrystallisation. The activation energies measured from the Arrhenius plots ranged between 16.0 to 20.0 KCal/⁰ mole.

In order to have an overall idea about the crystallographic orientations in both the cold-worked and recrystallised alloys, detailed texture measurements were undertaken using both the conventional pole-figure and the O.D.F. (Orientation Distribution Function) methods. The {110} pole-figures for all the three cold-rolled alloys with different initial heat-treatments showed a moderately strong {111} <112> and a rather weak {111} <110> texture components. In general, the deformation textures of alloys A1 and A5 were found to be somewhat sharper as compared to those of alloy A4.

The O.D.F. plots, while supporting the pole-figure results, indicated that, in all the three alloys, the major texture components were $\{111\} \langle 112 \rangle$ and $\{111\} \langle 110 \rangle$ while the minor components were of the type $\{337\} \langle 110 \rangle$, $\{337\} \langle 776 \rangle$, $\{112\} \langle 111 \rangle$ and $\{112\} \langle 110 \rangle$. In addition, some rather low intensity texture components like $\{110\} \langle 001 \rangle$, $\{001\} \langle 110 \rangle$, $\{110\} \langle 110 \rangle$ and $\{310\} \langle 001 \rangle$ were also found.

Detailed analysis of the O.D.F. results has shown the presence of a reasonably strong $\{111\}$ fibre texture component in both the alloys A4 and A5, whereas alloy A1 did not show any $\{111\}$ fibre. Again, a weak $\{11, 11, 4\}$ fibre has been observed in alloy A4, which is not so well-developed in alloy A5, while the same may be treated as weak and incomplete in case of alloy A1. $\{337\} \langle uvw \rangle$ orientations do not comprise a fibre-component in either alloy A1 or A5, although alloy A4 may be supposed to have a rather weak and incomplete $\{337\}$ fibre texture.

The $\{110\}$ pole-figures for the alloys in the recrystallised condition have been found to be basically similar to the ones for the corresponding cold-deformed materials, with the difference that the pole-densities are somewhat weaker in the former. O.D.F. plots have shown the presence of a rather sharp $\{111\}$ fibre component in both the alloys A4 and A5, whereas no such fibre could be obtained in alloy A1. The intensity of the $\{111\}$ fibre has been found to be somewhat stronger in the alloy A5 than in A4. The behaviour of the other two important texture components, namely, $\{11, 11, 4\} \langle uvw \rangle$ and $\{337\} \langle uvw \rangle$ have been found to be similar to that in the cold-deformed alloys. A major difference

in the recrystallisation texture in alloys A4 and A5 is that, a stronger {111} fibre is obtained in the former at the lower recrystallisation temperature of 650°C and in the latter at the higher annealing temperature of 800°C.

The theoretically determined \bar{r} -values for the three recrystallised alloys have shown that while alloy A1 has \bar{r} -values <1.0, the corresponding values for alloys A4 and A5 are >1.0. Out of the three alloys the alloy A5 seems to have a distinct edge over the other two so far as the \bar{r} -values are concerned.

The above experimental results on the recrystallisation behaviour and texture development in the experimental alloys have been systematically analysed and compared with results of other investigators working on similar or related steel compositions. The suitability of these steels for deep-drawing applications have been commented upon and suggestions put forward for possible further improvement in this direction.

Contents

	Page
Chapter I Introduction	1
Chapter II Literature Review	5
2.1 Historical Development	5
2.2 Composition and Heat-treatment of Dual-phase Steels	7
2.2.1 Typical Compositions	7
2.2.2 Selection of Alloying Elements	8
2.2.3 Heat-treatment Cycles	11
2.2.4 Formation of Austenite in Dual-Phase Steels During Intercritical Annealing	14
2.3 Structure of Dual-Phase Steels	15
2.3.1 Distribution of Phases	15
2.3.2 Effect of Heat-treatment on Micro-structure	17
2.3.3 Effect of Tempering on Microstructure	19
2.4 Mechanical Properties of Dual-Phase Steels	19
2.4.1 Typical Stress-strain Curves for Dual-Phase Steels	19
2.4.2 Strength and Ductility	20
2.4.3 Deformation Behaviour	23
2.4.4 Sheet Formability	24
2.5 Recrystallisation and Texture Development in Dual-Phase Steels and Conventional Deep-Drawing Quality Steels	27
2.5.1 Phenomenon of Recrystallisation	27
2.5.1.1 Nucleation	28
2.5.1.2 Effect of Second Phase	31
2.5.1.3 Effect of Solid Solutions	32
2.5.1.4 Texture Development During Grain Growth	33
2.5.2 Texture and Its Representation	34
2.5.3 Development and Control of Annealing Textures in Conventional Deep-Drawing Quality Steels and Dual-Phase Steels	38
2.5.3.1 Conventional Deep-Drawing Quality Steels	38
2.5.3.2 Textures in Dual-Phase Steels	44
Chapter III Experimental Procedure	51
3.1 Materials and Their Preparation	51
3.2 Heat-treatment and Production of the Dual-Phase Structure	52
3.3 Tensile Testing	53
3.4 Cold-Rolling and Recrystallisation Treatment	54
3.5 Optical Metallography	56
3.5.1 Specimen Preparation and Examination	56
3.5.2 Quantitative Metallography	57

	Page
3.6 Transmission Electron Microscopy	59
3.7 Microhardness Measurements	60
3.8 Determination of Recrystallisation Kinetics	61
3.9 Determination of Texture	63
3.10 Determination of r -values	67
Chapter IV Experimental Results	68
4.1 Characterisation of the Dual-Phase Structures in the Three Alloys Produced by Different Initial Heat-treatments	68
4.1.1 Optical Microstructures	68
4.1.2 Electron Microstructures	72
4.1.3 Mechanical Properties	74
4.2 Characterisation of the Cold-Worked Materials	77
4.2.1 Microstructure	77
4.2.2 Deformation Texture	94
4.3 Recrystallisation Characteristics of the Alloys	136
4.3.1 Microstructural Changes	136
4.3.2 Recrystallisation Texture	142
4.3.3 Kinetics of Recrystallisation	149
4.4 Estimation of ' r '-values	199
Chapter V Discussion	211
5.1 Characterisation of the Starting Materials	211
5.2 Microstructures and Textures of the Deformed Alloys	215
5.3 Microstructures and Textures of the Recrysta- llised Alloys	219
5.4 Formability Characteristics of the Alloys	227
Chapter VI Conclusions	239
References	243

Chapter I

Introduction

For many decades most of the steels used in automobile bodies have been plain low-carbon steels cold-rolled to thicknesses upto 2 mm or hot-rolled to thicker gauges. It is easy to understand that if steels with higher strength were used, the usable sheet metal thickness could be correspondingly reduced causing a significant reduction in the weight of the automobile. The high strength steels, generally considered at later stages, include primarily the microalloyed high strength low alloy (H.S.L.A.) steels.

The major problems of the H.S.L.A. steels are a lack of dynamic stiffness and poor formability, although they maintain a rather high yield strength. In spite of these shortcomings, significant quantities of H.S.L.A. steels are being used in the current models of a number of automobiles.

The formability problem with the H.S.L.A. steels has been sought to be overcome by the induction of the 'dual-phase' steels around 1975. The dual-phase steels have a microstructure consisting of the 'soft' ferrite phase with islands of 'hard' martensite dispersed in it. Typically, in a commercial dual-phase steel, the martensite phase occupies about 20% by volume of the entire microstructure.

The dual-phase structure in steels may be produced by annealing either hot or cold-rolled strips at a temperature in the two-phase ($\alpha + \gamma$) region of the Fe-C-X equilibrium diagram, followed by cooling at a rate which ensures that the γ -phase transforms to martensite.

Compared to the conventional H.S.L.A. steels, the dual-phase steels were expected to have better formability characteristics due to their low initial yield strength, continuous yielding behaviour, high work-hardening rate at the early stage of straining and a rather large total elongation before fracture. The formability, as indicated by the forming limit diagram in Figure 1.1 [1] for a dual-phase steel (GM980X) is found to be superior to that of H.S.L.A. steels of the same strength under conditions where the minor strain is positive (i.e., the mode of deformation is stretching, a strain pattern commonly encountered in automobile industries).

The deep-drawability of the dual-phase steels, however, has been found to be inferior to that of the conventional steels used in the automotive industries. For example, the 'r'-values of dual-phase steels, produced by intercritical annealing, have been found to be around 1.0 whereas for some killed steels it can be as high as 1.6-1.8 or even more. It would, therefore, be highly interesting and useful to try to develop dual-phase steels with high enough 'r'-values, because in that case the superior mechanical properties of these steels such as high strength and large uniform and total elongation can also be taken advantage of.

It is known that high 'r'-values in a sheet steel can always be associated with the presence of a strong {111} fibre texture in the material. Hence, attainment of a high 'r'-value in sheet steels can ultimately be linked to the ease of nucleation and growth of {111} oriented grains in the sheet material. The industrial processing of dual-phase steels involves both hot deformation and intercritical annealing. Thus the final microstructure in a dual-phase steel is derived as a result of these thermal and mechanical processing.

In order to gain a basic understanding of the nucleation and growth of the grains in the dual-phase steels during normal processing and the way they affect the development of texture, it would seem tempting to study their deformation and recrystallisation characteristics. However, a study of the relevant literature has shown that there has been hardly any systematic research in this direction. It is, therefore, envisaged to investigate the response of three C-Mn-Si-V dual-phase steels to the processes of cold-deformation and subsequent recrystallisation. An attempt has been made to carry out a thorough structural characterisation of the cold-worked and recrystallised states using a transmission electron microscope (T.E.M.) in order to gain information at the micro-level. Side by side macroscopic textures of the corresponding materials have been determined by using the conventional pole-figure as well as the O.D.F. (Orientation Distribution Function) methods. Further, the kinetics of recrystallisation was studied in the usual manner.

It was hoped that the present study would lead to a basic understanding of the formation of the recrystallised grains, specially the desired $\{111\}$ types, in the experimental dual-phase steels during thermomechanical processing. This, coupled with detailed textural studies, was expected to help in designing suitable parameters so as to yield an optimum texture in the material leading to improved deep-drawing characteristics. This is very important since the present indications are that the dual-phase steels are going to be used in much larger quantities in the future in the automobile and other industries in sheet-form.

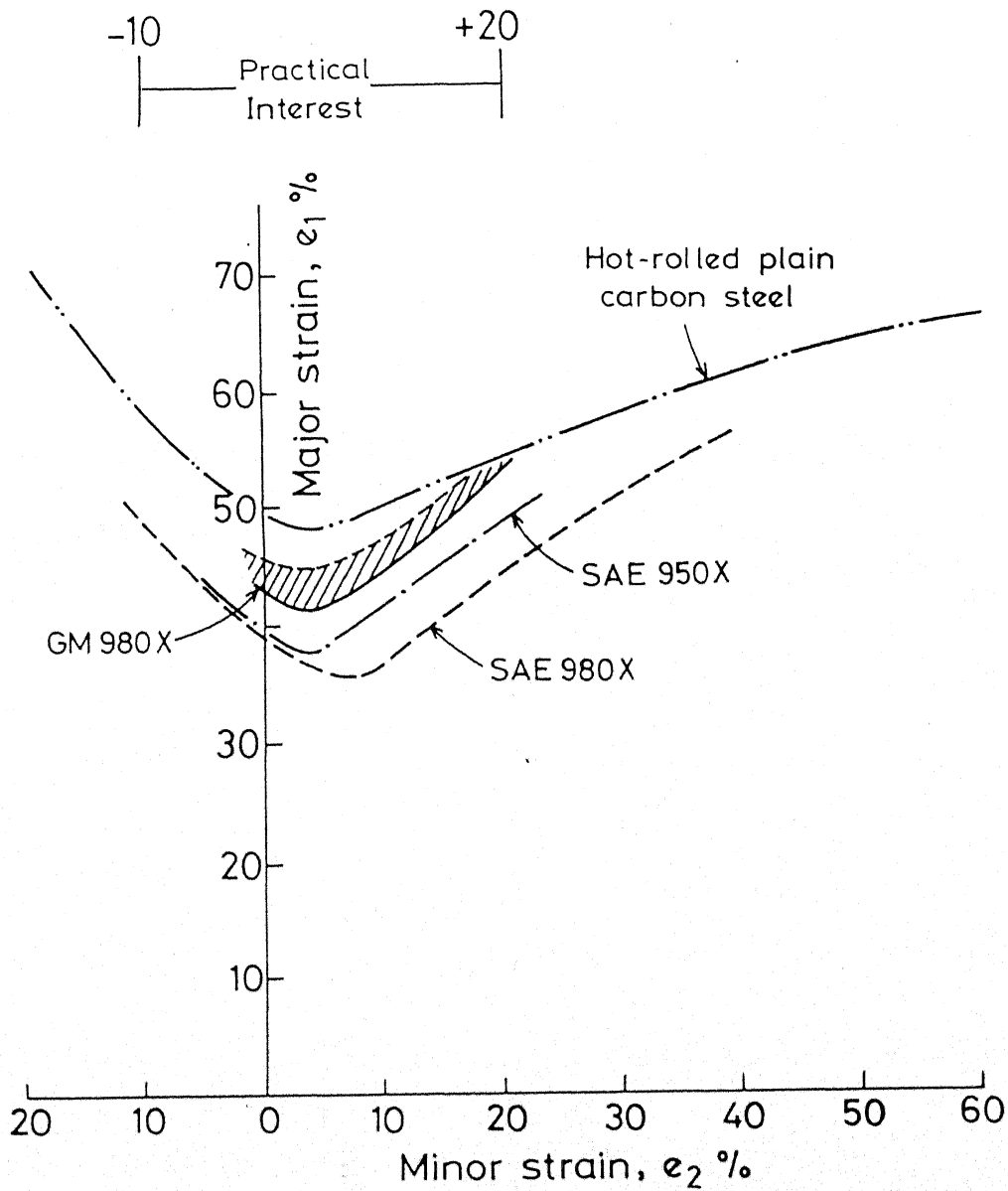


Fig.1.1 Range of the forming limit diagrams (FLD) of dual-phase GM 980X steel compared with that of plain carbon steel and SAE 950X and 980X steels. [58]

Chapter 11

Literature Review

2.1 Historical Development

A number of routes to develop low-cost high-strength steels with good formability have been explored in response to the performance requirements, which resulted from the car manufacturers' targets for weight saving and energy conservation. Earlier efforts concentrated on the development of high strength steels, such as microalloyed controlled-rolled, high strength low alloy (H.S.L.A.) steels [2, 3, 4] or some other variety [5] to meet the above requirements. But it was soon found out that these high strength steels suffer from two major problems, e.g., the lack of dynamic stiffness and poor formability. The formability problem with the H.S.L.A. steels has been sought to be overcome by the more recent discovery of the dual-phase steels. These dual-phase steels consist essentially of about 80-90% low carbon ferrite and 10-20% of a hard second phase, mostly martensite. Little amounts of retained-austenite and some low carbon bainite may also be present as minor constituents. The dual-phase steels are characterised by continuous yielding, relatively low initial flow stress, a high ultimate tensile strength and very rapid and sustained workhardening giving rise to high uniform elongation. The dual-phase structure is produced by annealing either hot- or cold-rolled steel strip at a temperature in the two-phase ($\alpha + \gamma$) region of the equilibrium diagram, followed by cooling at a rate which ensures that the remaining γ -phase transforms to martensite. Hayami and Furukawa [2] first demonstrated the superior formability of the dual-phase steels

on the basis of the results of deep drawing tests. Several parallel developments [6-11] at this stage led to the development of dual-phase microstructures in steels where manganese is the main element used to retard the diffusion-controlled transformation of austenite. Silicon and chromium were also used to control the hardenability, so that the addition of the above three elements can produce dual-phase structures by box-annealing. With the idea of restricting ferrite grain growth and to have sufficient hardenability of the austenite formed during intercritical annealing, the controlled-rolled microalloyed H.S.L.A. steels have been considered to be suitable starting materials in producing dual-phase steels. Rashid [1, 10] found that a small concentration of microalloying element like vanadium can furnish the required hardenability. Morrow and coworkers [11-13] observed the same effect with the addition of very small amount of molybdenum. Rashid [1] has demonstrated that a high strength dual-phase steel with a total elongation of as much as 30% can be obtained in CM 980X-V [1, 10] which contains very small amount of V in addition to substantial amounts of the solution strengtheners like Mn (1.5%) and Si (0.5%). Morrow and coworkers used similar concentrations of Mn and Si in their successful development of microalloyed dual-phase steels containing Mo. However, better mechanical properties have been obtained in the steels containing V than the ones containing Nb and/or Mo [11]. Similar dual-phase properties have also been reported for a manganese-bearing steel by Matsouka and Yamamori [14] who noted a high workhardening rate, good press formability and spot weldability. Using the cyclic austenitisation technique of Grange [15] for grain refinement, Koo and Thomas [16-18] produced dual-phase properties in a few Mn-Si-Cr steels. Davies [19-23] studied the

properties of dual-phase structures produced in a variety of Fe-Mn-C alloys and found that the strength of the dual-phase structure is dependent on the ferrite grain size and the volume fraction of martensite.

In an alternative method, dual-phase structures can be produced by controlling the cooling rate after hot rolling in the mills. Here the elements added to control hardenability need to be more selective in their effects. Coldren and Tither [24] have considered the production of dual-phase structure in a steel containing 0.6% Cr-0.4% Mo-% C by hot rolling and subsequent coiling. The necessary C.C.T. diagram (Figure 2.1) developed by them clearly indicates that the coiling temperature needs to be controlled to fall within the area known as the 'coil-window' [24] in order that the austenite may transform to a tempered martensite at a very slow cooling rate. The product has been found to have excellent tensile strength and good formability, although the total elongation is not as large as that which can be developed in intercritically annealed dual-phase steels. In a similar development in Japan [25], known as 'dual-phase rolling', a low carbon steel containing 0.4% Si-1.4% Mn has been coiled at a very low temperature (below M_s temperature of the austenite), thus transforming the austenite before coiling. This process gives rise to inferior tensile strength properties as compared to that described by Coldren and Tither [24], but the total elongation remains the same.

2.2 Composition and Heat-Treatment of Dual-Phase Steels

2.2.1 Typical Compositions

The composition of all dual-phase steels is based primarily on low carbon and low alloy content. The lack of hardenability causing formation of ferrite-carbide transformation products during cooling from ($\alpha + \gamma$)

intercritical range, may be overcome by minor addition of vanadium, niobium, chromium, molybdenum etc. It is common practice to use aluminium-killed steels, although the Japanese steels high in silicon are usually deoxidised with silicon. All dual-phase steels maintain low sulphur content and are given a sulphide particle shape-control treatment, usually with rare earths or zirconium. Typical compositions of some dual-phase steels either in production or at an advanced stage of development are given in Table 2.1.

2.2.2 Selection of Alloying Elements

The superior properties of dual-phase steels arise from their essential structural features. The enhanced ductility at a given tensile strength is a consequence of the dispersion of a strong martensite in a high strength, highly ductile ferrite matrix. There are many combinations of alloying elements such as Mn, Si, Cr, Mo and V that can be added to low carbon iron to obtain the desired hardenability of the austenite [26, 27] for transformation to martensite even at a mild cooling rate. The alloying elements are chosen according to the facilities available and properties required. It is possible to produce a family of dual-phase steels with various combinations of strength and ductility. The strength of dual-phase steels depends on the strength of both the phases. The results for some silicon-containing steels [28] show that besides increasing the hardenability of austenite, silicon reduces the interstitial carbon content of ferrite which ultimately leads to a cleaner and more ductile ferrite. On the other hand, as a means of strengthening ferrite by substitutional solute elements, Si and P are considered to be very effective [29]. Mamui and Takechi [30] showed that substitutional strengthening by silicon and manganese resulted in the best combination of strength and ductility.

Table 2.1
Compositions of Some Common Dual-Phase Steels

	Composition, wt. %								References
	C	Mn	Si	Ni	Cr	Mo	V	Nb	
A. Carbon-manganese series	0.01	1.45	-	-	-	-	-	-	44
	0.06	0.33	-	-	-	-	-	-	78
	0.052	0.90	-	-	-	-	-	-	63
	0.11	0.78	-	-	-	-	-	-	63
B. Carbon-silicon series	0.10	-	2.00	-	-	-	-	-	50
C. Carbon-manganese-silicon series	0.15	1.50	0.01	-	-	-	-	-	44
	0.22	1.55	0.01	-	-	-	-	-	44
	0.10	1.45	1.20	-	-	-	-	-	53
	0.06	1.47	0.23	-	-	-	-	-	32
	0.12	1.47	0.24	-	-	-	-	-	32
	0.16	1.53	0.24	-	-	-	-	-	32
	0.20	1.53	0.25	-	-	-	-	-	32
	0.29	1.51	0.24	-	-	-	-	-	32
D. Carbon-manganese-silicon-vanadium series	0.21	2.00	1.03	-	-	-	0.20	-	53
	0.10	1.45	1.20	-	-	-	0.15	-	53
	0.10	1.44	0.49	-	-	-	0.075	-	52
E. Carbon-manganese-silicon-nickel-chromium-vanadium series	0.072	1.26	0.30	0.02	0.02	-	0.08	-	51
	0.11	1.29	0.29	0.02	0.03	-	0.065	-	51
F. Carbon-manganese-silicon-chromium-molybdenum series	0.062	1.19	0.02	-	0.49	0.03	-	-	34
	0.07	0.90	1.20	-	0.57	0.29	-	-	52

As a more or less accepted principle of the duplex ferrite-martensite alloy development, the initial alloy composition and the volume percent martensite in the processed steel have to be controlled so that the carbon concentration in martensite is maintained at 20.3 wt. %. This is to produce 'lath' instead of 'twinned' martensite so that the product does not suffer from severe brittleness [31]. However, the effect of substitutional alloying elements on the carbon content of austenite should also be kept in mind while choosing a favourable overall composition. Silicon and sometimes manganese are added to improve the drawing properties of the ferrite, but the primary function of Mn and other alloying elements, like V, Mo, Cr etc., is to increase the hardenability of the austenite. At the intercritical annealing temperature these alloying elements partition to a significant extent in the austenite. In this respect, a number of investigators [1, 11] have considered vanadium to be a much more effective addition than niobium which may be due to the higher equilibrium concentration of V than Nb in the austenite. The diffusion of all the substitutional elements may be so slow at the intercritical annealing temperature as to give rise to a lack of equilibrium partitioning [32] resulting in a severe chemical heterogeneity within individual austenite islands. Though carbon moves an order of magnitude faster than the substitutional alloying elements, the local equilibrium concentration of carbon is determined by the type and concentration of substitutional elements present. Thus severe carbon-concentration gradients may also be set up within individual austenite islands. This type of segregation can lead to the formation of a mixture of transformation products within a single island, and may be averted to some extent by annealing the steel in the single γ -phase before cooling to the intercritical annealing temperature [33].

Besides increasing the hardenability, Cr retards the process of bainite formation. According to Tanaka et al [34] Cr is the most favourable alloying element for the production of dual-phase steel, since it decreases the dissolved carbon content by promoting the partition of carbon between austenite and pearlite. It does not cause solid solution hardening in ferrite [35]. Manganese has an effect similar to that of Cr except that it causes solid-solution hardening of ferrite. Molybdenum also increases the hardenability of austenite. Being a ferrite former, it does not decrease carbon solubility in ferrite and moreover, it causes a large solid-solution hardening effect [36]. The addition of niobium to the steel results in the formation of finer ferrite grain size and precipitation of carbonitrides. This precipitation in turn leads to the formation of a substructure in the ferrite and as a consequence the tensile strength is increased. The desirability of various alloying elements has to be assessed with an eye to produce a simple economical steel with favourable structure and required properties.

2.2.3 Heat-Treatment Cycles

Depending on the chemical composition dual-phase steels can be produced by cooling from the intercritical annealing temperature at any cooling rate between those of batch annealing and water quenching. With the idea of decreasing the cooling rate required by adding small quantity of alloying elements, dual-phase steels with a variety of chemical compositions and cooling rate have been developed. This has led to considerable variation in the physical properties. More explicitly, it may be said that the dual-phase microstructure is a strong function of the combined effects of the starting structure prior to intercritical annealing, the annealing temperature and the cooling rate which, in other words, comprise

the heat-treatment cycle. The different types of heat-treatment cycles used for the production of dual-phase structures may be classified as :

1. Intermediate annealing (I.A.)
2. Intermediate normalising (I.N.)
3. Intermediate quenching (I.Q.)
4. Step quenching (S.Q.)
5. Continuous annealing (C.A.)

Steels containing coarse and fine ferrite and pearlite are used for intercritical annealing in intermediate annealing and intermediate normalising cycles respectively. When the structure of steel before intercritical annealing is fully martensitic, the process is called intermediate quenching. In step quenching, the steel is transferred to the intercritical annealing temperature from the austenitisation temperature. In all of these cycles, the steel is soaked at the intercritical annealing temperature for a specified time and cooled to room temperature at a suitable rate.

Continuous annealing corresponds to obtaining dual-phase structure in steels in the as hot-rolled condition. The steel sheets are coiled after adequate hot rolling. The cooling rate during coiling is controlled so as to get the required dual-phase structures. Many investigators have simulated the coiling conditions so as to get the dual-phase structure similar to that obtainable on continuous annealing [24, 33, 53].

Whatever heat-treatment cycle may be chosen, the intercritical annealing has to be carried out at a temperature which is between Ae_3 (the upper limit of the critical range) and Ae_1 (the beginning of the transformation range). As the equilibrium conditions are rarely maintained in the steels of commercial purity, the temperatures of practical utility are

Ac_1 and Ac_3 . These critical temperatures can be related to the chemical composition of a steel as follows [37]:

$$Ac_1 = 723 - 10.7 \text{ Mn} - 16.9 \text{ Ni} + 29.1 \text{ Si} + 16.9 \text{ Cr} + 290 \text{ As} + 6.38 \text{ W}$$

$$Ac_3 = 910 - 203 \sqrt{C} - 15.2 \text{ Ni} + 44.7 \text{ Si} + 104 \text{ V} + 31.5 \text{ Mo} + 13.1 \text{ W}$$

The annealing temperature in the $(\alpha + \gamma)$ phase field controls the volume percent of austenite and establishes the austenite carbon content, thus affecting the hardenability of austenite-pools. The hardenability of austenite [38-40] during intercritical annealing decreases with increasing annealing temperature. The increased hardenability at lower intercritical annealing temperatures is apparently due to the higher carbon content of the austenite formed at those temperatures. In some typical dual-phase steels containing Nb and V, it has been observed that after intercritical annealing at 760°C and 810°C the periphery of the austenite pool transforms, on cooling, to new ferrite in the same orientation as the ferrite retained during intercritical annealing. Thus the ferrite forms by an epitaxial growth mechanism without the formation of new interface or grain boundary. In the carbon enriched interior of the austenite pool beyond the epitaxial ferrite [38], only martensite forms in the specimen annealed at 760°C , but various mixtures of ferrite and cementite form in the specimen annealed at 810°C . The latter structure include lamellar pearlite, a degenerate pearlite, and cementite interphase precipitation. However, the cooling rate dictates the balance between shear and diffusion controlled austenite transformation products. At higher cooling rate, the austenite present transforms fully to martensite. However, during slow cooling the austenite pool first decreases in size by epitaxial-ferrite growth on retained ferrite. With continued cooling the remaining austenite, enriched

in carbon, transforms to martensite, bainite or pearlite depending on the alloy content and cooling rate. A schematic microstructure map showing the volume percent of various phases present as a function of cooling rate is shown in Figure 2.2 [41].

2.2.4 Formation of Austenite in Dual-Phase Steels During Intercritical Annealing

As the mechanical properties of dual-phase steels are primarily dependent on the amount, distribution and carbon content of the martensite phase [42], the mechanism of formation of austenite during intercritical annealing of these steels is of considerable importance. The earlier data [43-46] on the kinetics of austenite formation in dual-phase steels shows that at higher temperatures the growth of austenite is controlled by carbon diffusion in austenite phase, and the time for completion of this step is of the order of a few seconds. The austenite formed at lower temperatures follows the simple inverse rule which relates the amount of austenite formed to the carbon content. In fact, at low temperatures, the growth of austenite is controlled by manganese diffusion in ferrite and the time for completion of this step is much longer. The various steps [43] that might be occurring during the transformation of the ferrite-pearlite structure into a ferrite-austenite one are classified into three steps: 1) nucleation of austenite at the ferrite-pearlite interface and its very rapid growth into pearlite until pearlite dissolution is complete; 2) slower growth of austenite into ferrite at a rate that is controlled by carbon diffusion in austenite at high temperature ($\sim 850^{\circ}\text{C}$), and by manganese diffusion in a ferrite at low temperature ($\sim 750^{\circ}\text{C}$); and 3) very slow final equilibration of ferrite and austenite at a rate that is controlled by manganese diffusion in austenite.

Garcia and Deardo [44] described the formation of austenite from 'quenched and tempered' (exhibiting spheroidised Fe_3C in recrystallised ferrite matrix) and 'quenched and tempered plus cold-rolled' (exhibiting spheroidised Fe_3C in a cold-rolled ferrite matrix) starting structures during intercritical annealing of a series of 1.5% Mn-steels containing various carbon concentrations (0.01%, 0.05%, 0.15% and 0.22%). They showed that the kinetics of austenite formation at 725°C , for quenched and tempered starting structure, is not only slow but is also independent of the amount of austenite formed. On the contrary, the formation of austenite was extremely rapid at 850°C ; the reaction being completed in less than one second. Austenite appeared to form slightly more rapidly from quenched and tempered plus cold-rolled starting structures than from only quenched and tempered or ferrite-pearlite starting structures.

2.3 Structure of Dual-Phase Steels

2.3.1 Distribution of Phases

The various heat-treatments and processing schedules have a marked effect on the distribution and morphology of constituent phases in the dual-phase steels [47]. Thus, the intermediate quenching process results in a distribution of fine fibrous martensite in the ferrite matrix, whereas intermediate annealing or intermediate normalizing give rise to a distribution of fine globular martensite along the ferrite boundaries. In the step quenching process, on the other hand, the resulting structure consists of coarse martensite surrounded by ferrite matrix. Evidently the dual-phase microstructure depends on the prior austenite grain size. This being larger in case of step-quenching, the resulting distribution of

phases tends to be coarser here than those obtained from the original martensitic and hypoeutectoid structures.

The ferrite grain size in dual-phase steels is very fine ($\sim 10 \mu\text{m}$ dia.) because it is formed by intercritical annealing of either cold-rolled sheets for very short times or microalloyed controlled-rolled sheets for somewhat longer times. The ferrite is remarkably clean [1, 8, 10, 11, 13] containing insignificant amount of fine carbides, because most of the dispersed carbides present in the as-rolled pearlitic steel dissolve readily on intercritical annealing. Transmission electron microscopy of ferrite reveals unusually high density of dislocations, particularly in the vicinity of the martensite islands. On cooling from the intercritical annealing temperature, usually some ferrite separates out from the austenite producing an extra concentration of carbon in the still untransformed austenite. This new ferrite, forming epitaxially on the old ferrite, is thought to have little or no partitioning of the alloying elements, except carbon, during separation from the austenite. The extent to which ferrite separates is greatly influenced by the balance between ferrite stabilisers such as silicon and austenite stabilisers such as manganese, chromium, vanadium and molybdenum. On further cooling, the remaining austenite transforms to dislocated (lath) martensite or to twinned (acicular) martensite depending on whether the carbon concentration is below or above about 0.35%. This limiting carbon content is greatly influenced by the presence of other alloying elements.

When twinned martensite forms, the final structure always contains some retained austenite, the volume fraction of which increases with increasing carbon content and decreasing M_s -temperature. Many microalloyed dual-phase steels exhibit surprisingly large volume fraction (5-10%) of

retained austenite much of it in small isolated volumes [48-50]. Retained austenite, usually in small volume fractions, is also found in dislocated martensite structures formed from alloyed austenite [9].

2.3.2 Effect of Heat-Treatment on Microstructure

A survey of the literature shows that hardly any systematic study has yet been made to determine the effect of heat-treatment on the fine structure of dual-phase steels. Of course, T.E.M. studies made on different intercritically-annealed dual-phase steels have shown that the fine structure is characterised by regions of high dislocation density close to the ferrite-martensite interfaces and regions of low dislocation density in ferrite grain interiors [34].

Careful T.E.M. studies [47] on dual-phase structures produced in a Fe-2 Si-0.1 C alloy by intermediate quenching, intermediate annealing and step-quenching, have shown no remarkable difference in their structure. The substructure of martensite was found to be similar in all cases. The ferrite regions showed the formation of subgrains in the intermediate quenched and intercritically annealed structures but not in the step-quenched structure.

The typical microstructural features of dual-phase Fe-Mn-Si-0.1 C steels, with and without vanadium, after different treatments have been studied by Nakagawa et al [51]. The results showed that after iced-brine quenching from the intercritical annealing temperature of 800°C, the steels (with or without vanadium) produced a structure consisting of dislocated (lath) martensite islands embedded in the ferrite matrix. The iced-brine quenched steels with vanadium showed a narrow zone of discontinuous precipitation of carbides near the martensite-ferrite interface, whereas

steels without vanadium did not show such features. The microstructures obtained after air cooling from 800°C showed ferrite and a mixture of pearlite and upper bainite in both the alloys (with or without vanadium). After air cooling from 900°C (solution treatment) the steel without vanadium, produced microstructure similar to that obtained by air cooling from 800°C . The small addition of vanadium improved the hardenability to a significant extent causing partial martensitic transformation in spite of the presence of undissolved vanadium carbides after 900°C annealing. An uneven distribution of fine precipitates, assumed to be $\text{V}(\text{C}, \text{N})$, throughout the ferrite matrix has also been reported in an intercritically annealed V-N steel strip [52]. Specimens, intercritically annealed for short periods of time (1-3 min.) at 790°C produced precipitates consisting of two particle size ranges, namely, a finer 40 to 80 \AA size and a coarse 100 to 300 \AA size range. After a longer period of anneal (~ 20 min.) the majority of finer particles disappear, while no change in distribution of larger particles was observed. Intercritical annealing of a Nb-microalloyed dual-phase steel has been found to produce a fine precipitation in the retained ferrite [38]. The precipitates have been assumed to be mainly Nb-carbonitrides, the precipitate dispersion was found to coarsen with increasing annealing temperature.

It has been reported by earlier investigators [48, 53, 54] that small quantity ($\sim 5\%$) of retained austenite may be present in slowly cooled dual-phase steels, especially those containing carbide forming elements. The retained austenite stabilised at room temperature is believed to exist in the form of small equiaxed islands rather than thin films as typically observed in lath martensitic structures [9].

2.3.3 Effect of Tempering on Microstructure

The microstructural changes occurring on tempering the martensite in dual-phase steels are similar to those produced by tempering quenched, conventional low-alloy steels [9]. It has been reported that tempering between 200 and 300°C has an important influence on the ferrite [55] reducing the carbon in solution. Koo and Thomas [56] did not observe any appreciable change in the martensite morphology after tempering their dual-phase steels containing 30% martensite at 200°C for one hour.

2.4 Mechanical Properties of Dual-Phase Steels

2.4.1 Typical Stress-Strain Curves for Dual-Phase Steels

Typical stress-strain curves for a plain-carbon steel, a high strength low alloy SAE 980X steel and an intercritically annealed dual-phase SAE 980X steel are shown in Figure 2.3 [58]. The low yield strength, continuous yielding, high initial work-hardening, large uniform and total elongations — these are the characteristics which distinguish the dual-phase steel from the other two.

The strain-hardening exponent for low carbon and microalloyed steels can be determined from the linear behaviour of the $\log \sigma$ versus $\log \epsilon$ plots obeying the power law of Hollomon [57]:

$$\sigma = K \epsilon^n$$

where σ is the true stress, ϵ is the true plastic strain, n is the work-hardening exponent and K is the strengthening co-efficient. Similar behaviour has been obtained for a number of dual-phase steels also [58, 59]. However, deviation from linearity has been observed for a few other

dual-phase steels [60], indicating that the power relation may not be applicable there. In such a situation, the work-hardening exponent can be evaluated at any specified strain level from the slope of the curve at that point [10]. In fact, considerable variation has been noticed in the value of n_i which stands for an incremental value of n for a small increment of plastic strain for small straining. For alloys exhibiting multiple n -behaviour, the analysis suggested by Crussard [61] and Jaoult [62] has been found to be more suitable than Hollomon's analysis. They used the Ludwik equation [63] :

$$\sigma = \sigma_y + K \epsilon^n$$

where σ_y is the yield strength and K and n are constants. In the Jaoult-Crussard analysis, the Ludwik equation was re-written as :

$$\ln\left(\frac{d\sigma}{d\epsilon}\right) = \ln(Kn) + (n - 1) \ln \epsilon$$

The plot of $\ln\left(\frac{d\sigma}{d\epsilon}\right)$ versus $\ln \epsilon$ delineates several distinct stages of strain-hardening during deformation, particularly at low strains. Similarly, an analysis based on the Swift equation ($\epsilon_p = \epsilon_0 + C \sigma^m$, where ϵ_p is the true plastic strain and ϵ_0 , C , m are constants) utilises a $\ln \frac{d\sigma}{d\epsilon}$ versus $\ln \sigma$ plot to determine the parameters ϵ_0 , C and m .

2.4.2 Strength and Ductility

The high strength steels [64] to be used for automobile components must possess two important mechanical properties, namely, high tensile strength, which is roughly proportional to both the fatigue and crush resistance; and large total elongation which may be taken as a reasonable

measure of formability. Yield strength, on the other hand, appears to be relatively unimportant from an engineering or application viewpoint. Figure 2.4 [65] shows a plot of total elongation as a function of ultimate tensile strength for some of the commercially available high strength steels. The much superior performance of dual-phase steels compared to the conventional high strength steels is quite apparent from this figure.

It is now generally agreed that the strength of dual-phase steels is linearly proportional to the volume fraction of martensite present in the structure. Figure 2.5 [21] shows the variation of the 0.2% flow stress and the tensile strength as a function of percent martensite for a series of Fe-Mn-C dual-phase steels. These steels were heat-treated in the intercritical region and then quenched to give structures containing various amounts of martensite, and martensite with different carbon contents. It also appears that the strength of these dual-phase steels is independent of the carbon content of the martensite.

It has been pointed out [66, 67] that the dual-phase steels obey the theory of composites. This theory makes three basic assumptions :

- a) the two-component phases and the composite obey the power law,
- b) perfect interface matching exists between the component phases, and
- c) the second-phase is in the form of aligned fibres.

It has been reported by Koo and Thomas [56] that ferrite and martensite in dual-phase steels have perfect interface matching. Although martensite in dual-phase steel is not aligned, at least during the initial stages of deformation, it has been suggested by Davies [28] that this basically geometric consideration may be unimportant in calculating the load bearing capacity of these steels. The theory predicts that, to a first approximation, the tensile strength of the composite is proportional

to the amount of second phase (law of mixtures), and that the ductility will be less than that indicated by the law of mixtures [66]. Numerous analytical expressions [21, 42, 50, 68, 69] have been suggested by a number of workers to calculate the tensile strengths of dual-phase steels from the volume fractions of martensite.

It has been found out that the tensile strength of dual-phase steels increases with increase in the strength and hardness of the constituent ferrite phase. In fact, it has been suggested that for optimum mechanical properties in a dual-phase steel, the ferrite should be very fine-grained ($\sim 3 \mu$ size), free of fine precipitates and strengthened by substitutional alloying additions, such as silicon, which do not have much effect on ductility.

A number of studies [21, 22] on several series of dual-phase steels have shown that, for dual-phase steels with upto about 30% martensite, the ductility of the composite is sensitive to the strength and ductility of the matrix. In other words, the ferrite matrix should be as strong as possible, maintaining at the same time a high ductility. However, it is common knowledge that higher the strength of the ferrite, the lower will be its ductility. The only way to get around this problem is to add some substitutional solute atoms which may increase the strength of ferrite proportionally more than the decrement they cause in the ductility values [22].

Superior strength/ductility combinations imply superior work-hardening behaviour [64]. A plot of the work-hardening rate as a function of strain for a number of conventional and dual-phase steels (Figure 2.6) show that the dual-phase steels have significantly higher work-hardening rates at all strains. Thus a fundamental understanding of the superior strength/ductility behaviour of dual-phase steels must involve the

understanding of the mechanisms of work-hardening in these steels.

2.4.3 Deformation Behaviour

Attempts have been made for predicting the deformation behaviour of dual-phase steels by using models [66] developed for composites. Dual-phase steels have been considered as composites of strong martensite and soft and ductile ferrite [17, 56, 71]. Two limiting models are available for two-phase composites. These are the equal-strain and the equal-stress models. The equal-strain case in dual-phase steel is not fulfilled [72] as because there is partitioning of strain as well as stress, between the ferrite and the martensite, such that the strain is considerably lower in the harder component than the softer. The equal-stress case seems to be totally unrealistic since it requires a very small fraction of ferrite which undergoes an extremely large strain [73]. For dual-phase steels containing a hard phase distributed in a soft matrix, an intermediate situation seems to be valid [74]. This means that neither the strains nor the stresses are equal in the two phases. However, Öström [73] concluded that the analysis, on the basis of the intermediate theory, suffers from a number of drawbacks. In fact, all the above theories completely overlook the size, shape, number and the distribution of the martensite islands in ferrite matrix which influence the deformation behaviour of dual-phase steels. These aspects should have to be considered in order to propose a realistic model to explain the mode of deformation and the mechanical properties of dual-phase steels.

The fracture behaviour of dual-phase steels has also been studied by a number of workers [75, 76]. A number of mechanisms have been proposed by them to explain the fracture of dual-phase steels caused by tensile

and other kinds of load. Systematic work done on a number of Mn-Si-V dual-phase steels [77] has indicated that no single fracture mechanism operates in dual-phase steels. On the contrary, all of the following mechanisms could be operating almost simultaneously. These are (1) decohesion at ferrite-martensite interface, (2) fracture of martensite, (3) crack formation in ferrite with localised high stresses, and (4) void formation around inclusions. It has been suggested that [77] during tensile loading the load will be transferred via the softer ferrite matrix to the harder martensitic phase which, as a result, will be subjected to an excess of stress. During the later stages of this process decohesion of the martensite-ferrite interfaces may occur. Nearing the end of the uniform elongation stage, some of the martensitic areas, where sufficient stress has already been built up, may fracture. At the same time voids may be formed around the larger inclusions due to the tensile stress. These large voids may be linked up by small-sized microvoids initiated at smaller inclusions. As a result of all these, the effective cross-sectional area of the specimen will go on decreasing very fast leading to necking. At this stage the ruptured martensitic areas may act as sharp notches leading to cleavage cracks in the ferrite which finally leads to cleavage fracture of entire ferrite grains.

2.4.4 Sheet Formability

The formability of sheet metals depends, to a large extent, on their mechanical properties, in particular, their ability to distribute strain. This is characterised by the dimensionless parameter, $\frac{1}{\sigma} \frac{d\sigma}{d\epsilon}$, where σ is the current value of flow stress and $\frac{d\sigma}{d\epsilon}$ is the current rate of hardening. This parameter decreases in successive stages, as the strain

increases, with the consequence that the material becomes progressively less able to spread the strain to less deformed parts. The strain ultimately concentrates into a diminishing volume causing a ductile fracture by void growth and coalescence [59]. Therefore, the property requirements which strongly influence the formability of sheet metals are :

- a) its work-hardening behaviour which may be estimated from its work-hardening coefficient, ' n ',
- b) plastic anisotropy,
- c) strain-rate sensitivity, ductility and also the temperature of forming.

All metallurgical factors which influence these properties can be used to improve or control the formability of a sheet metal.

The work-hardening coefficient ' n ' can be used to measure the degree to which a material can distribute strain or work-hardening effectively. Materials with high ' n '-value will be able to sustain work-hardening more and will prevent localised strain concentrations within the material.

The property of having different strengths in the plane of the sheet and normal to the sheet is called 'normal anisotropy' and the property of having different strengths along different directions in the plane of the sheet itself is termed as 'planar anisotropy'. It is common practice to refer to both the properties simply as 'plastic anisotropy'. Press performance, combining stretching and drawing operations, correlates with both strain-hardening exponent ' n ' and plastic anisotropy. The directionality of properties is characterised by the ' r '-value (also called the plastic strain ratio) which was originally suggested by Lankford et al [78]. It is defined as :

$$r = \frac{\epsilon_w}{\epsilon_t} = \frac{\ln \frac{w_o}{w_f}}{\ln \frac{t_o}{t_f}}$$

where ϵ_w and ϵ_t are the true strains in the width and thickness directions, w_o and w_f are the initial and final widths, and t_o and t_f are the initial and final thicknesses. Considering the fact that the strength in the plane of the sheet itself can be different along different directions, an average strain ratio can be determined by averaging over the strain measured parallel (r_o), transverse (r_{90}) and at 45° (r_{45}) to the rolling direction; i.e.,

$$\bar{r} = \frac{r_o + 2r_{45} + r_{90}}{4}.$$

In general, it is found that r_o , r_{45} and r_{90} have significantly different values for a given sheet material. This condition leads to the formation of 'ears' in thin sheets. It has been found necessary to adopt yet another parameter Δr defined as follows :

$$\Delta r = \frac{r_o + r_{90} - 2r_{45}}{2}$$

For a sheet metal which is fully isotropic, \bar{r} would then be equal to unity and Δr equal to zero. $\bar{r} > 1$ indicates that the average strength in the plane of sheet is lower than that across the thickness and vice versa for the situation when $\bar{r} < 1$. Consequently, sheet steels with \bar{r} -values much larger than unity will be highly resistant to uniform thinning and therefore very desirable for the purpose of deep-drawing. Whiteley et al [79, 80] have demonstrated that in drawing, the higher the \bar{r} -value of the material the deeper is the draw.

Although the stretch formability of dual-phase steels is excellent in relation to their strength level, the deep drawability tends to be less impressive because of the following facts. Firstly, it is difficult to develop the appropriate crystallographic texture necessary for high normal anisotropy (high \bar{r} -value) because of alloy additions as well as fine carbide dispersions which must be present in the hot band prior to cold rolling. Secondly, it has been shown [81-83] that even when texture is suitable, the hard martensite phase perturbs the ferrite deformation and so reduces the \bar{r} -value of the steel. Kurihara et al [82] showed that this degradation of the \bar{r} -value is dependent on the volume fraction and proximity of the martensite islands and the hardness ratio for the martensite and the ferrite constituents. Hutchinson [84] showed that both normal and planar anisotropy are reduced by the presence of martensite constituent in dual-phase steels. This reduction is due to the superimposition of an isotropic hardening component on an anisotropic matrix. An additional factor which may influence drawability of dual-phase steel [85] is the presence of a strength differential between tension and compression and this effect may be expected to increase the flow stress in the flange deformation zone relative to the base or wall of the pressing. Such a situation will lead to a reduction in deep-drawability.

2.5 Recrystallisation and Texture Development in Dual-Phase and Conventional Deep-Drawing Quality Steels

2.5.1 Phenomenon of Recrystallisation

The normal process of recrystallisation of deformed metals consists in the nucleation of small regions of nearly defect-free crystals or grains and their growth into the surrounding deformed material. It is now widely accepted that recrystallisation does not involve nucleation in

the classical sense [86], but is a continuous process of growth in which the embryo is at all stages stable with respect to its surroundings. The growth process, however, does not occur with a constant velocity. There is an initial incubation period in which only slow change or growth (primary) takes place, normally followed by a very sharp rise in rate, known as the secondary growth stage. Three conditions must be satisfied if a given volume of cold-worked matrix is to generate a recrystallised grain by growth from a cell or subgrain. A high local stored energy (small cell size) should be present to provide a high driving force. There should be a steep spatial gradient of stored energy (wide distribution of cell sizes or cell-boundary misorientations) to develop local instability, and finally there should be a sharp lattice curvature so that a growing embryo can quickly achieve a high-angle boundary.

2.5.1.1 Nucleation

The driving force for primary recrystallisation is the stored energy of the previous working processes. However, nucleation appears to be a highly heterogeneous phenomenon [87-93] occurs mainly at particular features of the microstructure such as prior grain boundaries, deformation bands and inclusions. As a consequence, to investigate the process of nucleation, studies on the detailed microstructure of the identified potential nucleation sites in the deformed material [94, 95] are required. This has been done by means of a number of direct observation techniques such as high-voltage electron microscopy [96, 97] or photo-emission electron microscopy [98, 99]. The indirect approach includes highly resolving metallographic techniques such as transmission electron microscopy (T.E.M.) [94, 95] along with selected area diffraction facility and Kossel X-ray diffraction [98, 100, 101] technique. It is now known that nucleation

consists of the selective growth of preexisting subgrains [102, 103] that have, or very rapidly acquire a misorientation of greater than 15° - 20° with respect to the immediate neighbourhood. Such subgrain structures are produced in the deformed state in very heavily deformed metals. Although in a few cases coalescence of several smaller subgrains leading to a large one [104-108] is required before nucleation could occur, it does not necessarily mean that coalescence is always necessary. Since coalescence is apparently a slow process [109, 110], if an enlarged subgrain with a high local misorientation has been produced by the deformation process alone, then nucleation can occur without any subgrain coalescence [111]. In most of the cases, however, growth of subgrains takes place by way of subgrain-boundary migration, leading ultimately to the formation of a recrystallisation nucleus.

Nucleation within grains is commonly observed only after moderately high deformations, since at low strain the lattice curvature is not sufficient to allow a high-angle boundary to be created. Dillamore et.al. [111, 112] have found out that in the substructure of a heavily deformed material, the local value of the strain energy varies with the orientation of the rolling plane. Thus in cold-rolled iron, for a $[110]$ rolling direction, the stored energy calculated by Dillamore et.al. [112] rises as the rolling plane alters from (001) , through $(1\bar{1}2)$ and $(1\bar{1}1)$ to $(1\bar{1}0)$. It was pointed out by them that this sequence of increasing stored energy corresponded to an increasing Taylor M-value ($= \sum d\gamma/dc$, where $\sum d\gamma$ is the sum of the shears on the operating slip planes and dc is the largest principal strain). On the basis of the above ideas, it may be concluded that the ease of nucleation would be orientation sensitive. The variation

of the rate of nucleation with orientation, according to these models, is shown schematically in Figure 2.7. As per this figure, during subsequent recrystallisation anneal, the (011) and (111) texture components should nucleate first and therefore have the longest available time for growth before impingement occurs. The very low density of the (011) orientation in the cold-worked material, however, means that this is unlikely ever to become very strong. The least favoured orientation, (100), is predicted to disappear on annealing due to its consumption by the growth of grains having other orientations. Thus, the most favoured orientation after the recrystallisation anneal is going to be (111) and predominance of this texture component has, in fact, been confirmed in recrystallised steels [113].

So far as nucleation at grain boundaries is concerned, two mechanisms have been suggested which may lead to formation of recrystallised grains. Either the existing boundary may bow out into the grain which has the higher stored energy at the boundary, or else the nucleus may develop from a subgrain close to that grain boundary. For both types of mechanism, the new grain orientations would be close to the orientation of the matrix in which they formed. However, the relevant matrix orientations near to the grain boundaries are generally rotated away from that of the grain centres. Therefore, the above two mechanisms would be expected to introduce recrystallisation texture components that have orientations near to, but not at, the deformation texture components.

When the deformation of metals is constrained, as in polycrystals, single grains are often observed to deform inhomogeneously leading to mutually misoriented blocks (deformation bands) separated by narrow boundaries which accommodate the misorientations between the blocks. These

boundaries have been named micro-bands [94] or transition bands [95]. These are made up of closely spaced sub-boundaries, which manifest cumulative misorientations. Because of the high local stored energy and the rapid change of orientation across the elements of a transition band, a high angle boundary can be easily generated there and this will, therefore, favour nucleation in those sites. Dillamore et.al. [111] showed that for b.c.c. metals like iron the most favourable orientations for nucleation at transition bands are $\{110\} \langle 00 \rangle$, $\{100\} \langle 011 \rangle$ and $\{11, 11, 8\} \langle 4, 4, 11 \rangle$ (near $\{111\} \langle 112 \rangle$ orientation) in that order. A second kind of transition bands may be formed in crystals of almost any orientation at low or moderate strains [114]. Nucleation at these sites is expected to contribute to the weak or random recrystallisation textures so often observed following low deformations. Nucleation within transition bands differs from that described earlier in the sense that the orientations of the new grains upon recrystallisation may differ widely from those of the deformation textures.

2.5.1.2 Effect of Second Phases

As a general rule, presence of widely spaced coarse particles enhances nucleation and the rate^{of}/recrystallisation if present before deformation [115], while finely dispersed particles normally reduce the recrystallisation kinetics, having a greater retarding influence on nucleation than on growth [116]. Precipitation during recrystallisation (discontinuous precipitation) should theoretically be capable of increasing the growth rate, though there does not seem to be any clear evidence for such behaviour in practice.

The recrystallisation textures are greatly affected by the way in which second phases influence the process of recrystallisation. Depending

on the particular system used, similar effects may be obtained where the second phase is precipitated before deformation or in a deformed structure prior to recrystallisation. Fine dispersions of second phase particle, like niobium carbide [117] and titanium carbide [118] (forming before deformation) or aluminium nitride [119] and copper [120] (forming in the deformed structure prior to recrystallisation), all have been found to have a relatively larger retarding effect on the overall nucleation rate than on the growth rate. In such cases the recrystallisation texture will show increased selectivity and will become even more strongly biased towards the most favoured orientation nuclei. In case of steel, precipitates, such as AlN, NbC and Cu have precisely this effect under suitable circumstances, and lead to considerable strengthening of the {111} texture components at the expense of those near {100}. In addition to the overall retardation of nucleation rate, it is possible that fine scale precipitation may interact adversely with certain types of nucleation site. For example, where AlN is effective in strengthening {111} textures in steel, it also acts to suppress the {110} sheet-plane texture [121] and particularly the Goss component {110} <001>.

2.5.1.3 Effect of Solid Solutions

It is common to observe that the addition of second elements, which form solid solutions in the parent metal, also give rise to changes in texture. As an example may be cited the works by Hu and Goodman [122], and Hughes and Page [123] in steels with varying manganese contents. They showed that reduction in manganese level (except at very low levels) causes an increase in the {111} texture components and therefore an improvement

in normal anisotropy and drawability. Giles et.al. [124] also found similar results in a comparative study of normal and low-Mn steels. In general, the effect of solid solution elements is to weaken the sharp textures found in pure metals and to lead to extensive retention of rolling texture components in cases where solute drag is particularly strong.

2.5.1.4 Texture Development During Grain Growth

After primary recrystallisation is complete there is usually a rather diffuse spread of orientations together with the recrystallisation texture components, which are often not very strong. These components strengthen at the expense of the diffuse spread, and there is sometimes a redistribution of density between different components during the subsequent grain-growth process. By this process of texture sharpening the densities of the Goss component and the {111} sheet plane orientations are enhanced in steel where these are present after recrystallisation [125]. The explanation of this behaviour is to be found in the mechanism of grain growth and the structure produced by recrystallisation [126]. During grain growth, large grains grow at the expense of small ones in a manner which Hillert [127] has described by the equation

$$\frac{dR}{dt} = K \left(\frac{1}{R_{cr}} - \frac{1}{R} \right)$$

where R is the radius of the grain under consideration and R_{cr} is a characteristic or average grain size. Grains larger than R_{cr} grow, while those that are smaller shrink and disappear. If the grain-size distribution for grains of a particular texture component is biased to larger sizes than the average distribution, then these grains will prosper during the growth

process and their texture will be correspondingly strengthened. The constituent grains of the recrystallisation texture are those that nucleated first and therefore have had the longest time for growth into the cold-worked matrix. They may also have been favoured by an enhanced growth rate. In cases where the initial growth stage has been strongly impeded, for example, by solute drag, the orientation-dependence of grain size may be reduced with the result that subsequent grain growth causes little change in the texture.

When second-phase particles are present in sufficient numbers these may provide a constant reaction to the movement of grain-boundaries, thus modifying the fundamental equation of growth to

$$\frac{dR}{dt} = K \left(\frac{1}{R_{cr}} - \frac{1}{R} + Z \right)$$

where Z is the reaction term due to particles, which always acts to decrease the absolute value of dR/dt .

2.5.2 Texture and Its Representation

It is now known that for hot-rolled or cold-rolled and fully annealed metals and alloys there exists a certain degree of preferred orientation or texture of the grains with respect to some crystallographic planes and directions. Texture affects, amongst others, the mechanical and physical properties of materials. For example, sheet formability of a metal is very much influenced by its annealing or recrystallisation texture. In fact, examination of textures can provide useful complementary informations in the study of recrystallisation and related phenomena.

Textures are usually represented by means of pole-figures. These are simple stereographic projections which show the distribution of particular crystallographic directions in the assembly of grains that constitute the metal. Of course, the pole-figure does not have any meaning unless it contains some reference directions. These are normally taken as some well-defined direction in the specimen itself. For example, in case of rolled sheet material the rolling direction (RD), the transverse direction (TD) and the normal direction (ND) are usually taken as the reference directions in the corresponding pole-figure. Figures 2.8(a) to (e) illustrate the procedure for representing texture by pole-figures. In fact, the sheet is considered to sit at the centre of the stereographic sphere with RD, TD and ND directions as the X, Y and Z axes (Figure 2.8a). The orientation of a single grain in the sample can then be easily represented by plotting, say, its three (100) poles in a pole-figure. Normally, all the poles concerned are projected on to the equatorial plane producing a stereographic projection (Figure 2.8b). For a polycrystalline sample the (100) poles for all the grains should be similarly plotted in the pole-figure. If the resulting plot shows that the poles are distributed rather uniformly over the area of the projection then there is obviously no texture and the specimen is said to possess a 'random' texture. In practice, however, the poles tend to cluster together in certain areas of the pole-figure to produce a texture (Figure 2.8c). It is usual to collect data from many grains simultaneously and to present this in the form of density contours on the pole-figure (Figures 2.8d-e). The density values are expressed relative to that which would be expected for a specimen having a random orientation.

In texture work the most important method in the past and probably also in the coming years is to measure pole-figures by X-ray diffraction. Uptil now many interesting goniometer variations have been developed and it is possible now to draw fairly accurate pole-figures from X-ray diffraction data. Two X-ray diffraction methods must be used to cover the whole pole-figure. The first of these, called the transmission method, is due to Decker, Asp and Harker [128] and the second method, called the reflection method, is due to Schulz [129]. No quantitative measurement of texture is, however, possible from pole-figures. The fundamental reason for this is that a general orientation has three degrees of freedom whereas a pole-figure specifies only two independent variables. Such figures are, therefore, only 'projections' of the three-dimensional orientation distribution function (O.D.F.) which is the full description of a texture. Mathematical methods have been developed which allow O.D.F.'s to be calculated using numerical data obtained from several pole-figures. The procedure of Williams [130] uses an iterative least squares solution while Roe [131] and Bunge [132] independently proposed methods using generalised spherical harmonics. The latter methods have been most widely used.

An O.D.F. describes the orientation density in a three-dimensional orientation space formed by the three Euler angles ψ_1 , ϕ and ψ_2 , which describe the rotation of the crystallographic into the specimen co-ordinate system. Figure 2.9 shows how, using the Euler angles, the transformation of the sample frame S into the crystallite frame C occurs by a set of three consecutive rotations namely :

1. A first rotation ψ_1 around the normal direction ND transforming the transverse direction TD and the rolling direction RD into the new directions TD' and RD' respectively. ψ_1 has to have such a

value that RD' will be perpendicular to the plane formed by ND and $[001]$.

2. A second rotation ϕ around the new direction RD' with having such a value that ND is transformed into $[001]$ ($= ND'$) and TD' into TD'' .
3. A third rotation ψ_2 around $[001]$ ($= ND'$) with ψ_2 having such a value that RD' is transformed into $[100]$ and TD' into $[010]$.

The O.D.F. is then mostly plotted by contour lines in a series of sections through the Euler space. The O.D.F. can, in practice, be obtained if the different orientations and their volume fractions are known. In this way three-dimensional O.D.F.'s could be derived for a number of metals and alloys from selected area diffraction measurements done on their foils in a transmission electron microscope. This method, however, is extremely laborious. Therefore, now-a-days the O.D.F. is mainly reproduced from a series of pole-figures by the application of the series expansion method. In this method the O.D.F. is expanded in a series of generalised spherical harmonics $C_{\lambda}^{mn} T_{\lambda}^{mn}(\psi_1 \phi \psi_2)$ and the expansion coefficients C_{λ}^{mn} are derived from the corresponding series expansions of the pole-density distributions (pole-figures).

Although the methods involved in determining an O.D.F. are quite complicated as compared to a conventional pole-figure, the much higher resolution of the former in comparison to that of the latter more than justifies taking all the trouble to go for an O.D.F.

2.5.3 Development and Control of Annealing Textures in Conventional Deep-drawing Quality Steels and Dual-Phase Steels

2.5.3.1 Conventional Deep-drawing Quality Steels

Conventional deep-drawing quality steels basically fall into two categories, namely, rimming and aluminium-killed. The differences in composition primarily relate to their oxygen content, i.e., deoxidation practice. Rimmed steels have a low \bar{r} -value, around 1.0-1.3, and are characterised by a very flat (weak) texture. The strongest components in this weak texture are $\{111\} \langle 110 \rangle$ and $\{111\} \langle 112 \rangle$, but there is also present a significant amount of the detrimental $\{100\} \langle 001 \rangle$. Al-killed steels yield much higher \bar{r} -values (1.6-1.8) and are characterised by a much stronger $\{111\}$ -type texture and much weaker $\{001\}$ component. The recently developed low-Mn and P containing steels also exhibit strong $\{111\}$ texture and high \bar{r} -values [133].

The interstitial-free Ti-stabilised steels have higher \bar{r} -values than Al-killed steels and are characterised by a sharp $\{554\} \langle 225 \rangle$ texture which differs from the $\{111\} \langle 112 \rangle$ orientation by only 6° [134]. Steels stabilised with Nb also yield high \bar{r} -values and exhibit a sharp $\{554\} \langle 225 \rangle$ type texture.

The control of \bar{r} -values in deep-drawing steels would obviously depend on the control of the development of a suitable texture which, in turn, involves the careful control of metallurgical processing parameters and composition. The effects of these parameters are discussed below.

a) Composition : The major compositional factors which contribute to the formation of annealing textures in deep-drawing quality steels are : carbon content and cementite, the aluminium nitride reaction in killed steels, nitrogen content and nitrides, manganese content and its

interactions, effect of phosphorous, titanium and niobium plus the effect of some other elements like Si, Ni, Cr etc.

In general, for a steel, \bar{r} -value increases progressively with decrease in the amount of carbon. In conventional commercial practice a carbon content around 0.05% is satisfactory for the production of deep-drawing quality steels. However, at much higher carbon contents, the percent cold reduction and the annealing cycle have to be suitably modified [135]. The prior cold reduction that correspond to the maximum \bar{r} -value is found to change from ~70% for higher carbon steels to ~90% for the lowest [135, 136]. The above behaviour has been observed after box annealing with slow heating. Later work have indicated that carbon levels and carbide dispersions are even more critical during continuous annealing. Experience has shown [137-140] that final textures are improved by coiling the hot band at higher temperature, i.e., above ~700°C, which causes much coarser dispersion of cementite. With progressively higher coiling temperatures, the carbide constituents become coarser and more widely dispersed. Although there has been much discussion as to why a coarse carbide dispersion is favourable for texture development during rapid annealing, some disagreement still remains. Much evidence has now been accumulated [137, 138, 141, 142] to show that the major factor here is the purity of the ferrite matrix with respect to carbon during the annealing process. If the carbides are widely spaced and if the steel is heated rapidly after cold-rolling, it is possible for recrystallisation of ferrite to take place before significant re-solution of the carbon can take place. The resulting texture contains a strong {111} component.

In case of Al-killed steels, it is desirable to have an optimum

soluble aluminium content of 0.025-0.040% and nitrogen level of 0.005-0.01% for the best \bar{r} -values [143]. Leslie et al [119] confirmed that recrystallisation of cold-rolled steel could be modified by the precipitation of aluminium nitride (AlN), and identified quantitatively the necessary conditions for successful processing. Like the nuclei of other orientations, the growth of the more strongly driven {111} nuclei must also be hindered by the AlN, but, in the absence of competitive nuclei, eventually come to dominate the final texture. So far as is known, the dissolved aluminium and nitrogen play no special role during cold-rolling, but strongly influence recovery and recrystallisation on subsequent annealing. During slow heating a process of agglomeration of nitrogen and aluminium occurs, which retards structural changes in the steel and modifies the resulting texture.

The condition of maximum plastic anisotropy is accompanied by a maximum grain elongation or 'pancaking' and also corresponds to a maximum grain size in the annealed product [144]. It is now agreed that the pancake grain structure after recrystallisation results from the reduced nucleation frequency and the extended growth range of the new grains, combined with the tendency for AlN precipitation to occur in 'sheets' on prior grain-boundaries and sub-boundaries.

Tungsten additions [145] yield large \bar{r} -values; however, resistance to strain aging in these steels is not satisfactory. Duggan and Hutchinson [146] reported a strong (111) type annealing texture in a steel containing 1.2% copper. Addition of large amount of Cu gives rise to diminishing stretchability and also shows a poor resistance to strain aging. Large amount of work has been carried out in recent years on Ti and Nb-treated deep-drawing steels. Addition of Ti and Nb in sufficient quantities to

remove carbon and nitrogen from solid solution, considerably increases the \bar{r} -values of the steels [118, 134, 136, 147, 148]. A ratio (wt. %) of $[\text{Ti}]/\{[\text{C}] + [\text{N}]\} > 10$ and a ratio (wt. %) of $[\text{Nb}]/\{[\text{C}] + [\text{N}]\}$ of about 8 seem to be optimum [150, 151, 152].

It is now-a-days agreed [136, 148, 150-153] that annealing textures in Ti and Nb-treated deep-drawing steels are controlled by precipitated carbonitride particles, which interfere with the nucleation and growth of recrystallised grains. Hu [133] has reported that the characteristic texture of AlN steels is $\{111\} \langle 110 \rangle$, whereas with Ti, Nb and most other recently developed steels the texture is usually centred on $\{111\} \langle 112 \rangle$ or, more precisely, on $\{554\} \langle 225 \rangle$. Besides improving \bar{r} , Ti or Nb-addition also helps in controlling strain-aging.

The addition of vanadium, which is also a carbonitride former can increase the \bar{r} -value [143], but not to the same extent as Ti or Nb. The new generation of extra-deep-drawing steels is therefore expected to be primarily treated with these elements.

Manganese, which almost invariably represents the largest alloy content in deep-drawing steels, is perhaps also the most complex addition in its effects on annealing-texture formation. A low Mn-content [122, 133, 154], preferably below 0.05%, is found to be effective in increasing \bar{r} in low-carbon steels, which is associated with strong $\{111\}$ texture components. When the level of Mn goes below 0.005% an erratic behaviour is observed showing drastic drop in \bar{r} , suggesting a possible role of other impurities. As Mn-content increases above 0.1%, a decrease in $\{111\}$ component intensity during recrystallisation followed by a gradual increase through grain growth, has been observed [133, 155].

The influence of P-addition on the drawing properties of low-carbon steel sheets is characterised by their usually high \bar{r} and low Δr -values in almost direct proportion to the percentage of phosphorous [156-161]. The recrystallisation texture of these steels consist of a very strong $\{111\} \langle 112 \rangle$ component. According to Matsudo et al [162] phosphorous improves the texture only when carbides are present and when slow heating is used. In the absence of carbon, P is clearly deleterious to texture. It is important to note that P also acts as an antidote to the deleterious effects of Mn and dissolved carbon [158].

Tungsten and copper additions [145, 163] are found to increase the \bar{r} -values of deep-drawing steels. Additions of silicon in quantities upto 0.1% seem to have little influence on recrystallisation or the resulting texture [122].

b) Processing Variables : The final quality of cold-rolled and annealed low carbon sheet materials depends on every stage in the processing history, which includes hot-rolling, cold-rolling and annealing cycles. It is certainly necessary to control the conditions of hot-rolling appropriately along with the critical soaking treatment preceeding this, especially with Al-killed steels during recrystallisation anneal. For practically all types of deep-drawing steels it is required to finish rolling slightly above A_{r3} transformation temperature with the intention of producing a fine hot-band grain size while avoiding the presence of deformed ferrite or premature precipitation of AlN [164-166]. In case of Nb-treated extra low carbon steels, the final \bar{r} -values increase with heavy reductions, low finishing temperature, and high rolling speed, apparently

in relation to the grain size and carbide dispersions in the resulting hot band [167].

The effect of cold-rolling reduction in controlling the texture and deep-drawability of annealed steels is of utmost importance [113, 168-170]. With small cold reductions, a weakly developed texture is finally obtained which contains the Goss component, $\{110\} \langle 001 \rangle$, in addition to the $\{111\} \langle 110 \rangle$ orientation. On increasing cold-reduction the Goss component is weakened and the $\{111\}$ intensity increases and the centre of spread changes from $\{111\} \langle 110 \rangle$ to $\{111\} \langle 112 \rangle$ which is very near to the $\{554\} \langle 225 \rangle$ orientation [171]. After still higher deformation the $\{111\}$ component continues to increase, but is accompanied by near- $\{100\}$ components, such as $\{411\} \langle 148 \rangle$ and $\{411\} \langle 011 \rangle$ which are very harmful to useful plastic anisotropy. The optimum amount of cold reduction of about 70-80% has been considered fruitful for both rimmed and Al-killed steels to achieve the best \bar{r} -values [113, 143].

The coiling temperature of the hot-rolled strip and the heating rate in the annealing cycle following cold-rolling are two other process variables of great significance. These parameters, generally show their combined effect on texture development, and also interact in a complex way with other variables [144, 150, 172, 173]. Figure 2.10 summarises a number of typical behaviour patterns for various classes of deep-drawing quality steels.

Higher annealing temperatures will generally improve the anisotropy of the product, but a temperature above the eutectoid causes austenite transformation and coarse grain boundary cementite precipitations during the subsequent slow cooling stage. They may have a very adverse effect on ductility. In order to avail annealing temperature even upto

900°C, it is advisable to remove carbon by open coil decarburisation or by combination with Nb or Ti [174]. Above this temperature, the $\alpha \rightarrow \gamma \rightarrow \alpha$ phase transformations cause the ferrite texture to be almost randomised so that any anisotropy is destroyed. In case of continuous annealing practice, the cooling rate is sufficiently high to avoid the problem of grain boundary cementite precipitation, and so annealing in the intercritical range can be employed with advantage.

2.5.3.2 Textures in Dual-Phase Steels

Only a limited amount of results on texture studies in dual-phase steels is available in the literature. It is known that dual-phase microstructures can, in theory, be obtained practically in all sheet steels reheated to the intercritical range, where both austenite and ferrite co-exist, followed by accelerated cooling which transforms the austenite phase into martensite. Alternatively, dual-phase steels can be produced directly from the rolling heat in hot-strip mills. It has been shown [175] that for the former type of processing texture components of the type $\{111\} \langle 110 \rangle$, $\{111\} \langle 112 \rangle$, $\{337\} \langle 110 \rangle$ and $\{337\} \langle 776 \rangle$ may be obtained in dual-phase steels. The intensity of the $\{111\} \langle uvw \rangle$ components have been reported to be quite moderate, whereas $\{337\} \langle uvw \rangle$ components have extremely low intensity. It has been suggested that both $\{111\}$ and $\{337\}$ type fibre textures may be present in intercritically annealed dual-phase steels in addition to some minor components such as $\{310\} \langle 001 \rangle$ and $\{110\} \langle 001 \rangle$.

It has also been reported [176] that the textures in hot-rolled dual-phase steels can be described as $\{111\} \langle 011 \rangle + \{111\} \langle 112 \rangle$ for some and $\{112\} \langle 110 \rangle$ for other compositions. In an "as hot-rolled"

chromium-molybdenum steel, the texture has been found to change from $\{110\} \langle 001 \rangle$ type near the sheet-surface to $\{100\} \langle 011 \rangle + \{111\} \langle 112 \rangle$ type towards the mid-section [177].

Very little research effort seems to have been devoted to the development of dual-phase steels with good deep-drawing properties. It is known that for the purpose of producing a dual-phase steel with good deep-drawability, it is necessary to develop a strong $\{111\}$ texture in the annealed sheet. Work by Ray [178] on a 0-Mn-Si-V dual-phase steel has shown that cold-deforming the intercritically annealed (at 750°C) steel by 50%, 70% and 80% produced a texture consisting of a moderately strong $\{111\} \langle 112 \rangle$ and a rather weak $\{111\} \langle 110 \rangle$ component. The value of the maximum of the $\{111\} \langle 112 \rangle$ component increased from 4-random for the 50% cold-rolled material to 6-random for the 80% cold-rolled material. Ray [178] has further reported that, in the same material, intercritically annealed at the higher temperature of 790°C , 50% and 70% cold-rolling produced the same texture components as before, although of much lower intensity. In contrast, however, the pole-figure for the 80% cold-rolled material showed a nearly random texture. Annealing the cold-worked sheets at 700°C led to recrystallisation of the alloy by an in situ mechanism whereby the deformed regions recrystallised giving rise to strain-free grains of almost the same orientation. This has been cited as the reason why the annealing textures of the above materials were found to be rather similar to those of the corresponding cold-rolled materials.

Further work by Ray [179, 180], using the quantitative texture measurement technique, on the same material as above, indicated that although reasonably strong $\{111\}$ and $\{337\}$ fibre-textures could be developed easily in this steel, the values of the Lankford parameter,

'r', have been found to be rather low (around unity). One other significant result from this work was that the material was found to be practically insensitive to variation of martensite volume fraction within the range 25% to 41%, so far as the development of {111} fibre texture was concerned. The results also pointed to the possibility that in order to develop a larger 'r'-value in this material, intercritical annealing to produce a much lower volume fraction of the martensitic phase ($<25\%$) might be beneficial.

Researches carried out in this direction on a Si-P dual-phase steel [181] have indicated that it is indeed possible to reach a \bar{r} value as high as 1.8 in such a dual-phase steel which contained only upto a maximum of nearly 4% martensite by volume, sufficient to eliminate the yield-point elongation and to increase the initial strain-hardening rate.

It is, of course, at once apparent that such a material will not be strong enough although it will possess an excellent deep-drawing characteristics. Therefore, this method will not lead to the production of a high-strength dual-phase steel with good deep-drawability. Thus the question of devising ways and means to achieve such a material is still very much open to-day. Further work is definitely needed in this direction.

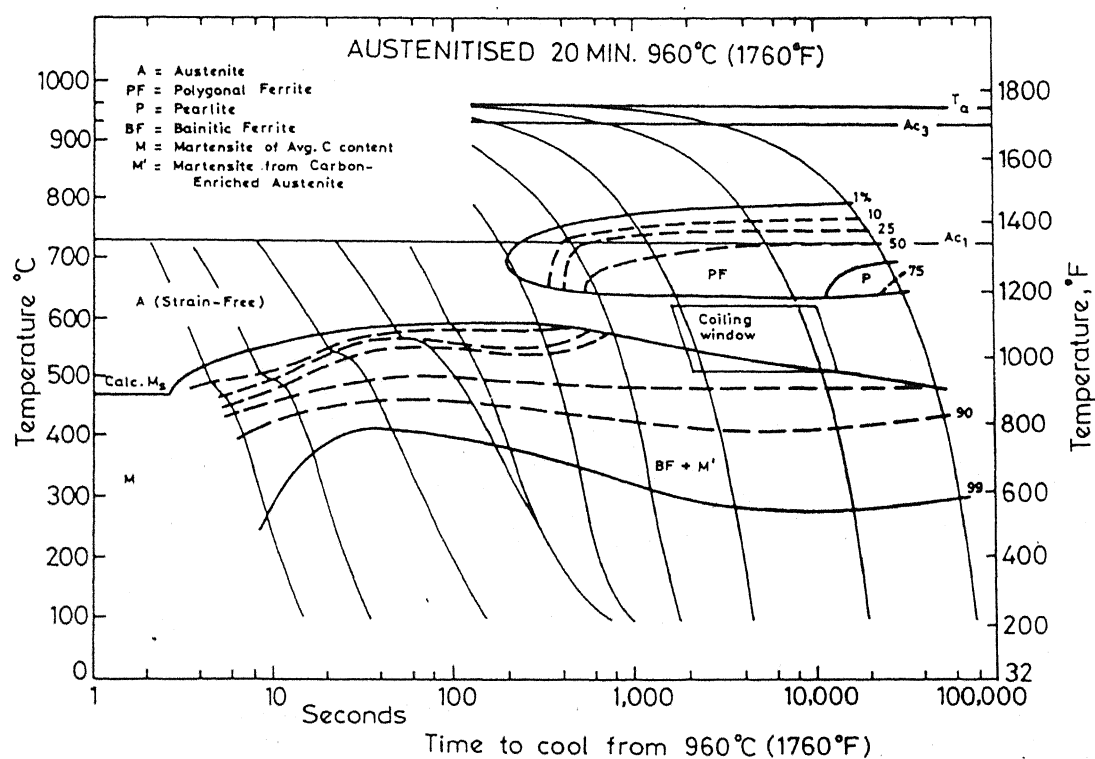


Fig.2.1 C.C.T. curves for a low carbon Mn-Si-Cr-Mo steel developed by Coldren and Tither.[24]

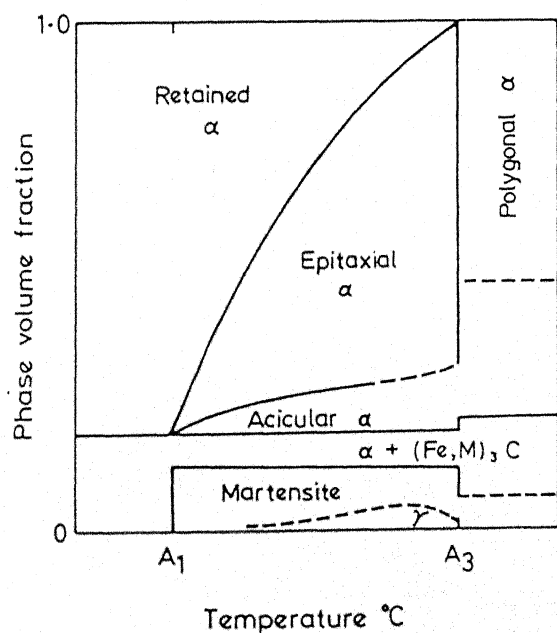


Fig.2.2 Schematic microstructure map showing the volume percent of the various phases present as a function of cooling rate. [41]

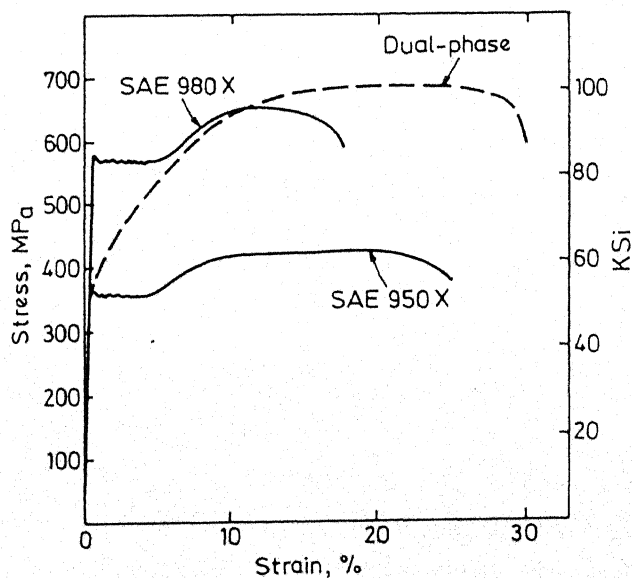


Fig.2.3 Typical stress-strain curves for SAE 950X and 980X steels and an intercritically annealed dual-phase steel. [58]

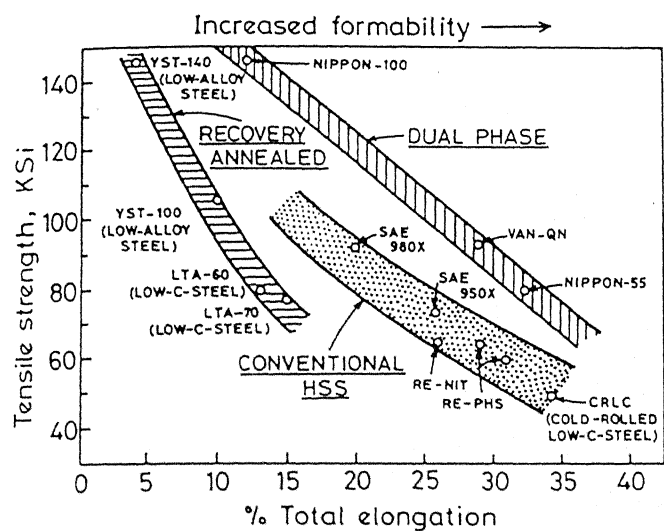


Fig. 2.4 Total elongation as a function of ultimate tensile strength for some of the commercially available high strength steels. [65]

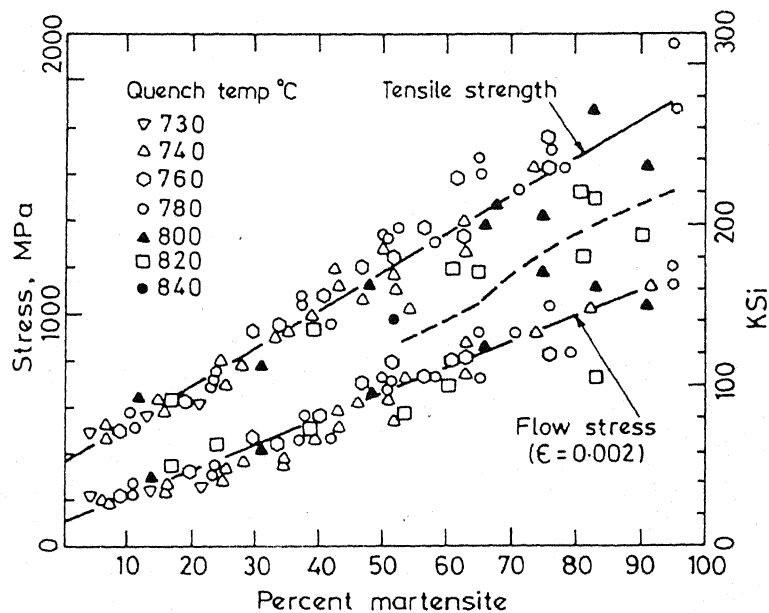


Fig. 2.5 The 0.2 pct. flow stress and the tensile strength as a function of percent martensite for the Fe-Mn-C alloys. [21]

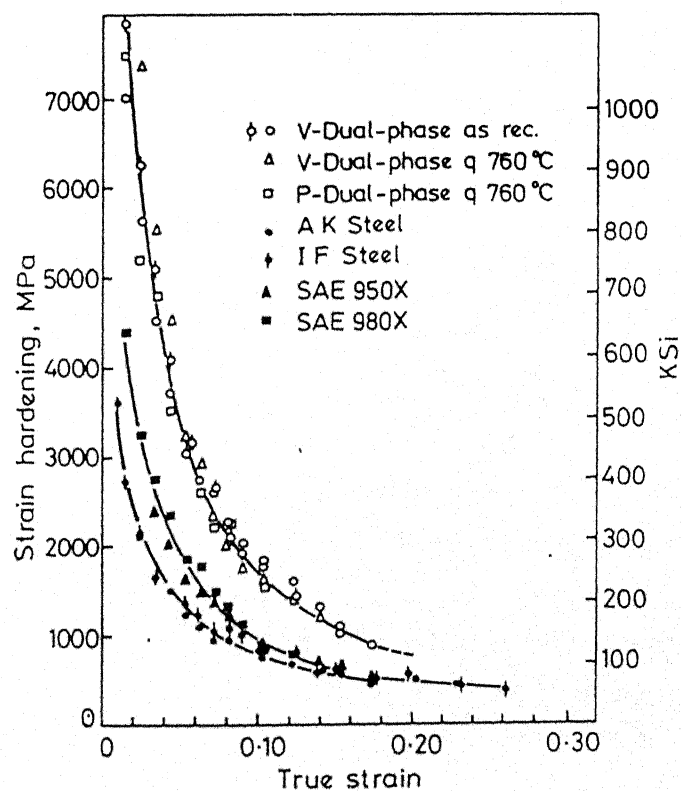


Fig. 2.6 Strain hardening as a function of strain for dual-phase, conventional high strength and low carbon steels. [70]

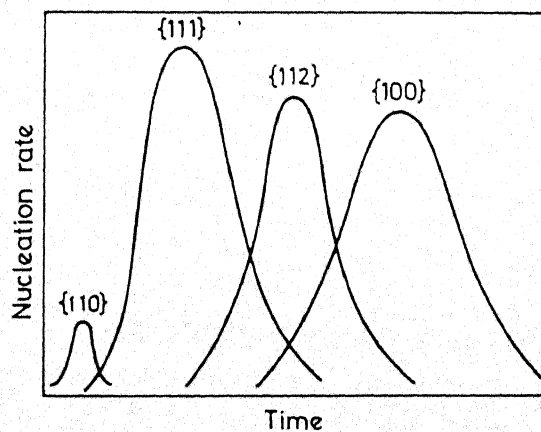


Fig. 2.7 Schematic representation of nucleation sequence of recrystallised grains during annealing of cold-rolled steel. [86]

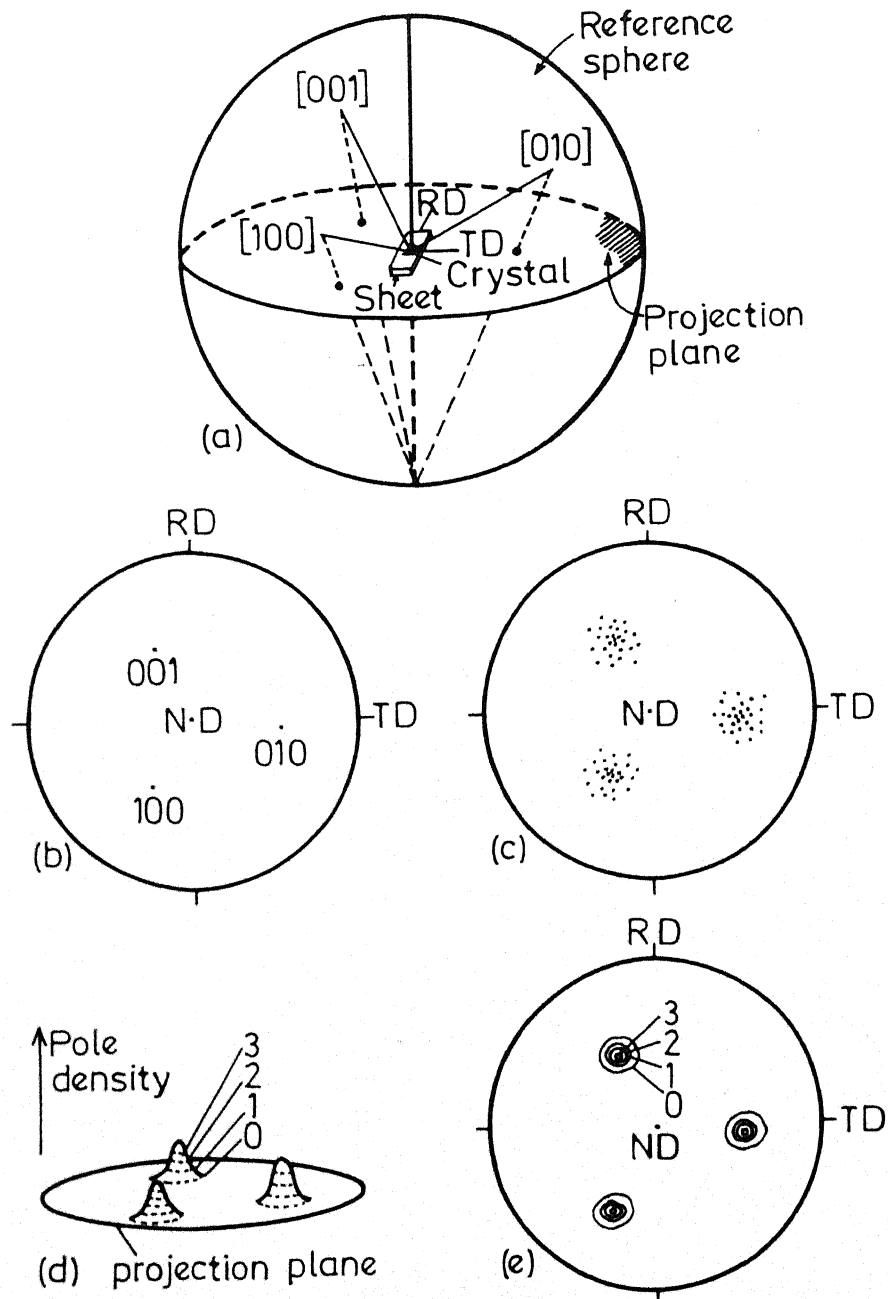


Fig.2.8 (a) Projection sphere and reference directions,
 (b) Projection of poles for a single grain,
 (c) Projection of poles from textured grains,
 (d) Pole density distribution,
 (e) Contour map of pole density. [127A]

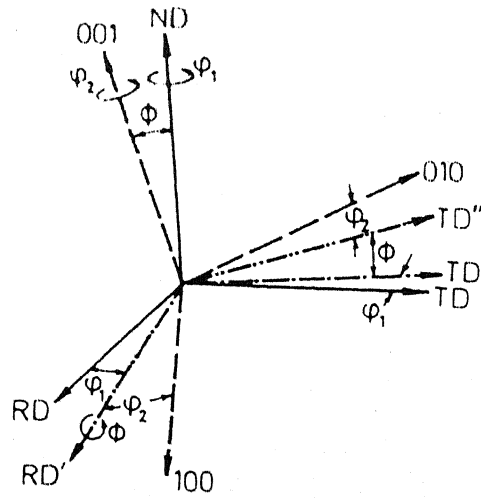


Fig.2.9 Definition of the Euler angles ψ_1, Φ, ψ_2 . [132]

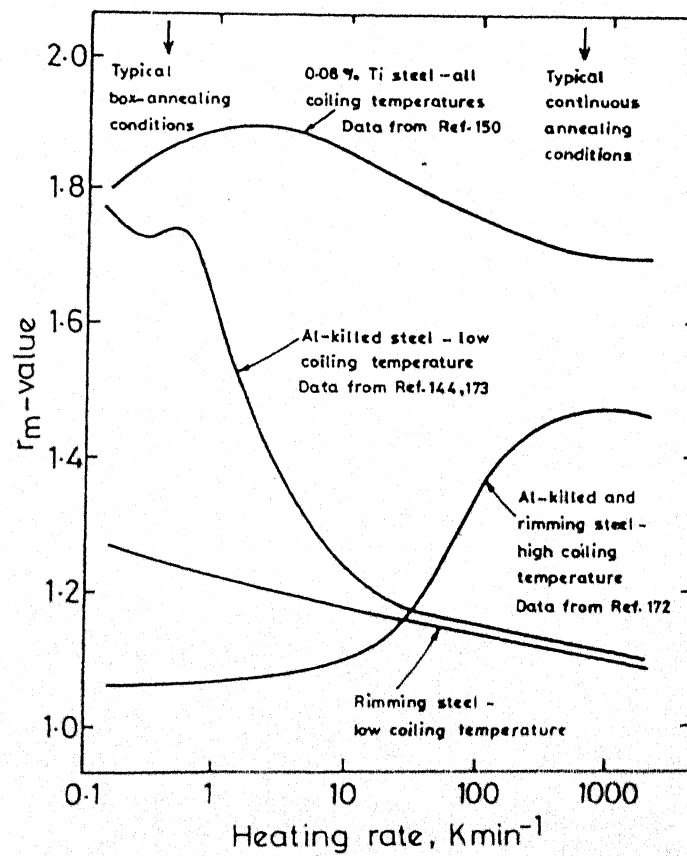


Fig.2.10 Variation of mean plastic strain ratio r_m with heating rate during final anneal for various coiling temperatures and classes of steel.[144,150,172,173]

Chapter III

Experimental Procedure

3.1 Materials and Their Preparation

The chemical compositions of the steels used in the present investigation are shown in Table 3.1.

Table 3.1
Composition of Steels

Alloy designation	Weight percentage of elements					
	C	Mn	Si	S	P	V
A1	0.11	Trace	1.52	0.011	0.018	0.09
A4	0.12	1.51	1.47	0.021	0.016	0.09
A5	0.11	1.48	Trace	0.027	0.014	0.08

The alloys were melted in the form of 30 kg ingots in an induction furnace and cast into preheated cast iron moulds. All the heats were deoxidised by aluminium shots and also treated with misch-metal. The cross-sectional area of each ingot was 12 cm x 12 cm (approximately). The ingots were initially forged into bars of square cross-section (25 mm each side).

A few tensile test specimens of standard dimensions were prepared from a portion of these forged rods. In addition, metallographic samples

CENTRAL LIBRARY
106232

having sizes 25 mm x 25 mm x 10 mm were cut out and these were used for both optical and electron microscopic studies.

3.2 Heat-Treatment and Production of the Dual-Phase Structure

The forged rods, metallographic samples and tensile test pieces were coated carefully with a commercial ceramic paint to prevent decarburisation and oxidation during subsequent heat-treatment. These were homogenised by the process of austenitisation which involved heating at a temperature of 910°C for a period of one hour. The heat-treatment was carried out in a high temperature muffle furnace whose temperature was maintained within an accuracy of $\pm 5^{\circ}\text{C}$. The forged rods as well as the metallographic samples were cooled to room temperature from the austenitisation temperature in two different ways. Half of them were quenched in water while the remaining half were air-cooled. All the samples for tensile testing were, however, only air-cooled.

In order to produce the dual-phase structure, half of the air-cooled samples were kept at the intercritical annealing temperature of 750°C while the remaining half were kept at 810°C for thirty minutes and then directly quenched in water. The initially water-quenched samples were also similarly treated. All the above heat-treatments were carried out in a muffle-furnace where the temperatures were maintained within an accuracy of $\pm 5^{\circ}\text{C}$. For each alloy, all the above treatments produced four different initial dual-phase structures. Therefore, for the three alloys under investigation, twelve different initial structures could be developed in the forged rods and the metallographic samples. On the other hand only two different initial dual-phase structures were produced in the

tensile samples from each of the alloys. Two identical tensile samples were given the same heat-treatment. The twelve different initial dual-phase structures produced in the three experimental alloys along with the relevant heat-treatment procedures and the designations used to identify the structures, are listed in Table 3.2.

Table 3.2

Twelve Different Dual-Phase Structures Produced in the Three Experimental Alloys along with the Relevant Heat-treatment Procedures

Alloys	Designation of dual-phase structures	Heat-treatments for the production of dual-phase structures
Al, A4, and A5	AC 750/WQ	Austenitised at 910°C for 1 hr. and air-cooled, then annealed intercritically at 750°C for 30 min. and quenched in water.
	AC 810/WQ	Austenitised at 910°C for 1 hr. and air-cooled, then annealed intercritically at 810°C for 30 min. and quenched in water.
	WQ 750/WQ	Austenitised at 910°C for 1 hr. and water-quenched, then annealed intercritically at 750°C for 30 min. and quenched in water.
	WQ 810/WQ	Austenitised at 910°C for 1 hr. and water-quenched, then annealed intercritically at 810°C for 30 min. and quenched in water.

3.3 Tensile Testing

A number of cylindrical tensile test specimens of standard dimensions having gauge length 28 mm, were used for tensile testing. The

tensile tests were performed at room temperature using an Instron (Model 1195) machine. A cross-head speed of 0.5 mm/minute, a chart speed of 20 mm/minute and a full scale load of 5000 kg were used during testing. From the charts 0.2% proof stress, ultimate tensile strength and uniform and total elongation values were calculated.

As mentioned before, two identical tensile samples were given the same heat-treatment. On testing, quite reproducible results could be obtained for both. The load-elongation data, read from the charts, were converted to true stress (σ) and true plastic strain (ϵ). The strain-hardening exponent 'n' was determined by plotting $\ln \sigma$ -values against $\ln \epsilon$ -values and finding out the slopes in each case. The work-hardening rate, $\frac{d\sigma}{d\epsilon}$ was also calculated at different values of true plastic strain. Further, the ability of the material to distribute strain corresponding to the elapsed strain was characterised by plotting the dimensionless parameter, $\frac{1}{\sigma} \frac{d\sigma}{d\epsilon}$ as a function of strain. It is important to mention that the instability in uniaxial tension occurs when $\frac{1}{\sigma} \frac{d\sigma}{d\epsilon} = 1$.

3.4 Cold-Rolling and Recrystallisation Treatment

The intercritically annealed bars were cleaned by surface grinding to remove surface scales etc. and then each bar was sliced into two halves lengthwise. These were then cold-rolled to approximately 60% reduction in thickness in all cases. The amount of reduction was kept at around 60% on the basis of trial experiments when it was found that the intensity of the cold-rolled texture for the material intercritically annealed at higher temperature of 810°C did not show any increase beyond that amount; rather the intensity was found to show a decrement after

that amount of deformation. In order to keep all the treatments comparable, the material intercritically annealed at the lower temperature of 750°C , was also subjected to the same amount of deformation. The cold-rolling operation was carried out in a two-high laboratory rolling mill using paraffin oil as a lubricant. The strips were reversed end to end after each pass. In between any two successive passes the strips were dipped into a bucket of cold water to minimise temperature rise due to deformation as far as practicable. The final thicknesses of the cold-rolled strips varied between 4.5 and 5.0 mm.

Small samples of sizes 6-7 mm x 3 mm (approximately) were cut out from the cold-rolled strips. These specimens were then coated with a very thin layer of borax and annealed at different temperatures, namely, 650°C , 700°C , 750°C , 800°C and 850°C for different lengths of time, varying between 2 seconds and a few minutes at each temperature. The above recrystallisation anneal was performed in a molten salt bath using a commercial I.C.I. salt (Crescent). The salt bath was contained in a stainless steel pot of 5.0 cm internal diameter and about 20 cm height. The container with the salt was heated in a vertical electrical resistance tube furnace. The temperature of the melt was checked from time to time using a calibrated chromel-alumel thermocouple kept in a thin-walled stainless steel tube dipping below the surface of the melt. The samples were held in a constant temperature zone in the bath which was found out by carefully measuring the temperatures at different regions over a length of time. After each recrystallisation anneal, samples were quickly taken out from the bath and dropped in a large bowl of water.

3.5 Optical Metallography

3.5.1 Specimen Preparation and Examination

To study the optical microstructures of the initial materials, metallographic samples (25 mm x 25 mm x 10 mm) were properly ground and subsequently polished in the usual manner. Each sample was prepared with repeated polishing and short etching treatments (3-4 seconds) using 2% nital to produce a defect-free microstructure, showing reasonably good contrast.

In order to reveal the sizes and shapes of austenite pools formed during intercritical annealing an improved etching technique [182] was used to characterise the structures of the experimental dual-phase steels. The process involved initially a conventional polishing and etching with a 4% picral solution (4 g picric acid in 100 cc methyl alcohol) for about a minute. This was followed by a short etching treatment using 2% nital with the intention of revealing the ferrite grain boundaries clearly. Finally, the samples were stained by holding them in boiling alkaline chromate solution (8-10 g CrO_3 in 75 cc H_2O and 40 g NaOH) for different lengths of time depending on the alloy compositions. The four dual-phase structures from alloy A1 took a minimum of 10-15 seconds for staining uniformly throughout the surface, while 25-30 seconds were needed for staining the dual-phase structures in alloy A4. Similar staining operation was performed in case of alloy A5 for a total period upto about 10-15 minutes. The different periods of staining were selected on the basis of trial and error. The above staining method led to martensite etching dark and new ferrite (formed during cooling from intercritical

temperatures) etching bright. The old (untransformed) ferrite appeared gray in contrast to the other microconstituents. After staining, the specimens were washed in running water and rinsed with methanol and dried. Photomicrographs were taken from both the conventionally etched surfaces (using 2% nital) and the specially stained surfaces (using boiling alkaline chromate solution).

Structural characterisation of the cold-worked and recrystallised samples were also carried out by studying their optical microstructures taken from the transverse sections of the cold-rolled and annealed strips. The small samples, as described earlier, were mounted in plastic moulds and prepared metallographically by grinding, polishing and etching treatments using 2% nital.

3.5.2 Quantitative Metallography

Multiphase stereology relationships developed by Cribb [183] were used for quantitative analysis of the ferritic matrix, the "second-phase" microconstituent (martensite) and the transformed ferrite (new ferrite) for the twelve initial dual-phase structures. Standard point counting and line intercept measurements [182] were used along with these relationships to determine the volume percents of the old ferrite, new ferrite, martensite and the original austenite pools. In addition, the mean free paths in ferrite between austenite pools, mean particle diameters of the austenite pools and also the mean particle diameters of old ferrite were determined. Point counting was carried out using an eye-piece fitted with a 100-point square grid with points 0.5 cm apart at 10X. For each structure, the results of measurements from five random fields were averaged out.

For the purpose of quantitative metallography, a Leitz "Metallovert" microscope was employed and measurements were made at 1000X.

The relationships used for the measurement of the above mentioned parameters are given below :

$$V^{OF} = \text{Volume fraction of old ferrite}$$

$$V^{NF} = \text{Volume fraction of new ferrite}$$

$$V^M = \text{Volume fraction of martensite}$$

$$V^{NF+M} = \text{Volume fraction of new ferrite and martensite}$$

$$\sigma^A = \text{Mean free path in old ferrite between austenite pools}$$

$$= \frac{4V^{OF}}{2P_L^{OF,A}}$$

where, $P_L^{OF,A}$ = Old ferrite-austenite pool grain-boundary intercept counts per millimeter.

$$\lambda_g^{OF} = \text{Mean particle diameter of old ferrite phase}$$

$$= \frac{4V^{OF}}{2P_L^{OF,A} + 4P_L^{OF,OF}}$$

where, $P_L^{OF,OF}$ = Old ferrite grain-boundary intercept count per millimeter.

$$\lambda_g^{NF+M} = \text{Mean particle diameter of the austenite pool}$$

$$= \frac{4V^{NF+M}}{2P_L^{OF,A}}$$

3.6 Transmission Electron Microscopy

Slices having an area of 25 mm x 25 mm and a thickness of 0.5 mm were cut, using a Biehler Isomet diamond cutting saw, from metallographic samples (25 mm x 25 mm x 10 mm) of the three different alloys given different initial heat-treatments followed by intercritical annealing at 750°C and 810 °C. Thin slices were also obtained in a similar manner from the transverse sections of the different cold-rolled strips. A few slices from the cold-rolled strips were given a partial recrystallisation anneal at selected temperatures for specified periods of time.

All the slices from the initial dual-phase structures, cold-rolled samples and partially recrystallised materials were mechanically thinned down to a thickness of ~0.06 mm by polishing on moistened emery papers. To start with, these mechanically thinned down specimens were first cleaned with acetone and finally electropolished using the Bollmann technique. When the edge of the sample, dipped into the electrolyte, became sufficiently thin, a foil was cut out from the sample using a scalpel blade, taking care that the cut-edge was as parallel to the transverse direction as possible. After examining the foil in the T.E.M. at low magnification, it was found out that there was a very good correspondence between the cut-edge of the foil and the general direction of plastic flow as specified by the long direction of the cold-worked cell-structure.

Since electropolishing by the above method was found to be rather tedious and it was difficult to control the electrothinning conditions accurately, this method of foil preparation was later on discontinued.

Instead, 3 mm discs were punched out from the mechanically thinned and cleaned samples with the help of a die and a punch.

Final electropolishing of the discs was carried out to produce a thinned central region supported by a thicker outside rim using a jet-polishing device (Tenupol unit). For this purpose, an electrolyte containing 10 vol. % perchloric acid in glacial acetic acid was used at a temperature of $<10^{\circ}\text{C}$ and at a potential difference of ~ 40 volts. The thinned perforated foils were rinsed with running water, then with ethyl alcohol and finally dried. Transmission electron microscopy of the thin foils was carried out in a Philips EM400 machine operated at 120 KV.

It may be mentioned here once again that all T.E.M. work was carried out on thin foils made from the transverse sections of the rolled sheets. S.A.D. patterns taken from the foils indicated the rolling direction (R.D.) straightaway. Taking into account the relative angular displacement between the image and the corresponding S.A.D., the crystallographic orientation of the transverse direction (T.D.) was found out from the microstructural features (major direction of elongation of the cells or subgrains). The normal direction (N.D.) was then determined by taking the cross-product of R.D. and T.D. From this the indices of the rolling plane (R.P.) could be found out. The orientation of a selected area was then expressed in the usual way, by specifying the rolling plane and the rolling direction.

3.7 Microhardness Measurements

The microhardness values of the ferrite phase present in the twelve initial dual-phase structures from the three alloys as well as in the

cold-rolled, partially recrystallised and fully recrystallised samples, were determined on the polished and etched specimens already used for optical microscopic studies. The measurements were performed in a Leitz MINILOAD2 microhardness tester. The etched specimens were focussed at 500X and the ferrite grain to be examined was located exactly under the cross-wire. In case of the initial twelve dual-phase structures a load of 5 g was selected to obtain consistent impression in all cases. On the other hand, in case of cold-rolled, partially recrystallised and fully recrystallised samples, a load of 15 g gave measurable impressions in each case. The diagonals of each impression were measured and averaged out giving a value which was ultimately converted to the required Vicker's pyramidal number from the appropriate table. For each sample, the microhardness of the ferrite field was averaged from atleast ten grains. An attempt was also made to determine the microhardness of the martensitic phase in different samples. However, the indentation marks could not be properly distinguished from the background and hence this attempt was finally abandoned.

3.8 Determination of Recrystallisation Kinetics

The kinetics of primary recrystallisation of ferrite in the cold-rolled dual-phase steels were analysed from the relevant microhardness data using an Avrami-type relationship. It is based on the following equation :

$$x = 1 - \exp\left\{-\left(\frac{t}{\tau}\right)^m\right\}$$

with

$$x = \frac{H_0 - H}{H_0 - H_{\min}}$$

where H_0 is the initial hardness of ferrite in the cold-worked material, H the hardness after an annealing period t and H_{\min} is the minimum hardness corresponding to 100% recrystallisation. Here, it is assumed that the recrystallised volume fraction x at any time t is directly proportional to the relative drop in hardness. Further, ' τ ' represents a time constant in seconds, and corresponds to 63% recrystallisation. ' m ' is a time exponent which depends on the geometrical character of the recrystallisation process and also on the time dependence of the nucleation rate, i.e., whether the recrystallisation is one, two or three dimensional.

The above equation can be re-written as :

$$\ln \ln \frac{1}{1-x} = m \ln t - m \ln \tau$$

$\ln \ln \frac{1}{1-x}$ was plotted against $\ln t$ (known as Avrami plot) giving rise to straight lines from which the time constant τ was obtained through extrapolation of the function $\ln \frac{1}{1-x}$ to a value of 1. The recrystallisation time exponent ' m ' for different stages of recrystallisation process was determined from the slopes of these straight line plots.

Furthermore, the time constant ' τ ' can be defined as :

$$\tau = \text{Constant} \frac{1}{D} = K \exp\left(\frac{Q}{RT}\right),$$

where D represents the diffusion co-efficient, Q is the activation energy, R the universal gas constant and T the absolute temperature. For

different initial dual-phase structures, $\ln \tau$ -values were plotted against corresponding $\frac{1}{T}$ (known as Arrhenius plots) giving rise to straight lines from which $\frac{Q}{R}$ -values were obtained by measuring the slopes and activation energies Q for 63% recrystallisation were determined. Similarly, times for 50% recrystallisation as well as 80% recrystallisation were plotted against $\frac{1}{T}$ and the respective activation energies were calculated from the slopes of those curves.

3.9 Determination of Texture

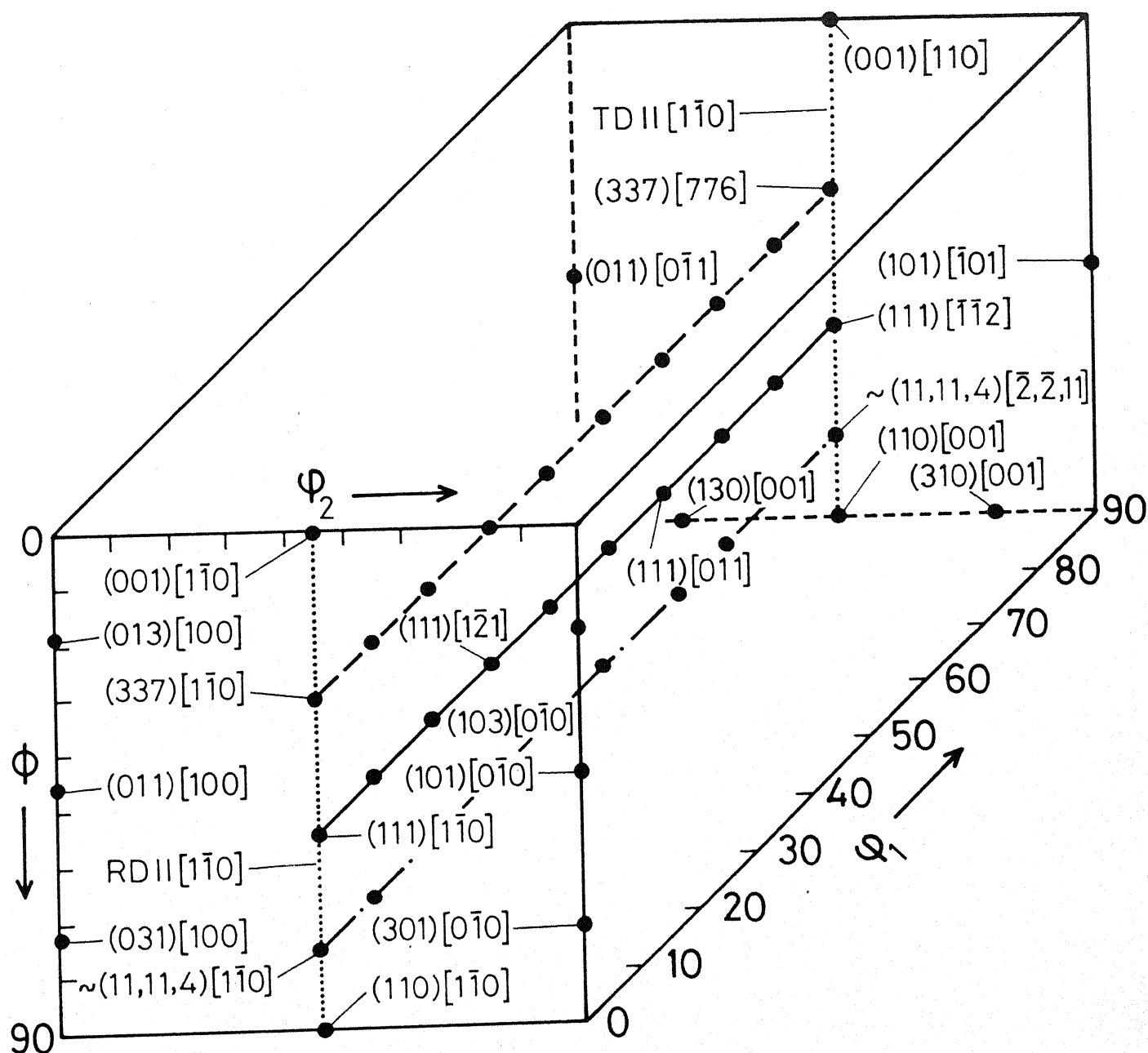
In the present investigation, crystallographic textures were determined from the mid-sections of a number of selected samples, both cold-worked and fully recrystallised. Specimens of the size 24 mm x 14 mm were cut out from rolled sheets for this purpose. All the twelve initial dual-phase structures from the three alloys, in the 60% cold-rolled condition, were used for texture determination. Two samples from each one of these cold-rolled materials were subjected to a recrystallisation anneal at 650°C and 800°C respectively and textures were determined from them.

A little less than half of the total thickness was removed from one of the flat surfaces in all texture specimens by milling. The specimens were then ground and polished metallographically and then lightly etched with 2% nital to remove any disturbed layer. {110} pole-figures were determined from these texture samples by the Schulz reflection method [184] using CoK_α radiation with an iron filter. Intensity levels on the pole-figures were determined by comparison with the intensity obtained from a solid specimen of pure iron which had been randomised by repeated deformation and annealing.

To have a better resolution of the texture components in the pole-figures and also to have a more complete idea regarding the textures of the cold-worked and recrystallised samples, O.D.F.'s were measured from each one of them. For this kind of analysis the method of incomplete pole-figures [129] was used. For this purpose incomplete pole-figure (within the range $0-85^\circ$) intensity data were obtained for $\{110\}$, $\{200\}$ and $\{112\}$ reflections using the Lücke automated texture goniometer system [185, 186] with CoK_α radiation.

In the present investigation, the O.D.F. analysis technique as developed by Roe [131, 187] and mainly by Bunge [132, 188] has been followed. In this method the orientation of a crystallite in a polycrystalline specimen is specified with respect to the specimen co-ordinate system by the three Eulerian angles ψ_1 , ϕ and ψ_2 . A function, known as the orientation distribution function, $f(g)$, which represents the relative intensity of orientations, is computed in the form of a series expansion of generalised spherical harmonics from series expansion of generalised pole-figures. All the computations involved were carried out in a Cyber 175 computer using the programme system supplied by Pospiech and Jura [189, 190].

The Cartesian Euler angle space, with the three-dimensional orientation distribution function within, is normally represented, for B.C.C. materials, in the form of sections, $\psi_1 = \text{Constant}$ ($\psi_1 = 0, 5, 10, \dots, 90 \text{ deg.}$). Most of the important crystallographic orientations for B.C.C. materials appear in these sections. Figure 3.1 represents an isometric view of the three-dimensional Eulerian space with the positions of a few important ideal orientations marked therein. Some



- · — $\Phi = 75^\circ, \Psi_2 = 45^\circ; [11,11,4] \parallel \text{ND FIBRE}$
- $\Phi = 55^\circ, \Psi_2 = 45^\circ; [111] \parallel \text{ND FIBRE}$
- $\Phi = 30^\circ, \Psi_2 = 45^\circ; [337] \parallel \text{ND FIBRE}$
- Ideal Positions

Fig. 3.1 Three-dimensional Euler Space showing locations of ideal orientations.

Table 3.3
Euler Angles for Ideal Orientations

Ideal orientations		Euler angles		
		Ψ_1	ϕ	Ψ_2
(111) $[0\bar{1}1]$		60	55	45
(111) $[1\bar{1}0]$		0	55	45
(111) $[1\bar{2}1]$		30	55	45
(111) $[\bar{1}\bar{1}2]$		90	55	45
(337) $[1\bar{1}0]$		0	31	45
(733) $[0\bar{1}1]$		49	68	67
(011) $[100]$		0	45	0
(110) $[001]$		90	90	45
(101) $[0\bar{1}0]$		0	45	90
(013) $[100]$		0	18	0
(031) $[100]$		0	72	0
(103) $[0\bar{1}0]$		0	18	90
(301) $[0\bar{1}0]$		0	72	90
(130) $[001]$		90	90	18
(310) $[001]$		90	90	72
(010) $[101]$		45	90	0
(100) $[0\bar{1}1]$		45	90	90
(001) $[1\bar{1}0]$	$\Psi_1 + \Psi_2 = 45$	45	0	
(001) $[\bar{1}\bar{1}0]$	$\Psi_1 + \Psi_2 = 135$		0	
(110) $[1\bar{1}0]$		0	90	45
(011) $[0\bar{1}1]$		90	45	0
(101) $[\bar{1}01]$		90	45	90
(112) $[1\bar{1}0]$		0	35	45
(335) $[1\bar{1}0]$		0	40	45
near (445) $[1\bar{1}0]$		0	50	45
near (11, 11, 4) $[1\bar{1}0]$		0	75	45
near (11, 11, 4) $[\bar{2}, \bar{2}, 11]$		90	75	45

important ideal orientations for B.C.C. materials are also shown in a tabular form in Table 3.3.

3.10 Determination of r-values

In the present investigation no experimental determination of 'r'-values (Lankford parameter) was carried out. However, these values have been calculated theoretically on the basis of $\{hkl\} \langle 111 \rangle$ pencil glide from the experimentally determined O.D.F.'s using a computer programme developed by Bunge et al. [191]. The plastic strain ratio (\bar{r}) was then calculated on the basis of the formula $\bar{r} = (r_0 + 2r_{45} + r_{90})/4$ where the numerical subscripts denote angles from the rolling direction. In addition, values of the planar anisotropy parameter, $\Delta r = (r_0 + r_{90} - 2r_{45})/2$ have also been calculated.

Chapter IV

Experimental Results

4.1 Characterisation of the Dual-Phase Structures in the Three Alloys Produced by Different Initial Heat-treatments

As mentioned in Chapter III, dual-phase structures have been developed in the alloys A1, A4 and A5 by following different routes of heat-treatment. As a result of this, four different initial dual-phase structures have been obtained for each alloy. Attempts have been made to characterise these structures by optical and electron microscopy and at the same time to determine the mechanical properties of some of the structures in the usual way.

4.1.1 Optical Microstructures

The optical microstructures from the alloys A1, A4 and A5, with four different initial heat-treatments, are shown in Figures 4.1(a-d), 4.2(a-d) and 4.3(a-d) respectively. All these microstructures reveal a distribution of two phases, ferrite and martensite, in different proportions depending on the alloy composition as well as the heat-treatment. A summary of the quantitative metallographic measurements on these twelve initial structures is given in Table 4.1. A close look at the above micrographs and the table shows that for any specific initial heat-treatment, the volume percent of martensite in the microstructure changes in an increasing order from alloy A1 → A5 → A4. Again, in any particular alloy, intercritical annealing at the higher temperature of 810°C seems to

Table 4.1

Summary of the Quantitative Metallographic Measurements on Twelve Inter-critically Annealed Microstructures Developed in the Alloys A1, A4 and A5

Alloy designation	Heat treatment	V^{OF} %	V^M %	V^{NF} %	V^{NF+M} %	σ^A , mm	λ_g^{OF} , mm	λ_g^{NF+M} , mm
A1	AC 750/WQ	71.04	18.60	10.36	24.96	0.0146	0.0051	0.0045
A1	AC 810/WQ	65.83	20.25	13.92	30.17	0.0143	0.0043	0.0061
A1	WQ 750/WQ	66.97	20.66	12.37	26.03	0.0142	0.0061	0.0050
A1	WQ 810/WQ	60.46	23.97	15.57	35.54	0.0140	0.0050	0.0077
A4	AC 750/WQ	59.50	30.58	9.92	40.50	0.0075	0.0028	0.0054
A4	AC 810/WQ	38.02	51.10	10.88	61.98	0.0050	0.0022	0.0082
A4	WQ 750/WQ	46.01	42.97	11.02	53.99	0.0044	0.0020	0.0053
A4	WQ 810/WQ	33.75	54.27	11.98	66.25	0.0039	0.0019	0.0079
A5	AC 750/WQ	78.93	21.07	0.0	21.07	0.0089	0.0027	0.0024
A5	AC 810/WQ	76.72	23.28	0.0	23.28	0.0073	0.0027	0.0024
A5	WQ 750/WQ	71.90	28.10	0.0	28.10	0.0070	0.0026	0.0027
A5	WQ 810/WQ	68.05	31.95	0.0	31.95	0.0061	0.0021	0.0029

V^{OF} = Volume percent of old (untransformed) ferrite

V^M = Volume percent of martensite

V^{NF} = Volume percent of new (transformed) ferrite

σ^A = Mean free path in old ferrite between austenite pools

λ_g^{OF} = Mean particle diameter of old-ferrite phase

λ_g^{NF+M} = Mean particle diameter of austenite pool.

produce a larger volume fraction of martensite as compared to the intercritical annealing at the lower temperature of 750°C . The treatment WQ/WQ has been found to produce a somewhat larger volume percent of martensite as compared to the treatment AC/WQ. For the same kind of heat-treatment (AC/WQ or WQ/WQ), alloy A4 has been found to be much more sensitive to the change in intercritical annealing temperature as compared to the other two alloys. Thus, whereas intercritical annealing at 810°C is found to produce substantially larger volume percent of martensite as compared to intercritical annealing at 750°C in alloy A4, this effect has been found to be only marginal in case of the alloys A1 and A5.

The microstructures shown in Figures 4.1 to 4.3 were all taken from metallographic samples of the three alloys which were etched with a solution of 2% nital in alcohol. By this technique the ferrite appears bright, whereas the martensitic regions show a dark contrast. It is known that the major part of the ferrite in the dual-phase microstructure must have existed in conjunction with the austenite at the intercritical annealing temperature, whereas a part of it is supposed to form by the transformation of the austenite on cooling from intercritical annealing. It is impossible to distinguish between the old (untransformed) ferrite and the new (transformed) ferrite in all these micrographs using the nital etchant. In order to get more microstructural details, the samples were stained in a manner which has been outlined in Chapter III. Figures 4.4(a-d) show the optical microstructures from the stained samples of alloy A1. It is at once apparent from these micrographs that there are three distinguishable phases, namely, martensite (dark) surrounded by new ferrite (bright) embedded in a matrix of old ferrite (grey). The new ferrite areas appear

to be very clean in comparison to the old-ferrite which contains a large number of precipitates. The total area comprising any one martensitic region and the surrounding new ferrite delineates the original austenitic pool that existed at the corresponding intercritical annealing temperature just before final quenching. The original colour developed on the various phases due to staining treatment can be seen typically in Figures 4.5(a,b).

Optical micrographs from stained metallographic samples of alloy A4 are shown typically in Figures 4.6(a,b). Again, the three phases, namely, martensite, new ferrite and old-ferrite can be distinguished in these micrographs. However, in contrast to the distribution in alloy A1, here the new ferrite is not always found to form a zone surrounding the martensitic regions, but is also found within such regions, sometimes.

Quite in contrast to the alloys A1 and A4, staining was found much more difficult for the alloy A5. Not only that, after staining, practically very insignificant amount of new ferrite could be noticed in the microstructures for this alloy. This is shown typically in Figures 4.7(a,b). The amounts of new ferrite were so small as to preclude any accurate measurement and this is why in Table 4.1 the volume fractions of new ferrite in alloy A5 have been shown as zero.

Quantitative measurements made from the microstructural features in the stained samples are included in Table 4.1. This table shows, besides the volume percents of old ferrite, new ferrite and martensite, the volume percents of the original austenite pools also. In addition, the mean free paths in ferrite between austenite pools, mean particle diameters of the austenite pools and also the mean particle diameters of the old ferrite phases are given in this table. Some distinguishing features about the

three alloys are at once apparent from a study of this table. Thus, it is clear that the alloy A1 contains a larger amount of new ferrite as compared to alloy A4, whereas alloy A5 contains none. The mean particle diameter of old ferrite in alloy A1 is found to be nearly double of those in alloys A4 and A5. The mean particle diameter of the austenite pool in alloy A5 is nearly one-third of those in alloys A1 and A4. Again, the mean free path in ferrite between austenite pools in alloy A1 is nearly double the values obtained for the alloys A4 and A5. Finally, the volume percents of the total austenite pool for A1 and A5 are quite comparable and are substantially lower, about half, as compared to alloy A4.

4.1.2 Electron Microstructures

Although the optical microstructures of the dual-phase materials gave an idea about the nature and the distribution of the phases present, no insight into the internal details of the phases could be obtained from such study. Hence T.E.M. studies were carried out on a limited number of thin foils from each material.

T.E.M. studies did not reveal any major difference in the structural details of the phases, as a function of either the alloy composition or the initial heat-treatment. This will be apparent from the following transmission electron micrographs (Figures 4.8-4.10).

A typical electron microstructure from the alloy A1 is shown in Figure 4.8(a). In this micrograph martensite islands can be seen lying at the grain-boundaries of the ferrite-phase. The ferrite grains are found to be dotted with a fine distribution of precipitates. No serious attempt was made, in this investigation, to identify these precipitates.

An interesting feature to note in this micrograph is that the ferrite regions immediately adjacent to the martensitic islands are rather clean and practically devoid of any precipitate particles. Figure 4.8(b) shows another area where martensite is present all along the boundary between two ferrite grains. The ferrite grains, as before, are dotted with a dense distribution of precipitates and also contain a large number of dislocations.

In order to study the internal details of the martensite and the ferrite-martensite interface, micrographs at a higher magnification were also taken. One typical structure is shown in Figures 4.8(c) where the martensite appears to consist of a number of nearly parallel laths.

Figure 4.9(a) shows a typical transmission electron microstructure for the alloy A4. The ferrite here is again found to be dotted with a dense precipitation of fine particles. A precipitate-free narrow zone in ferrite in the immediate vicinity of the martensite islands can also be seen. Very often, in this alloy, which contains the maximum amount of martensite out of the three alloys, the martensitic regions appear in the form of colonies, as shown in Figure 4.9(b). A higher magnification micrograph shows the details from such a martensite colony, where this phase appears to consist of dislocated laths (Figure 4.9(c)). In many places in such a colony the martensitic regions appear to be arranged in more or less straight parallel bands (Figure 4.9(d)).

Figure 4.10(a) shows a typical electron microstructure taken from the alloy A5. As in case of the other two alloys, here too the ferrite has a fine distribution of small precipitates and dislocations. The dislocation density seems to be higher in the ferrite adjacent to the

ferrite/martensite interface. Micrographs taken at a higher magnification have revealed that in this alloy too the martensite is made up of a large number of nearly parallel laths (Figure 4.10(b)).

4.1.3 Mechanical Properties

As mentioned earlier, no significant difference in microstructure could be obtained in any of the alloys as a function of the initial heat-treatments. Therefore, mechanical property measurements of the initial materials were confined to the alloys given the AC/WQ treatment only. The idea was to evaluate the relative strength properties of the three steels in the dual-phase condition prior to cold-working and recrystallisation.

The load-elongation curves obtained from tensile tests of the three alloys showed low yield stress values, continuous yielding behaviour and comparatively high U.T.S. values — characteristics which are typical of dual-phase steels. Figure 4.11 shows the true stress-true strain plots derived from the corresponding load-elongation curves obtained by experiment. It is at once clear that the three alloys A1, A4 and A5 possess quite different strength values. In fact, alloy A4 is found to be the strongest, with alloy A1 coming next in strength, while alloy A5 is the weakest of the three. Table 4.2 shows 0.2% Y.S., U.T.S., uniform elongation % and total elongation % obtained for the three alloys from tensile testing.

Figure 4.12 gives the $\ln(\text{true stress})$ versus $\ln(\text{true strain})$ plots for the three alloys. For a particular alloy with a particular initial heat-treatment, most of the experimental points lie on a single

straight line. The slopes of these lines, which give the values of the strain-hardening exponent 'n', have been marked at appropriate places in the diagram. A look at Figure 4.12 shows that alloy A4 has the lowest set of n-values amongst the three alloys. It is interesting to note that intercritical annealing at the lower temperature of 750°C produces substantially higher values of 'n' in the alloys A1 and A5 as compared to intercritical annealing at the higher temperature of 810°C.

Table 4.2

Mechanical Properties of the Three Alloys A1, A4 and A5 After Different Initial Heat-treatments

Alloy designation	Heat-treatment	0.2% Y.S. (MPa)	U.T.S. (MPa)	Uniform elongation %	Total elongation %
A1	AC 750/WQ	449	771	25.8	32.3
A1	AC 810/WQ	510	829	19.6	23.1
A4	AC 750/WQ	571	992	26.7	33.9
A4	AC 810/WQ	612	1097	23.1	29.5
A5	AC 750/WQ	255	556	17.3	25.1
A5	AC 810/WQ	347	600	15.1	23.5

The rate of strain hardening has been plotted against true strain for the three alloys which were intercritically annealed at 750°C and 810°C (Figure 4.13). This figure shows that, to start with, alloy A4 has the highest strain-hardening rate, while A5 has the lowest strain-hardening

rate with alloy A1 coming in between. The $d\sigma/d\varepsilon$ values for alloy A4 come down drastically upto an ε -value of ~ 0.05 and then show a gradual decrease. On the other hand, the fall in the $d\sigma/d\varepsilon$ values with ε is less drastic in case of alloys A1 and A5. The normalised values of $d\sigma/d\varepsilon$, namely, $\frac{1}{\sigma} \frac{d\sigma}{d\varepsilon}$ have been plotted against ε in Figure 4.14. These curves show quite similar behaviour for all the three alloys. In each case the initial very high strain hardening rate comes down drastically upto an ε -value of ~ 0.05 after which the fall is found to be rather gradual. It is clear from both the Figures 4.13 and 4.14 that the values of rate of strain hardening at a particular value of ε for all the three alloys are systematically higher for lower intercritical annealing temperature of 750°C as compared to those at the higher intercritical annealing temperature of 810°C .

Microhardness measurements were carried out on the ferrite phase in all the initial microstructures of the three alloys. The results are given in a tabular form in Table 4.3. The table clearly shows that

Table 4.3

Microhardness Values (V.P.N.) of the Ferrite-Phase (Load 5 g)

Alloy designation	Heat-treatment			
	AC 750/WQ	AC 810/WQ	WQ 750/WQ	WQ 810/WQ
A1	200	264	221	227
A4	215	235	203	215
A5	164	162	168	200

ferrite in alloy A1 is decidedly the strongest amongst the three alloys. In general, the hardness of ferrite in alloy A4 is slightly lower than that of alloy A1. The lowest set of hardness values has been obtained for the ferrite in alloy A5. For any particular alloy, the variation of hardness values as a function of heat-treatment is not very significant, although intercritical annealing at the higher temperature of 810°C seems to produce a stronger ferrite in comparison to intercritical annealing at the lower temperature of 750°C .

4.2 Characterisation of the Cold-worked Materials

4.2.1 Microstructure

The microstructures of the cold-worked alloys, A1, A4 and A5, have been characterised by both light and electron microscopy. It has been found that the optical microstructures obtained from any one particular alloy are practically the same irrespective of the different initial heat-treatments the alloy was subjected to. Typical optical microstructures from the cold-worked alloys, A1, A4 and A5 are shown in Figures 4.15(a-c). All these micrographs show the original grains — ferrite as well as martensite — deformed and flattened out in the shape of pan-cakes. Some of the deformed grains also show a number of deformation bands (Figure 4.15(a)). It has been further noticed that the structural features are coarsest for alloy A1, rather coarse for alloy A5 and finest in case of alloy A4.

In order to have a clearer idea about the microstructural features of the cold-worked alloys, transmission electron microscopy (T.E.M.) of a

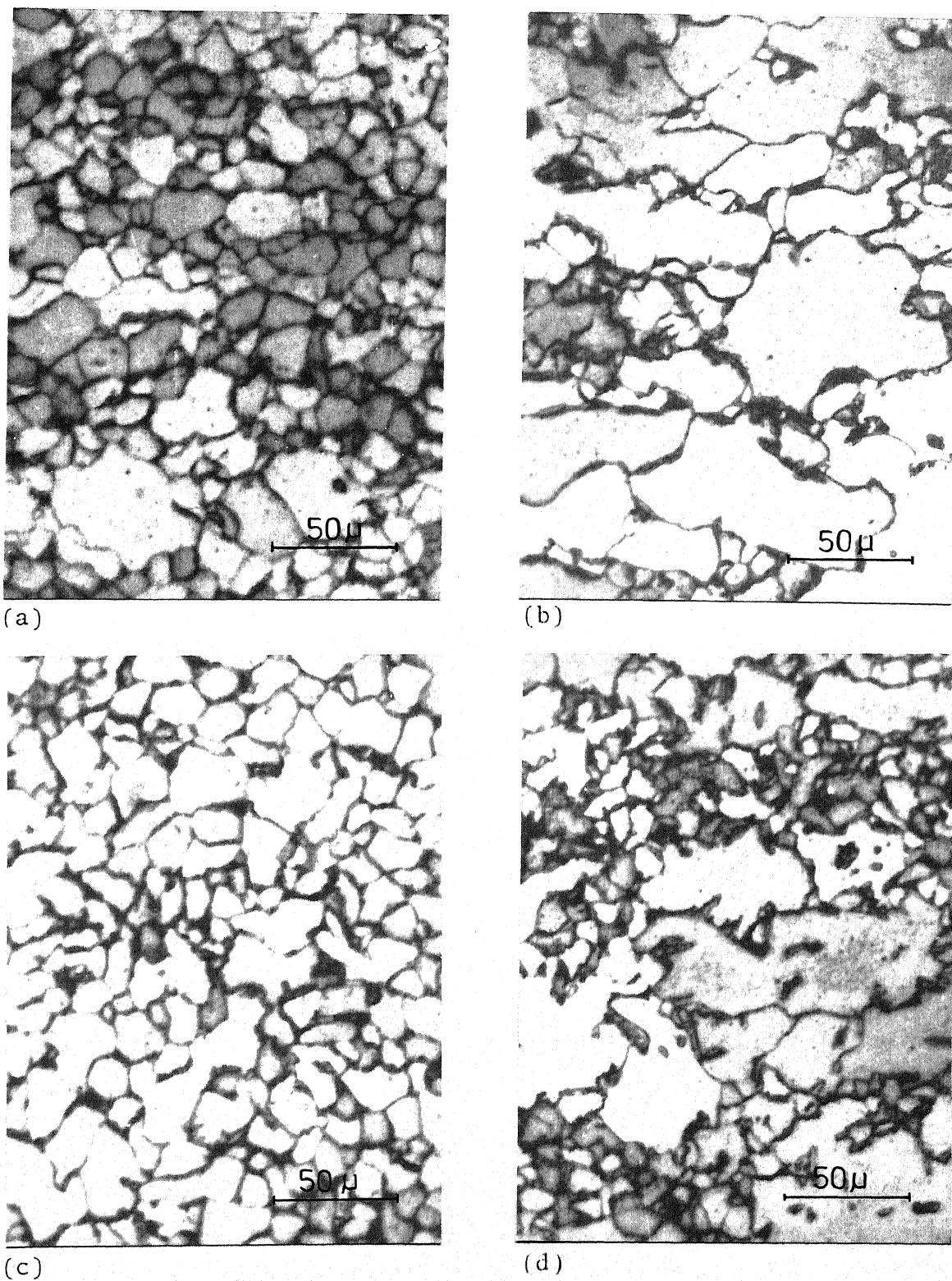
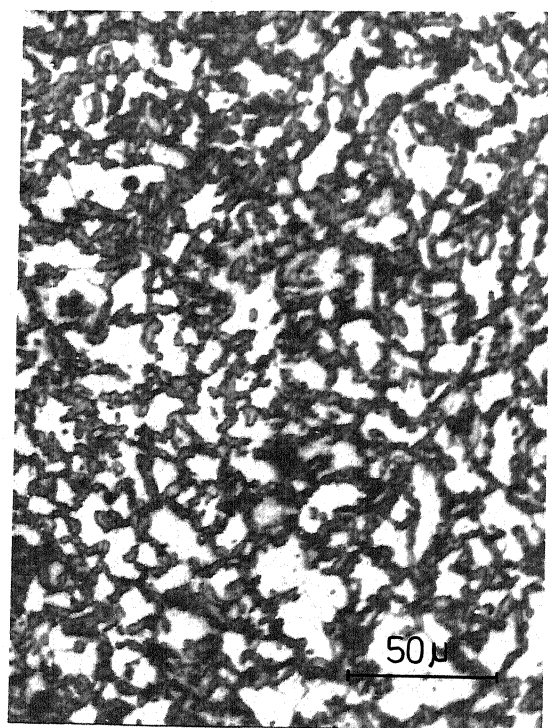
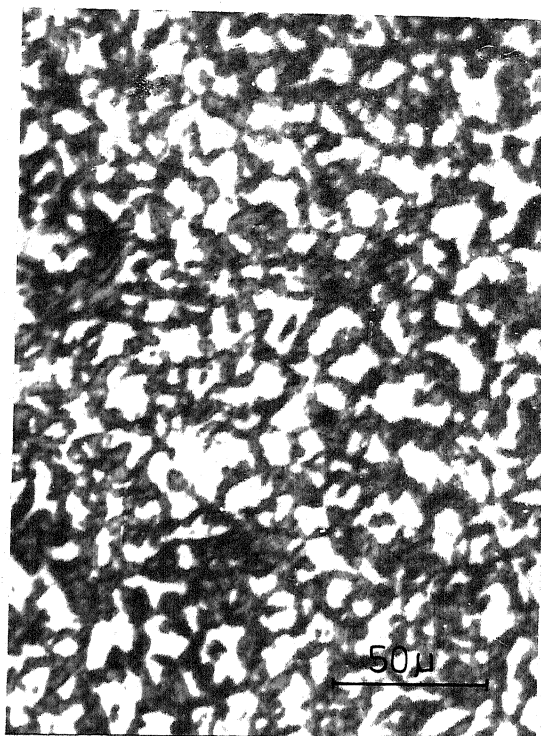


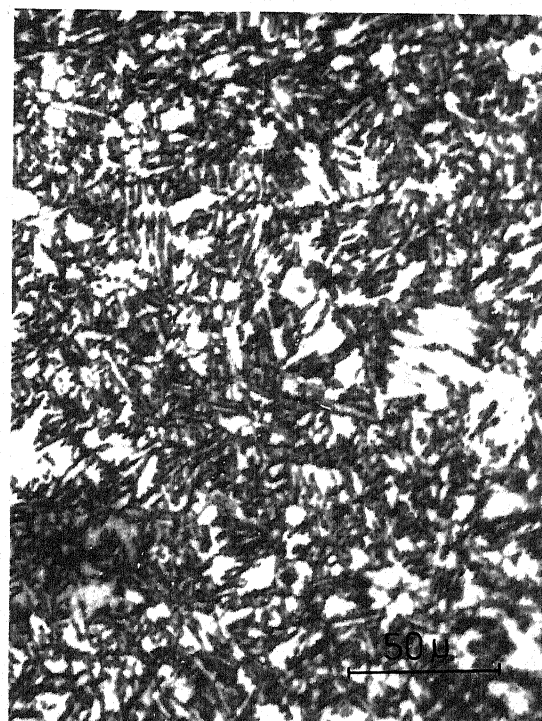
Fig. 4.1 Optical micrographs of alloy Al
(a) AC 750/WQ (b) AC 810/WQ
(c) WQ 750/WQ (d) WQ 810/WQ



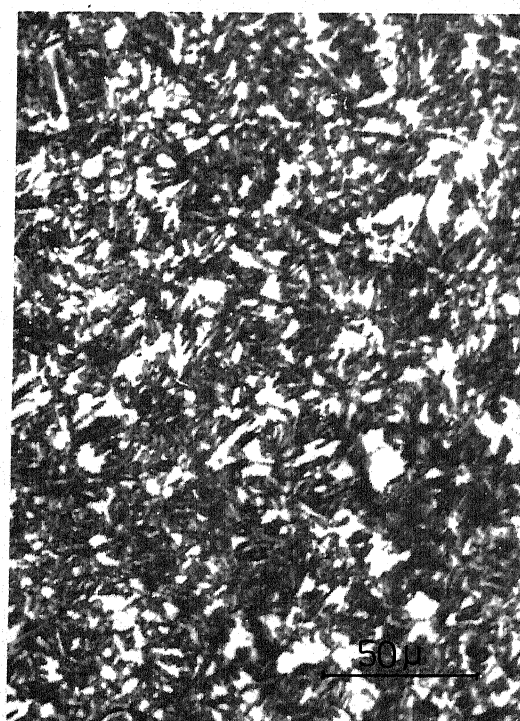
(a)



(b)

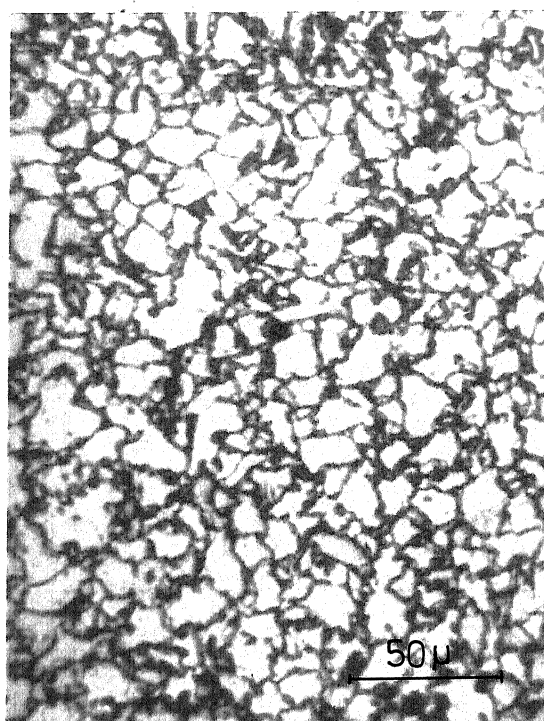


(c)

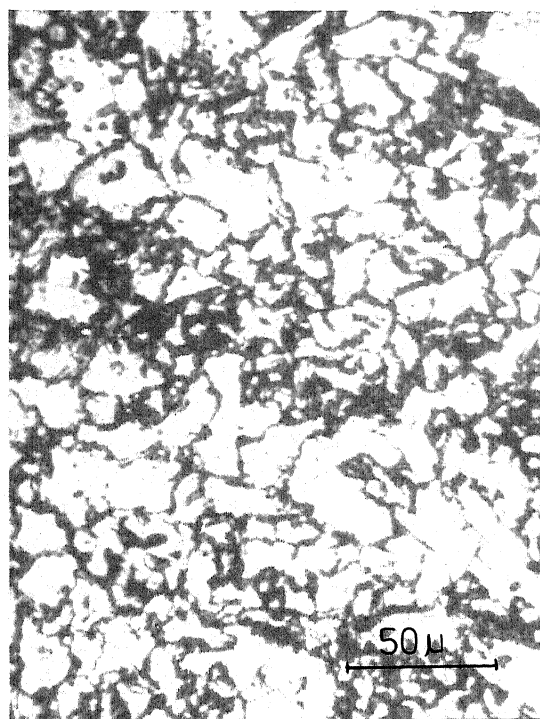


(d)

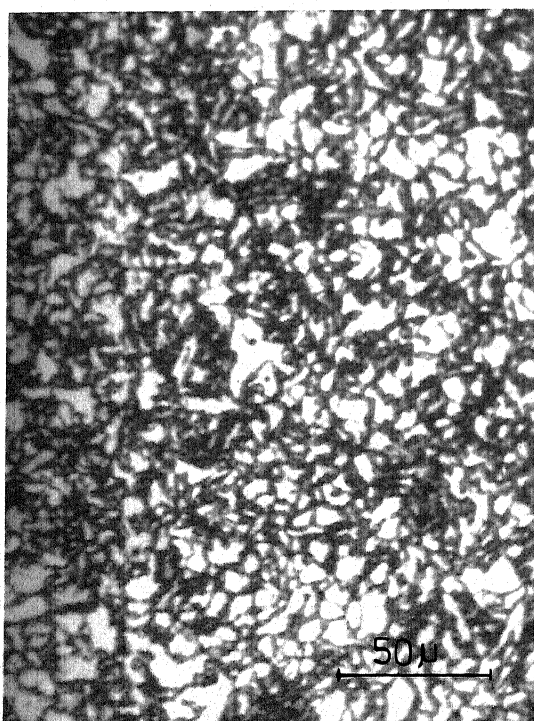
Fig. 4.2 Optical micrographs of alloy A4
(a) AC 750/WQ (b) AC 810/WQ
(c) WQ 750/WQ (d) WQ 810/WQ



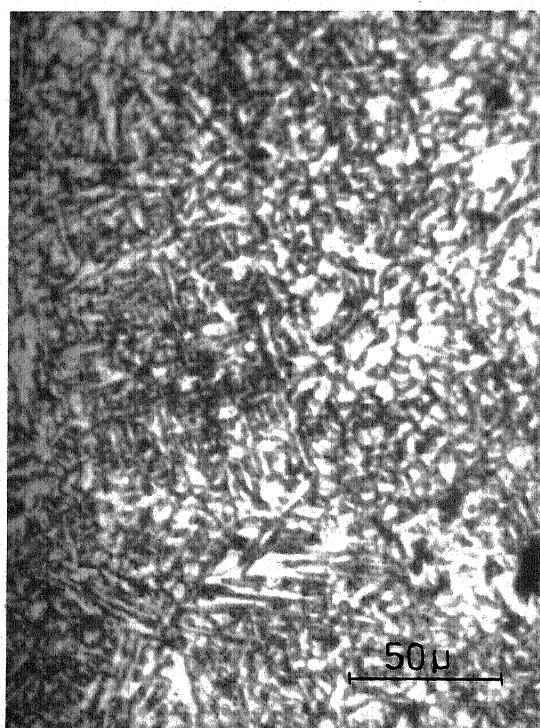
(a)



(b)

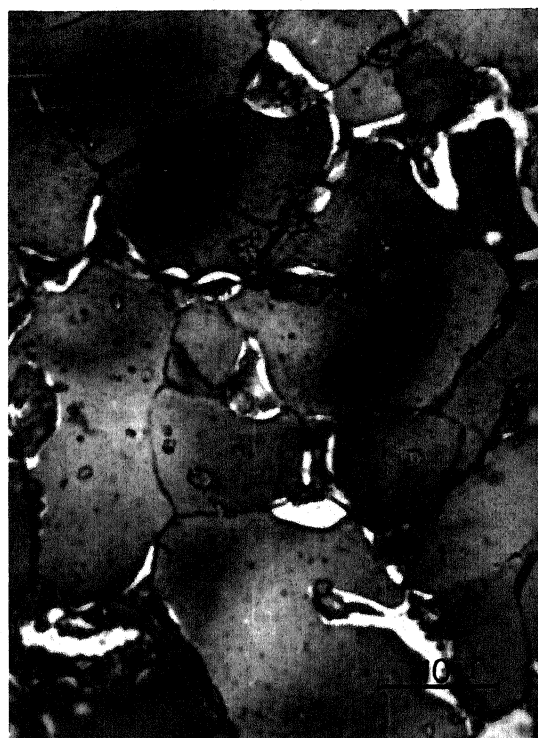


(c)



(d)

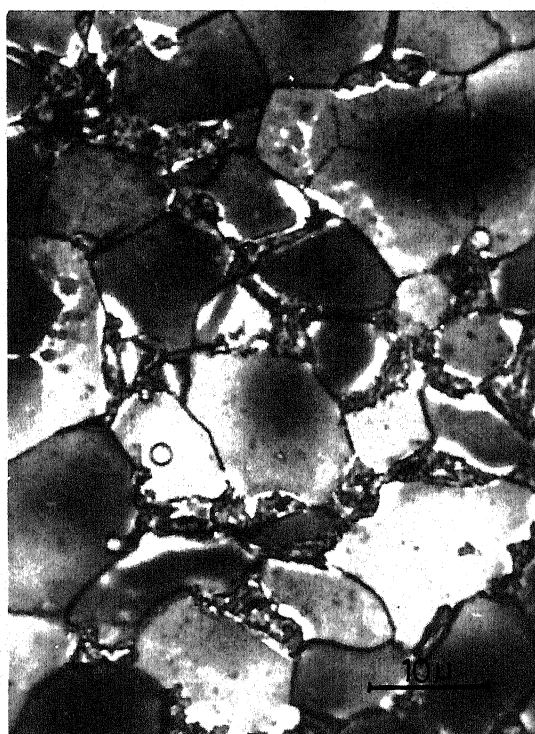
Fig. 4.3 Optical micrographs of alloy A5
(a) AC 750/WQ (b) AC 810/WQ
(c) WQ 750/WQ (d) WQ 810/WQ



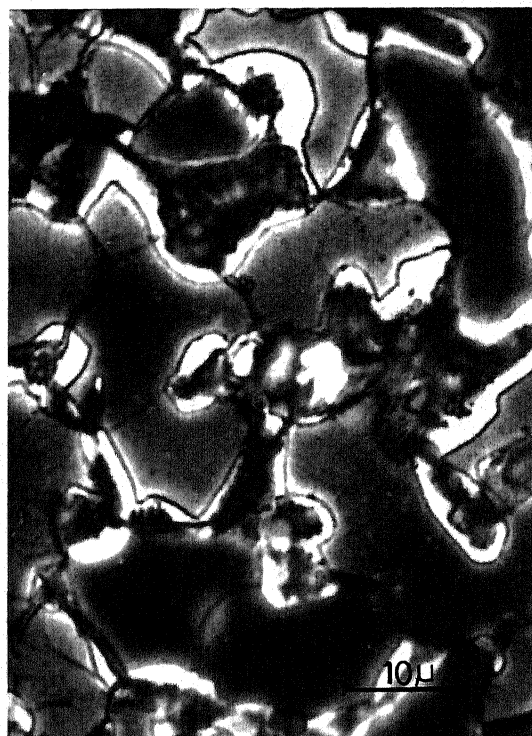
(a)



(b)

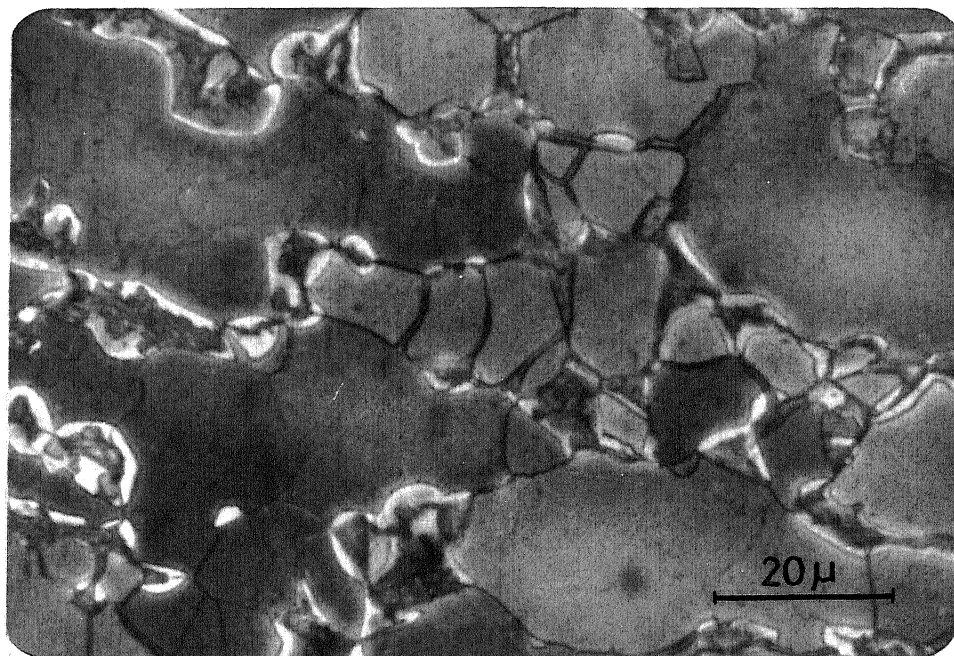


(c)

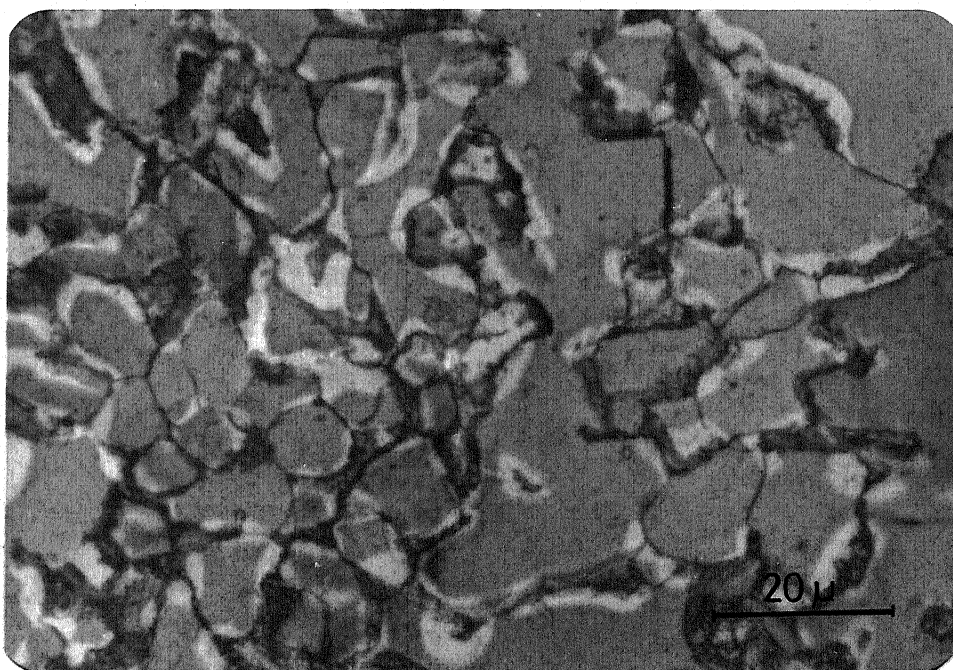


(d)

Fig. 4.4 Stained microstructures of alloy Al
 (a) AC 750/WQ (b) AC 810/WQ
 (c) WQ 750/WQ (d) WQ 810/WQ

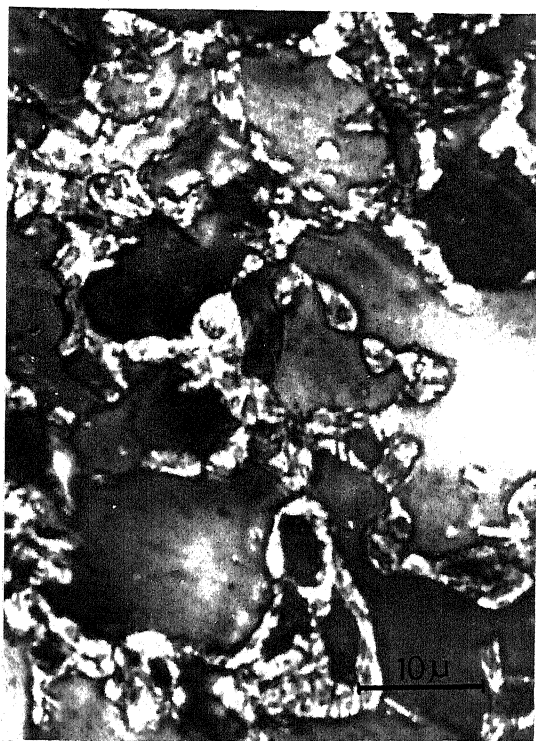


(a)



(b)

Fig. 4.5 Colour photographs of the stained microstructures of alloy Al
(a) AC 810/WQ (b) WQ 810/WQ

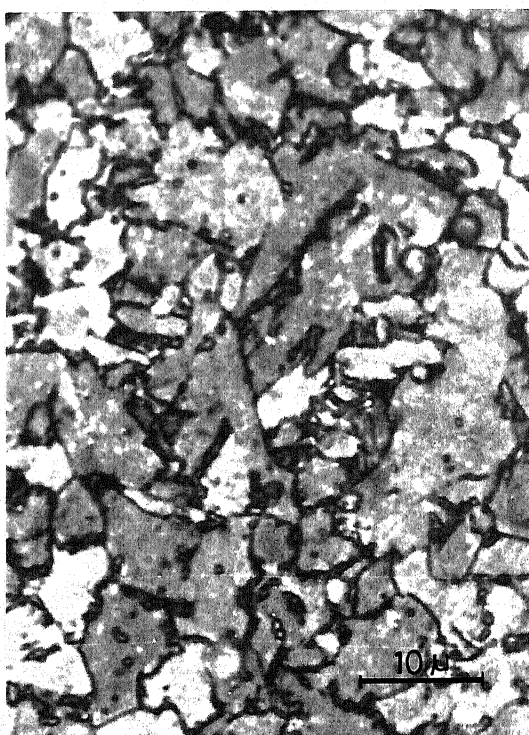


(a)



(b)

Fig. 4.6 Stained microstructures of alloy A4
(a) AC 750/WQ (b) AC 810/WQ

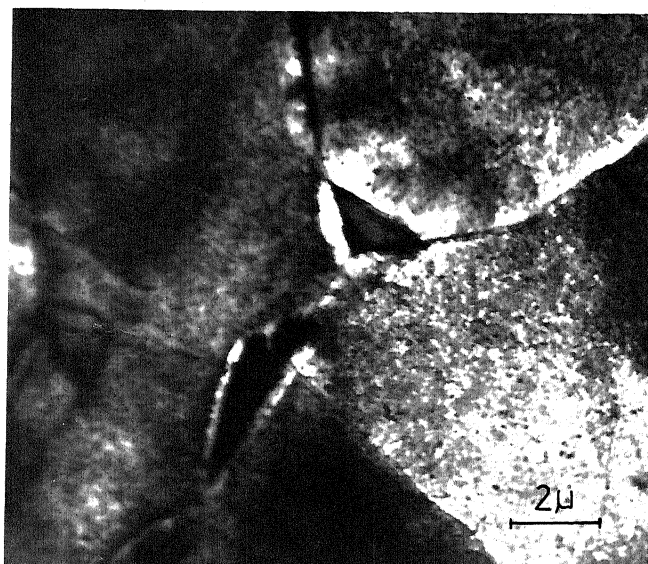


(a)

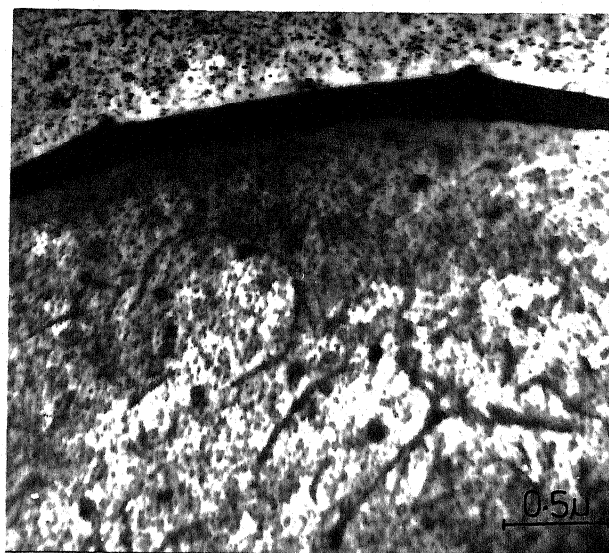


(b)

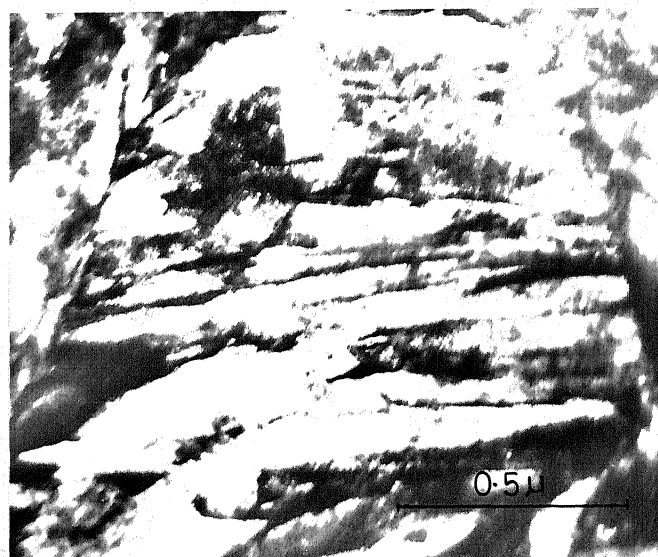
Fig. 4.7 Stained microstructures of alloy A5
(a) WQ 750/WQ (b) WQ 810/WQ



(a)

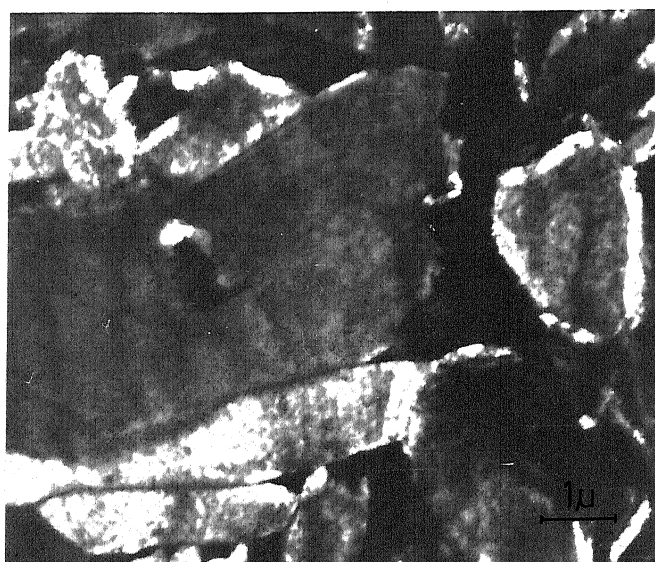


(b)



(c)

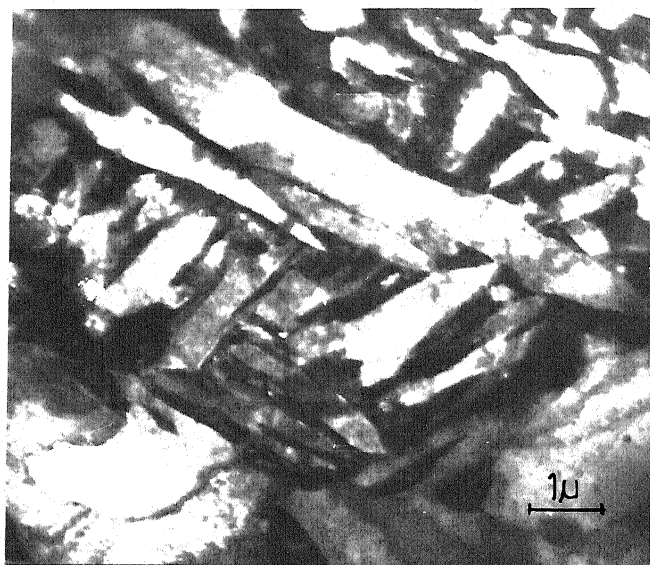
Fig. 4.8 Electron microstructures of alloy Al
 (a) AC 750/WQ (b) AC 750/WQ
 (c) WQ 750/WQ



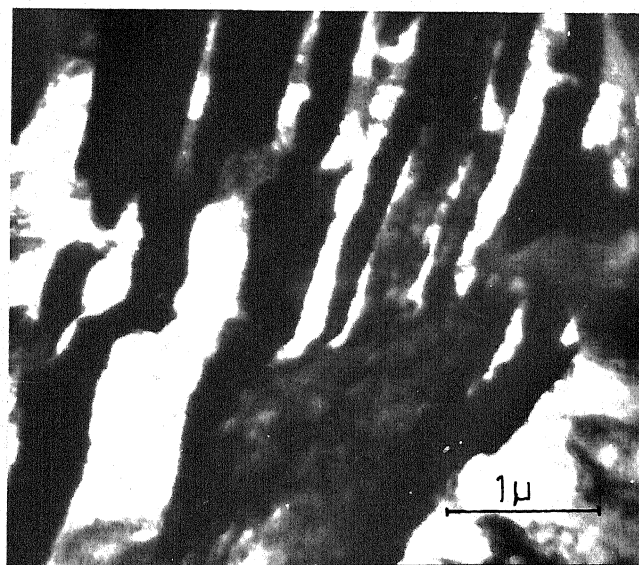
(a)



(b)



(c)

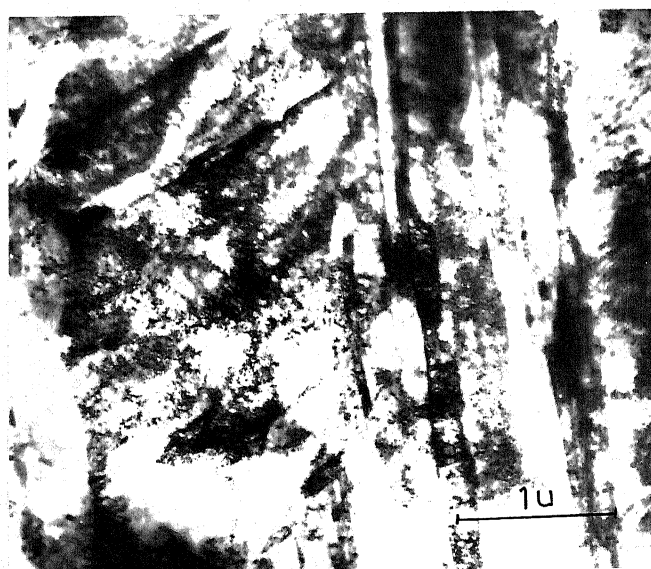


(d)

Fig. 4.9 Electron microstructures of alloy A4
(a) WQ 810/WQ (b) AC 810/WQ
(c) AC 750/WQ (d) AC 750/WQ



(a)



(b)

Fig. 4.10 Electron microstructures of alloy A5
(a) WQ 810/WQ (b) AC 810/WQ

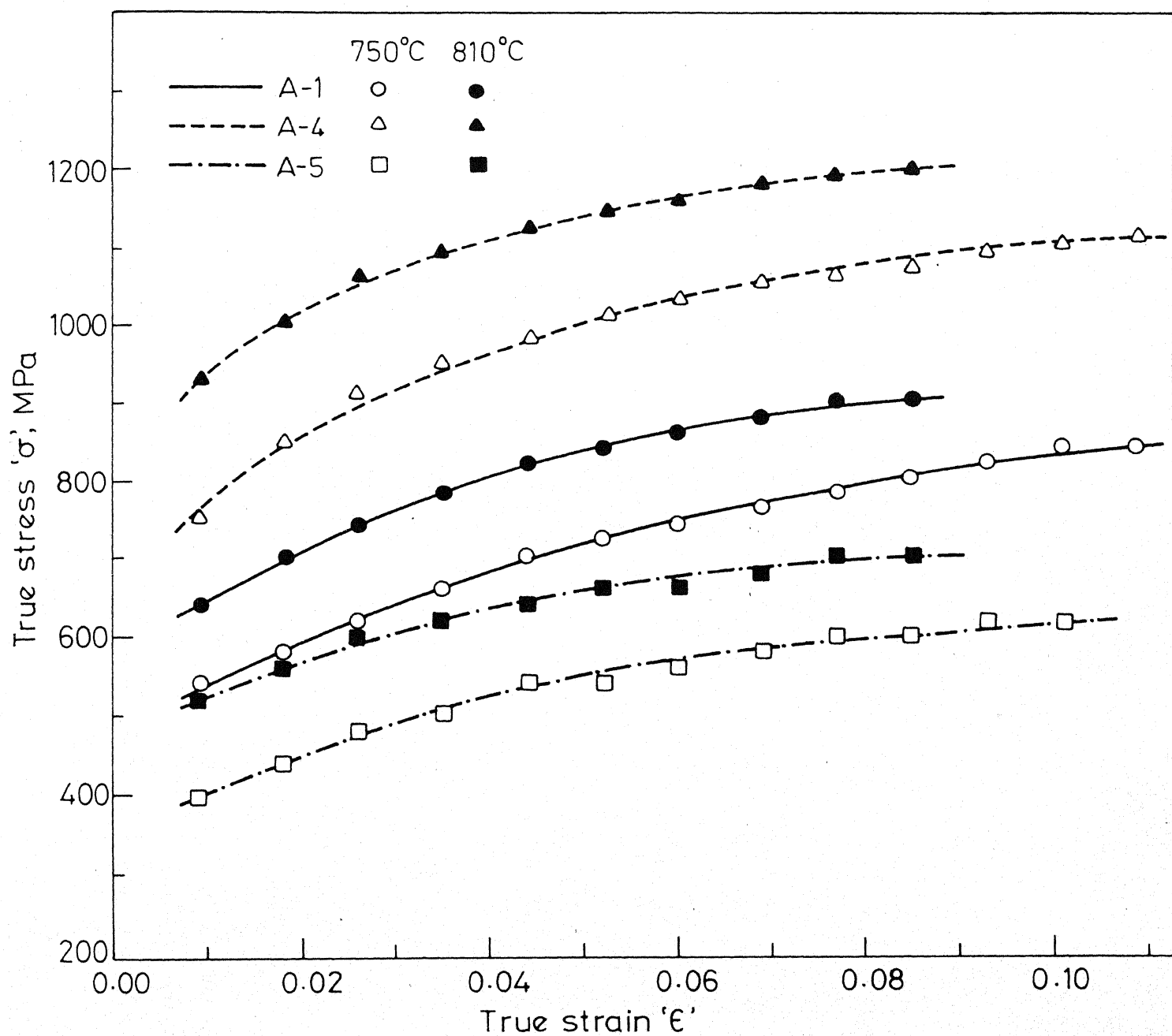


Fig.4.11 True stress versus True strain plots for the alloys air cooled after austenitisation and intercritically annealed at 750°C and 810°C.

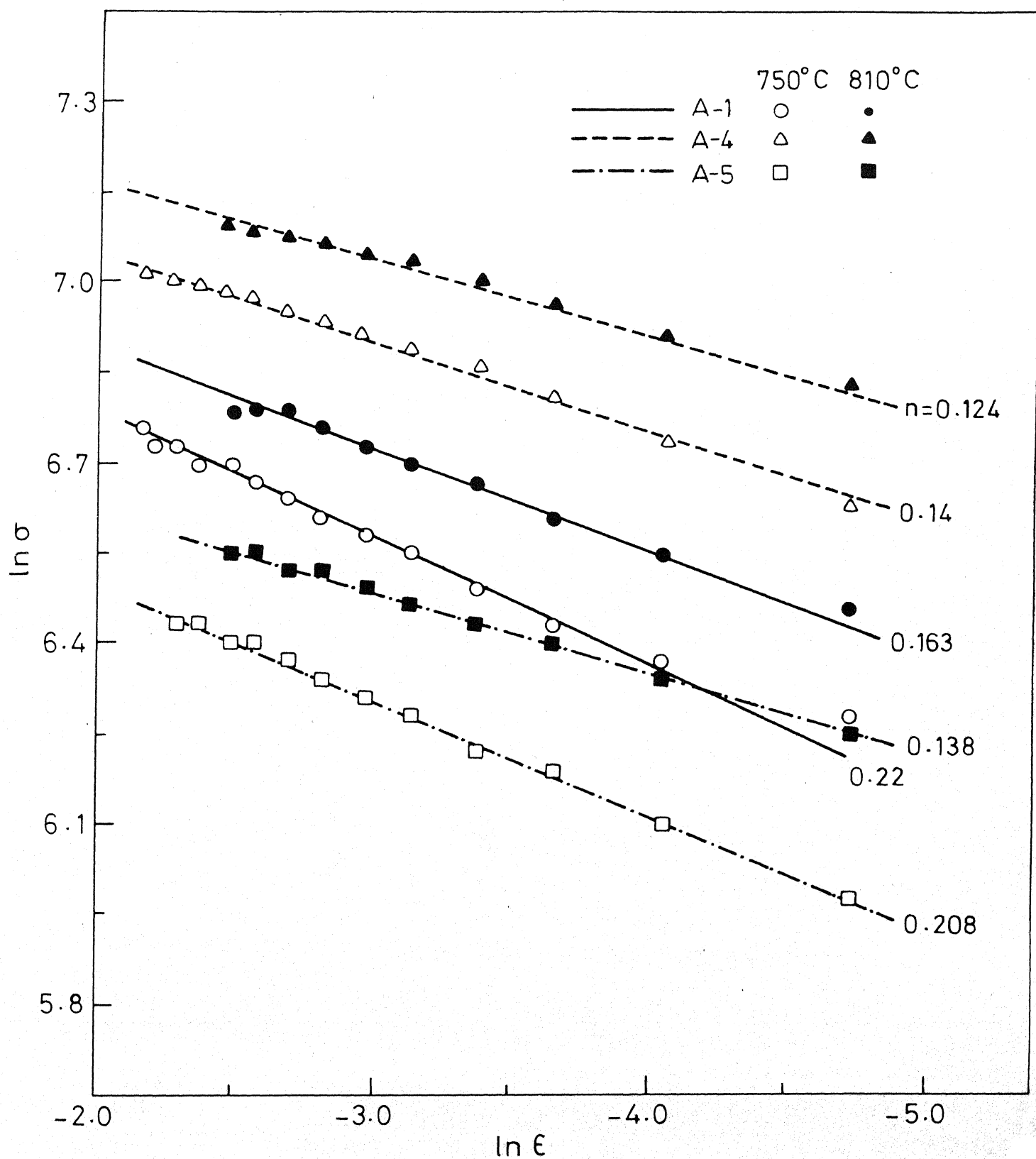


Fig.4.12 Plots of $\ln \sigma$ versus $\ln \epsilon$ for alloys air cooled after austenitisation and intercritically annealed at 750°C and 810°C and water quenched.

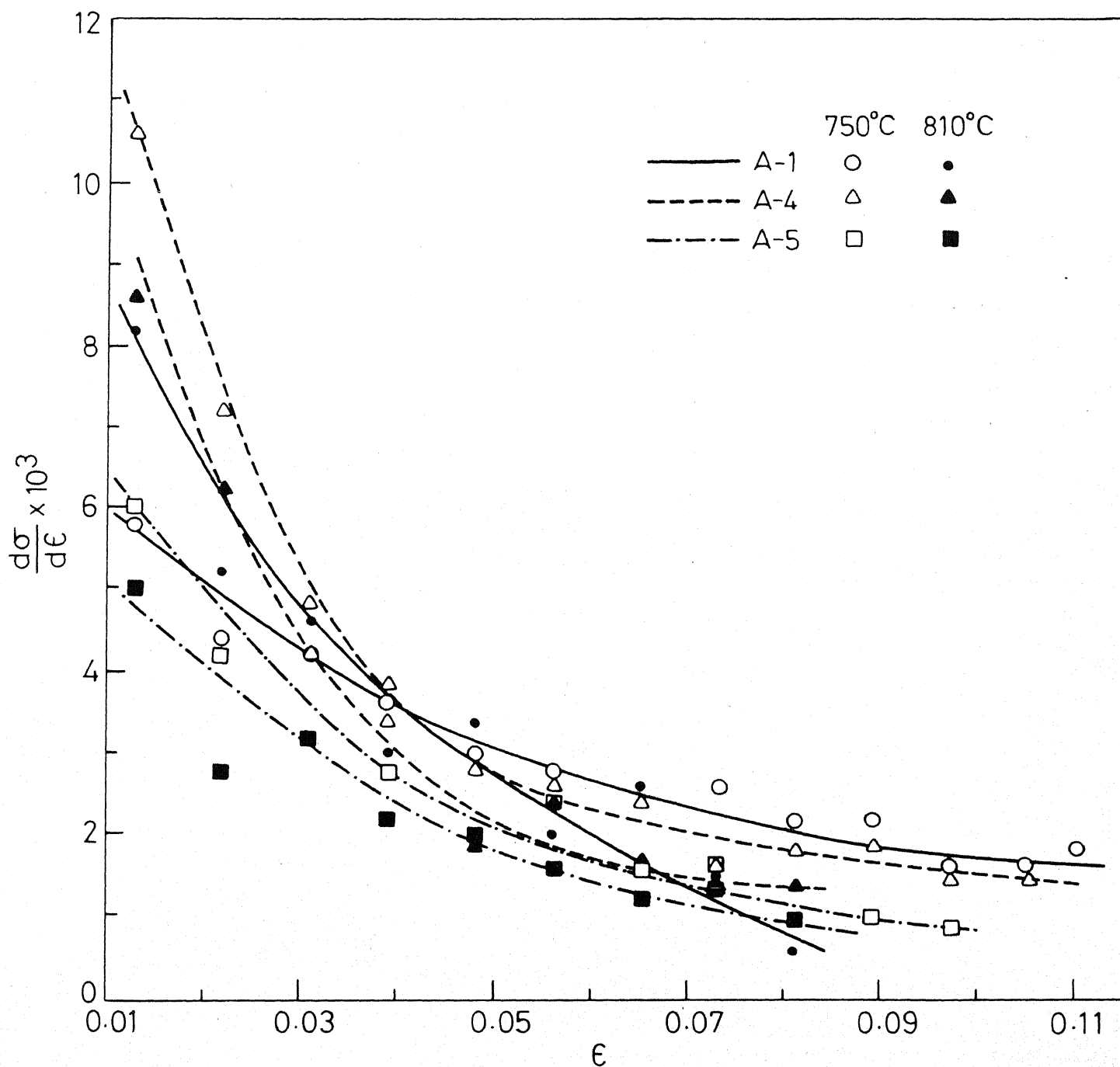


Fig.4.13 Rate of strain hardening as a function of true strain for alloys air cooled after austenitisation and intercritically annealed at 750°C and 810°C and then water quenched.

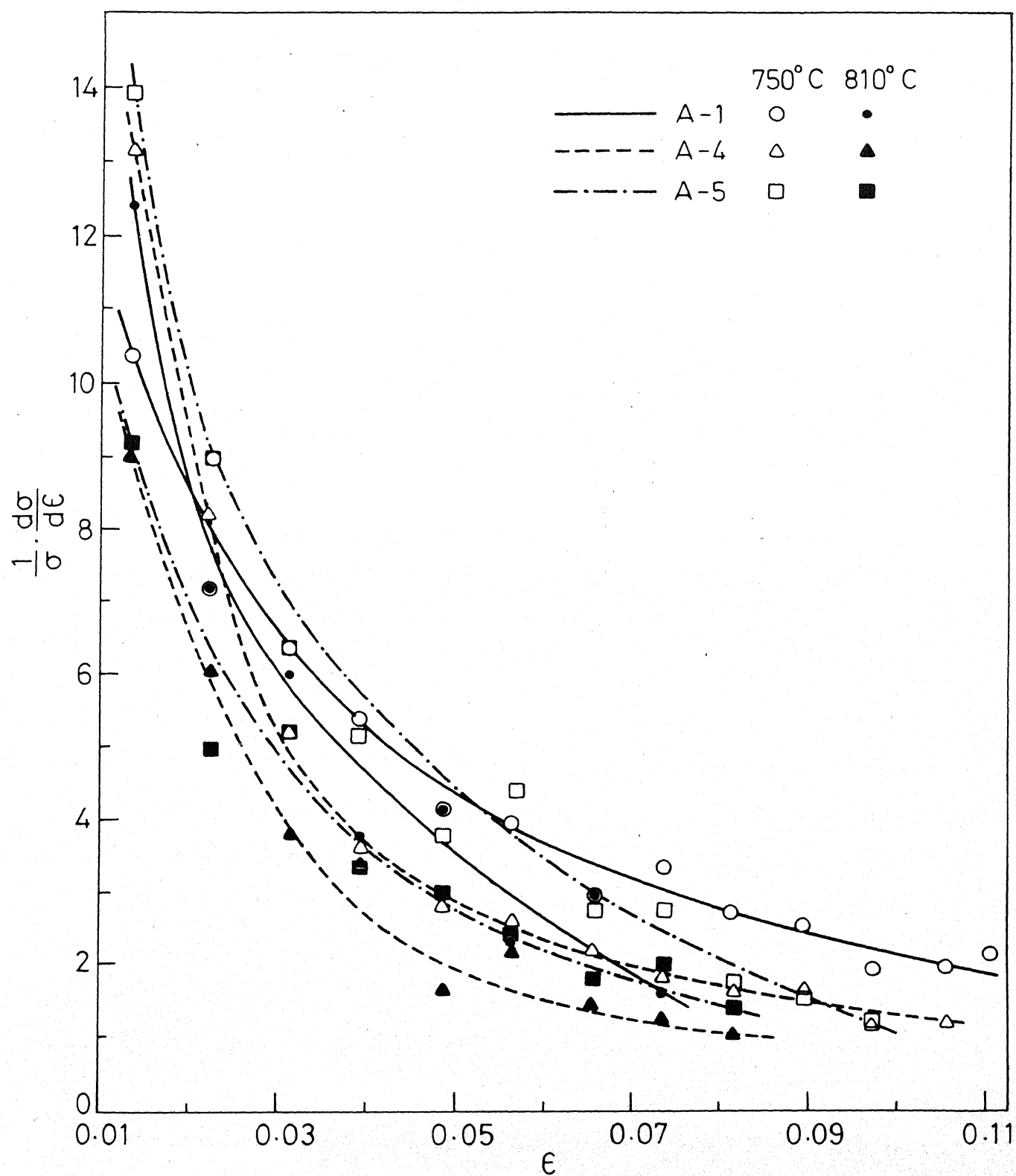


Fig.4.14 $\frac{1}{\sigma} \cdot \frac{d\sigma}{d\epsilon}$ as a function of true strain for alloys air cooled after austenitisation and intercritically annealed at 750°C and 810°C and water quenched.

large number of foils from the differently heat-treated and cold-worked alloys was carried out. In conformity with the optical microscopy results, the T.E.M. results have also shown that, in general, microstructures of any one of the cold-worked alloys are not very much a function of the initial heat-treatment.

A few typical electron microstructures of alloy Al in the cold-worked condition are shown in Figures 4.16(a-j). Figures 4.16(a) shows a general view of the cold-worked structure showing both deformed ferrite and martensite. Figure 4.16(b) shows another area with a deformed martensitic region at an original ferrite grain-boundary together with heavily cold-worked and dislocated ferrite grains. The microstructure of a heavily deformed ferritic region is shown typically in Figure 4.16(c). The structure here consists of a large number of nearly parallel elongated cells with a high dislocation density. The crystallographic orientation from the entire area has been found out to be $\{112\} \langle 111 \rangle$. In a few instances, colonies of parallel cells have been observed having an orientation $\{8, 9, 11\} \langle 133 \rangle$. In addition to these, deformed ferritic areas having orientations $\{110\} \langle 111 \rangle$ and $\{3, 1, 10\} \langle 113 \rangle$ have also been noticed. However, structurally these areas are no different than the areas shown in the above figures. All the above figures refer to the cold-rolled alloy Al where the dual-phase structure was produced by the AC 750/WQ heat-treatment cycle. Similar structures have been obtained for the cold-worked alloy with prior heat-treatment cycle AC 810/WQ. One typical microstructure for such a material is shown in Figure 4.16(d). Here the deformed ferrite regions A and B have been found to have the orientations $\{110\} \langle 111 \rangle$ and $\{112\} \langle 111 \rangle$ respectively. In addition to these

orientations, other orientations like $\{210\} \langle 120 \rangle$, $\{001\} \langle 120 \rangle$ and $\{125\} \langle 120 \rangle$ have also been detected in the thin foils.

A typical electron microstructure of the cold-worked Al alloy having an initial heat-treatment WQ 750/WQ is shown in Figure 4.16(e). The area shows a number of more or less parallel cells of ferrite, the central part of the figure showing a somewhat recovered structure. The S.A.D. from the central part shows that the crystallographic orientation here is $\{110\} \langle 111 \rangle$. At many places it has been observed that the deformed ferrite cells adjacent to a martensitic region are much finer as compared to the ones further away from it. This is shown typically in Figure 4.16(f). The corresponding S.A.D. pattern has shown that the deformed ferrite here has an orientation $\{221\} \langle 110 \rangle$. Almost perfect cube oriented regions, $\{100\} \langle 010 \rangle$, have often been encountered (Figure 4.16(g)). Such regions have been invariably found to consist of long ferrite cells with rather low dislocation density at the centre and exceptionally high density of dislocations at the cell boundaries. The martensitic regions are normally seen to align themselves along the direction of rolling (Figure 4.16(h)).

Figure 4.16(i) shows typical ferritic cells in the cold-worked alloy with the initial heat-treatment WQ 810/WQ. The S.A.D. taken from the entire region shows that these cells have a uniform orientation of $\{110\} \langle 111 \rangle$. Extended regions consisting of a large number of ferrite cells, as in this case, have also been detected having a uniform orientation of $\{130\} \langle 001 \rangle$ as shown in Figure 4.16(j). In this and the previous micrograph, the ferrite cells show a somewhat recovered appearance. Fine precipitates, very often associated with dislocations, can also be seen

within some of the recovered cells. In addition to the above orientations, the orientations $\{147\} \langle 311 \rangle$, $\{125\} \langle 210 \rangle$ and $\{112\} \langle 111 \rangle$ have also been commonly noticed in the thin foils.

The electron microstructures of the alloy A4, in the cold-worked condition, have shown that the structural features are quite similar irrespective of the initial heat-treatment. Some typical microstructures of this alloy are given in Figures 4.17(a-d). Heavily deformed elongated cells with high dislocation density constitute the typical structure of this cold-worked alloy. These features are shown in Figure 4.17(a) for the AC 810/WQ heat-treatment. Figure 4.17(b) shows another area where the deforming phase is predominantly martensite. Sometimes, the deformed martensitic regions show striations very similar to those of internal twinning (Figure 4.17c). Figure 4.17d shows another area containing heavily deformed ferrite cells; the crystallographic orientation of the whole area was found out to be $\{112\} \langle 111 \rangle$. In addition to the above-mentioned orientations, others like $\{123\} \langle 210 \rangle$, $\{110\} \langle 010 \rangle$ and $\{310\} \langle 010 \rangle$ have also been frequently encountered in the thin foils made from this alloy.

Irrespective of the prior heat-treatments, the electron microstructures of the cold-worked alloy A5 are quite similar. Figure 4.18(a) shows a typical microstructure in this alloy. This micrograph shows a band of nearly parallel highly dislocated cells flanked by wider cells on both sides. In many places, however, the ferrite cell structure in this alloy shows distinct signs of recovery leading to the formation of well-developed subgrains. One typical example is shown in Figure 4.18(b) where the central subgrains have been found to have an orientation

$\{110\} \langle 111 \rangle$. A group of parallel subgrains in a highly recovered stage are shown in Figure 4.18(c) having an orientation $\{147\} \langle 311 \rangle$. Figure 4.18(d) shows another area with a large enough subgrain at the centre which seems to have already developed a high-angle boundary on one side. The S.A.D. pattern taken from this subgrain shows that it has an orientation $\{310\} \langle 001 \rangle$. In addition to the above orientations, ferrite regions having $\{111\} \langle 110 \rangle$, $\{112\} \langle 111 \rangle$, $\{221\} \langle 011 \rangle$, $\{8, 9, 11\} \langle 313 \rangle$ and $\{110\} \langle 001 \rangle$ orientations have also been observed in a number of foils in this alloy.

4.2.2 Deformation Texture

The (110) pole-figures for all the three alloys in the cold-rolled condition are given in Figure 4.19(a-1). It can be clearly seen that all these pole-figures possess similar general features. In each case the texture was found to consist of a moderately strong $\{111\} \langle 112 \rangle$ component and a rather weak $\{111\} \langle 110 \rangle$ component.

For alloy A1, the value of the maximum of the $\{111\} \langle 112 \rangle$ texture component has been found to vary from 2X random to 4X random depending on the prior heat-treatment. The strongest texture has been obtained for the material having the prior heat-treatment WQ 750/WQ.

For the alloys A4 and A5, the maximum intensity of the $\{111\} \langle 112 \rangle$ component has been found to vary from 2X random to 3X random. In both the alloys the strongest texture has been obtained for the material having the prior heat-treatment AC 750/WQ.

For all the three alloys and for all the prior heat-treatments, the intensity of the minor component, $\{111\} \langle 110 \rangle$, does not seem to change

with heat-treatment.

In order to get a detailed idea about the deformation textures of the cold-rolled materials, the O.D.F. plots from all of them were made. These plots for the alloys A1, A4 and A5 are shown in Figures 4.20-4.22 respectively. These are nothing but contour-line representations of $f(g)$ in the form of sections, $\psi_1 = \text{Constant}$ ($\psi_1 = 0, 5, 10 \dots 90^\circ$), through a Cartesian Euler angle space. In each $\psi_1 = \text{Constant}$ section ϕ and ψ_2 vary from 0 to 90° . Intensities of a few maxima in the O.D.F. plots are indicated at appropriate places. It is at once clear from these figures that the intensity levels in both the pole-figures as well as the O.D.F.'s are rather low for alloy A4 in comparison to the alloys A1 and A5. A1 has been found to have the maximum intensity out of the three alloys. In other words, the deformation textures of alloys A1 and A5 are found to be much sharper as compared to that of alloy A4. It is interesting to note that whereas the pole-figures, in general, do not appear to be very sharp, the corresponding O.D.F. plots exhibit a distinct pattern with rather pronounced maxima at specific regions of the orientation space.

For alloy A1, for both the heat-treatments — AC/WQ and WQ/WQ — a higher value of $f(g)_{\text{max}}$ is obtained for the lower intercritical annealing temperature of 750°C as compared to the higher temperature of 810°C . Again, for both the intercritical annealing temperatures, WQ/WQ-treatment produces a higher value of $f(g)_{\text{max}}$ as compared to AC/WQ-treatment. For alloy A4, for the heat-treatment AC/WQ, a higher value of $f(g)_{\text{max}}$ is found for the lower intercritical annealing temperature of 750°C as compared to the higher temperature of 810°C . The effect of the intercritical annealing temperature on the $f(g)$ value for the WQ/WQ-treatment was found to be just

the reverse. Again, for the intercritical annealing temperature of 810°C , a high $f(g)_{\text{max}}$ value was obtained for the WQ/WQ treatment as compared to AC/WQ treatment. Intercritical annealing at the lower temperature of 750°C does not produce any difference in the $f(g)_{\text{max}}$ values for both the treatments.

For alloy A5, the effect of the heat-treatments AC/WQ as well as WQ/WQ on the $f(g)_{\text{max}}$ values for the materials intercritically annealed at different temperatures has been found to be rather similar to that in alloy A4. Although intercritical annealing at the higher temperature of 810°C does not make any difference in the $f(g)_{\text{max}}$ values for the materials subjected to either AC/WQ or WQ/WQ treatments, annealing at the lower temperature of 750°C has been found to produce a higher $f(g)_{\text{max}}$ value in case of AC/WQ treatment as compared to WQ/WQ treatment.

It has been previously shown [192] that the structure of an O.D.F. can be described with the help of peak-type components and complete or incomplete fibre components. The peak-type components are characterised by a more or less isotropic scattering ranges around certain ideal orientations. On the other hand, the presence of the well developed fibre components is characterised by a more or less uniform pole density along certain lines within the three-dimensional orientation space.

From a look at the O.D.F. plots it is at once apparent that there are a number of peak type components in each plot. The Euler angles for such peak type components have been read out from the relevant computer print-outs and the ideal orientations, $(hkl) [uvw]$, corresponding to those angles were obtained from the Table 3.3. In this way it can be shown that some of the major texture components in all the plots are $\{111\} \langle 110 \rangle$ and

whereas in the latter section the peak at $\phi = 55^\circ$ is reasonably large while the one at $\phi = 35^\circ$ is negligibly small. Figure 4.26 shows that for the material Al/WQ 810/WQ, in both the sections $\psi_1 = 0^\circ$, $\psi_2 = 45^\circ$ and $\psi_1 = 90^\circ$, $\psi_2 = 45^\circ$ a single peak appears at $\phi \approx 55^\circ$.

A close look at the above results does not clearly indicate the presence of any strong fibre texture. However, one thing is pretty clear from these plots and that is, the pole densities at the orientations $(111) [uvw]$ are the strongest in all cases, whereas the pole densities at other orientations are negligible as compared to this. Another striking point in all the above plots is that the pole densities in the section $\psi_1 = 0^\circ$, $\psi_2 = 45^\circ$ are significantly higher than those in the other section, namely, $\psi_1 = 90^\circ$, $\psi_2 = 45^\circ$. In order to check whether some kind of fibre texture may be present in these materials, $f(g)$ values have been plotted for (a) $\phi = 55^\circ$ and $\psi_2 = 45^\circ$ for $\psi_1 = 0-90^\circ$, (b) $\phi = 30^\circ$ and $\psi_2 = 45^\circ$ for $\psi_1 = 0-90^\circ$ and (c) $\phi = 75^\circ$ and $\psi_2 = 45^\circ$ for $\psi_1 = 0-90^\circ$. The reason behind the plots (a) is quite obvious. Plots (b) were conceived to check the possibilities of having incomplete $\{337\}$ fibre textures in these materials, since such a texture has been reported in the literature for similar materials [193]. Plots (c) were chosen because of the fact that significant pole densities were obtained in both the sections $\psi_1 = 0^\circ$, $\psi_2 = 45^\circ$ and $\psi_1 = 90^\circ$, $\psi_2 = 45^\circ$ at $\phi = 75^\circ$ in these materials subsequently recrystallised. All the above plots for the alloy Al after 60% cold-rolling are shown in Figures 4.27 to 4.30 for various initial heat-treatments. Figure 4.27 shows that, for the material Al/AC 750/WQ, the pole densities lie within a range $f(g) = 5$ to 7 for the $\{111\} \langle uvw \rangle$ orientations. In contrast to this, the $\{337\} \langle uvw \rangle$ pole densities show a very drastic

change from $\psi_1 = 0$ to 90° . It starts from a rather high value of $f(g) > 5$ at $\psi_1 = 0^\circ$ and decreases at a fast rate with increasing value of ψ_1 , attaining a value of zero at $\psi_1 = 40^\circ$. The third plot which is nothing but a plot of pole densities of the orientations $\{11, 11, 4\} \langle uvw \rangle$, however, shows a rather small but more or less uniform pole density all throughout.

Similar plots for the material Al/AC 810/WQ are shown in Figure 4.28. It is clear from this figure that a moderately strong incomplete fibre texture component of the type $\{111\} \langle uvw \rangle$ is present, whereas no clear cut $\{337\} \langle uvw \rangle$ or $\{11, 11, 4\} \langle uvw \rangle$ fibre components are discernible. Figure 4.29 shows that for the material Al/WQ 750/WQ there is practically no fibre component present. Out of the three, the pole densities of the $\{111\} \langle uvw \rangle$ orientations are the strongest and these lie within a range of $f(g) = 4$ to 9 . The pole densities of the $\{337\} \langle uvw \rangle$ orientations show a very wide variation from an $f(g)$ value of 6.5 at $\psi_1 = 0^\circ$ to an $f(g)$ value of zero at $\psi_1 = 50^\circ$ onwards. The pole densities of the $\{11, 11, 4\} \langle uvw \rangle$ orientations are rather weak. A moderately strong rather incomplete $\{111\}$ fibre texture is found to be present in the material Al/WQ 810/WQ (Figure 4.30), whereas the pole densities of the $\{337\} \langle uvw \rangle$ and $\{11, 11, 4\} \langle uvw \rangle$ orientations are found to be rather weak and do not give rise to any significant fibre texture.

The variation of $f(g)$ with ϕ along different ψ_1/ψ_2 lines for the alloy A4 with different initial heat-treatments followed by 60% cold-rolling, is shown in a graphical manner in Figures 4.31 to 4.34. An examination of these plots reveals that for all the four different materials, reasonably large peaks in pole density values are obtained at $\phi = 55^\circ$ in both the sections $\psi_1 = 0, \psi_2 = 45^\circ$ and $\psi_1 = 90^\circ, \psi_2 = 45^\circ$. The

most interesting thing to notice^{is} that, excepting A4/AC 810/WQ all the other three materials show nearly the same value of $f(g)$ in both the Ψ_1/Ψ_2 sections. In addition, moderately strong peaks in $f(g)$ have been obtained at $\phi = 75^\circ$ in both the Ψ_1/Ψ_2 sections for the materials A4/AC 750/WQ and A4/AC 810/WQ. Flat peaks at $\phi = 30$ to 35° have been obtained for the material A4/AC 810/WQ for both the Ψ_1/Ψ_2 sections.

A close look at the above plots gives sufficient indications of the presence of a reasonably strong $\{111\} \langle uvw \rangle$ fibre texture in all the four materials and a moderate $\{11, 11, 4\} \langle uvw \rangle$ fibre texture in at least two of the materials. All these possibilities have been systematically checked in a manner described above for the Al alloy. The relevant plots are shown in Figures 4.35 to 4.38. It is at once apparent from these plots that reasonably good $\{111\}$ fibre texture is obtained in all the four materials. Whereas the pole densities for all the components comprising this fibre are reasonably strong ($f(g) \approx 4$) for the materials A4/AC 750/WQ, A4/WQ 750/WQ and A4/WQ 810/WQ, the pole density values are nearly half of this in case of the material A4/AC 810/WQ. All these materials also show a reasonably good, though rather moderate $\{11, 11, 4\} \langle uvw \rangle$ fibre. The $\{337\} \langle uvw \rangle$ orientations are not found to be developed as a fibre texture and can at best be thought of as a rather weak and incomplete fibre texture component.

The variation of $f(g)$ with ϕ along different Ψ_1/Ψ_2 lines for the alloy A5, with four different initial heat-treatments and subsequently cold-rolled 60%, is shown graphically in Figures 4.39 to 4.42. In all the four plots reasonably strong peaks in $f(g)$ have been obtained at $\phi = 55^\circ$ in both the Ψ_1/Ψ_2 sections. The values of $f(g)$ in the first three materials are found to be nearly same in both the Ψ_1/Ψ_2 sections, whereas

there is a perceptible difference in the values of $f(g)$ in the two sections for the material A5/WQ 810/WQ. Practically, no other peak excepting the one mentioned above has been noticed in the above plots. These results clearly indicate the presence of a strong $\{111\}$ fibre texture in these materials. This possibility has been checked by following the same procedure as was done in case of the alloys A1 and A4. The relevant plots are given in Figures 4.43 to 4.46. A close look at these figures clearly confirms the presence of a reasonably strong $\{111\}$ fibre texture component in the first three of these materials; this component, though quite strong, is not that well developed in the material A5/WQ 810/WQ. A moderate reasonably good $\{11, 11, 4\}$ fibre texture component has also been obtained in these materials, although no $\{337\}$ fibre could be observed.

A comparison of the texture data for the three cold-rolled alloys A1, A4 and A5 clearly indicates the differences in their deformation textures. Thus, whereas a reasonably strong $\{111\}$ fibre texture component is obtained for both the alloys A4 and A5, no $\{111\}$ fibre is found to be present in alloy A1. Again, a weak $\{11, 11, 4\}$ fibre has been found in alloy A4, this same component appears as not so well developed in alloy A5, while this may be treated as a weak and incomplete fibre in case of alloy A1. So far as the $\{337\}$ $\langle uvw \rangle$ orientations are concerned, these do not comprise a fibre component in either alloy A1 or A5, although alloy A4 can be supposed to have a rather weak and incomplete $\{337\}$ fibre texture.

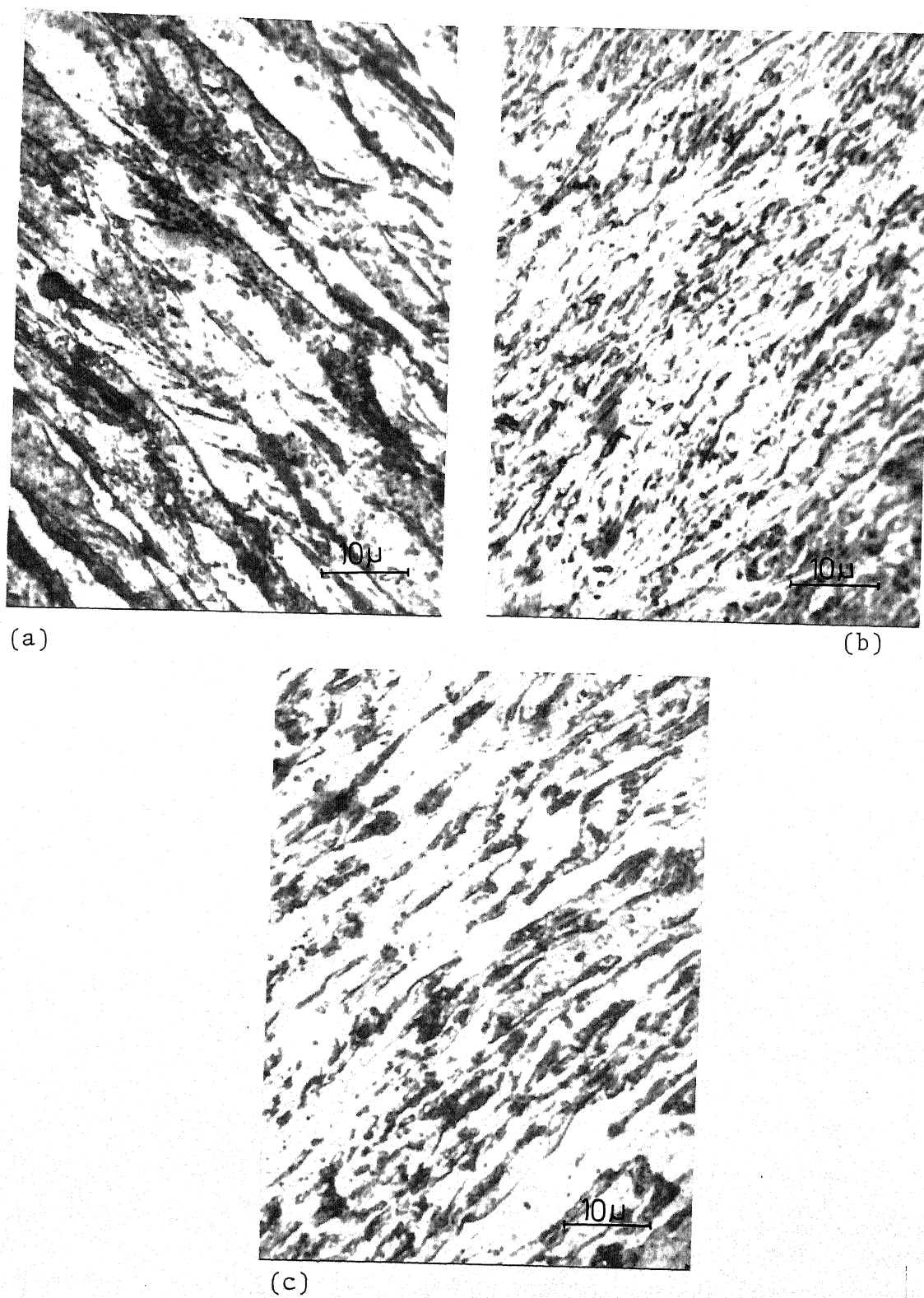
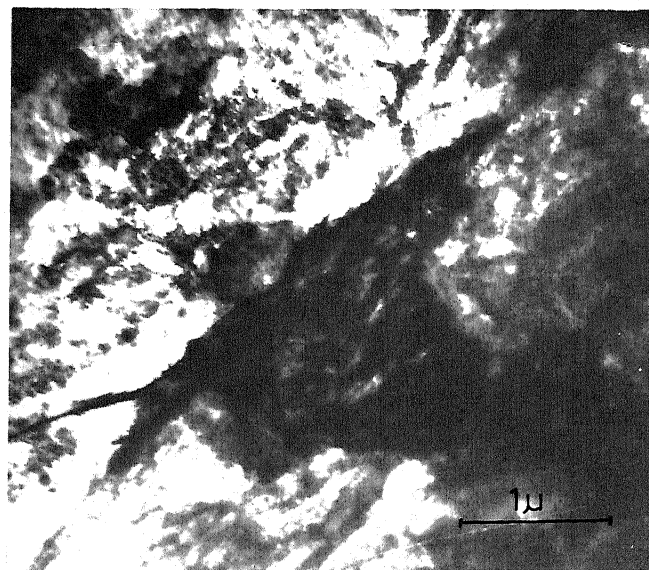


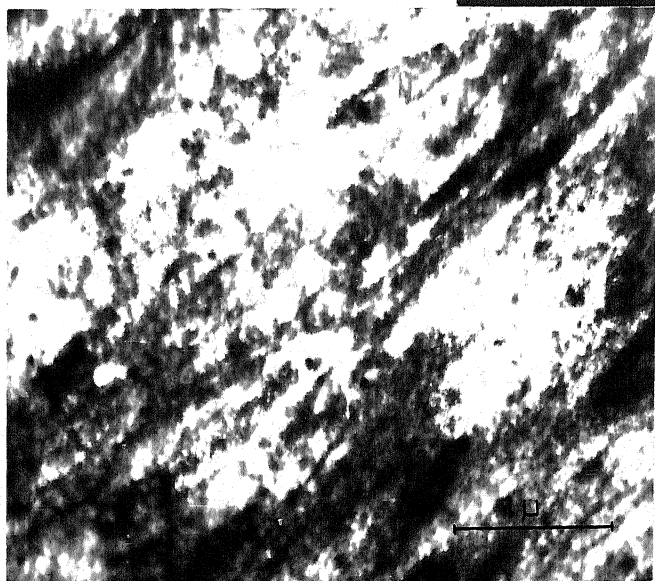
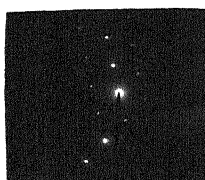
Fig. 4.15 Optical microstructures from cold-worked alloys
(a) Alloy A1, WQ 750/WQ, C.W. 60%
(b) Alloy A4, WQ 750/WQ, C.W. 60%
(c) Alloy A5, WQ 750/WQ, C.W. 60%



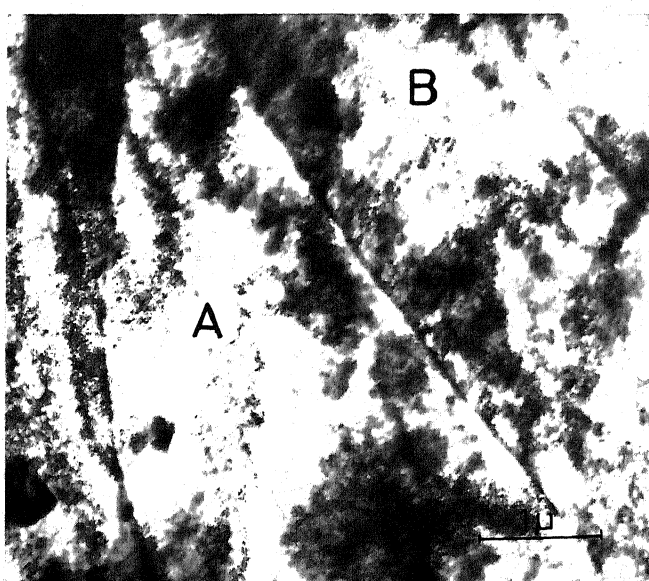
(a)



(b)

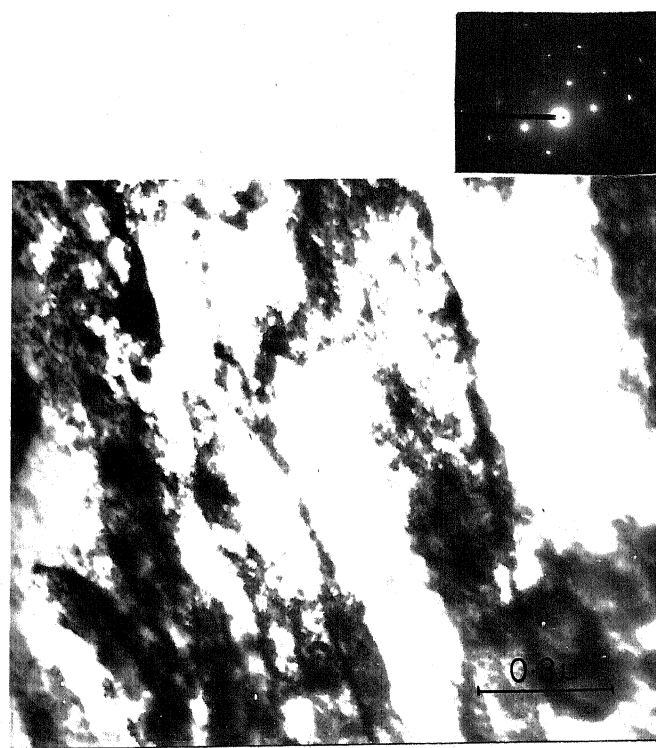


(c)

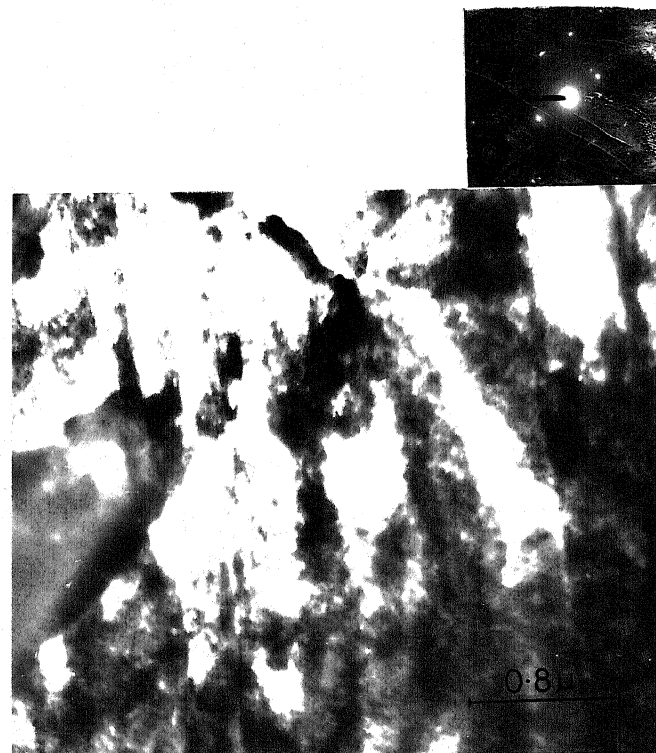


(d)

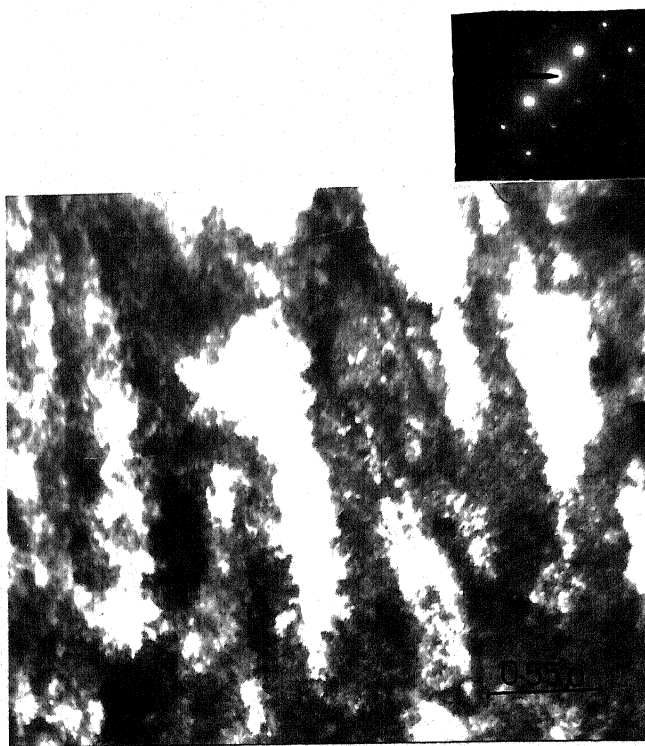
Fig. 4.16 Electron microstructures of 60% cold-worked alloy Al
 (a) AC 750/WQ (b) AC 750/WQ
 (c) AC 750/WQ (d) AC 810/WQ



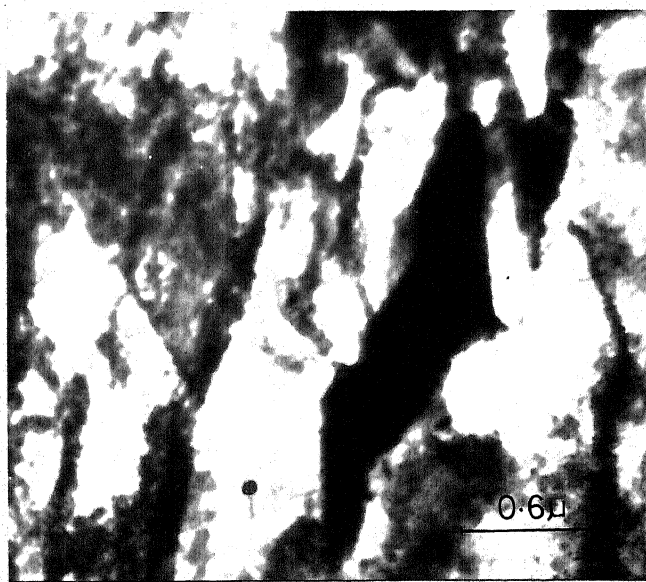
(e)



(f)

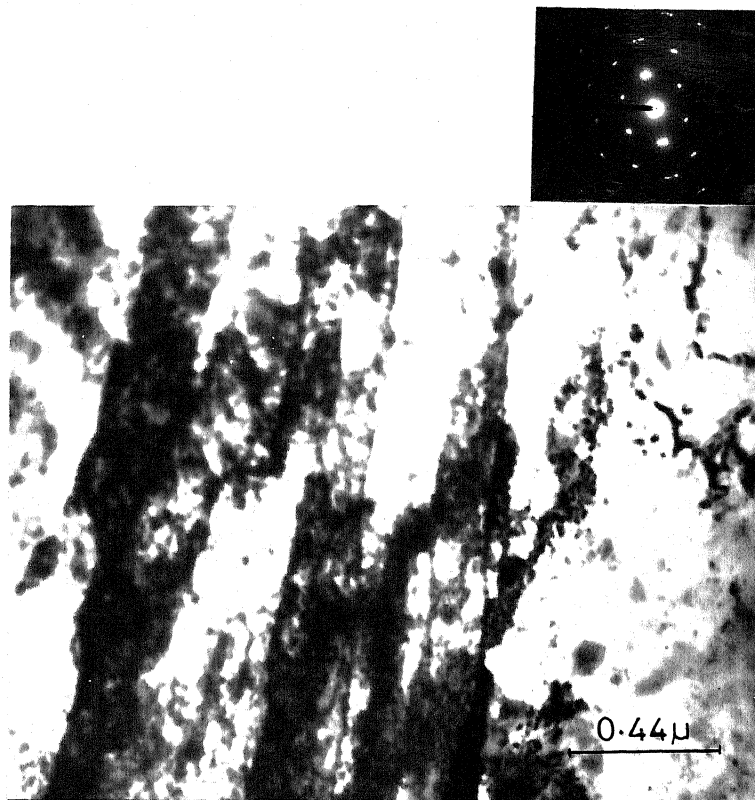


(g)

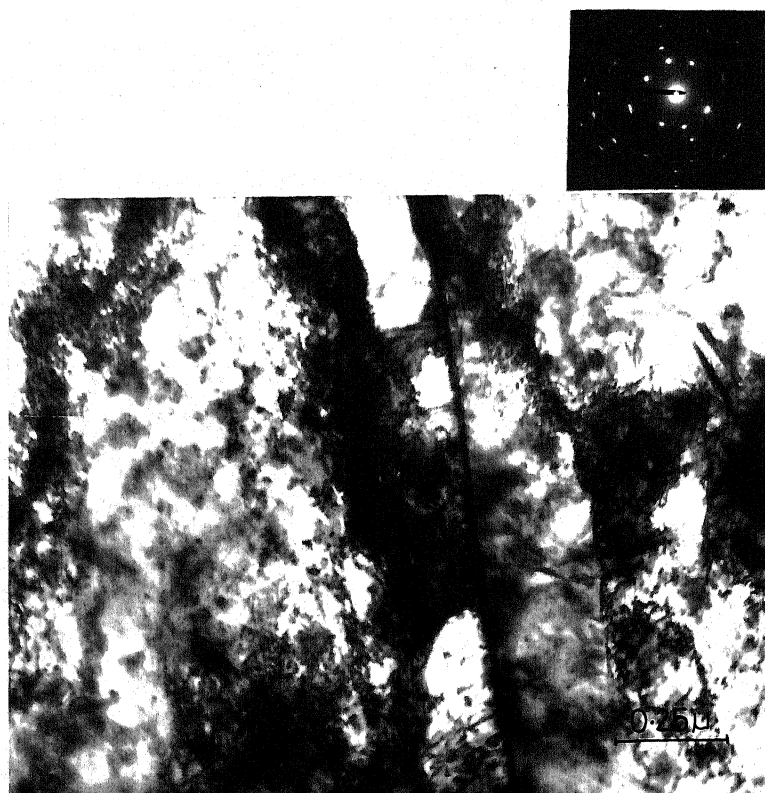


(h)

Fig. 4.16 Electron microstructures of 60% cold-worked alloy Al
 (e) WQ 750/WQ (f) WQ 750/WQ
 (g) WQ 750/WQ (h) WQ 750/WQ

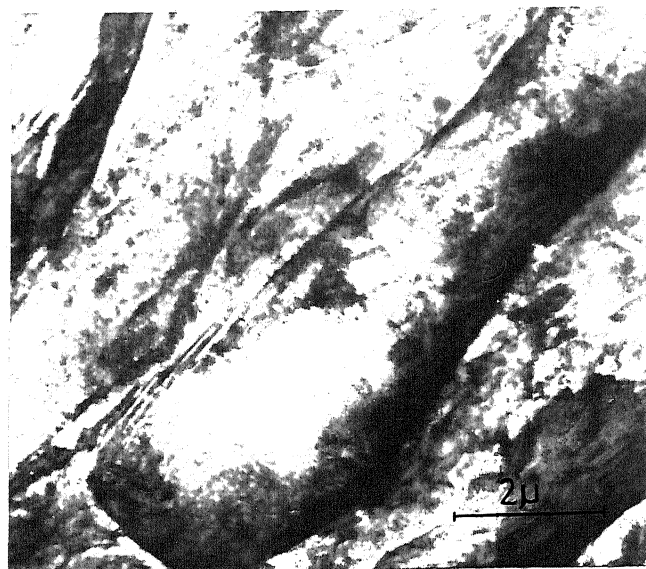


(i)



(j)

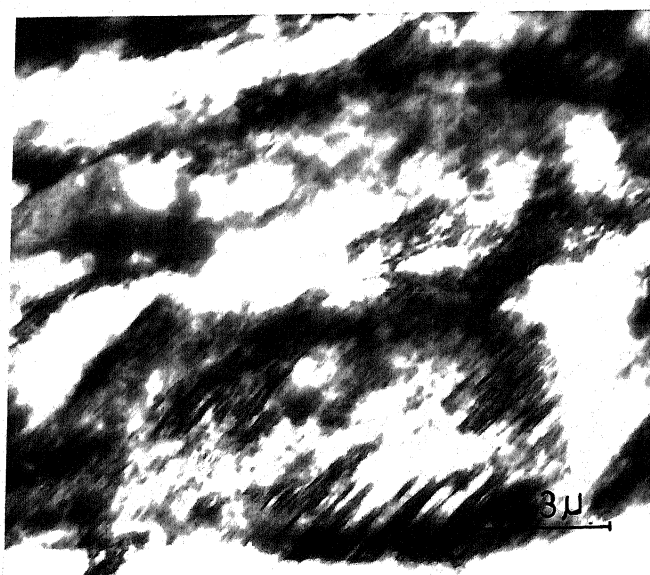
Fig. 4.16 Electron microstructures of 60% cold-worked alloy Al
(i) WQ 810/WQ (j) WQ 810/WQ



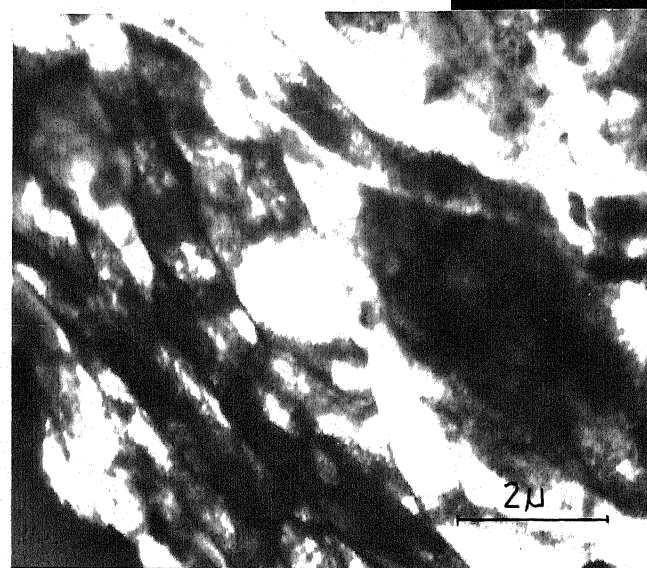
(a)



(b)



(c)



(d)

Fig. 4.17 Electron microstructures of 60% cold-worked alloy A4
 (a) AC 810/WQ (b) AC 810/WQ
 (c) WQ 810/WQ (d) WQ 810/WQ

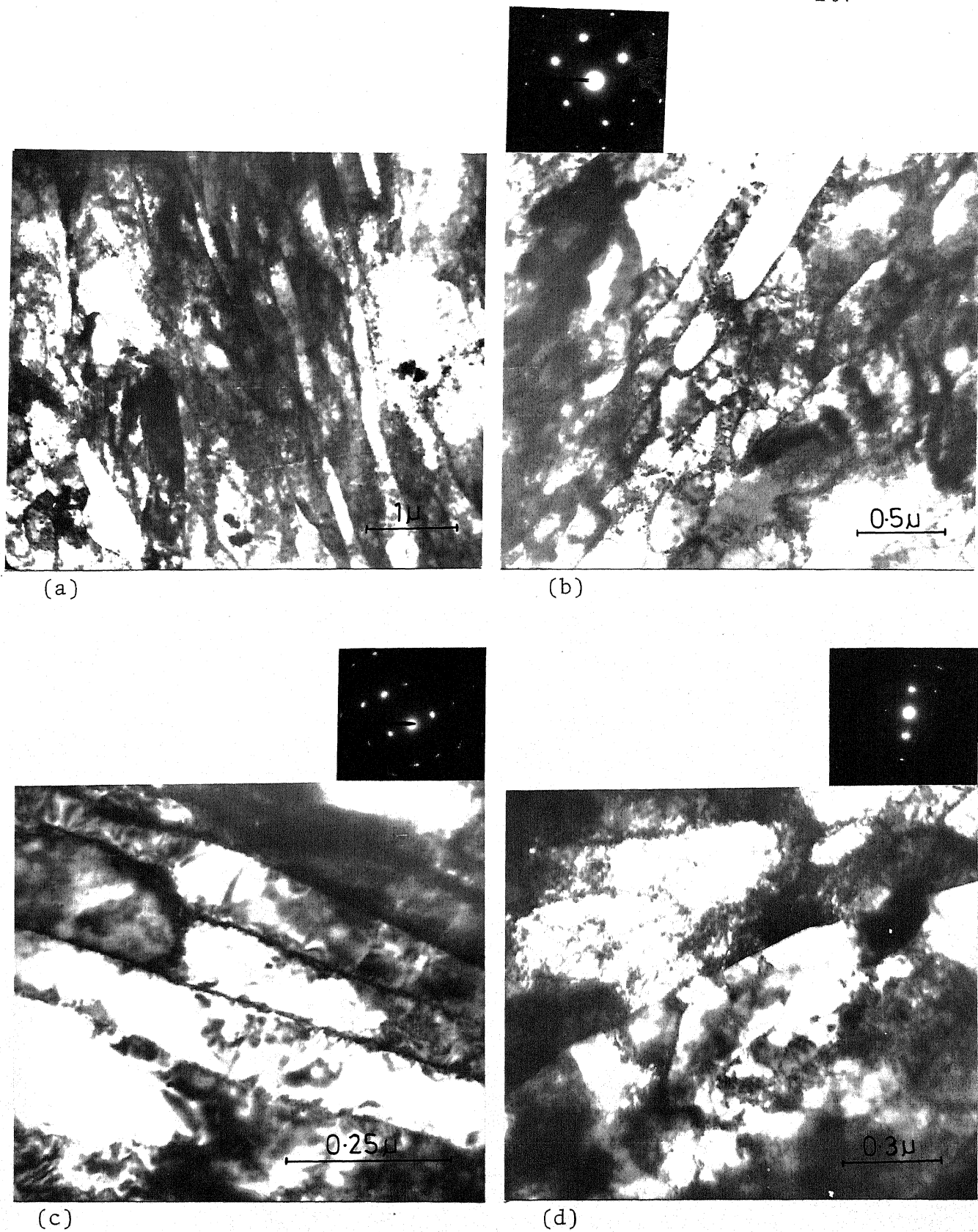


Fig. 4.18 Electron microstructures of 60% cold-worked alloy A5
 (a) AC 750/WQ (b) AC 750/WQ
 (c) WQ 810/WQ (d) WQ 810/WQ

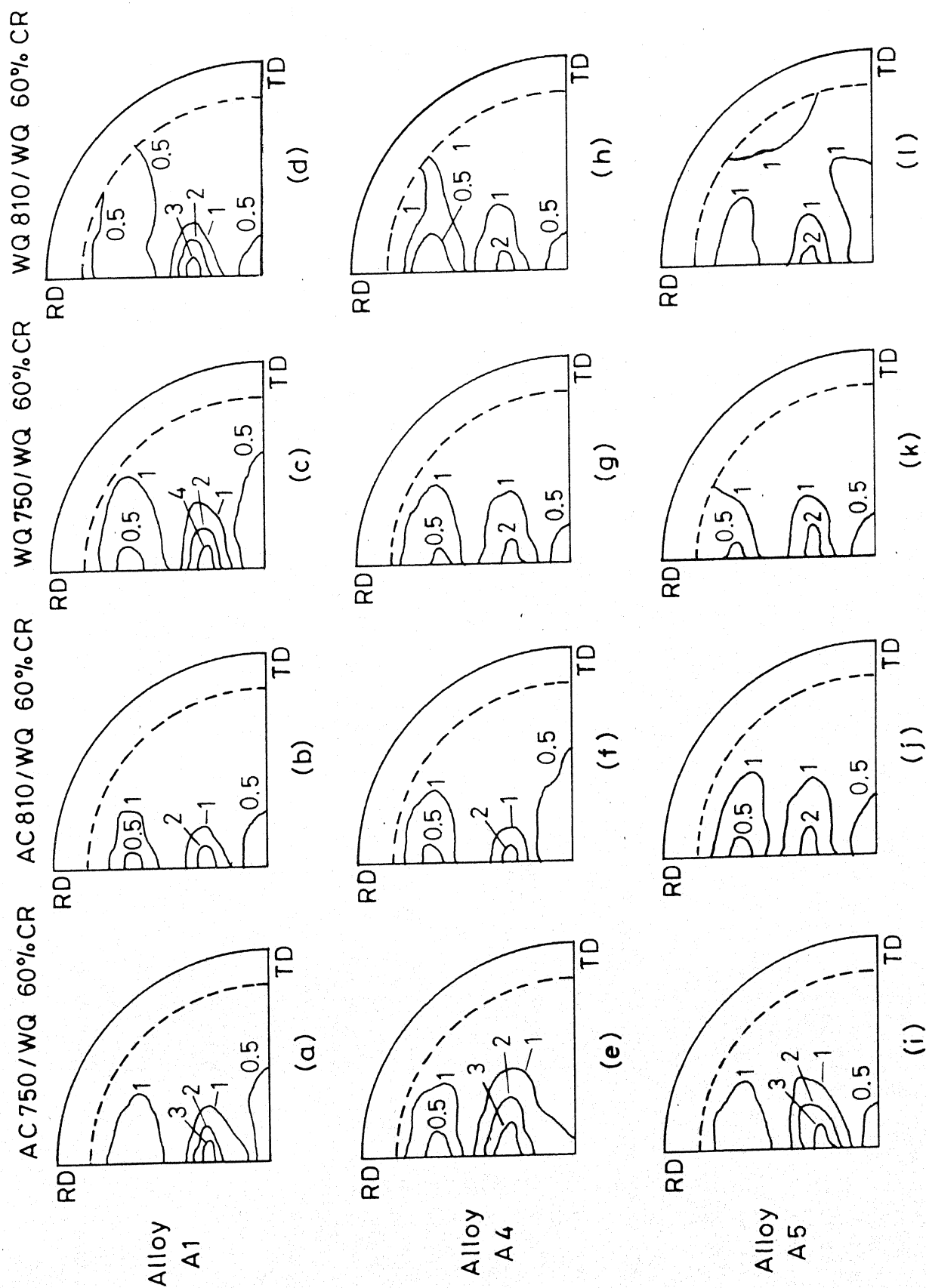


Fig. 4.19 (110) pole-figures of alloys A1, A4 and A5 after different initial heat treatments and 60% cold-rolling.

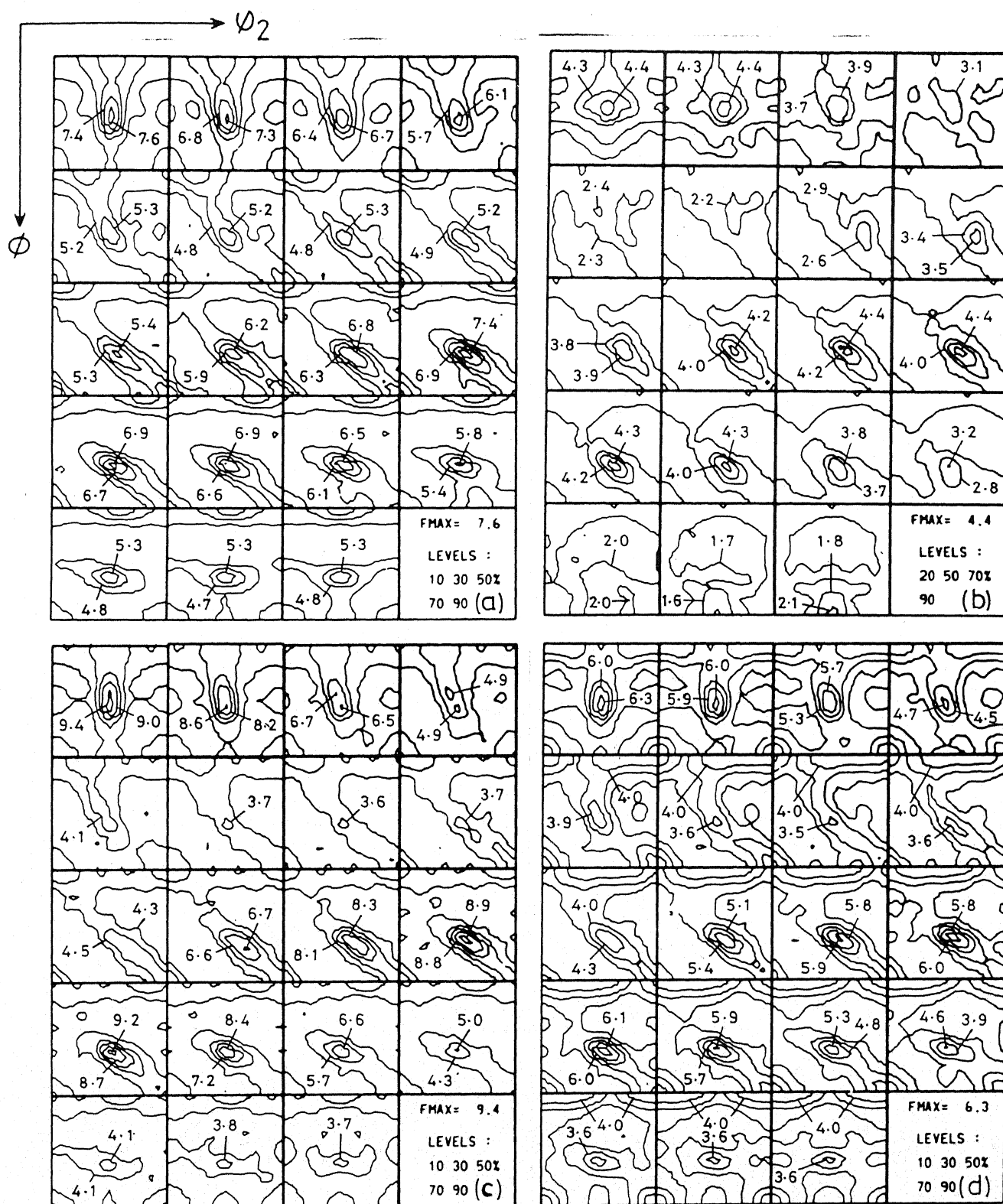


Fig. 4.20 - O.D.F's showing ϕ_1 sections for

- (a) A1/AC 750/WQ Cold-rolled 60%
- (b) A1/AC 810/WQ Cold-rolled 60%
- (c) A1/WQ 750/WQ Cold-rolled 60%
- (d) A1/WQ 810/WQ Cold-rolled 60%

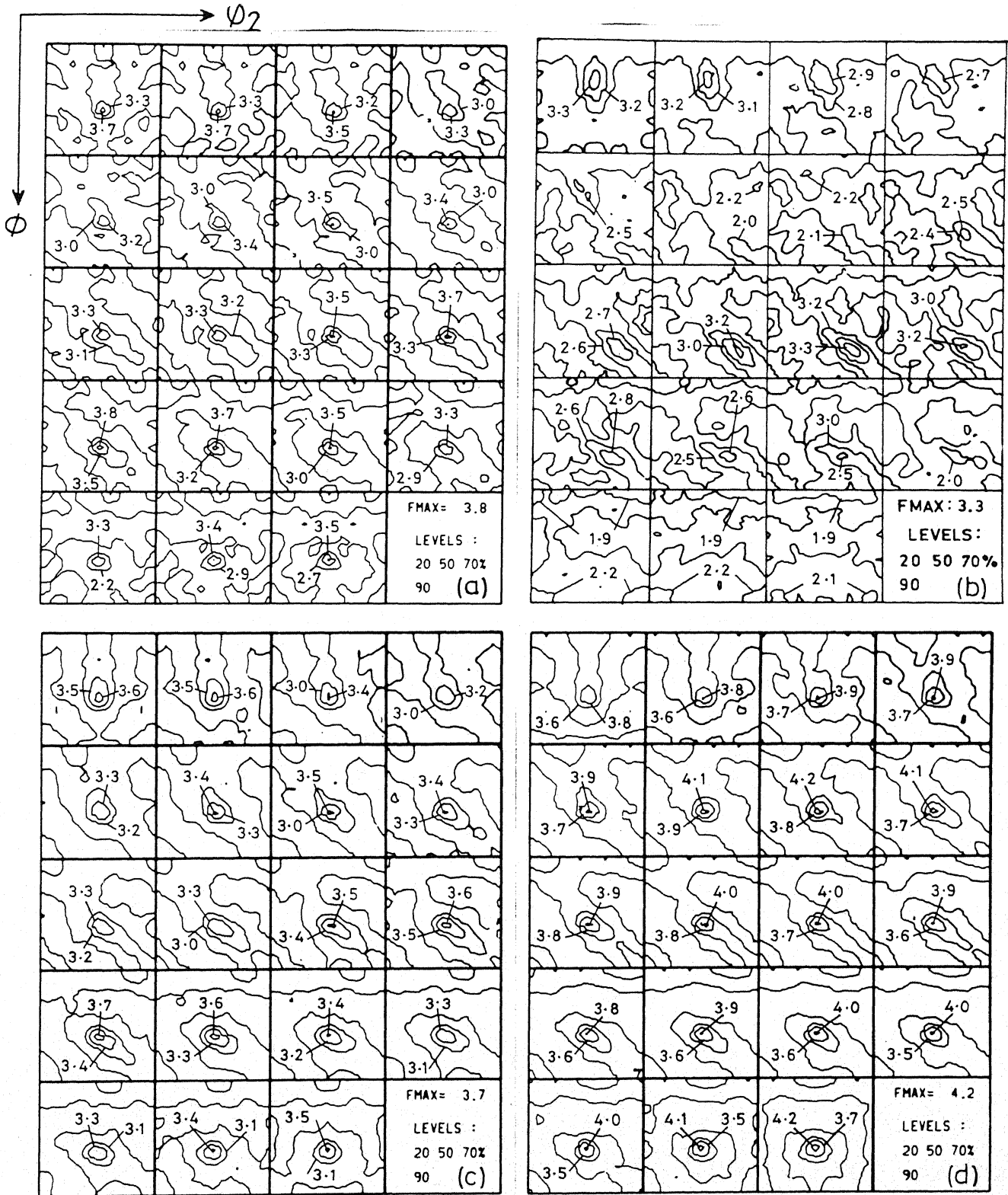


Fig.4.21 O.D.F's showing ϕ_1 sections for

- (a) A4/AC 750/WQ Cold-rolled 60%
- (b) A4/AC 810/WQ Cold-rolled 60%
- (c) A4/WQ750/WQ Cold-rolled 60%
- (d) A4/WQ810/WQ Cold-rolled 60%

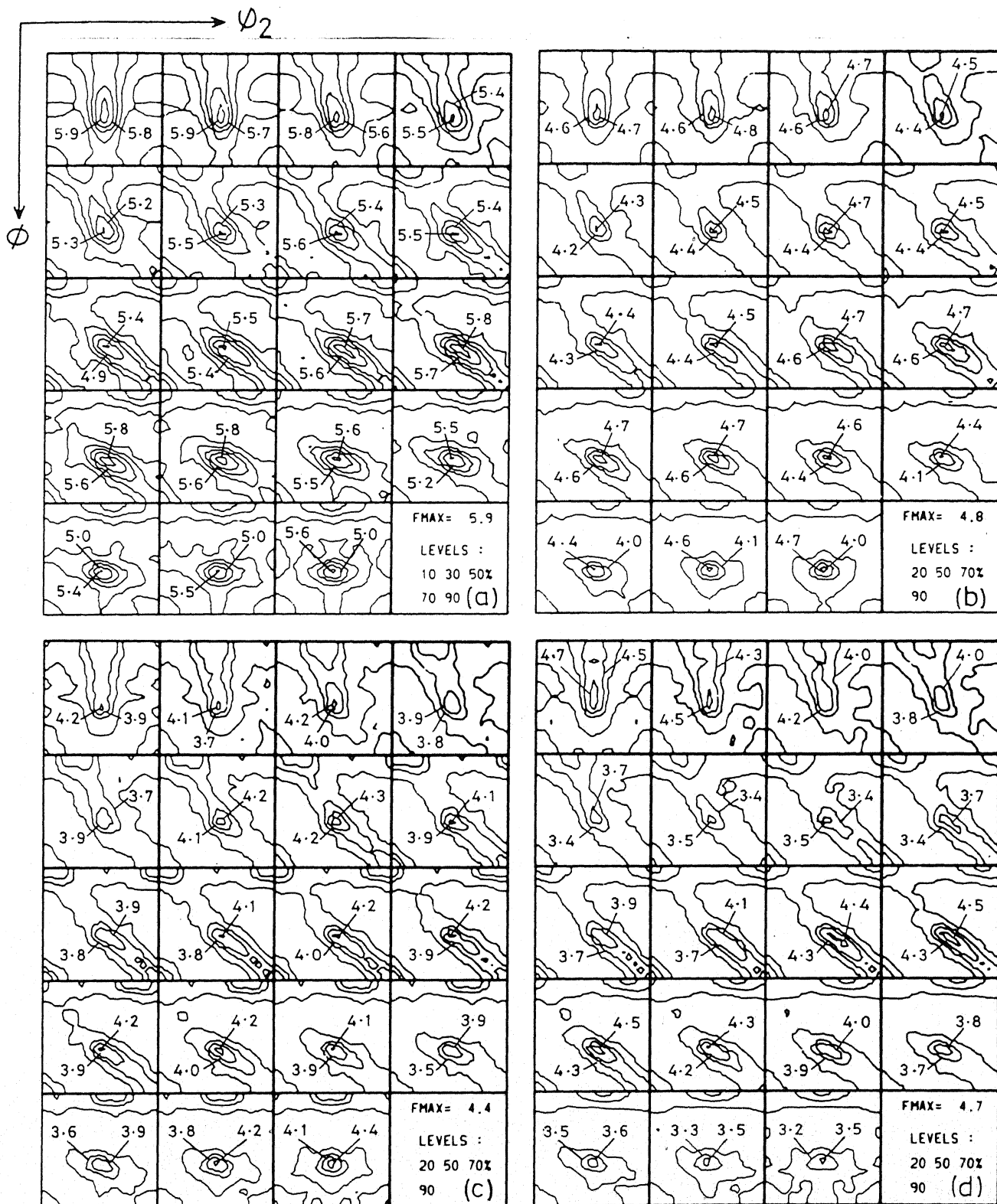


Fig.4.22 O.D.F.'s showing ϕ_1 sections for
 (a) A5/AC 750/WQ Cold-rolled 60%
 (b) A5/AC 810/WQ Cold-rolled 60%
 (c) A5/WQ 750/WQ Cold-rolled 60%
 (d) A5/WQ 810/WQ Cold-rolled 60%

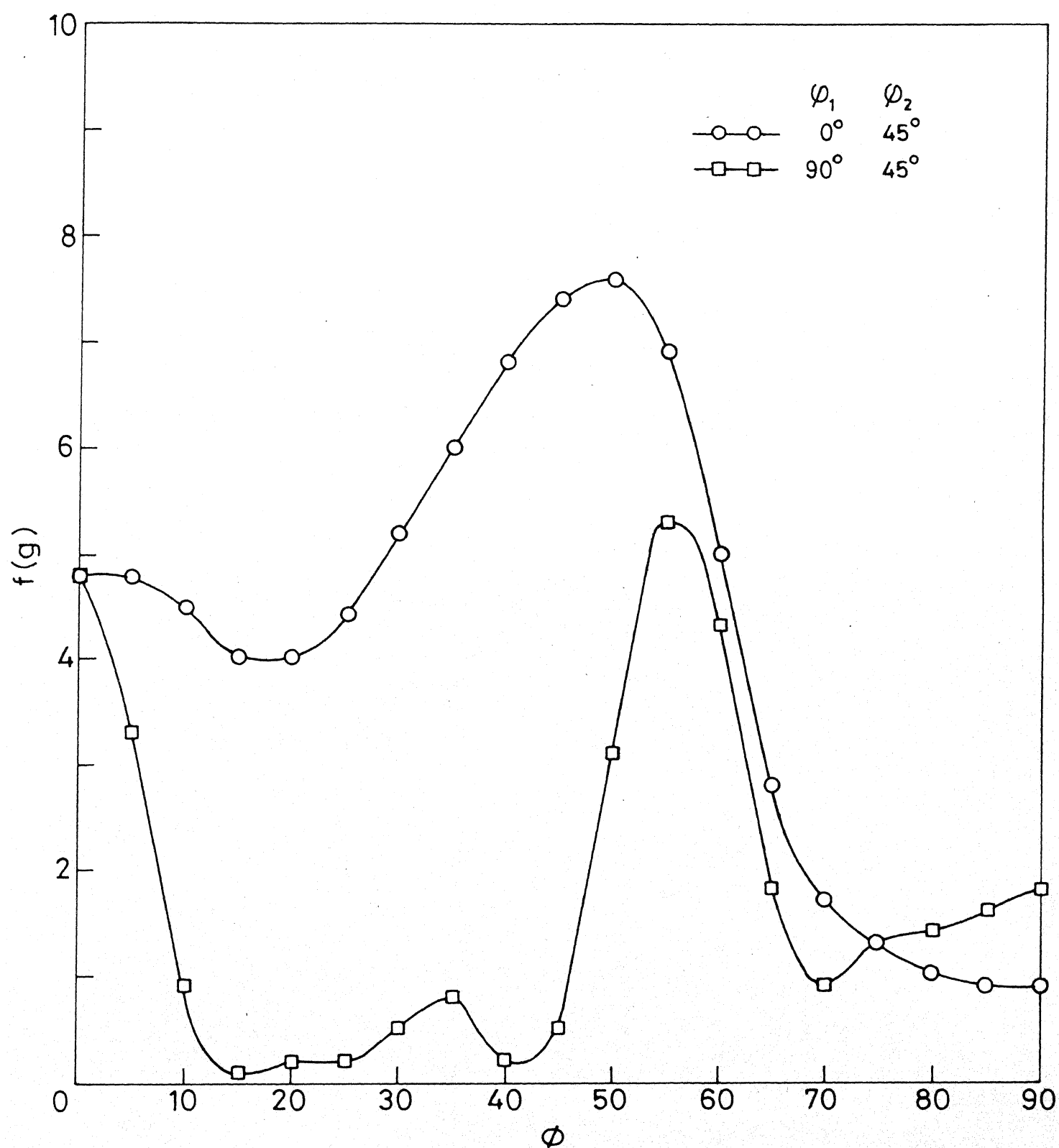


Fig.4.23 Variation of $f(g)$ with ϕ along different ϕ_1/ϕ_2 lines for A1/AC750/WQ after 60% cold rolling.

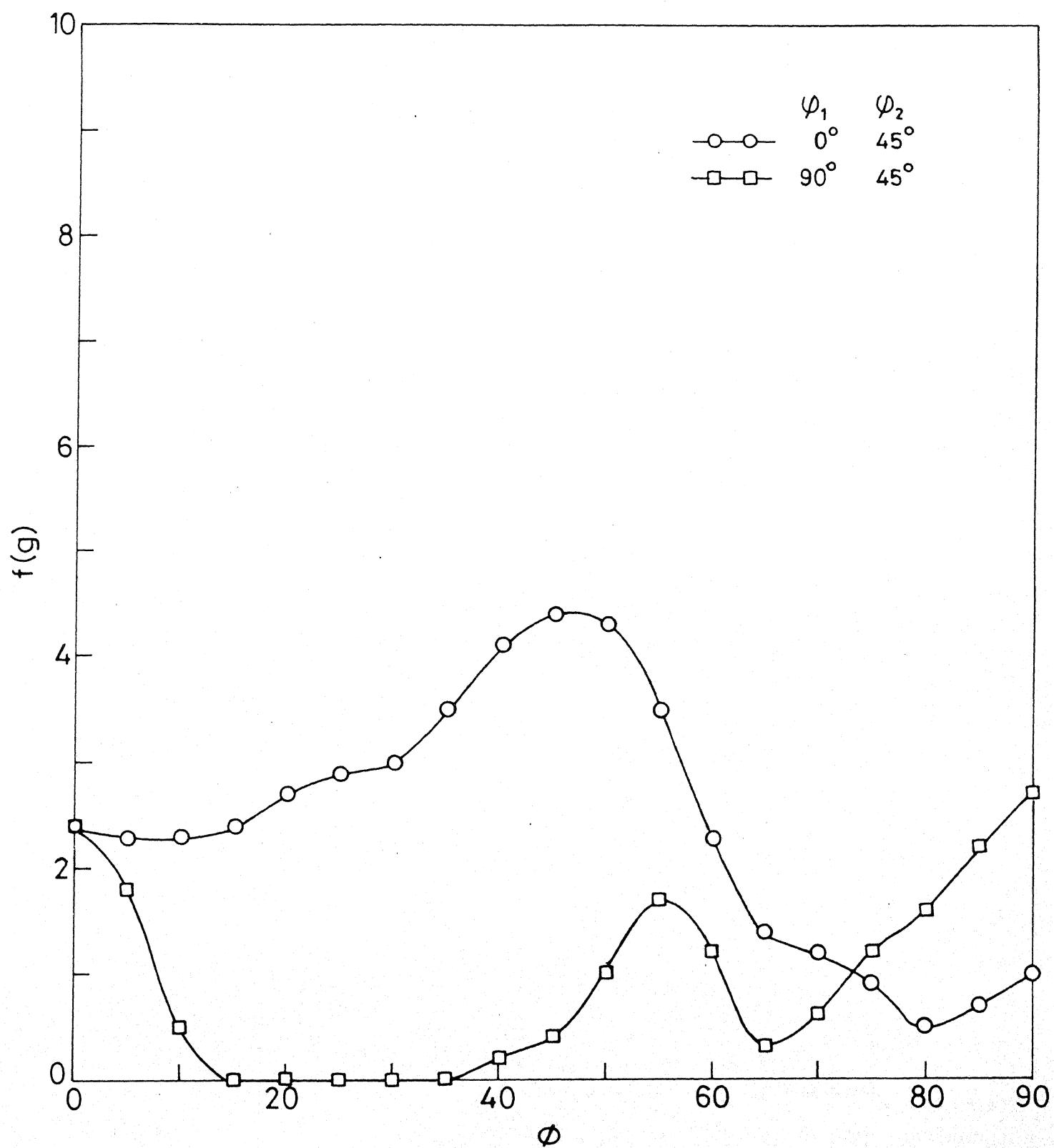


Fig. 4.24 Variation of $f(g)$ with ϕ along different ϕ_1/ϕ_2 lines for A1/AC810/WQ after 60% cold rolling.

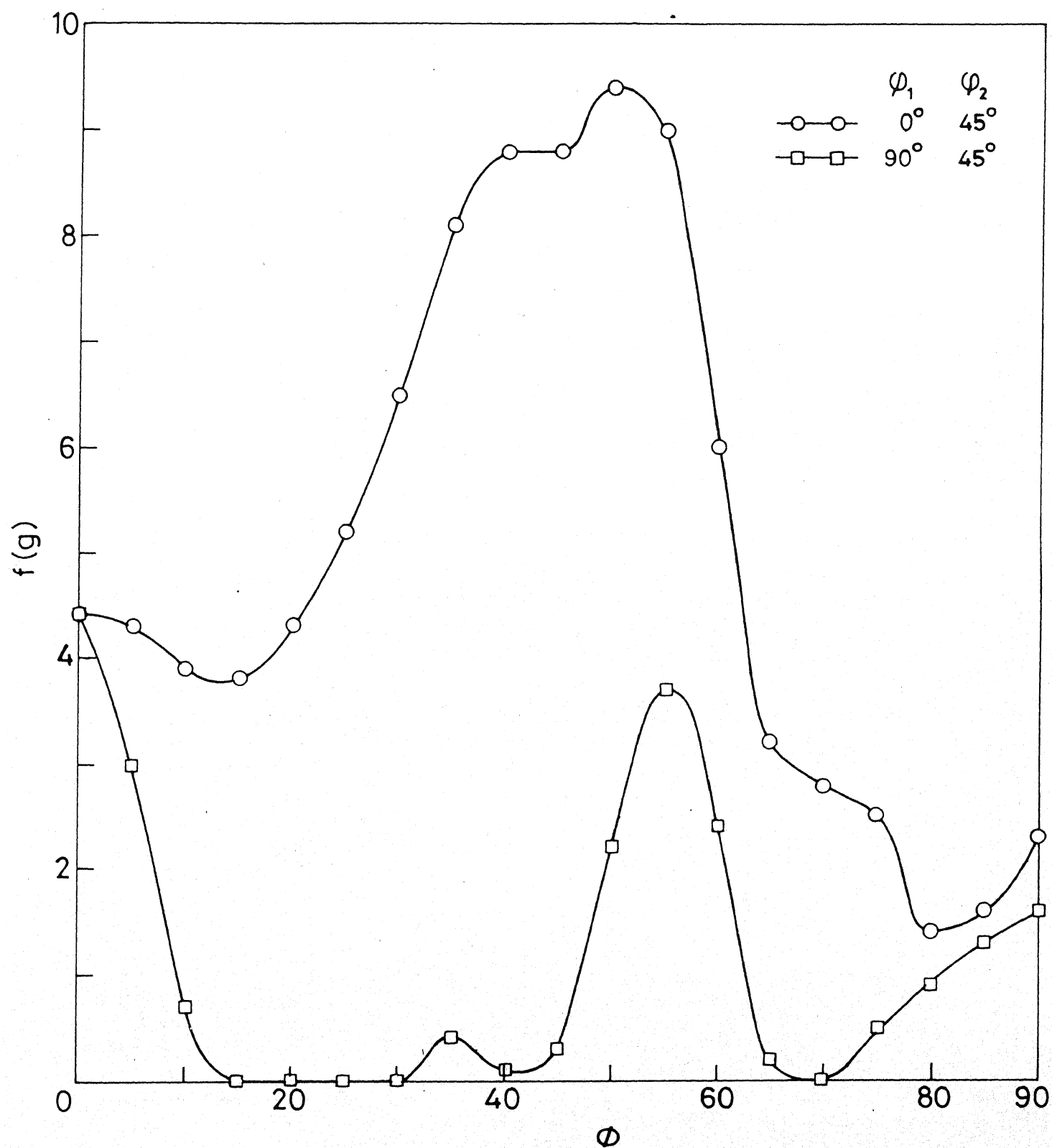


Fig.4.25 Variation of $f(g)$ with ϕ along different ϕ_1/ϕ_2 lines for A1/WQ750/WQ after 60% cold rolling.

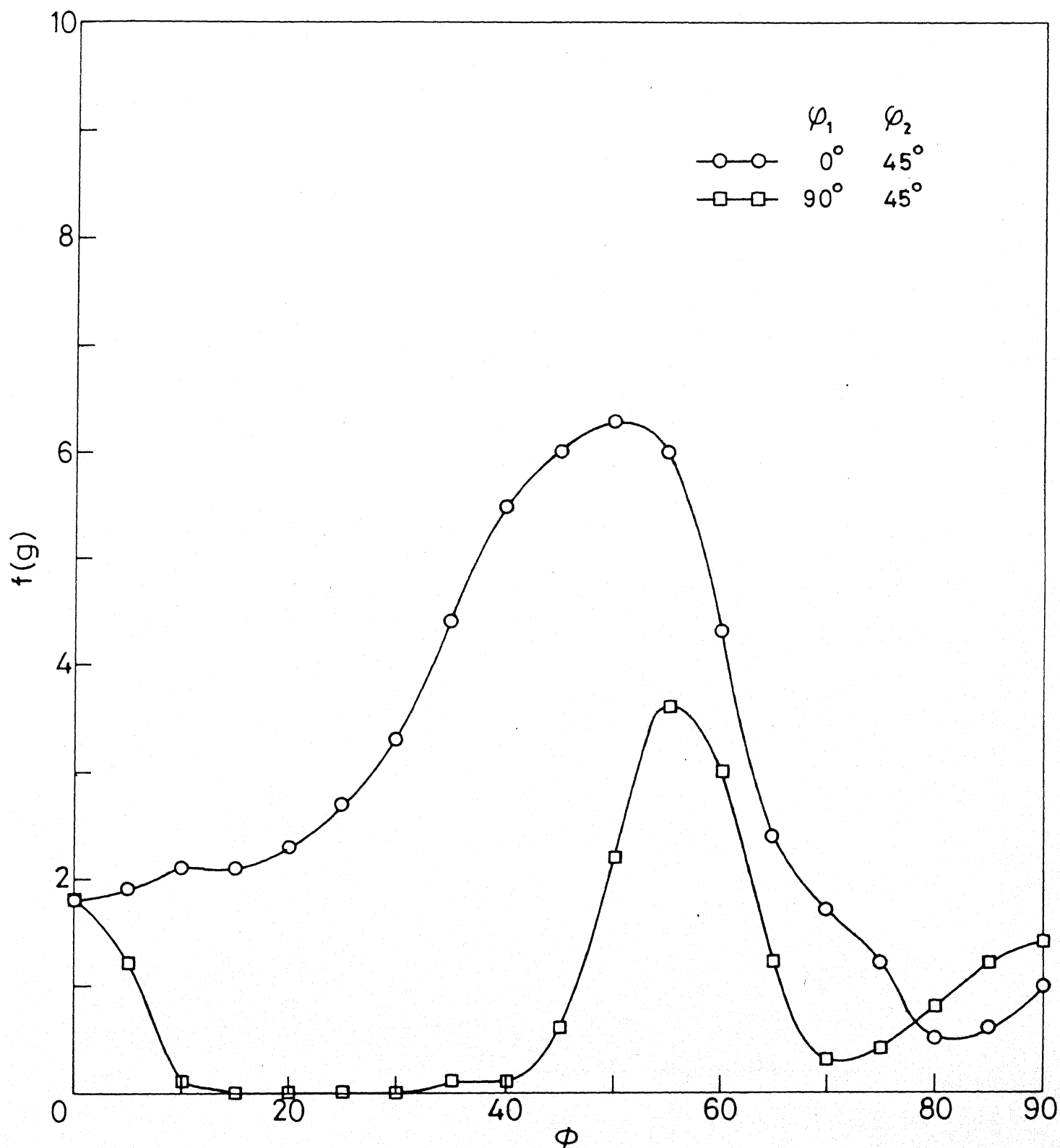


Fig.4.26 Variation of $f(g)$ with ϕ along different ϕ_1/ϕ_2 lines for A1/WQ 810/WQ after 60 % cold rolling.

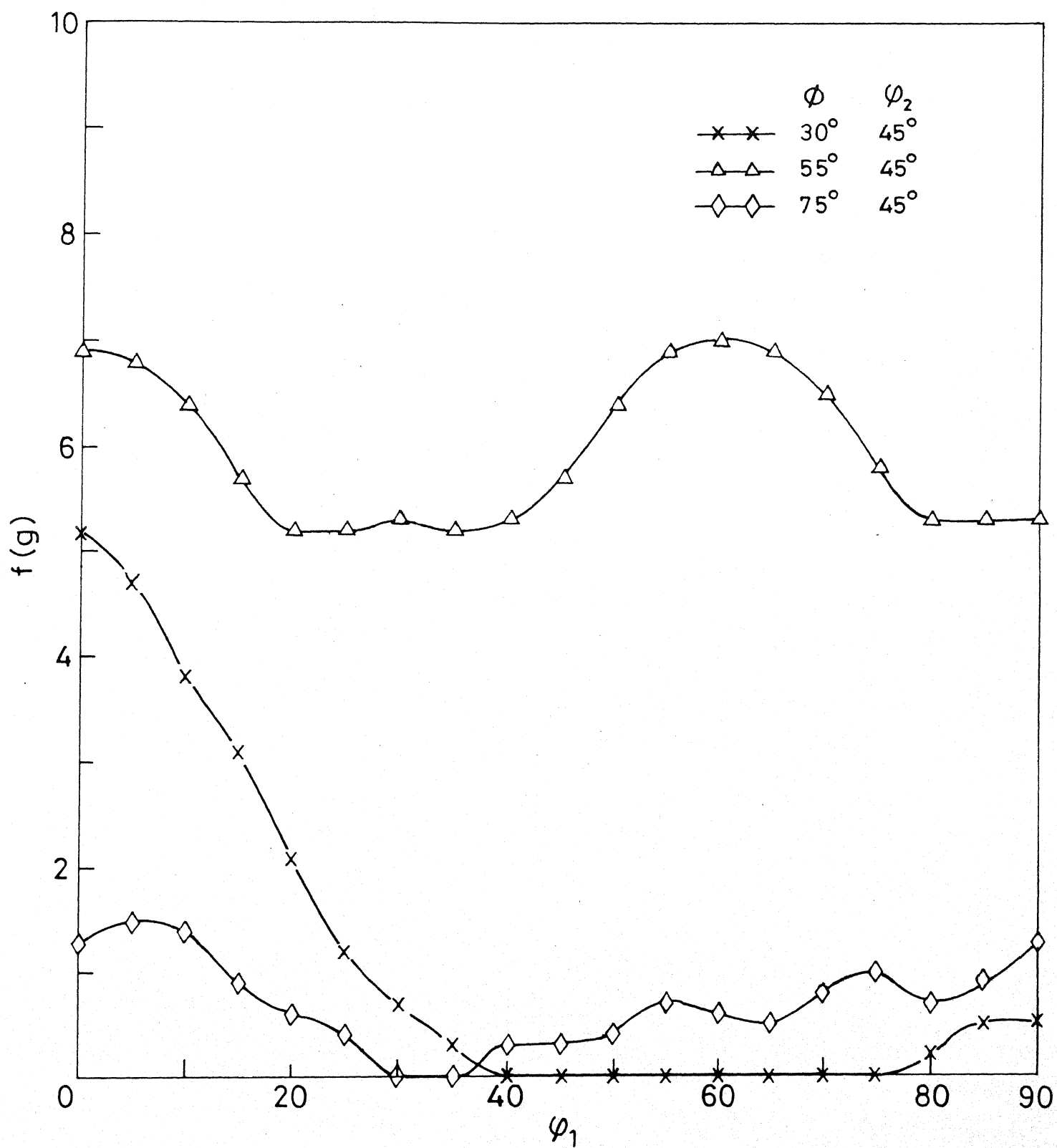


Fig.4.27 Variation of $f(g)$ with ϕ_1 along different ϕ/ϕ_2 lines for A1/AC 750/WQ after 60% cold rolling.

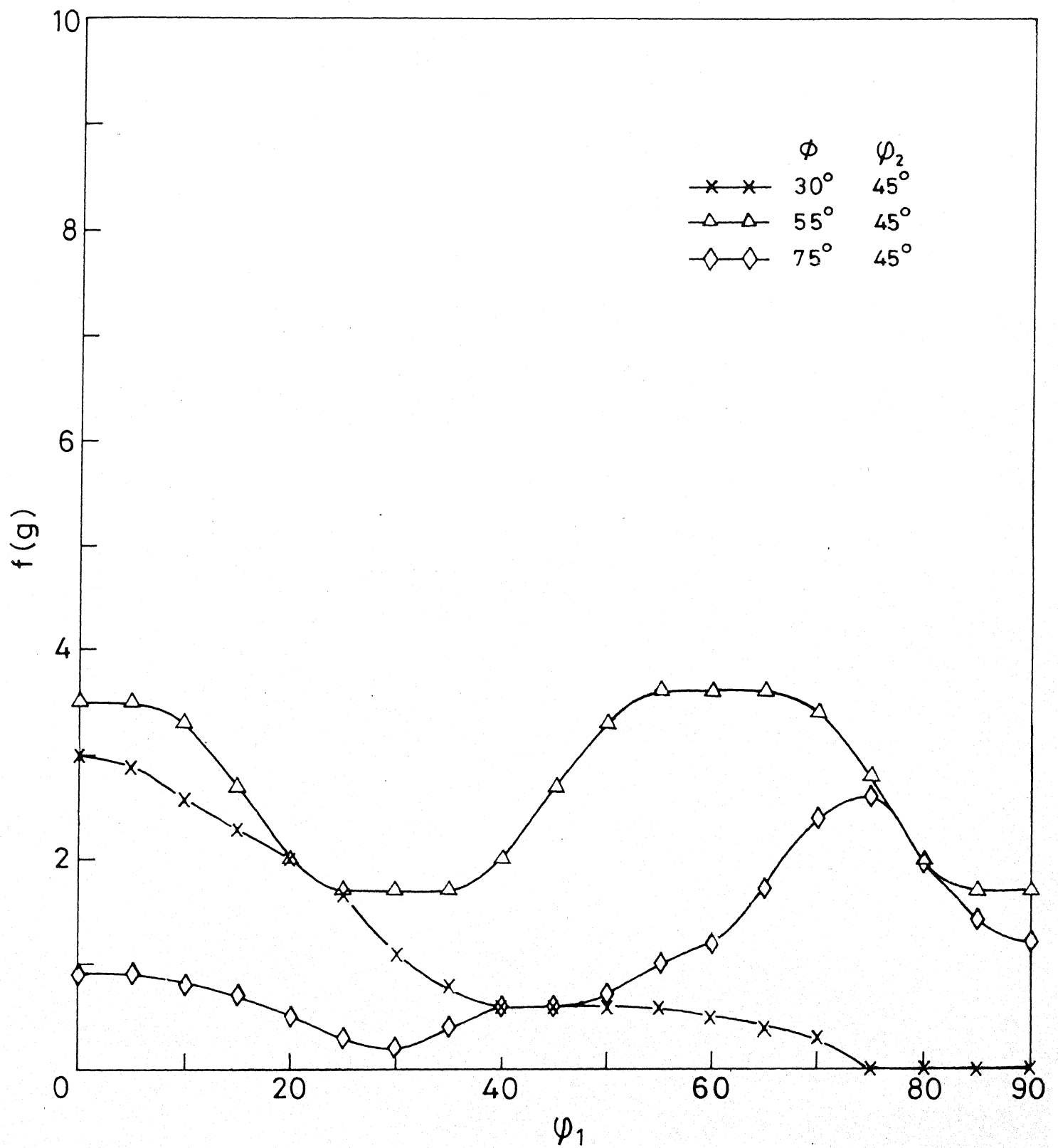


Fig. 4.28 Variation of $f(g)$ with ψ_1 along different ϕ/ϕ_2 lines for A1/AC 810/WQ after 60% cold rolling.

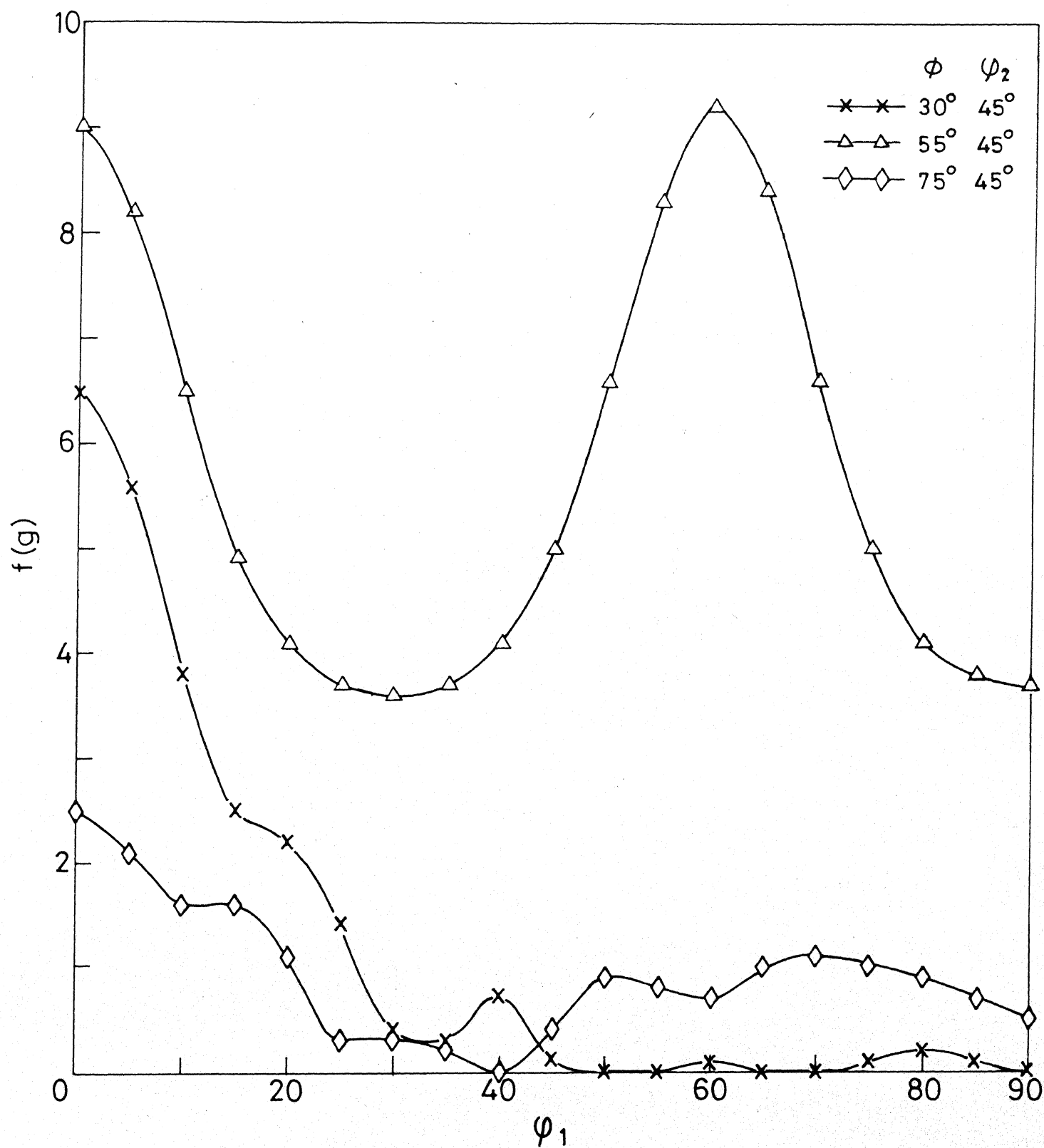


Fig.4.29 Variation of $f(g)$ with ϕ_1 along different ϕ/ϕ_2 lines for A1/WQ750/WQ after 60% cold rolling.

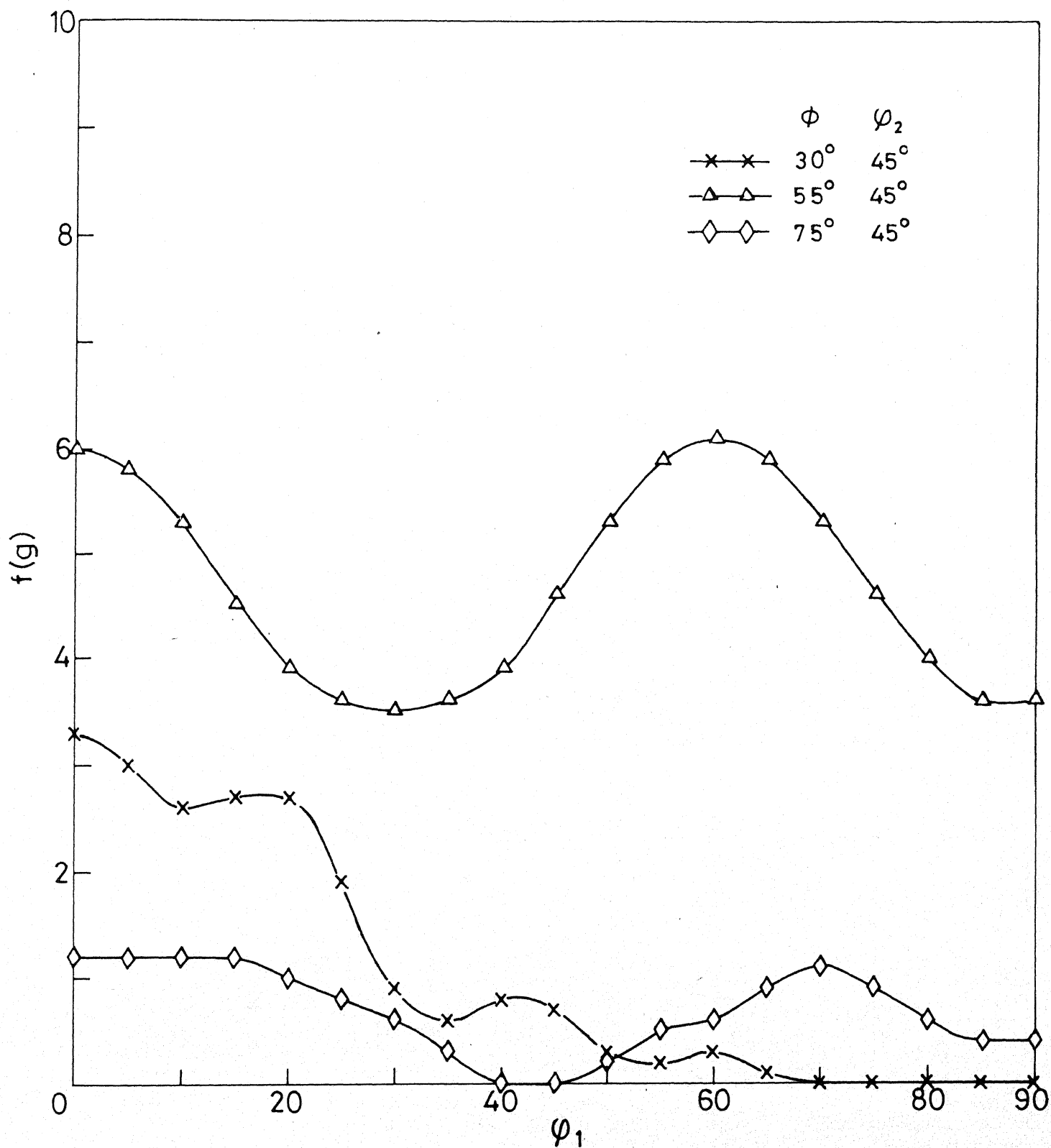


Fig.4.30 Variation of $f(g)$ with ϕ_1 along different ϕ/ϕ_2 lines for A1/WQ 810/WQ after 60% cold rolling.

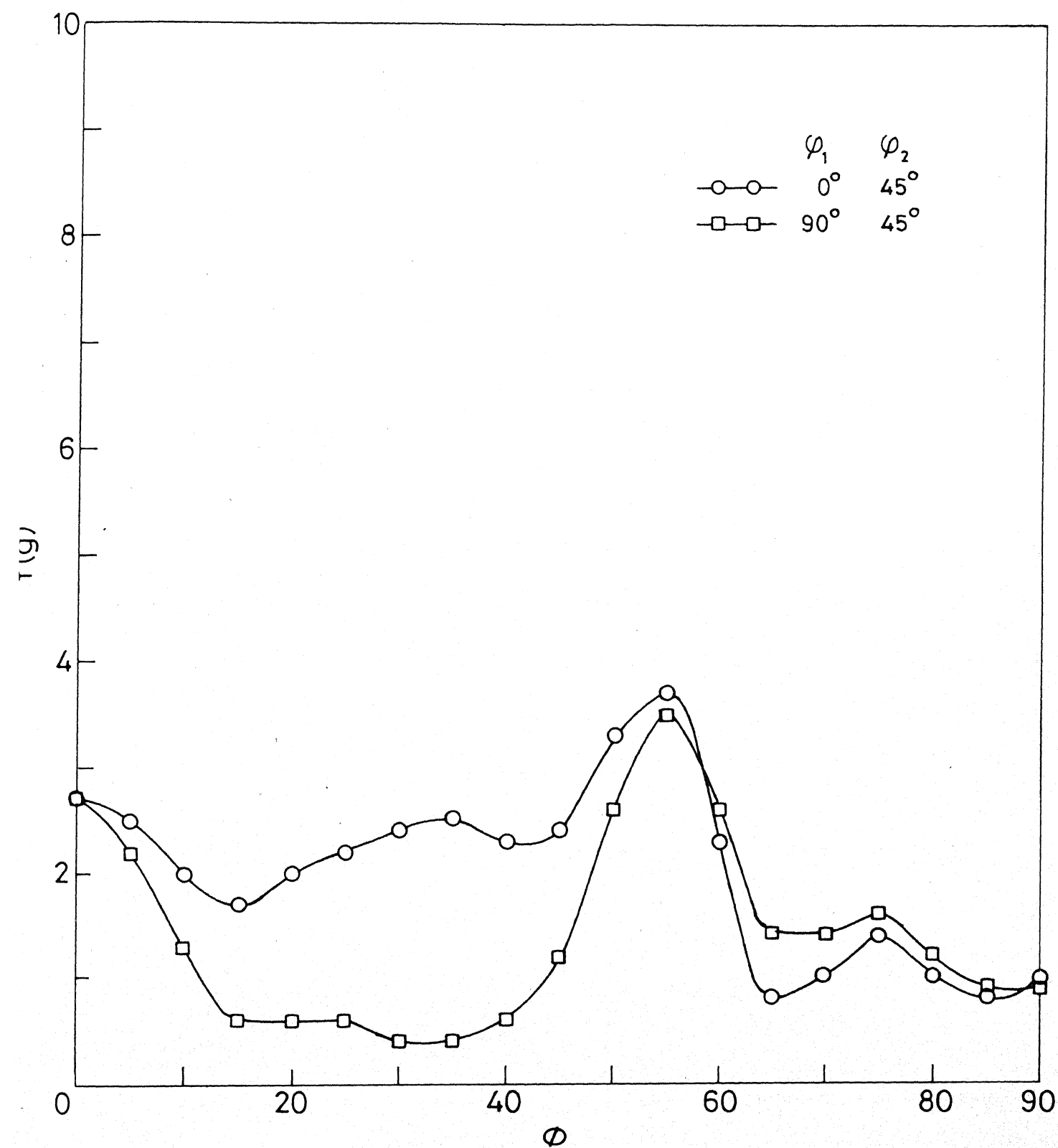


Fig.4.31 Variation of $f(g)$ with ϕ along different ϕ_1/ϕ_2 lines for A4/AC750/WQ after 60% cold rolling.

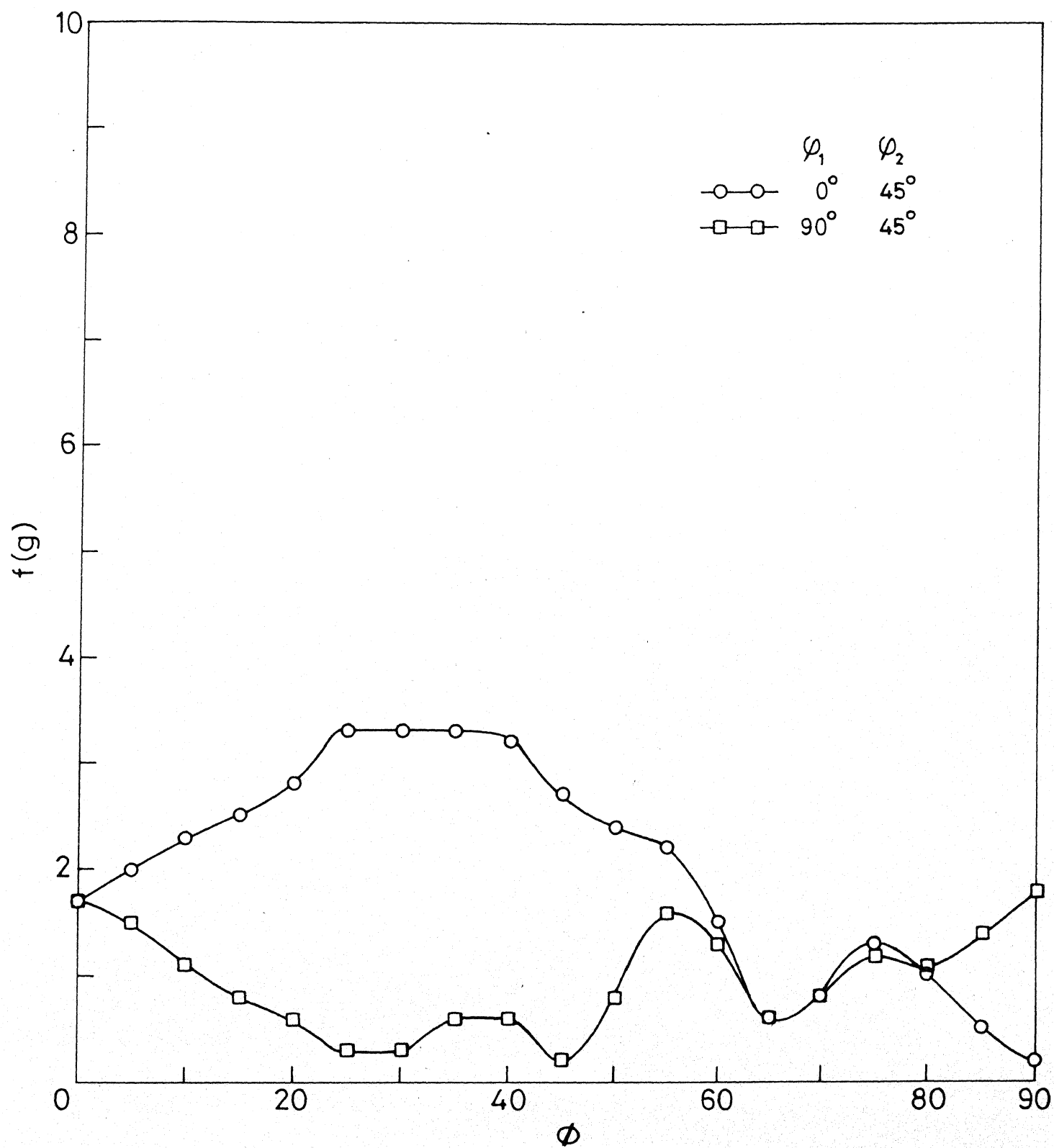


Fig.4.32 Variation of $f(g)$ with ϕ along different ϕ_1/ϕ_2 lines for A4/AC 810/WQ after 60% cold rolling.

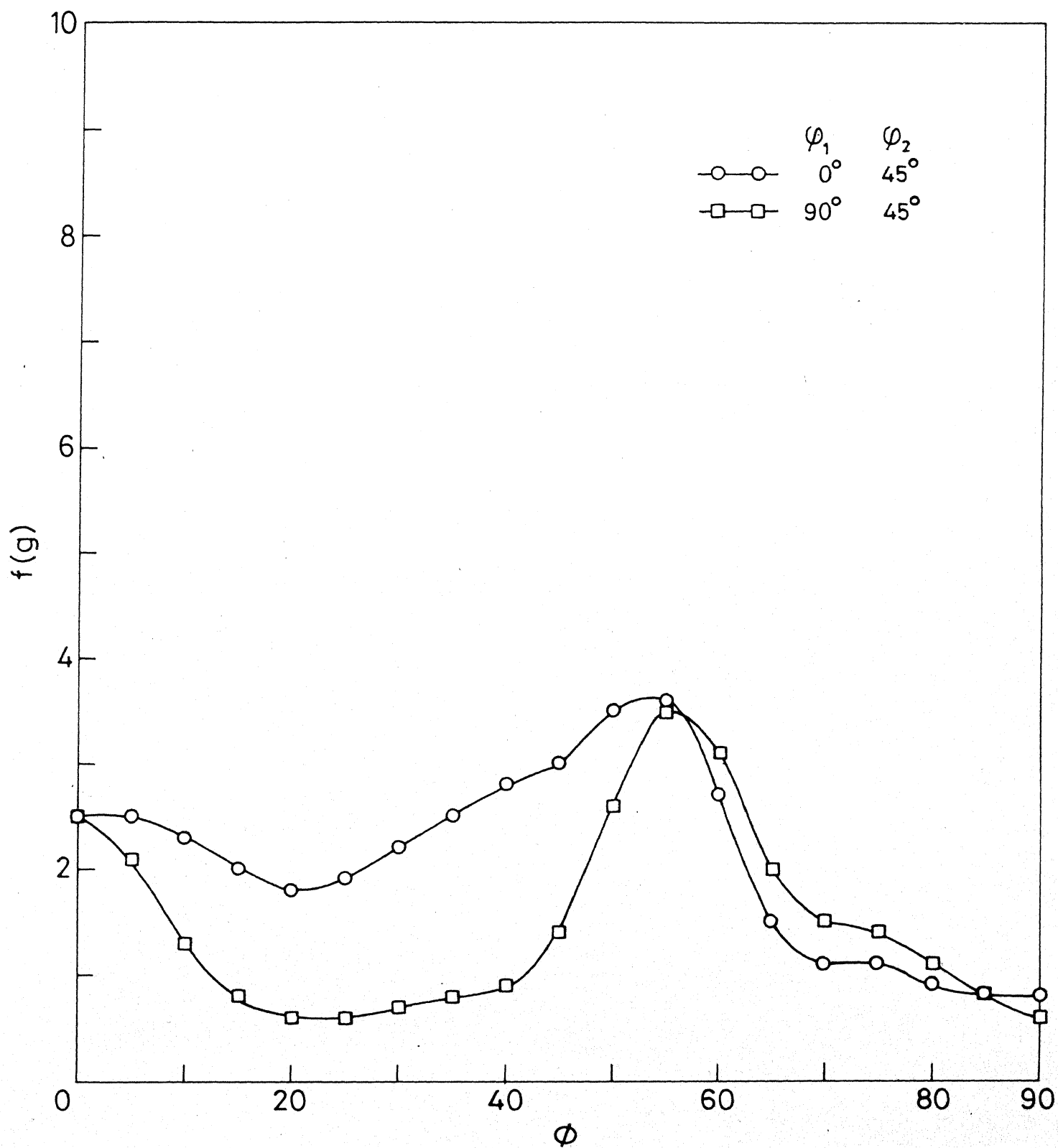


Fig.4.33 Variation of $f(g)$ with ϕ along different ϕ_1/ϕ_2 lines for A4/WQ 750/WQ after 60% cold rolling.

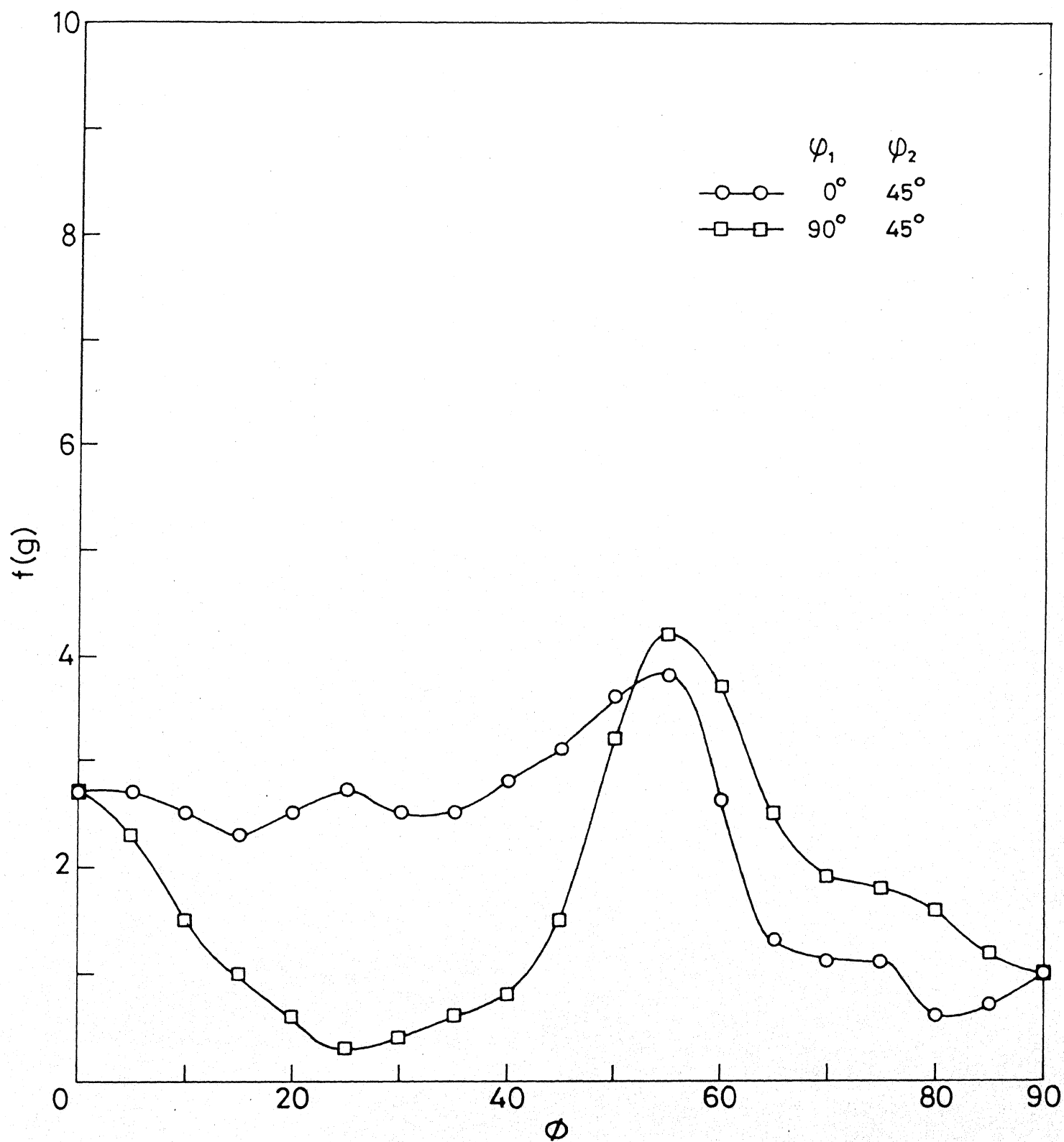


Fig.4.34 Variation of $f(g)$ with ϕ along different ϕ_1/ϕ_2 lines for A4/WQ 810/WQ after 60% cold rolling.

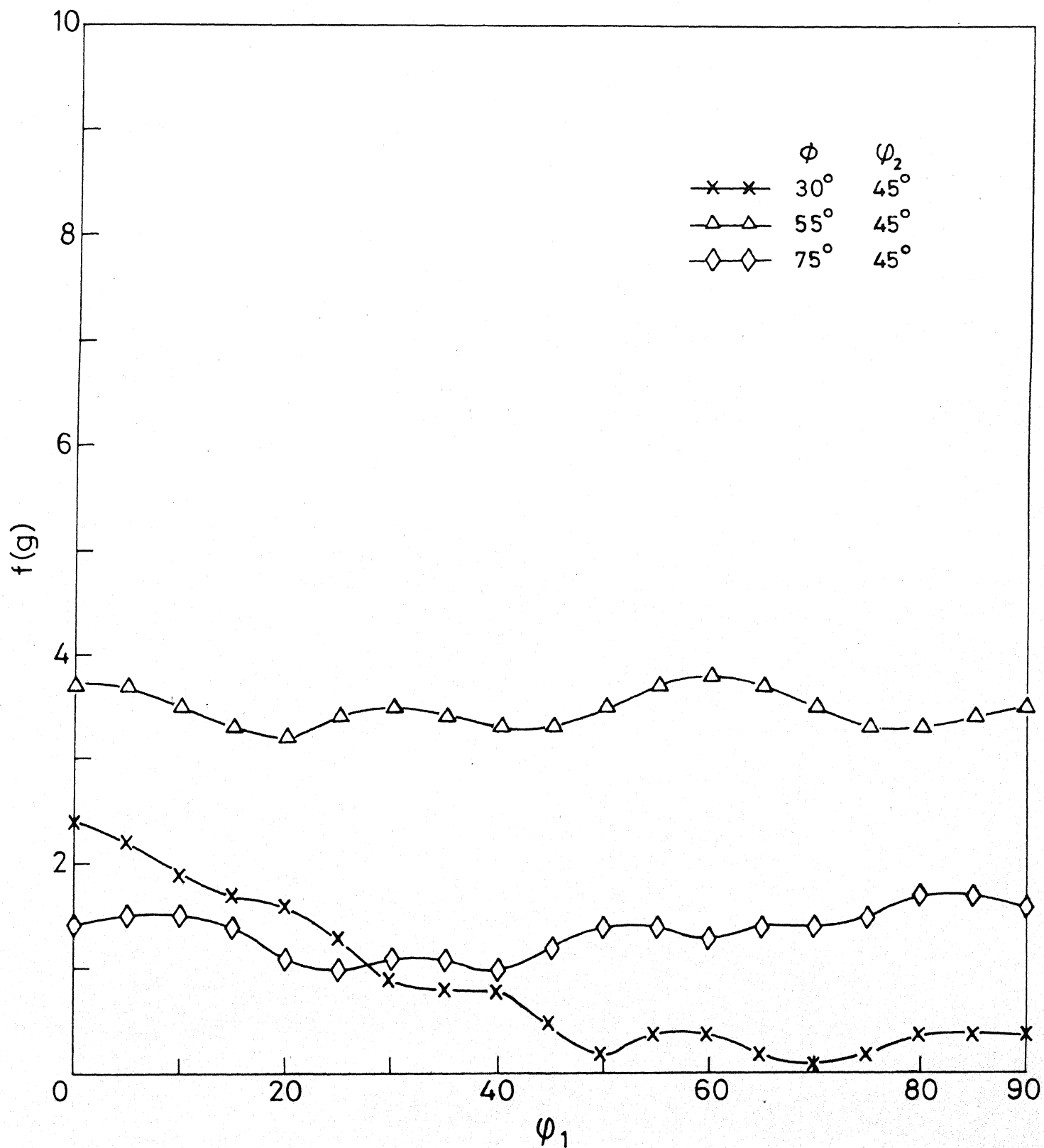


Fig.4.35 Variation of $f(g)$ with ϕ_1 along different ϕ/ϕ_2 lines for A4/AC750/WQ after cold rolling.

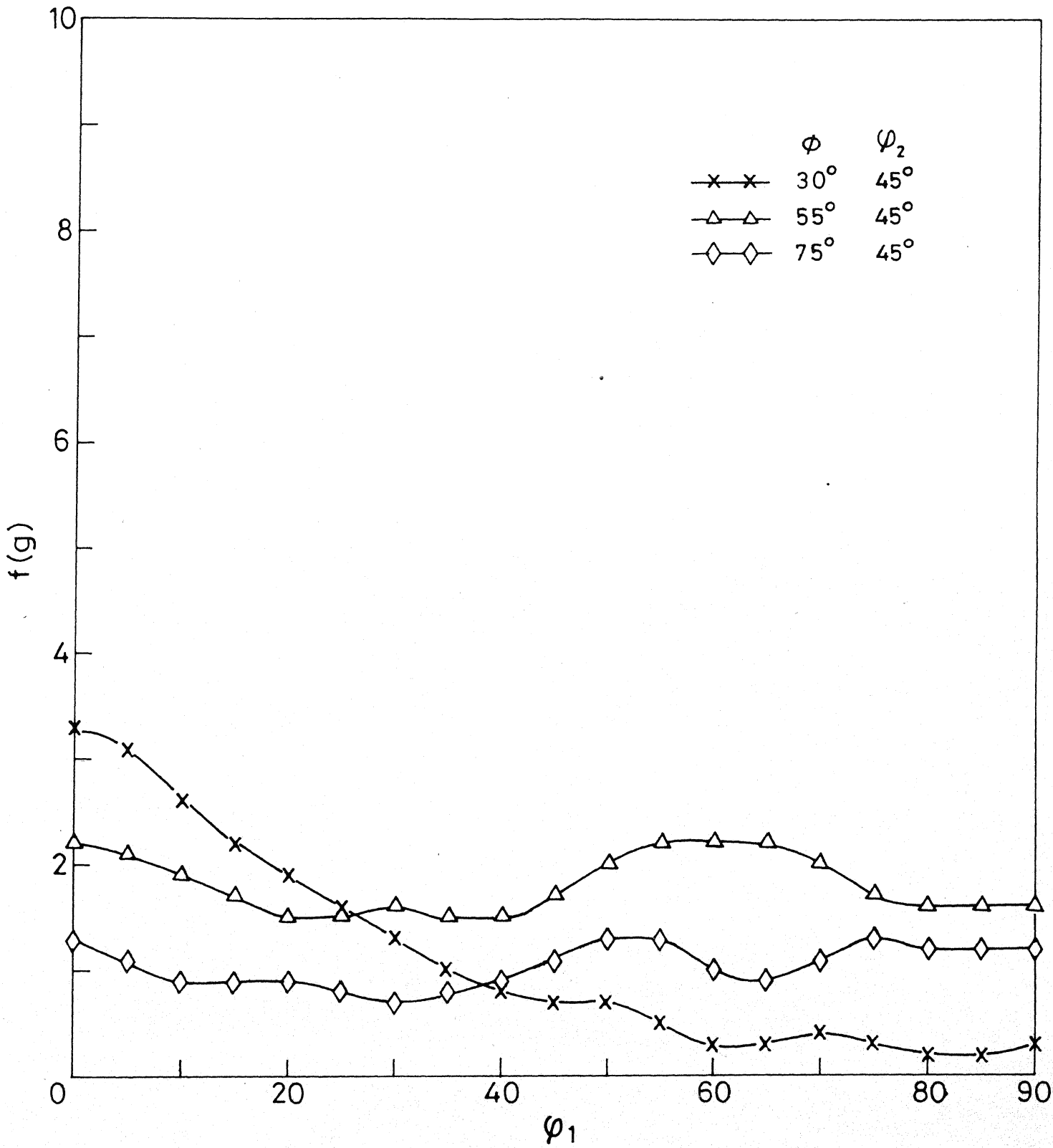


Fig.4.36 Variation of $f(g)$ with ϕ_1 along different ϕ/ϕ_2 lines for A4/AC 810/WQ after 60% cold rolling.

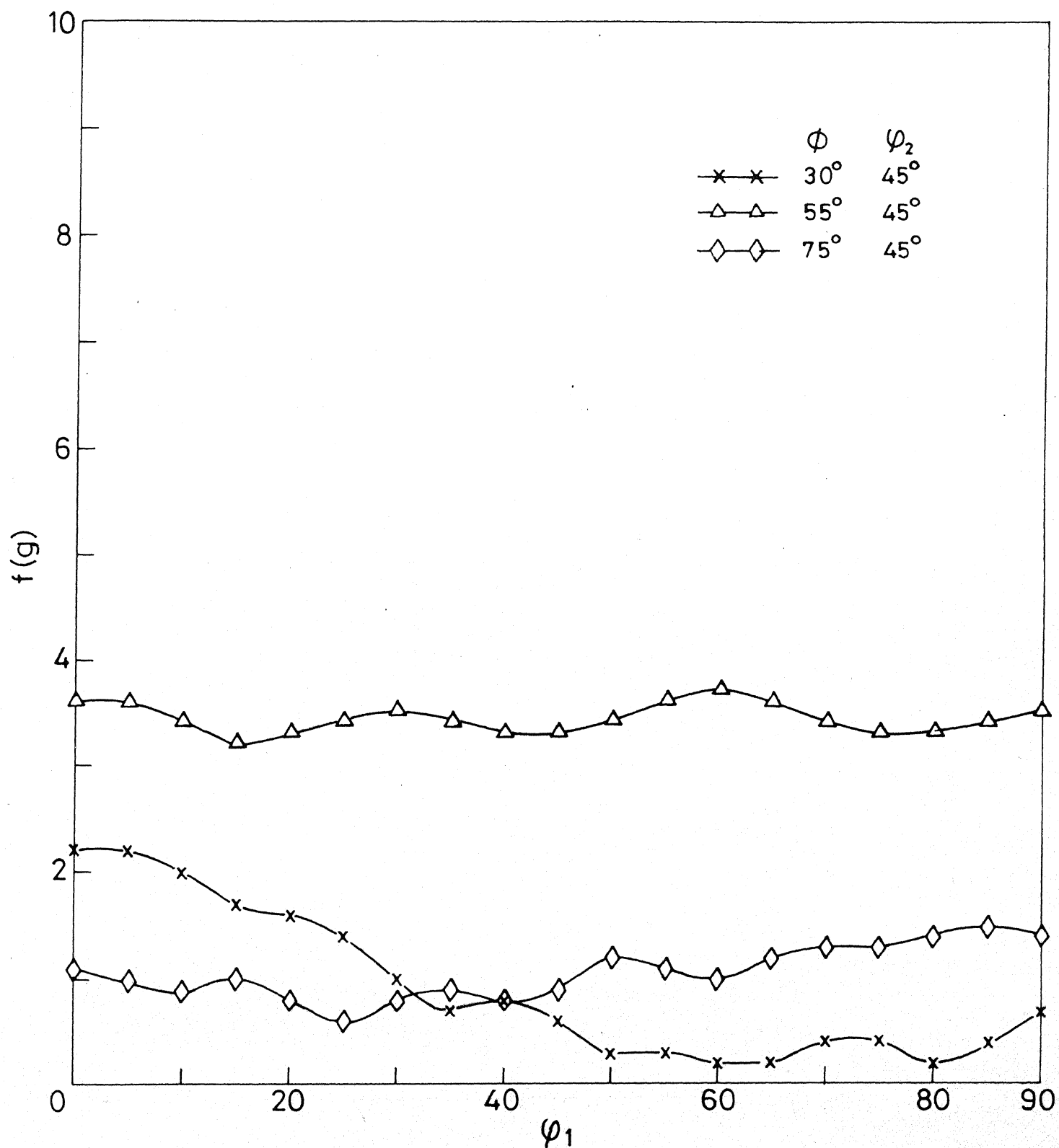


Fig.4.37 Variation of $f(g)$ with ϕ_1 along different ϕ/ϕ_2 lines for A4/WQ 750/WQ after 60% cold rolling.

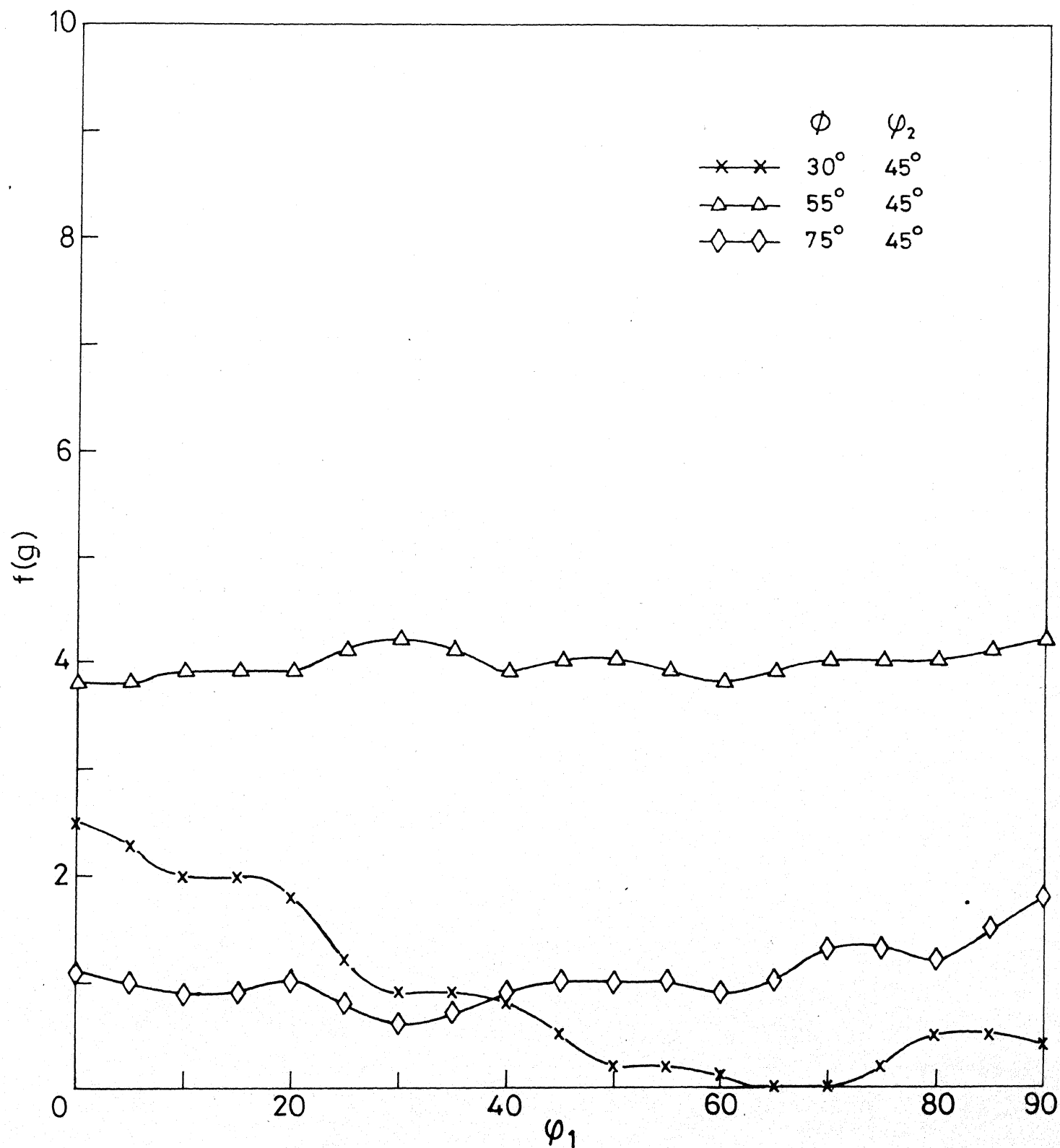


Fig.4.38 Variation of $f(g)$ with ϕ_1 along different ϕ/ϕ_2 lines for A4/WQ810/WQ after 60% cold rolling.

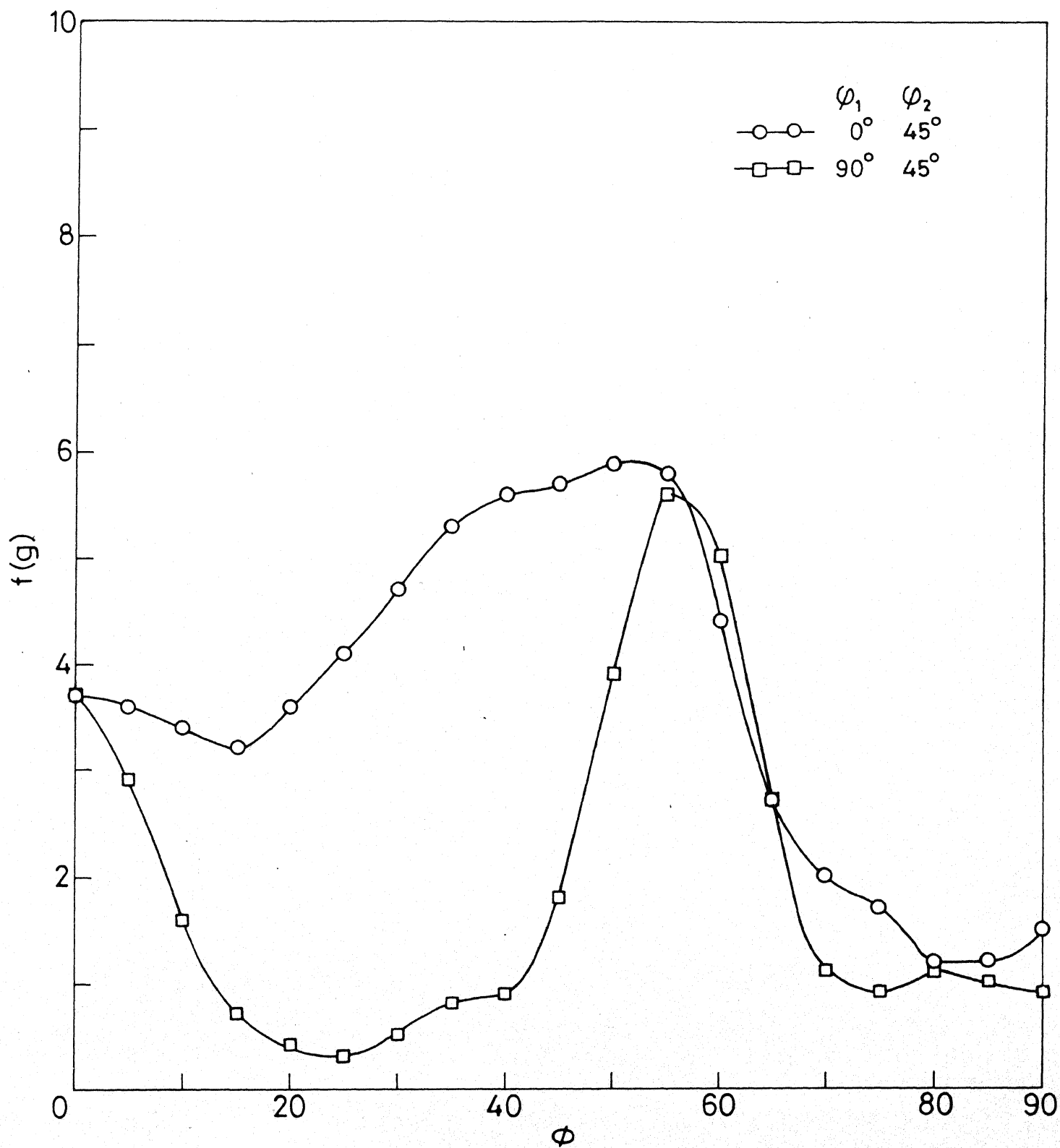


Fig. 4.39 Variation of $f(g)$ with ϕ along different ϕ_1/ϕ_2 lines for A5/AC750/WQ after 60% cold rolling.

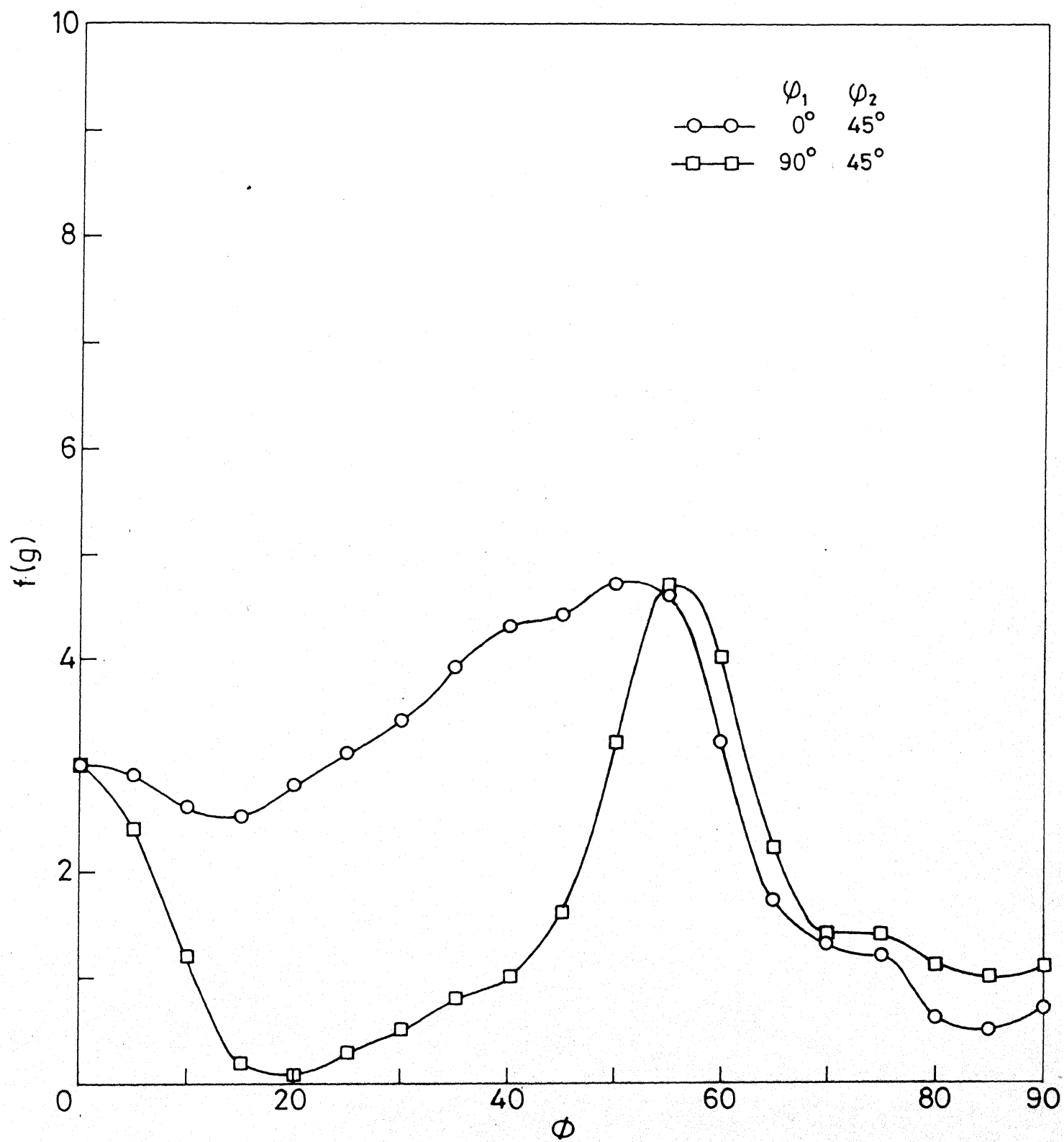


Fig.4.40 Variation of $f(g)$ with ϕ along different ϕ_1/ϕ_2 lines for A5/AC 810/WQ after 60% cold rolling.

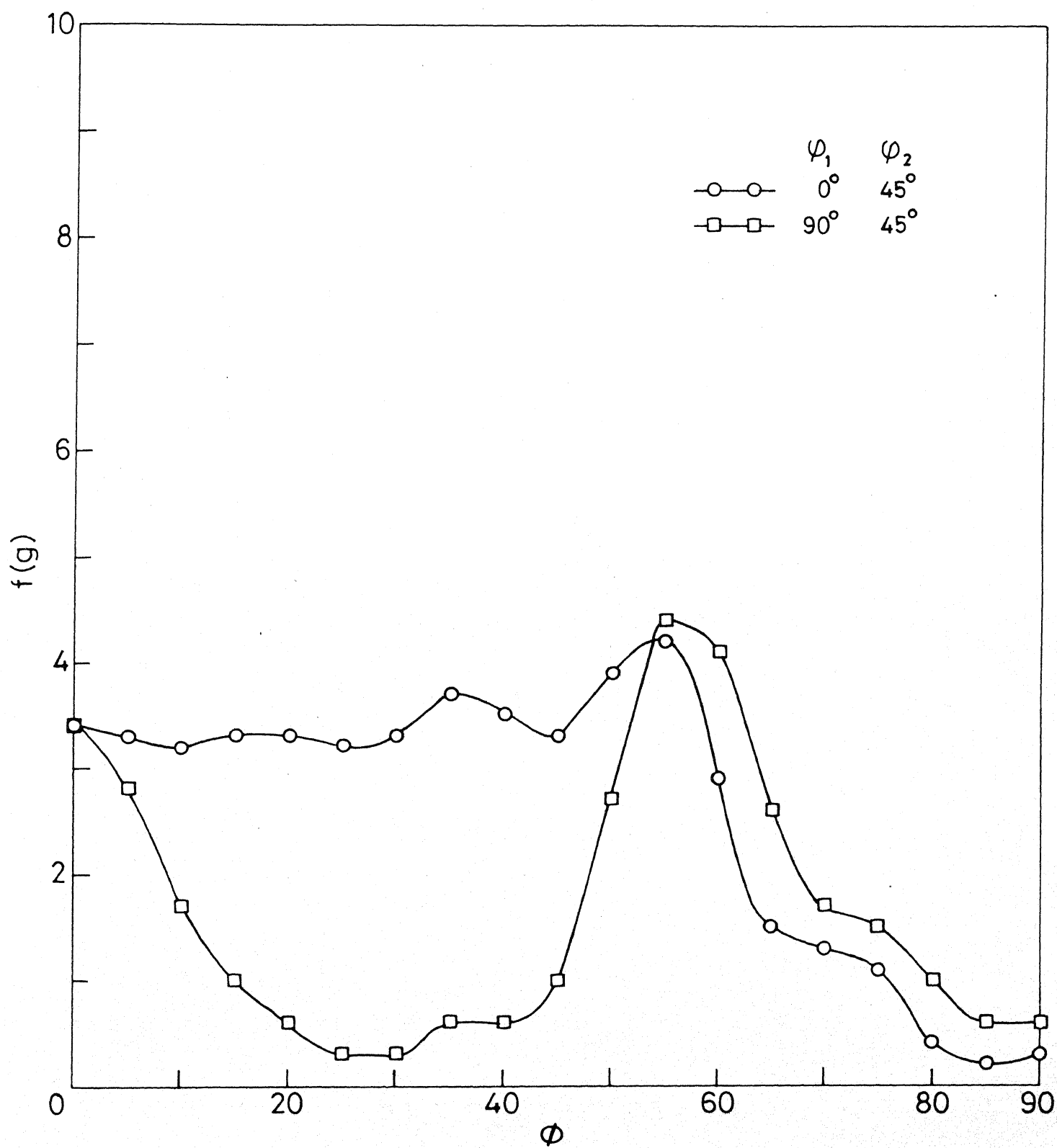


Fig.4.41 Variation of $f(g)$ with ϕ along different ϕ_1/ϕ_2 lines for A5/WQ750/WQ after 60% cold rolling.

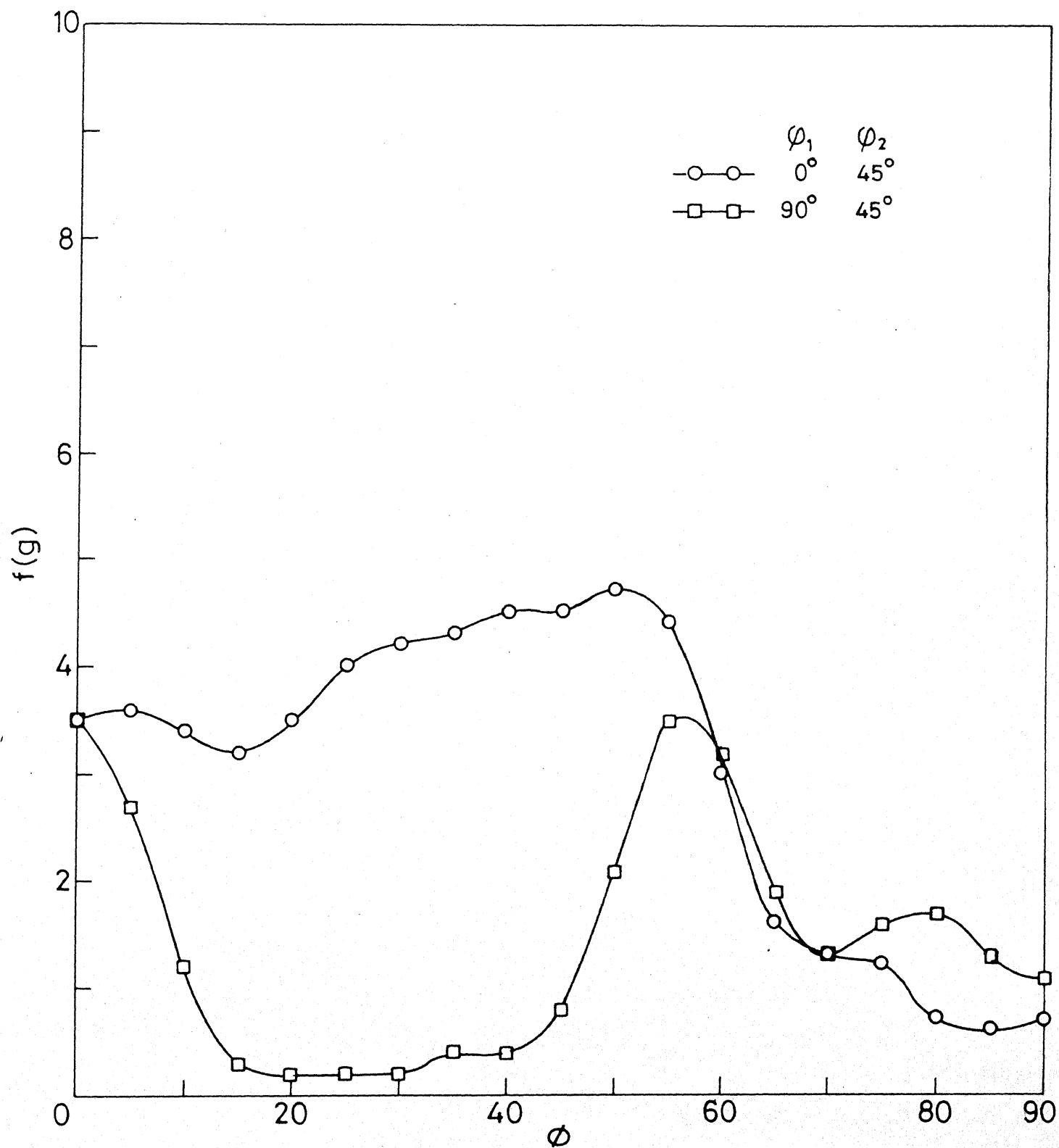


Fig.4.42 Variation of $f(g)$ with ϕ along different ϕ_1/ϕ_2 lines for A5/WQ 810/WQ after 60% cold rolling.

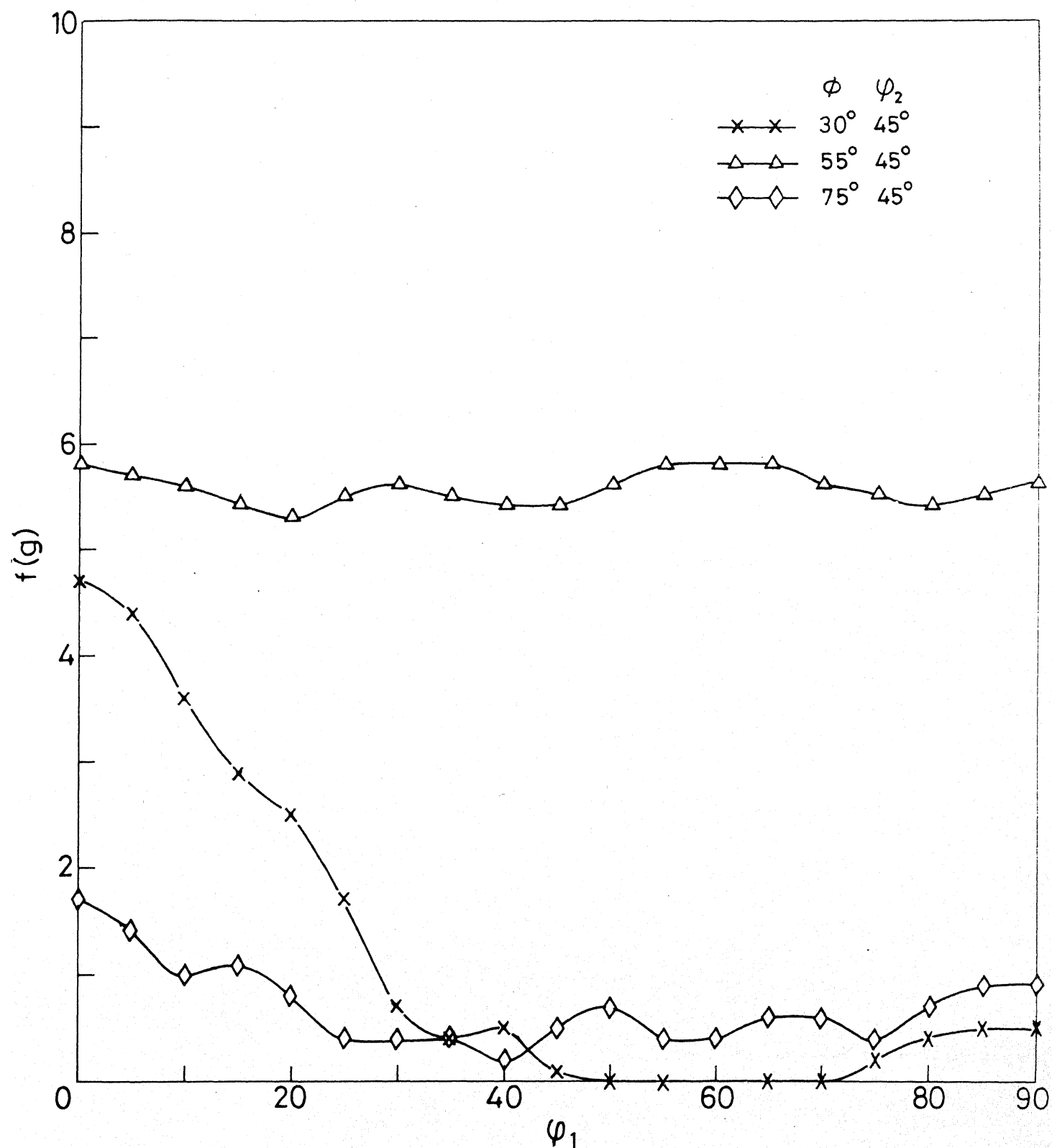


Fig.4.43 Variation of $f(g)$ with ϕ_1 along different ϕ/ϕ_2 lines for A5/AC750/WQ after 60% cold rolling.

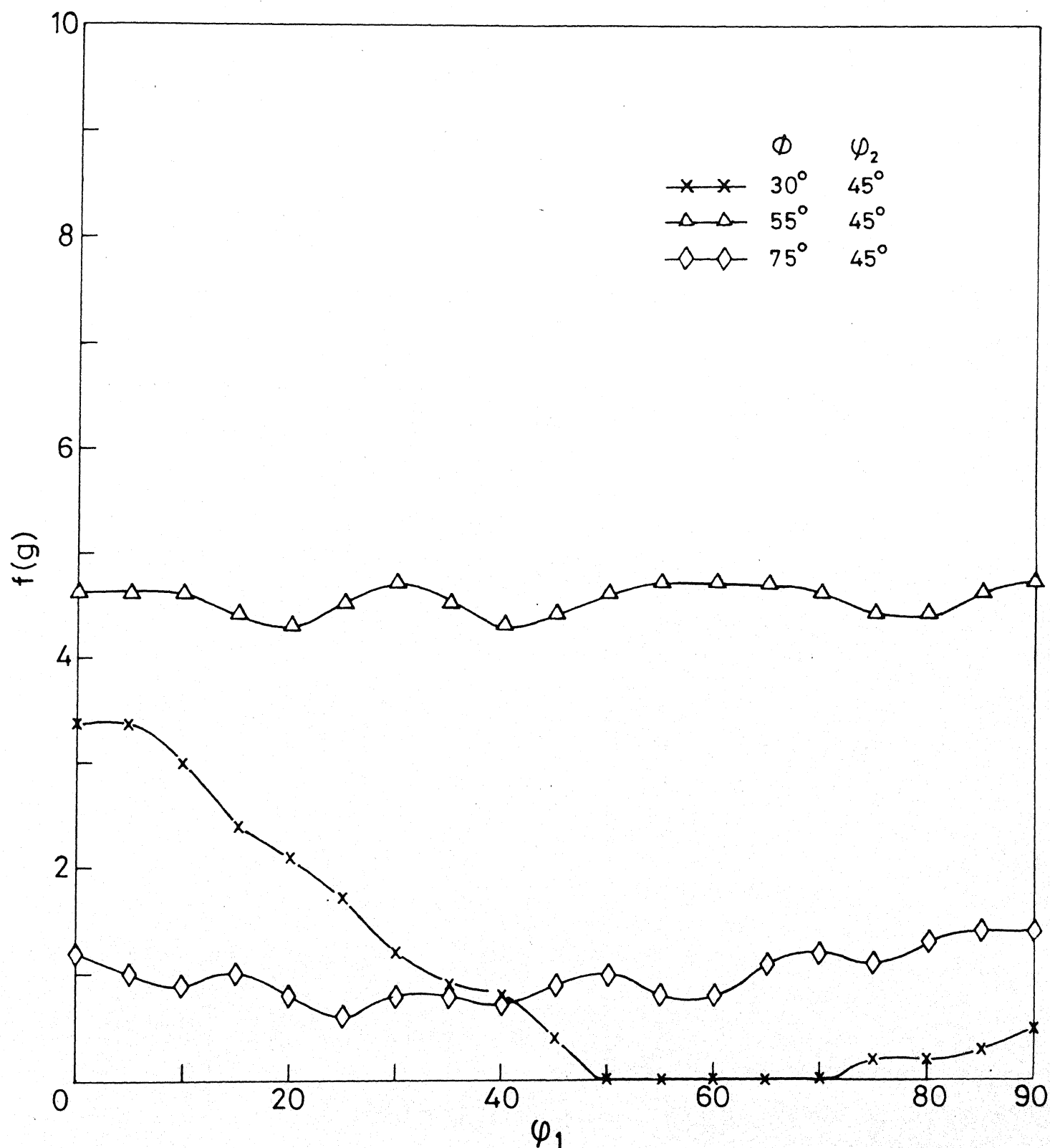


Fig.4.44 Variation of $f(g)$ with ϕ_1 along different ϕ/ϕ_2 lines for A5/AC 810/WQ after 60% cold rolling.

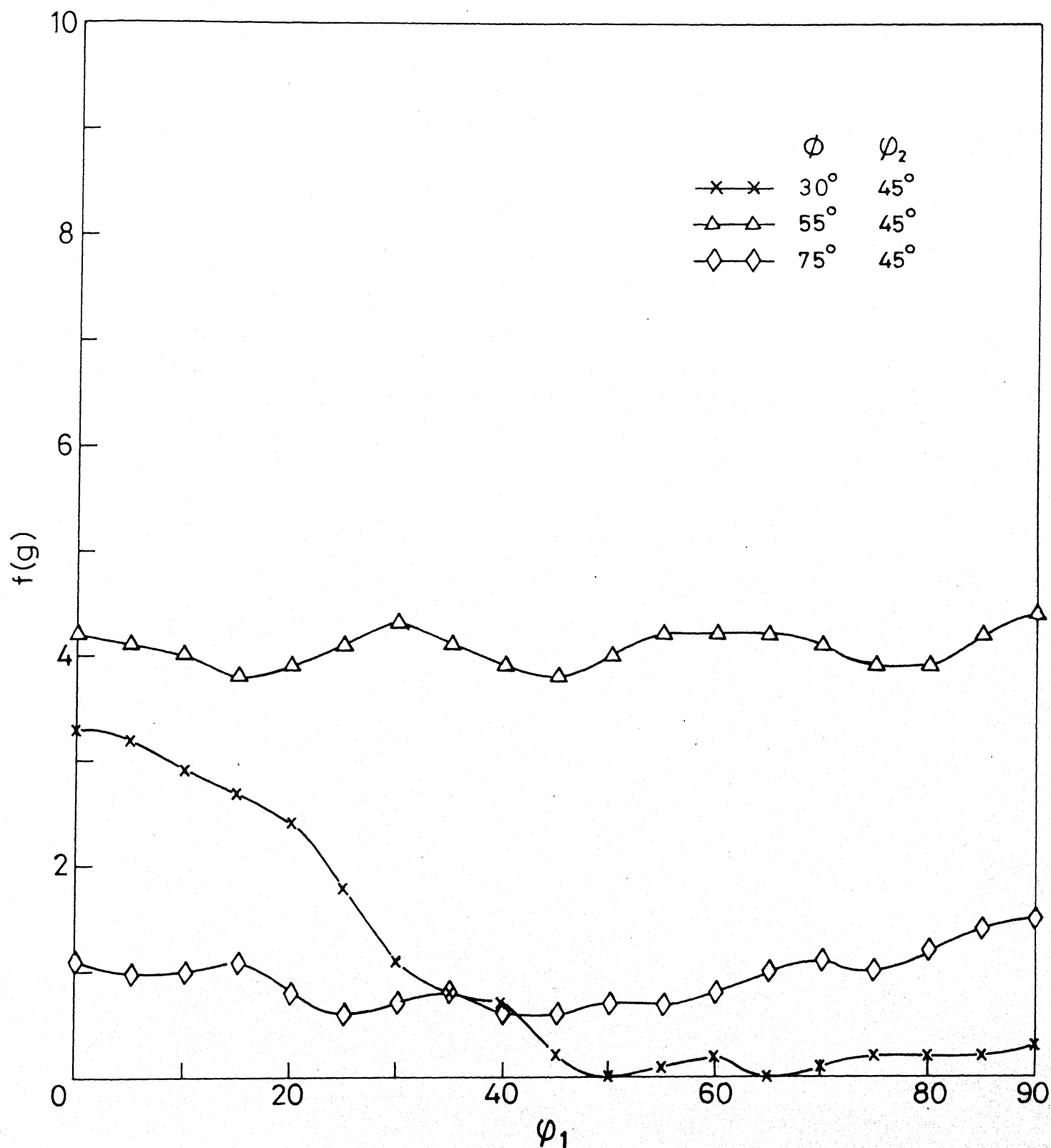


Fig.4.45 Variation of $f(g)$ with ϕ_1 along different ϕ/ϕ_2 lines for A5/WQ 750/WQ after 60% cold rolling.

4.3 Recrystallisation Characteristics of the Alloys

4.3.1 Microstructural Changes

The microstructural changes during the course of recrystallisation were determined by subjecting the cold-worked alloys to recrystallisation anneal at the temperatures, 650°C, 700°C, 750°C, 800°C and 850°C for various lengths of time. Out of these, the first two temperatures are below the lower critical temperature ($\sim 723^{\circ}\text{C}$) whereas the remaining three are above this temperature. The progress of recrystallisation was monitored by studying the microstructural changes using both the light and the transmission electron microscopy techniques. The changes in the optical microstructures with the progress of recrystallisation are shown typically in the series of optical micrographs shown in Figures 4.47(a-d) and 4.48(a-d). The first series of micrographs were taken from the alloy Al with a prior heat-treatment of WQ 810/WQ, given a recrystallisation anneal at 650°C; while the second series was taken from alloy A5 with a prior heat-treatment of AC 750/WQ, given a recrystallisation anneal at 800°C. It should be remembered that at the lower temperature of 650°C, the cold-rolled ferritic areas start recrystallising, whereas at the higher temperature of 800°C reaustenitisation of martensite and recrystallisation of cold-worked ferrite will take place simultaneously. A look at the Figures 4.47 and 4.48 shows that the recrystallised ferrite grains nucleate both at the ferrite-martensite interface as well as inside the deformed ferrite grains; on the other hand, austenite grains appear to form both at the ferrite-martensite interface and within the martensitic areas. The end product in both the cases will, of course, consist of islands of martensite embedded in the recrystallised ferrite matrix.

It was also noticed, during the course of the present investigation, that the volume percent martensite finally present in the dual-phase microstructure of any sample obtained by quenching from the recrystallisation temperatures of 750°C and above, was decidedly more than the corresponding value in the initially heat-treated starting material. Higher the recrystallisation temperature, larger was the increment in the martensite volume fraction.

In order to have a better idea about the nucleation sites of recrystallised grains with different orientations, as well as their growth behaviour, extensive studies were made, with the help of the T.E.M., on a large number of thin foils made from the different alloys, in both partially recrystallised and fully recrystallised conditions. The transmission electron microstructures taken from a number of thin foils of the alloy Al are given in Figures 4.49(a-d). No perceptible difference in the microstructure could be noticed in this alloy as a function of the initial heat-treatment. Figure 4.49(a) shows the formation of a number of recrystallised grains and subgrains of varying sizes in the cold-worked matrix in a material which has been recrystallised at 650°C for 10 seconds. S.A.D. patterns were taken from the large central recrystallised grain (B) as well as the cold-worked regions on both sides of it (areas A and C). The recrystallised grain B has been found to have the orientation $\{110\} \langle 001 \rangle$, whereas the cold-worked areas A and C have the orientations $\{110\} \langle 111 \rangle$ and $\{110\} \langle 001 \rangle$ respectively. The bulging grain boundary of the recrystallised grain towards region A indicates its preferential growth in that direction. Presumably this grain has nucleated from cold-worked region of the same orientation, namely, $\{110\} \langle 001 \rangle$. Another

interesting point to note in this micrograph is the presence of a fairly large number of fine precipitates within the recrystallised grains and subgrains and a number of relatively coarse precipitates at the grain/subgrain boundaries. Figure 4.49(b) shows a typical electron microstructure of the alloy in the fully recrystallised condition (temperature of recrystallisation 800°C). The structure essentially consists of a number of small recrystallised grains of ferrite with some martensitic islands distributed in the matrix. Not many precipitate particles can be seen in the ferritic areas. Sometimes, the grain boundaries of the ferrite grains in 650°C annealed materials are found to be dotted with precipitate particles (Figure 4.49(c)). Figure 4.49(d) shows a large recrystallised area with some recovered region at the centre. The S.A.D. patterns taken from the areas A and B indicate that the crystallographic orientations in both cases are the same, namely, $\{111\} \langle 110 \rangle$. This indicates that the area essentially consists of a large recrystallised grain with an orientation $\{111\} \langle 110 \rangle$, having lots of dislocation debris at the centre. In addition to the orientations mentioned above, recrystallised grains having the orientations $\{112\} \langle 110 \rangle$, $\{100\} \langle 001 \rangle$, $\{100\} \langle 011 \rangle$ and $\{221\} \langle 110 \rangle$ were also frequently seen in the electron microstructures taken from this alloy. As mentioned above, a fairly good amount of precipitates could be seen both inside as well as in the boundaries of the recrystallised grains/subgrains in the microstructure of the 650°C annealed material. However, it was not possible to identify them from S.A.D. patterns. In contrast to the 650°C annealed material, the material recrystallised at 800°C showed very few precipitates in the ferrite matrix.

No significant difference could be obtained in the electron micrographs of the recrystallised structures of alloy A4 as a function of prior

heat-treatment, excepting that the recrystallised grains appeared to be somewhat larger in size for the material subjected to the AC/WQ treatment as compared to WQ/WQ treatment. A typical overall view of the microstructure of this alloy in the recrystallised condition is shown in Figure 4.50(a). Evidently the structure here consists of ferrite and martensite grains with a large density of fine precipitate particles along grain boundaries as well as within the ferrite grains. Figure 4.50(b) shows a partially recrystallised area with a number of small recrystallised grains. It is interesting to note that here a number of precipitates can be seen within the highly dislocated cold-worked areas also in addition to precipitates lying at grain boundaries and also within the recrystallised grains. The precipitate particles lying along the grain boundaries appear to be somewhat larger in size as compared to those lying in the grain interior (Figure 4.50(c)). In contrast to this behaviour, the ferrite grains in the material recrystallised at 800°C showed only very few precipitate particles within (Figure 4.50(d)). The crystallographic orientations of the recrystallised grains most frequently obtained are $\{112\} \langle 111 \rangle$, $\{112\} \langle 110 \rangle$, $\{110\} \langle 111 \rangle$, $\{111\} \langle 110 \rangle$, $\{8, 9, 11\} \langle 313 \rangle$, $\{110\} \langle 001 \rangle$ and $\{147\} \langle 311 \rangle$.

Most extensive T.E.M. examination has been carried out on thin foils made from partially and fully recrystallised A5 alloy. Figure 4.51(a) shows an almost fully recrystallised area in alloy A5 which was given an initial treatment AC 750/WQ, then cold-worked 60% followed by annealing at 650°C for 10 seconds. The S.A.D. pattern taken from the entire area showed that it has the orientation given by $\{116\} \langle 331 \rangle$. Figure 4.51(b) shows another area with a large recrystallised grain (A) at the centre. The crystallographic orientation of this grain has been found out to be near $\{221\} \langle 110 \rangle$. The orientations from the areas marked B and C

flanking this big grain have been found to be $\{310\} \langle 001 \rangle$ and $\{125\} \langle 210 \rangle$ respectively. Some fine precipitates can also be seen along sub-boundaries and dislocations.

Recrystallisation at a higher temperature of 800°C in this alloy, with the same prior heat-treatment, leads to the formation of a coarse dispersion of a duplex ferrite martensite structure. This is shown typically in Figure 4.51(c). Figure 4.51(d) shows an area with ferrite grains recrystallising out of the deformed matrix. The S.A.D. patterns taken from the areas A, B and C show that both A and B have got the same orientation, namely, $\{2, 5, 13\} \langle 131 \rangle$, whereas C has got the orientation $\{110\} \langle 111 \rangle$.

Figure 4.52(a) shows typically a partially recrystallised area in the alloy A5, with a prior heat-treatment AC 810/WQ, 60% cold-rolled and then annealed at 650°C for 10 seconds. S.A.D.'s taken from areas A and B show that they have orientations given by $\{111\} \langle 110 \rangle$ and $\{112\} \langle 111 \rangle$ respectively. Another partially recrystallised ferrite area is shown in Figure 4.52(b). Widely varying orientations have been obtained from different areas of this micrograph. It has been found out from the corresponding S.A.D. patterns that the crystallographic orientations encountered from different areas in this micrograph are $\{100\} \langle 001 \rangle$, $\{3, 1, 10\} \langle 311 \rangle$ and $\{112\} \langle 111 \rangle$ respectively.

The alloy A5, with the same initial heat-treatment, but recrystallisation-annealed at the higher temperature of 800°C has been found to have a duplex ferrite-martensite structure with a substantial amount of martensite. This is shown typically in Figure 4.52(c) where the martensite is also found to be heavily twinned. Figure 4.52(d) shows, at the centre,

a ferritic area undergoing recrystallisation at 800°C . The central grain marked A and area marked C have been found to have the orientation $\{100\} \langle 001 \rangle$, whereas area B has the orientation given by $\{10, 1, 4\} \langle 146 \rangle$.

Figure 4.53(a) shows a partially recrystallised area from alloy A5, with an initial heat-treatment WQ 750/WQ, cold-rolled 60% and then given a recrystallisation anneal at 650°C for 10 seconds. The central subgrain here has been found to have an orientation $\{116\} \langle 331 \rangle$. Figure 4.53(b) shows a number of elongated subgrains in the same alloy in the same condition. The subgrains have been found to have widely varying crystallographic orientations. For example, the subgrains marked A, B and C in the micrograph have been found to have the orientations $\{147\} \langle 311 \rangle$, $\{310\} \langle 001 \rangle$ and $\{111\} \langle 110 \rangle$ respectively.

Recrystallisation anneal of the same material at the higher temperature of 800°C shows again a duplex ferrite-martensite structure with substantial amount of martensite. This is shown typically in Figure 4.53(c). A partially recrystallised ferritic area is shown in Figure 4.53(d). The S.A.D.'s taken from the areas marked A and C have shown that they have the same orientation, namely, $\{7, 12, 15\} \langle 331 \rangle$, whereas the area B has an orientation given by $\{145\} \langle 111 \rangle$.

A typical transmission electron microstructure of the A5 alloy with a prior heat-treatment WQ 810/WQ, 60% cold-rolled and recrystallisation-annealed at 650°C , is shown in Figure 4.54(a). The large recrystallised grain at the centre has been found to have an orientation $\{100\} \langle 001 \rangle$. Figure 4.54(b) shows another area with a number of subgrains surrounding a moderately large sized grain at the centre (marked A). The S.A.D. pattern indicates that this grain has an orientation given by $\{147\} \langle 311 \rangle$. The

crystallographic orientations of some of the subgrains surrounding A are $\{110\} \langle 111 \rangle$, $\{100\} \langle 011 \rangle$ and $\{112\} \langle 111 \rangle$.

The same material when recrystallised at the higher temperature of 800°C , shows a typical duplex ferrite-martensite structure. An example of this is given in Figure 4.54(c). Here the ferrite grain at the right is found to have a large number of dislocations in the area adjacent to the martensite phase. Figure 4.54(d) shows an almost fully recrystallised, predominantly ferritic area. The orientations of the recrystallised grains have been found to be $\{147\} \langle 311 \rangle$, $\{110\} \langle 111 \rangle$ and $\{100\} \langle 011 \rangle$.

4.3.2 Recrystallisation Texture

The (110) pole-figures of the alloys A1, A4 and A5, in the fully recrystallised condition, are shown in Figures 4.55 to 4.57 respectively. It is interesting to note from these pole-figures that their general features look very much the same as the corresponding pole-figures measured from the deformed materials. In other words, the texture components of the recrystallised alloys are basically $\{111\} \langle 112 \rangle$ and $\{111\} \langle 110 \rangle$ of which the former is much stronger than the latter.

For alloy A1, the intensities of the maxima for the $\{111\} \langle 112 \rangle$ component seem to be very nearly the same irrespective of the prior heat-treatments and the recrystallisation temperatures. In fact, these intensities are decidedly lower than those found in the deformation textures of this alloy.

The intensities of the texture components have been found to be cut down rather drastically in the recrystallisation textures of alloy A4 as compared to the corresponding deformation textures. In fact, Figure 4.56

clearly shows that, in some cases, the recrystallisation texture can be considered as practically random.

In contrast to the recrystallisation behaviour of alloys A1 and A4, the recrystallisation textures of alloy A5 (Figure 4.57) are found to be very much similar to the corresponding deformation textures (Figure 4.19) both in terms of texture components as well as their intensities.

In order to have a better insight into the textural changes taking place in the three alloys A1, A4 and A5, consequent upon recrystallisation, O.D.F. plots were made from all the three alloys having different initial heat-treatments. These plots are shown in Figures 4.58 to 4.63. Intensities of a few maxima in the O.D.F. plots are indicated at appropriate places.

A close look at these O.D.F. plots shows that for alloy A1, $f(g)_{\max}$ is slightly higher for the higher recrystallisation temperature. For alloy A5, $f(g)_{\max}$ is significantly higher for the higher recrystallisation temperature. On the other hand, for the alloy A4, $f(g)_{\max}$ is found to be lower for the higher recrystallisation temperature.

In general, for both the alloys A1 and A5, $f(g)_{\max}$ is higher for the materials intercritically annealed at the lower temperature of 750°C. On the other hand, for the alloy A4, $f(g)_{\max}$ is found to be higher for the materials intercritically annealed at the higher temperature of 810°C.

Again, in alloy A1, $f(g)_{\max}$ value has been found to be higher for the WQ/WQ treatment as compared to AC/WQ treatment. No significant variation in $f(g)_{\max}$ has been found for these two heat-treatments in alloy A4. No general trend regarding the effect of heat-treatment on the $f(g)_{\max}$ value in alloy A5 has been noticed.

From a look at the O.D.F. plots it is at once apparent that excepting in a few cases where the pole densities are significantly low (alloy A4, recrystallised at 800°C), all the other plots show a number of peak-type components in each case. The Euler angles for such peak-type components were read out from the appropriate computer print-outs. The ideal orientation, $(hkl) [uvw]$, corresponding to the Euler angles of the important maxima can be obtained from the Table 3.3. As in case of the deformation textures, the major texture components in the O.D.F.'s of the recrystallised alloys have been found out to be $\{111\} \langle 110 \rangle$ and $\{111\} \langle 112 \rangle$ type. The minor components of the type $\{337\} \langle 110 \rangle$, $\{337\} \langle 776 \rangle$, $\{112\} \langle 111 \rangle$, $\{112\} \langle 110 \rangle$, $\{11, 11, 4\} \langle 110 \rangle$ and $\{11, 11, 4\} \langle 2, 2, 11 \rangle$ have also been detected. In addition, some other low intensity texture components have also been found and these are $\{110\} \langle 001 \rangle$, $\{001\} \langle 110 \rangle$, $\{110\} \langle 110 \rangle$ and $\{310\} \langle 001 \rangle$ etc. So far as the peak-type components are concerned, there is not much significant difference in the deformation and the recrystallisation textures in these three alloys.

Next, the possibility of having fibre texture in the recrystallised materials has been checked by following the same procedure as was done for the deformation textures. The relevant plots for the alloy Al cold-rolled 60% and then fully recrystallised at the two temperatures of 650°C and 800°C are shown in Figures 4.64 to 4.67 for the different initial heat-treatments. All these plots show the variation of pole density, $f(g)$ with ϕ in the two sections $\psi_1 = 0$, $\psi_2 = 45^{\circ}$ and $\psi_1 = 90^{\circ}$, $\psi_2 = 45^{\circ}$. In the latter section, a reasonably sharp peak appears at $\phi \approx 55^{\circ}$ (corresponding to the orientation $(111) [\bar{1}\bar{1}2]$) for all the materials in this alloy having different initial heat-treatments and recrystallised at

two different temperatures. The pole densities corresponding to this orientation are remarkably similar for all the materials. In addition, in this section, another peak appears at $\phi \approx 75^\circ$ (corresponding to the orientation $(11, 11, 4) [\bar{2}, \bar{2}, 11]$). In contrast to this behaviour, in the section $\psi_1 = 0$, $\psi_2 = 45^\circ$, the plots of $f(g)$ versus ϕ show a much flatter variation with ϕ . The pole density levels encountered here are significantly higher as compared to those in the previous section. The positions of the major maxima in these plots are found to be shifted to somewhat lower values of ϕ and may be assumed to correspond to the orientation $\psi_1 = 0$, $\phi = 40^\circ$ and $\psi_2 = 45^\circ$ which is equivalent to the orientation $(335) [1\bar{1}0]$. In addition to these major maxima, peaks in $f(g)$ values have also been obtained at $\phi = 75^\circ$ which, in this section, corresponds to the orientation $(11, 11, 4) [1\bar{1}0]$.

From the above plots one thing is pretty clear and that is, the pole densities of the orientations $\{111\} \langle uvw \rangle$ and $\{335\} \langle uvw \rangle$ are the strongest in all cases. The pole densities of the $\{11, 11, 4\} \langle uvw \rangle$ orientations are also quite significant. However, it is not very apparent whether any strong fibre texture is present. In order to check the possibility of having some kind of complete/incomplete fibre texture in these materials, $f(g)$ values were plotted for (a) $\phi = 55^\circ$ and $\psi_2 = 45^\circ$ for $\psi_1 = 0-90^\circ$, (b) $\phi = 30^\circ$ and $\psi_2 = 45^\circ$ for $\psi_1 = 0-90^\circ$ and (c) $\phi = 75^\circ$ and $\psi_2 = 45^\circ$ for $\psi_1 = 0-90^\circ$. The reason behind going for these plots has already been given while describing the deformation texture results. All the above plots for the alloy Al are given in Figures 4.68 to 4.71.

Figure 4.68 shows that, for the materials with the heat-treatment AC/WQ where the intercritical annealing was done at 750°C , no sharp and strong

fibre texture could be obtained whatever may be the recrystallisation temperature. In fact, the $f(g)$ values with ψ_1 along $\phi = 55^\circ$, $\psi_2 = 45^\circ$ have been found to vary within a range 2.3 to 4.0, indicating that at best there may be a partial $\{111\}$ fibre texture. From a look at the other curves in the same plot it may be said that, there is a weak and incomplete fibre of the type $\{11, 11, 4\}$ and practically no fibre of $\{337\}$ type. Precisely similar results have been obtained for the material which was intercritically annealed at 810°C (Figure 4.69).

Figures 4.70 and 4.71 show that even for the WQ/WQ heat-treated materials of alloy Al, the results are quite similar to those with the AC/WQ heat-treatment in the sense that in all of them a strong partial fibre of the $\{111\}$ type, a weak incomplete fibre of the $\{11, 11, 4\}$ type and practically no $\{337\}$ fibre have been obtained. One interesting thing to notice in the above plots is that the pole density values for the $\{111\}$ partial fibre are all along higher for the higher recrystallisation temperature of 800°C .

The variation of $f(g)$ with ϕ along different ψ_1/ψ_2 lines for the alloy A4, with different initial heat-treatments followed by cold-rolling and recrystallisation at two different temperatures, is shown in a graphical manner in Figures 4.72 to 4.75. An examination of these plots reveals that for all the four different materials recrystallised at 650°C , reasonably sharp peak in pole density values are obtained at $\phi = 55^\circ$ in both the sections $\psi_1 = 0$, $\psi_2 = 45^\circ$ and $\psi_1 = 90^\circ$, $\psi_2 = 45^\circ$. Another interesting thing to notice is that in all of them the $f(g)$ values are nearly the same in both the ψ_1/ψ_2 sections. Peaks at $\phi = 55^\circ$ in both the ψ_1/ψ_2 sections have also been obtained for all the four

materials recrystallised at the higher temperature of 800°C . However, the intensities of these peaks were found to be significantly lower than those for the 650°C recrystallised materials. In addition to the peaks at $\phi = 55^{\circ}$, moderately strong peaks in $f(g)$ have also been obtained at $\phi = 75^{\circ}$ in both the ψ_1/ψ_2 sections.

A close look at the above plots gives sufficient indications of the presence of a reasonably strong $\{111\} \langle uvw \rangle$ fibre texture in all the four materials. Such a possibility has been systematically checked in a manner described earlier for the alloy Al. The relevant plots are shown in Figures 4.76 to 4.79. It is apparent from these plots that reasonably strong $\{111\}$ fibre texture is obtained in all the four materials recrystallised at 650°C . This fibre is found to be significantly weaker for the higher temperature of recrystallisation, namely, 800°C . In addition to this, a rather weak $\{11, 11, 4\} \langle uvw \rangle$ partial fibre can also be identified in all the above plots. The $\{337\} \langle uvw \rangle$ orientations are not found to be developed as a fibre texture and can at least be thought of as a rather weak and incomplete fibre texture component.

The variation of $f(g)$ with ϕ along different ψ_1/ψ_2 lines for the alloy A5 with different initial heat-treatments followed by cold-rolling and recrystallisation at two different temperatures, is shown in a graphical manner in Figures 4.80 to 4.83. From all these plots it is found that in the section $\psi_1 = 90^{\circ}$, $\psi_2 = 45^{\circ}$, a sharp peak appears at $\phi = 55^{\circ}$ (corresponding to the orientation $(111) [\bar{1}\bar{1}2]$) for all these materials in this alloy having different initial heat-treatments and recrystallised at two different temperatures. In addition, there are a few minor peaks in this section, but these are not of much significance because of their very

low intensity. In contrast to this behaviour, in the section $\psi_1 = 0$, $\psi_2 = 45^\circ$ the plots of $f(g)$ versus ϕ show comparatively strong but flatter peaks. The positions of the major maxima in these plots are found to be shifted to somewhat lower values of ϕ and may be assumed to correspond to the orientations $\psi_1 = 0$, $\phi = 40^\circ$, $\psi_2 = 45^\circ$ and $\psi_1 = 0$, $\phi = 50^\circ$, $\psi_2 = 45^\circ$, which are equivalent to the orientations (335) $[1\bar{1}0]$ and (445) $[1\bar{1}0]$ respectively. One significant observation from these plots is that the intensities of the peaks are much sharper for the material recrystallised at the higher temperature of 800°C as compared to the material recrystallised at the lower temperature of 650°C .

In order to check the possibility of having some kind of complete/incomplete fibre texture in these materials, $f(g)$ values have been plotted for (a) $\phi = 55^\circ$ and $\psi_2 = 45^\circ$ for $\psi_1 = 0-90^\circ$, (b) $\phi = 30^\circ$ and $\psi_2 = 45^\circ$ for $\psi_1 = 0-90^\circ$, and (c) $\phi = 75^\circ$ and $\psi_2 = 45^\circ$ for $\psi_1 = 0-90^\circ$. All the above plots for the alloy A5 are given in Figures 4.84 to 4.87. A look at these plots clearly shows the presence of a reasonably good $\{111\}$ type fibre texture in all the four materials. Out of these, the best fibre texture has been obtained for the material with the heat-treatment WQ/WQ which has been intercritically annealed at 810°C . In all the above plots the intensity of the $\{111\}$ fibre has been found to be much stronger for the higher recrystallisation temperature of 800°C . In addition to the strong $\{111\}$ fibre texture component no other fibre could be detected in alloy A5 in the recrystallised condition.

A comparison of the texture data for the three alloys A1, A4 and A5 in the recrystallised condition clearly indicates the differences in their recrystallisation texture. Thus, whereas sharp $\{111\}$ fibre texture

component has been obtained for both the alloys A4 and A5, no $\{111\}$ fibre could be found in alloy A1. Again, the intensity of the $\{111\}$ fibre is found to be significantly stronger in case of alloy A5 than A4. A weak partial $\{11, 11, 4\}$ fibre has been found in alloy A4, this same component is not at all developed in alloy A5, while the same component may be treated as a weak and incomplete fibre in case of alloy A1. So far as the components $\{337\} \langle uvw \rangle$ is concerned, these do not comprise a fibre component in either alloy A1 or A5, although it can be seen as a rather weak and incomplete fibre in alloy A4. One major difference in the recrystallisation textures of alloys A4 and A5 is that, whereas in the former alloy a stronger $\{111\}$ fibre is obtained for the lower recrystallisation temperature of 650°C , in the latter recrystallisation at a higher temperature of 800°C has been found to produce a strong $\{111\}$ fibre.

4.3.3 Kinetics of Recrystallisation

The recrystallisation kinetics in respect of the three alloys A1, A4 and A5 have been studied from measurements of the microhardness values of the cold-worked, partially recrystallised and fully recrystallised materials. Instead of carrying out the kinetics studies on all the four differently heat-treated initial materials in each alloy, measurements were made only on those materials which had an initial heat-treatment, such as, AC 750/WQ and WQ 750/WQ. This was done with the idea that, out of the four different heat-treatments in each alloy, these two produced larger volume fraction of ferrite in the dual-phase microstructure. It

is, of course, understood that the kinetics studies mentioned above refer to the ferritic phase only.

Results of recrystallisation kinetics studies are given in Figures 4.88 to 4.93. Each figure refers to the measurements made for any one alloy with a specific initial heat-treatment. In addition, each figure consists of (a) a plot showing the variation of microhardness of ferrite with time at different annealing temperatures, (b) Avrami plots of recrystallised volume fractions estimated from the microhardness data and (c) Arrhenius plots for the measurement of activation energies, Q .

A close look at the microhardness versus time plots at different annealing temperatures for all the three alloys shows that the microhardness of the ferrite phase decreases with increase in annealing time, as expected. However, at higher temperatures of annealing, the microhardness is found to decrease initially, then goes through a minimum before rising again at longer annealing times.

In general, the Avrami plots of recrystallised volume fractions shown in the above figures (Figures 4.88b to 4.93b) indicate two distinct regions which may be due to the occurrence of two distinct processes during recrystallisation. The corresponding ' m '-values have been marked at appropriate places in these diagrams.

Arrhenius plots for the measurement of activation energies are also incorporated in the Figures 4.88c to 4.93c. These diagrams have been drawn for (A) time $t_{0.5}$ for 50% recrystallisation, (B) time τ (estimated from Avrami plots) for 63% recrystallisation, and (C) time $t_{0.8}$ for 80% recrystallisation. These parameters have been so chosen as to cover both sides of the region of change-over of the slopes of the

Avrami plots. The measured values of the activation energies have been marked at appropriate places in the diagrams mentioned above. These values are also given in a tabular form in Table 4.4. It is clear from this table that, for a particular alloy, there is practically no significant variation in the Q-values as a function of either the difference in initial heat-treatment or due to measurements being made for three different levels of recrystallisation. Apparently, the two distinct stages indicated in the Avrami plots essentially have similar Q-values. The Q-values measured for all the three alloys are quite similar and range between 17 and 20 KCal/ $^{\circ}$ mole (Table 4.4).

Table 4.4

'Q'-values Obtained from Recrystallisation Data

Alloy designation	Initial heat-treatment	Q-values, KCal/ $^{\circ}$ mole		
		Time- $t_{0.5}$, for 50% recrystallisation	Time- τ for 63% recrystallisation	Time- $t_{0.8}$, for 80% recrystallisation
A1	AC 750/WQ	19.2	16.9	17.7
	WQ 750/WQ	18.4	17.8	18.6
A4	AC 750/WQ	18.7	18.7	20.6
	WQ 750/WQ	16.9	16.2	17.3
A5	AC 750/WQ	16.3	15.8	17.0
	WQ 750/WQ	20.2	17.3	17.3

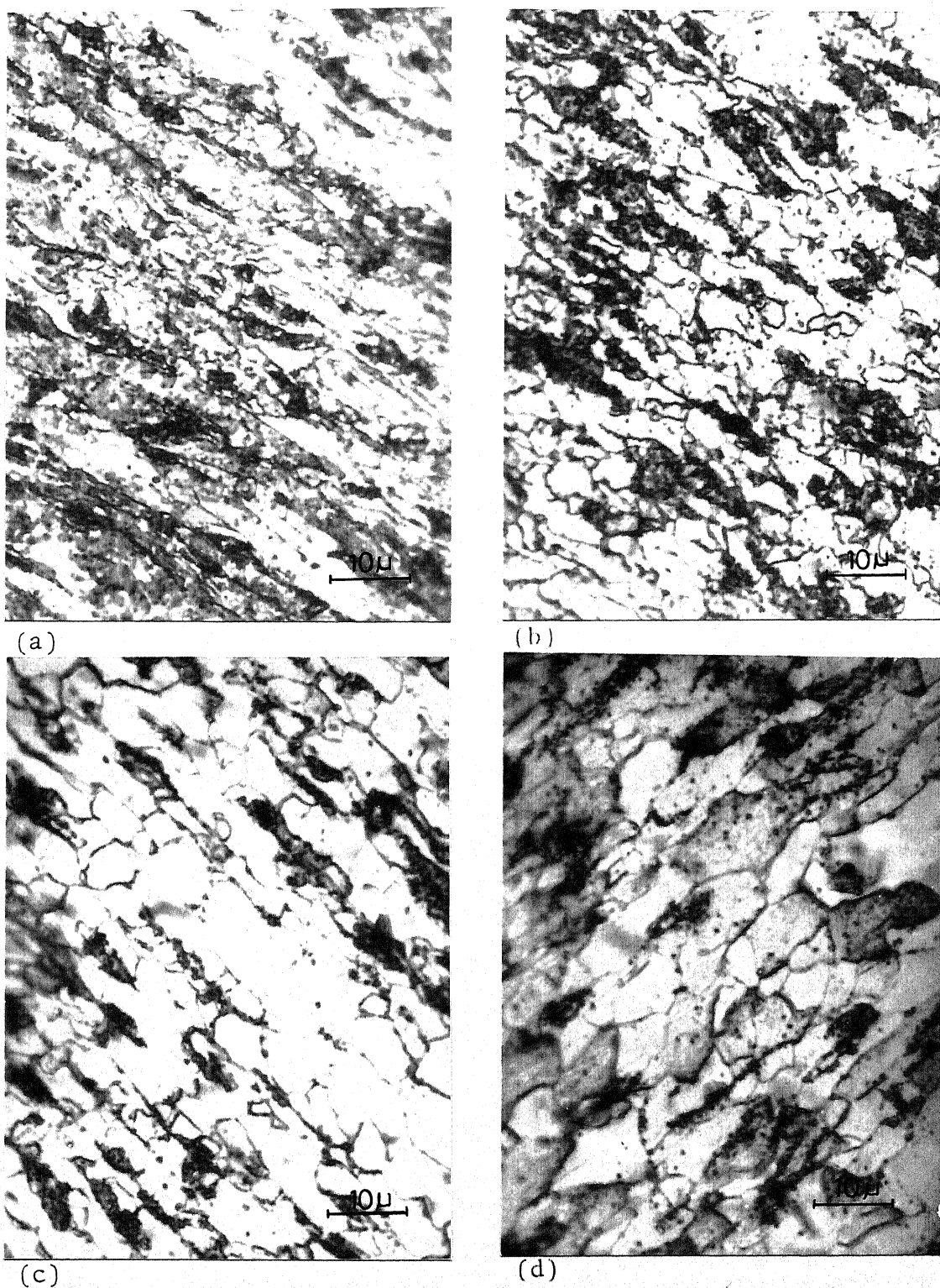
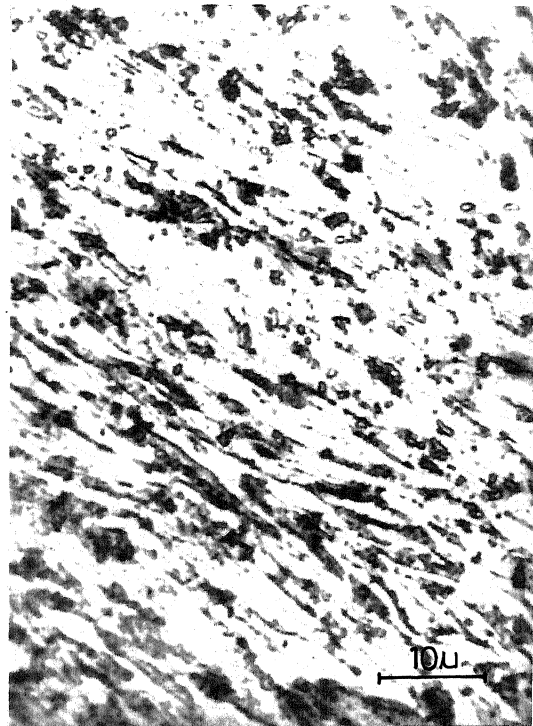
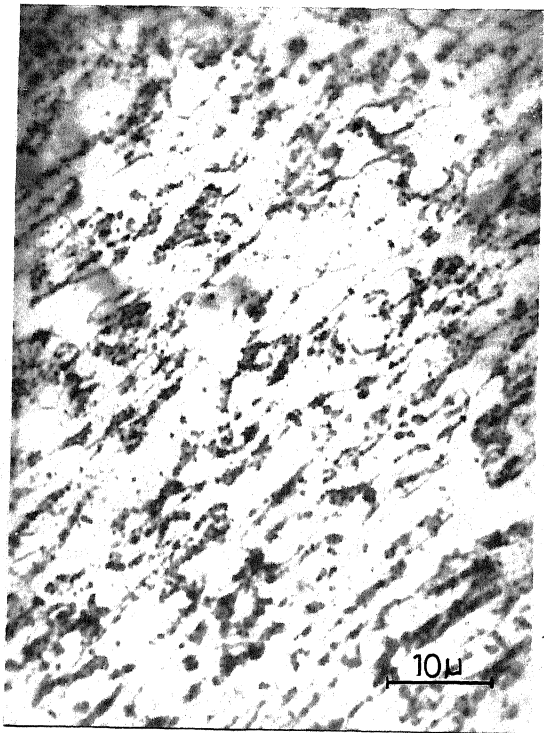


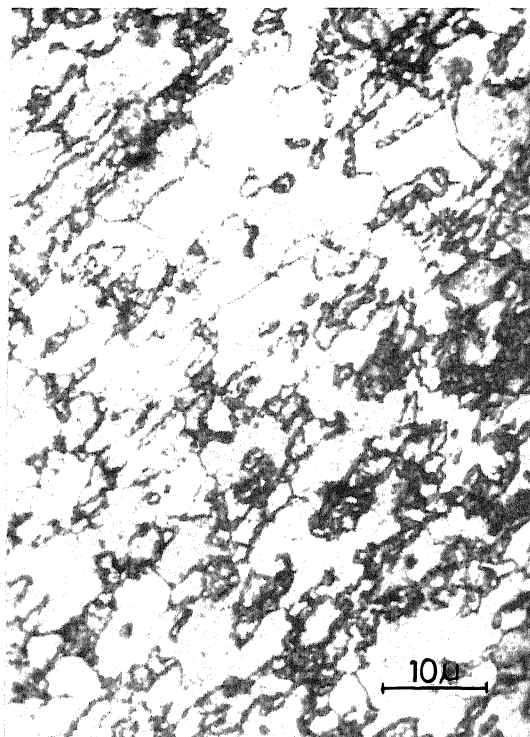
Fig. 4.47 Optical microstructures of alloy Al after recrystallisation anneal at 650°C for (a) 10 sec (b) 30 sec (c) 40 sec (d) 60 sec.



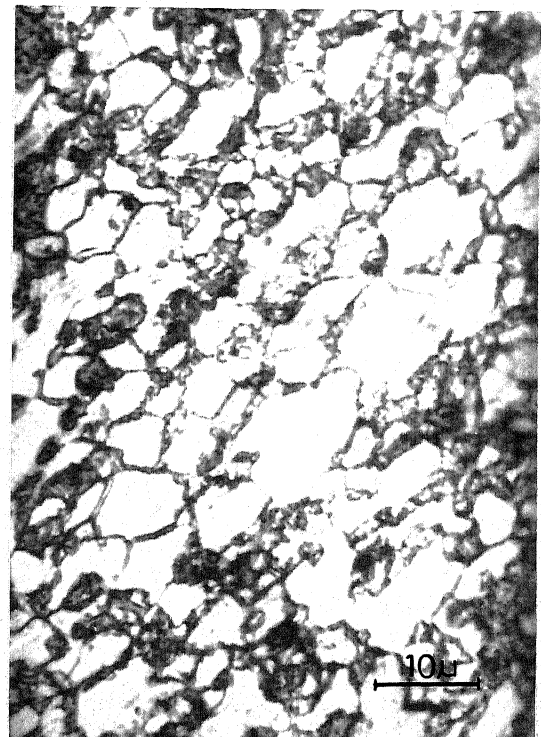
(a)



(b)

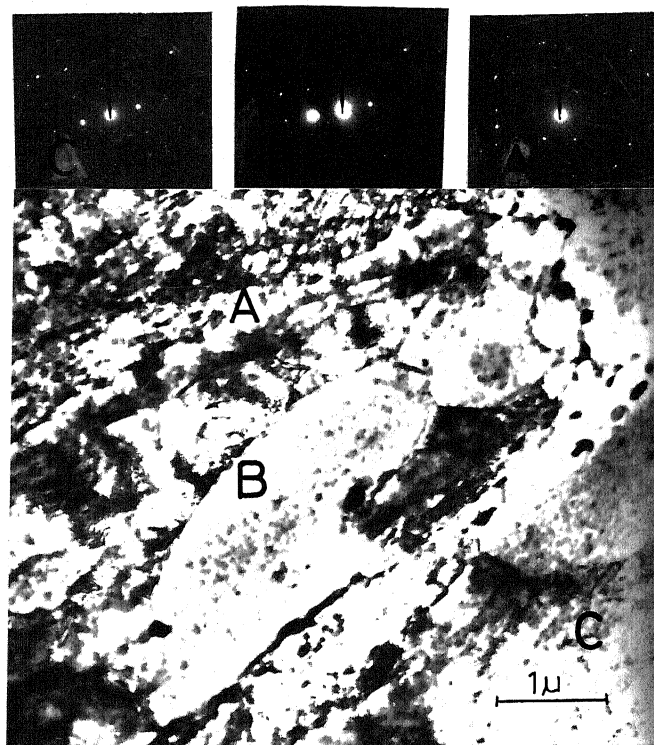


(c)

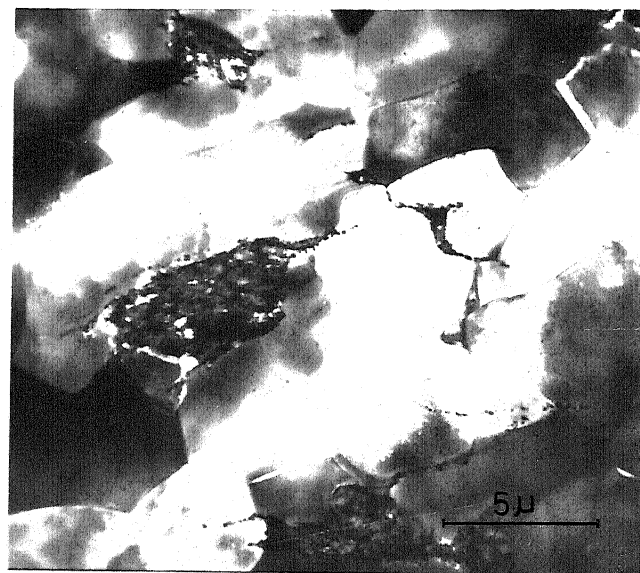


(d)

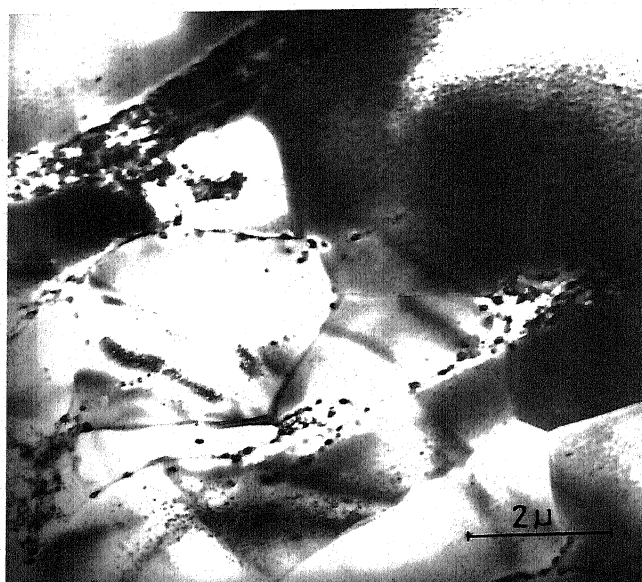
Fig. 4.48 Optical microstructures of alloy A5 after recrystallisation anneal at 800°C for (a) 5 sec (b) 7 sec (c) 10 sec (d) 30 sec.



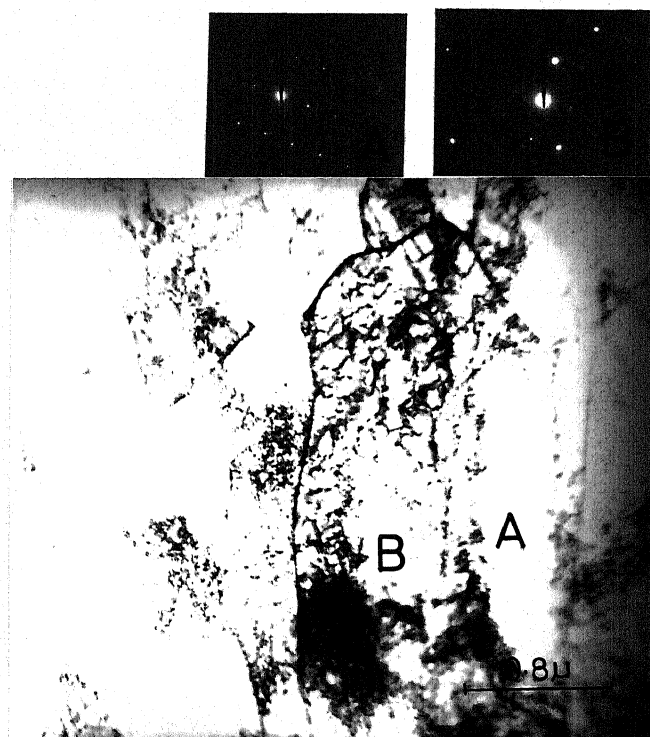
(a)



(b)

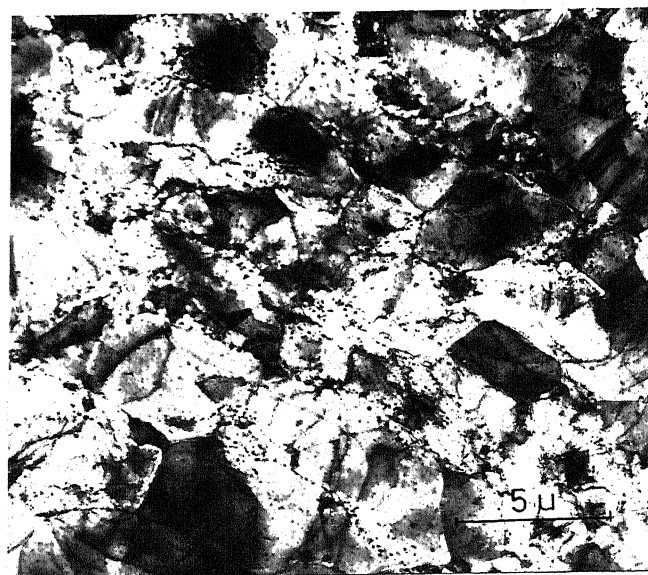


(c)

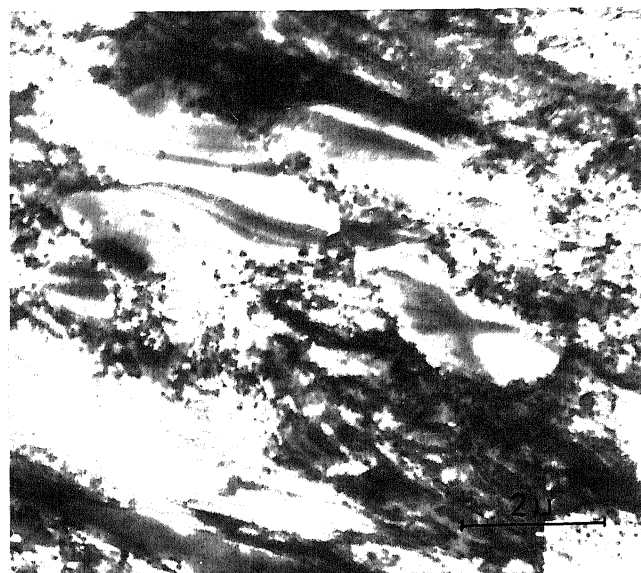


(d)

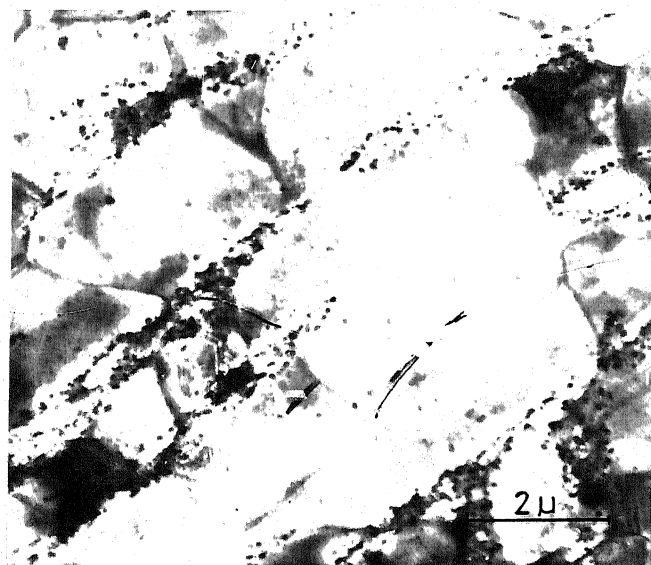
Fig. 4.49 Electron microstructures of recrystallised alloy Al
 (a) AC 810/Rex 650/10 sec (b) WQ 810/Rex 800/ 5 sec
 (c) WQ 750/Rex 650/10 sec (d) WQ 810/Rex 650/10 sec.



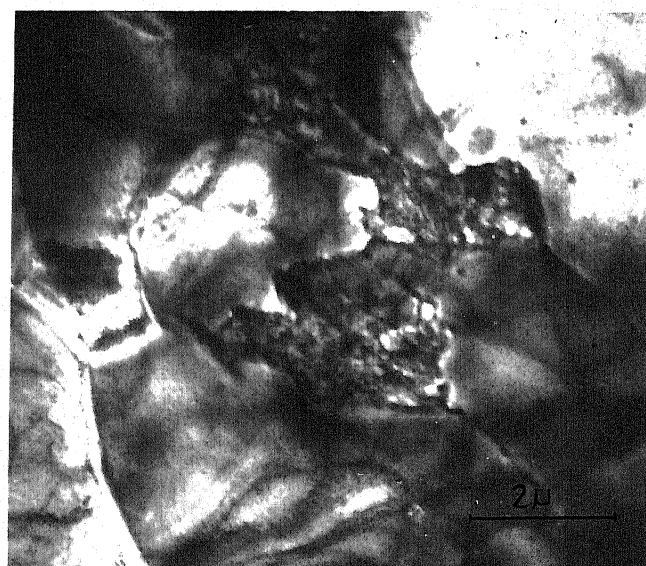
(a)



(b)



(c)



(d)

Fig. 4.50 Electron microstructures of recrystallised alloy A4
(a) WQ 810/Rex 650/10 sec (b) AC 810/Rex 650/10 sec
(c) WQ 750/Rex 650/10 sec (d) WQ 750/Rex 800/2 sec.

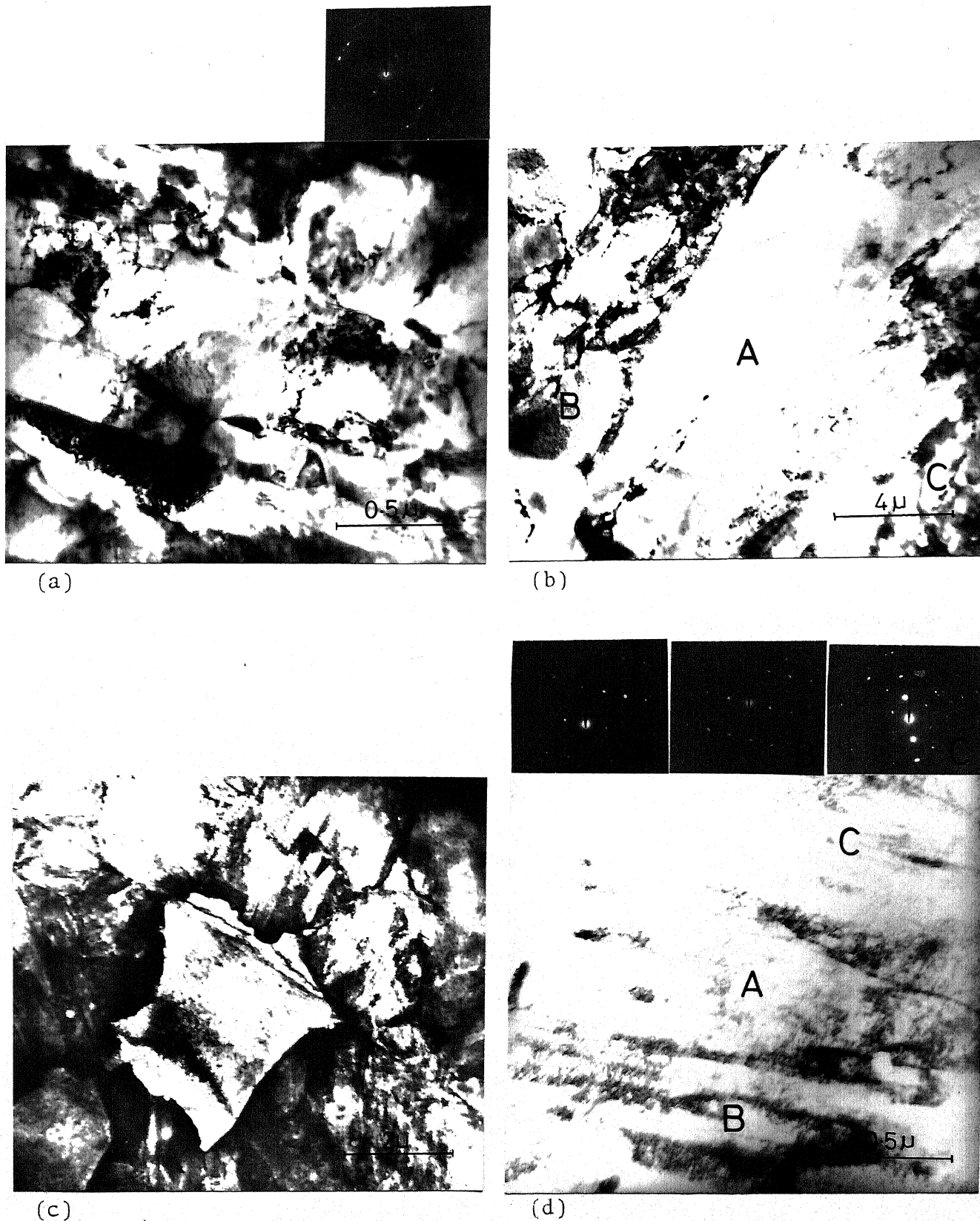
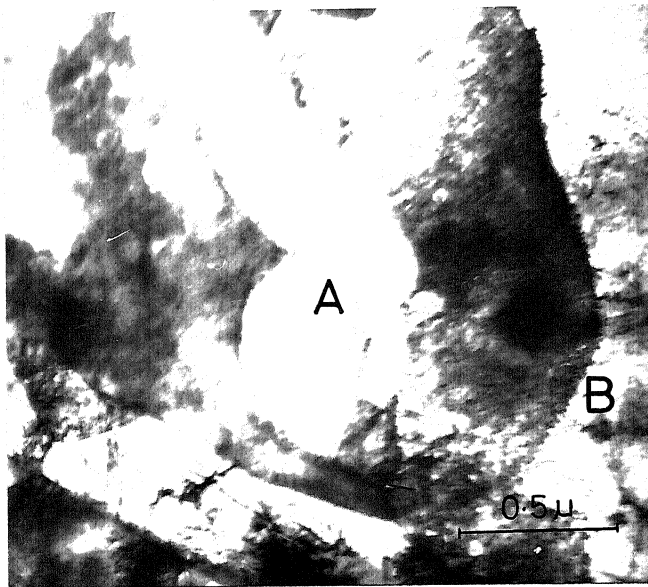
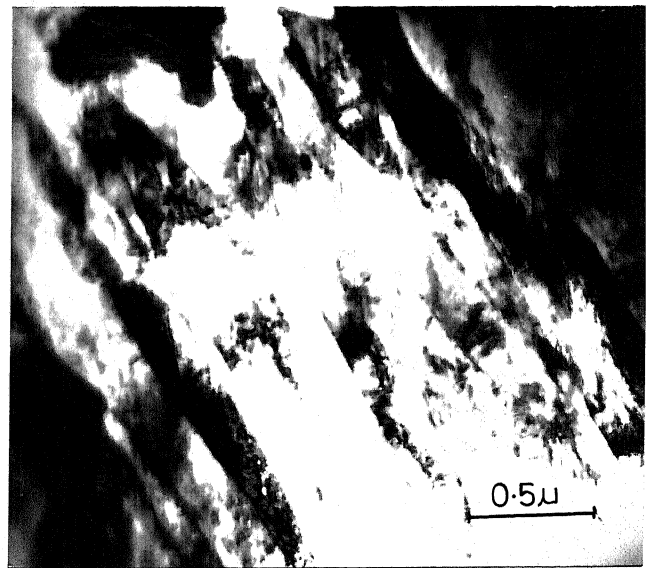


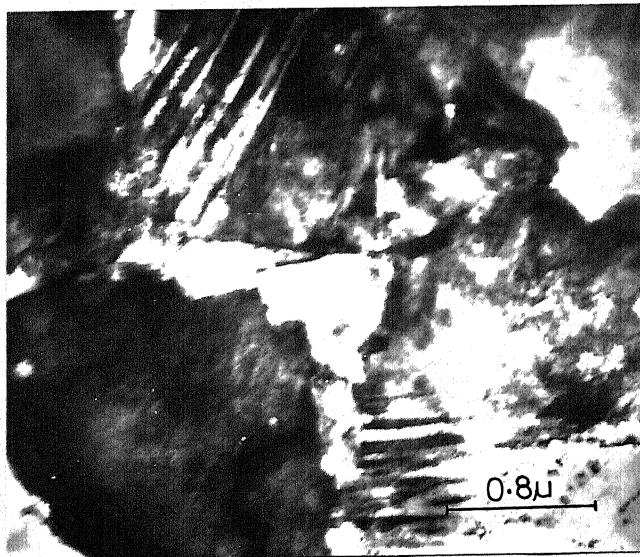
Fig. 4.51 Electron microstructures of recrystallised alloy A5/AC 750
 (a) Rex 650/10 sec (b) Rex 650/10 sec
 (c) Rex 800/5 sec (d) Rex 800/5 sec



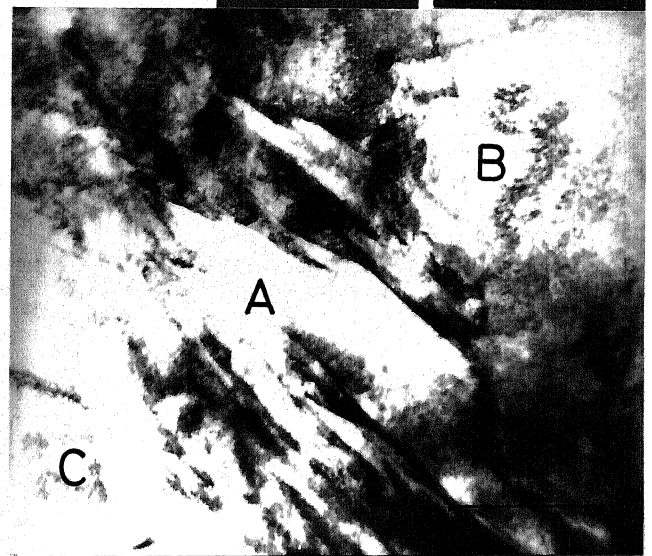
(a)



(b)

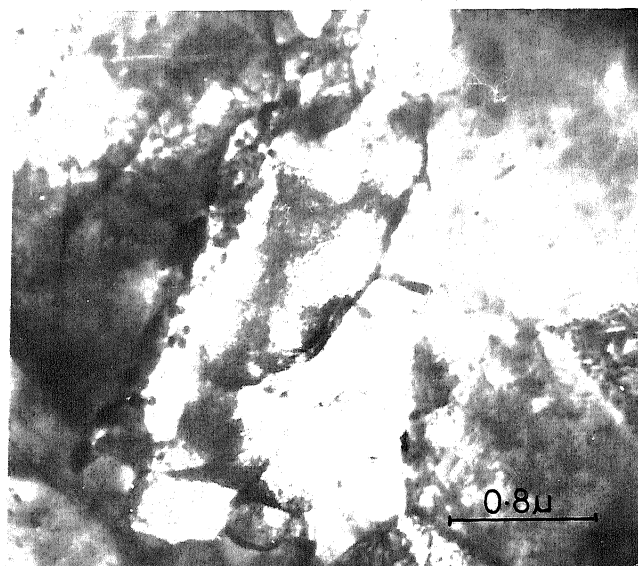


(c)

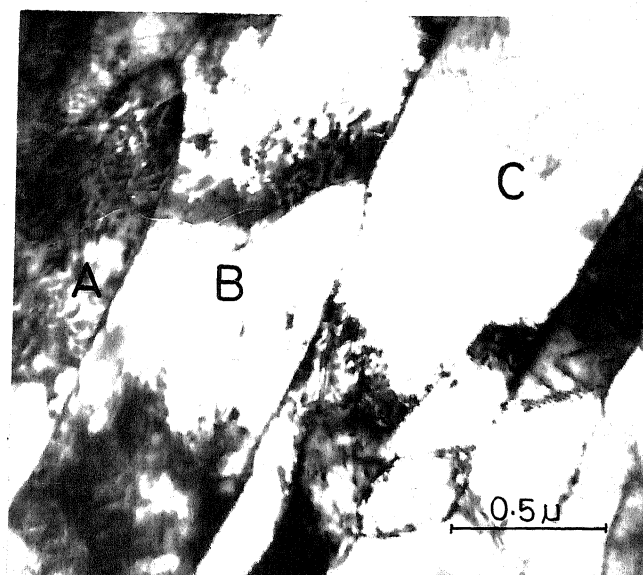


(d)

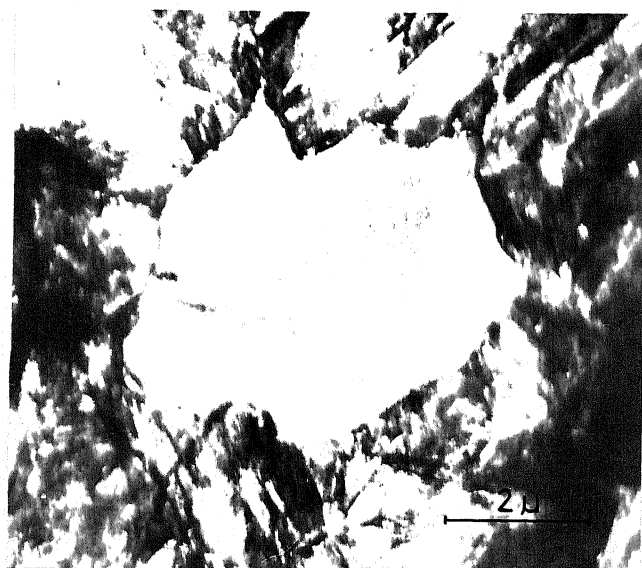
Fig. 4.52 Electron microstructures of recrystallised alloy
A5/AC 810
(a) Rex 650/10 sec (b) Rex 650/10 sec
(c) Rex 800/5 sec (d) Rex 800/5 sec



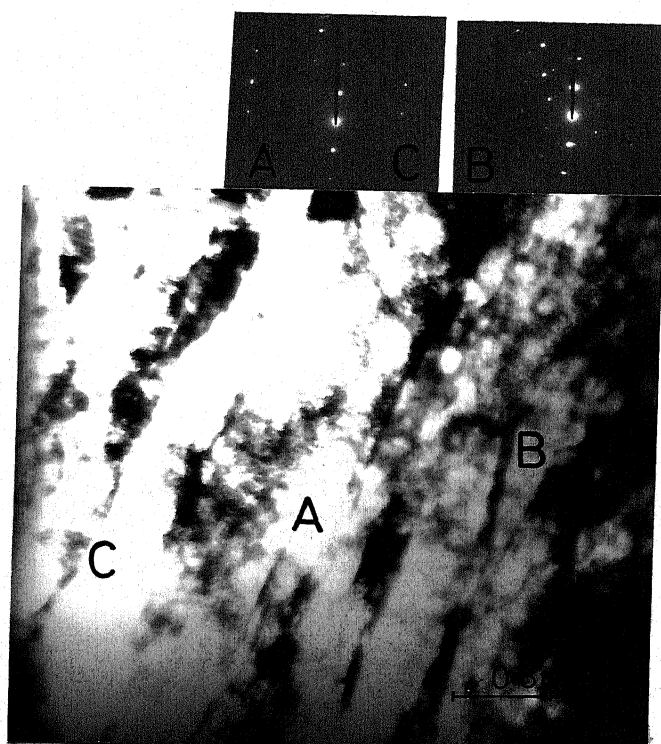
(a)



(b)

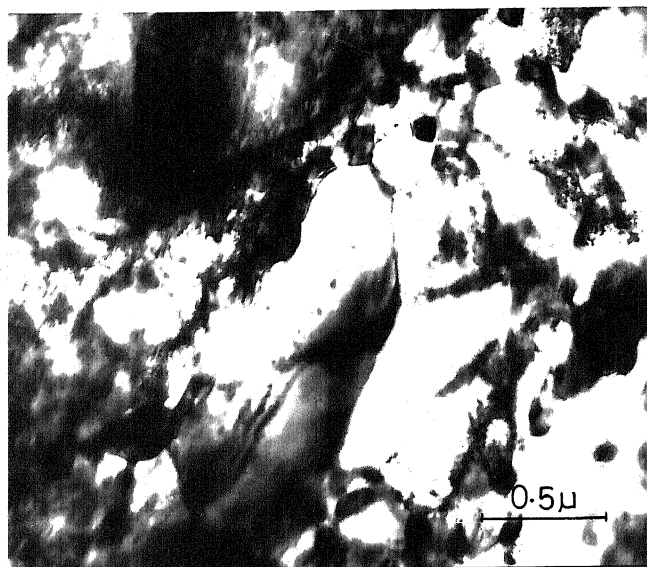
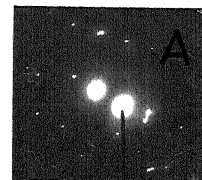


(c)

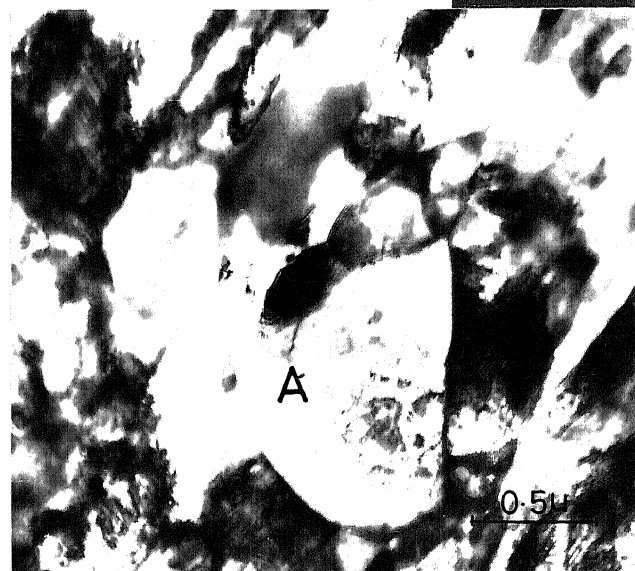


(d)

Fig. 4.53 Electron microstructures of recrystallised alloy
A5/WQ 750
(a) Rex 650/10 sec (b) Rex 650/10 sec
(c) Rex 800/5 sec (d) Rex 800/5 sec



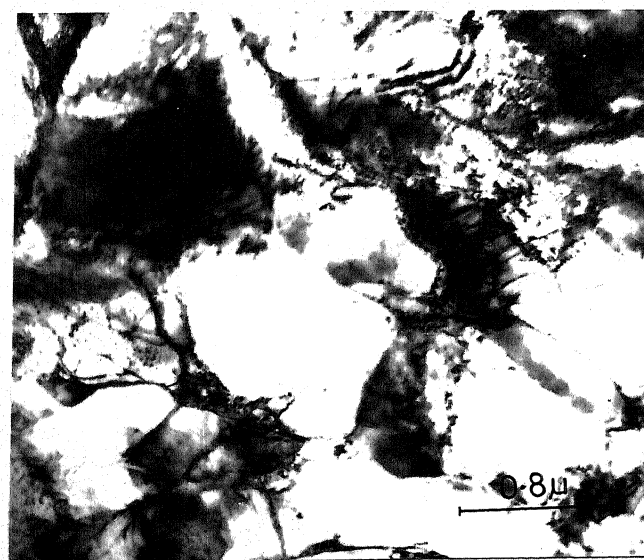
(a)



(b)



(c)



(d)

Fig. 4.54 Electron microstructures of recrystallised alloy
 A5/WQ 810
 (a) Rex 650/10 sec (b) Rex 650/10 sec
 (c) Rex 800/5 sec (d) Rex 800/5 sec

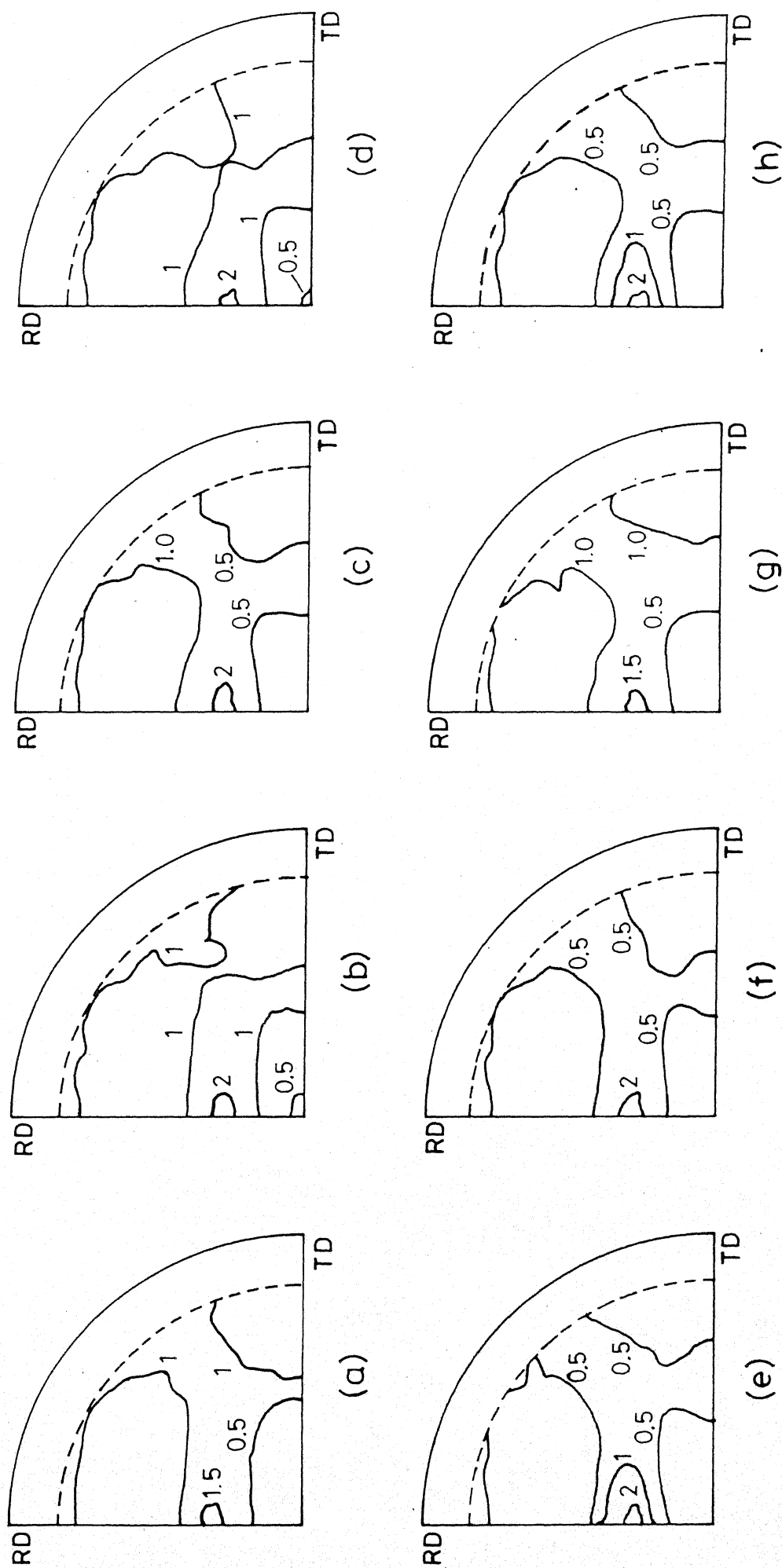


Fig. 4.55 (110) pole-figures of alloy A1
 AC750/WQ (a) Rex650 / 40s (b) Rex 800 /10s
 AC810 /WQ (c) Rex650 / 40s (d) Rex 800 /10s
 WQ750 /WQ (e) Rex650 / 40s (f) Rex 800 /10s
 WQ810 /WQ (g) Rex650 / 40s (h) Rex 800 /10s

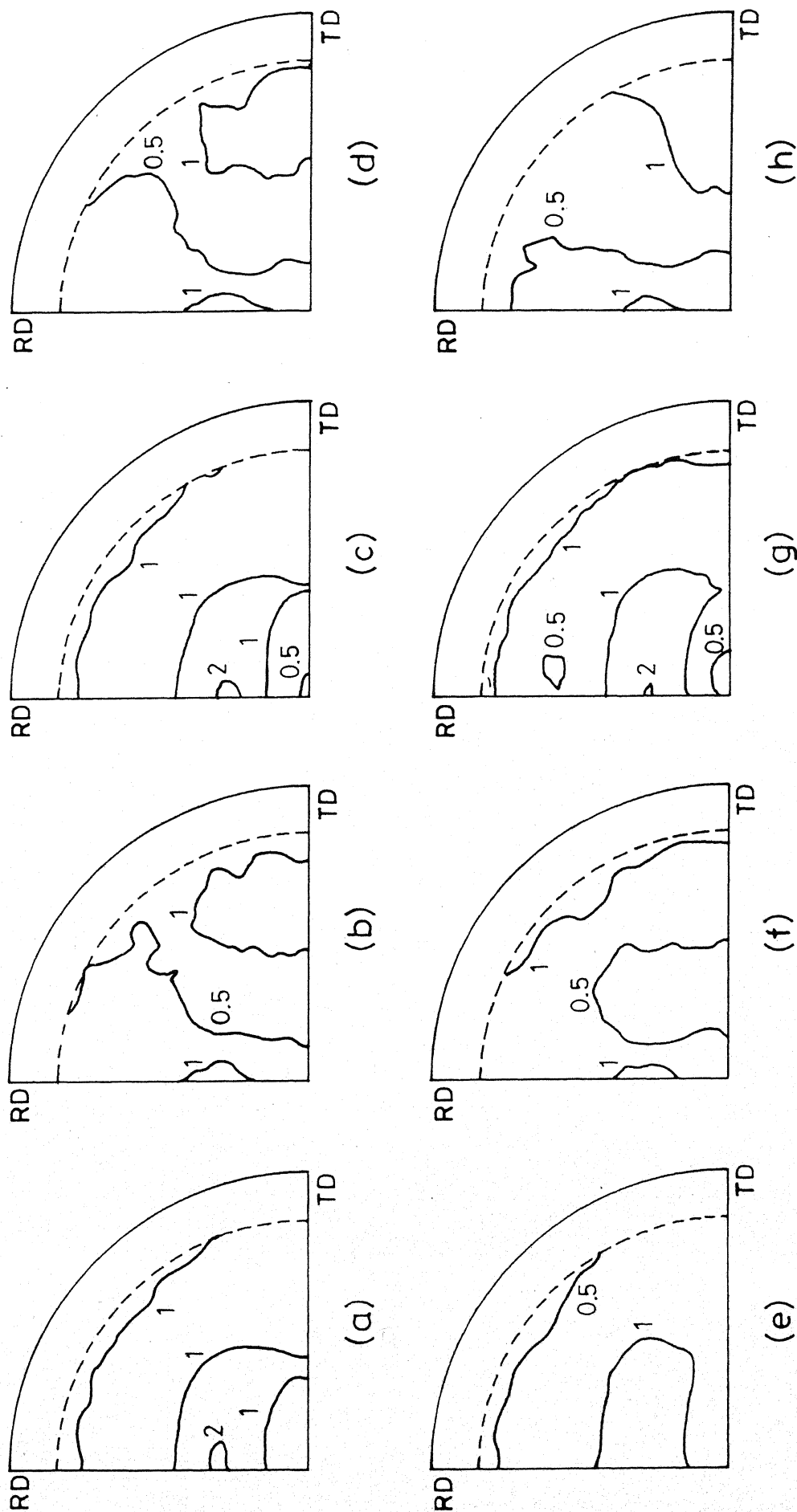


Fig. 4.56

(110) pole-figures of alloy A4

AC750/WQ (a) Rex 650/60s(b) Rex 800/10s
 AC810/WQ (c) Rex 650/60s(d) Rex 800/10s
 WQ750/WQ (e) Rex 650/60s(f) Rex 800/10s
 WQ810/WQ (g) Rex 650/60s(h) Rex 800/10s

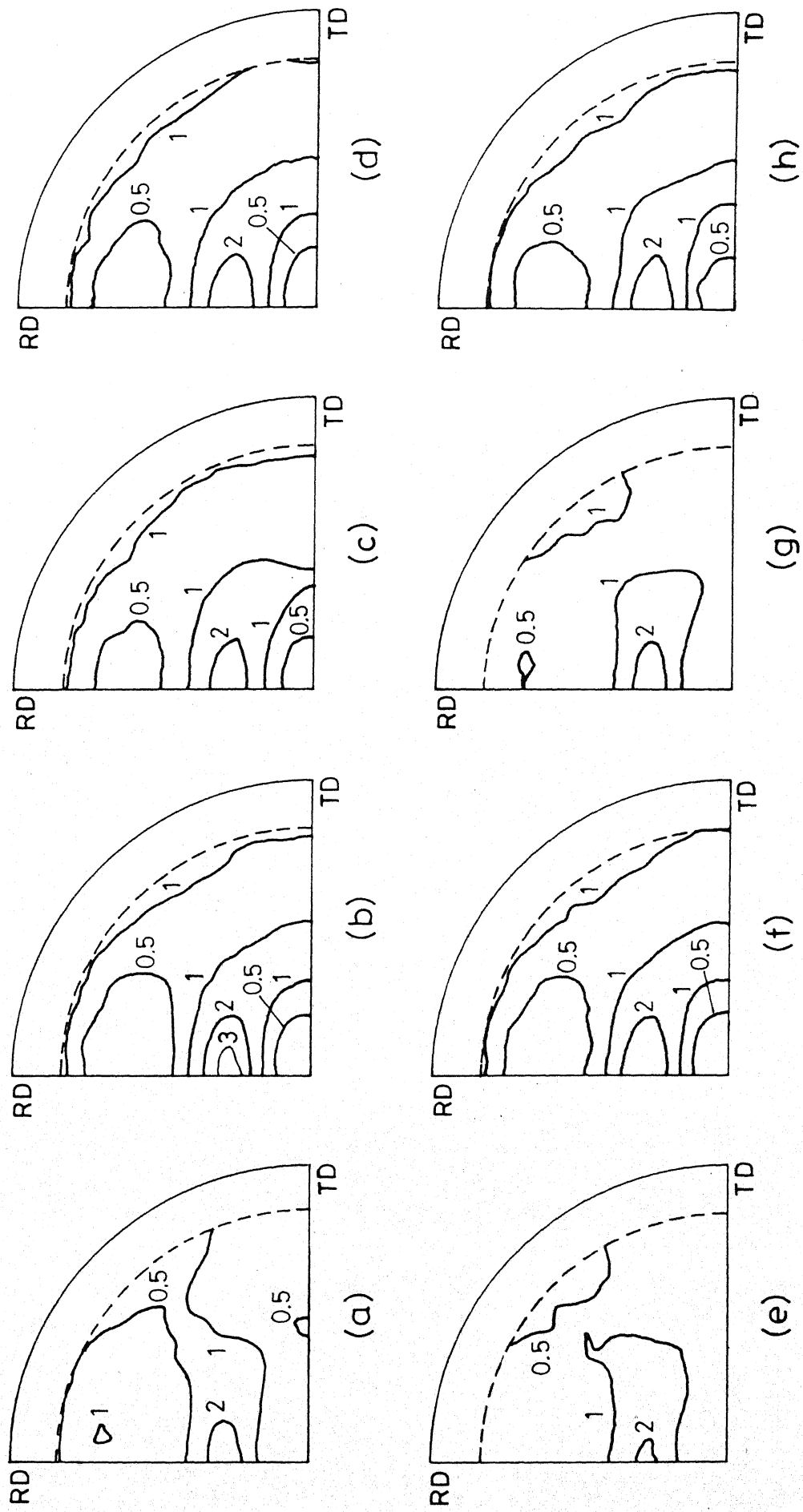


Fig. 4.57 (110) pole-figures of alloy A5
AC 750 / WQ (a) Rex 650 / 60s (b) Rex 800 / 10s
AC 810 / WQ (c) Rex 650 / 60s (d) Rex 800 / 10s
WQ 750 / WQ (e) Rex 650 / 60s (f) Rex 800 / 10s
WQ 810 / WQ (g) Rex 650 / 60s (h) Rex 800 / 10s

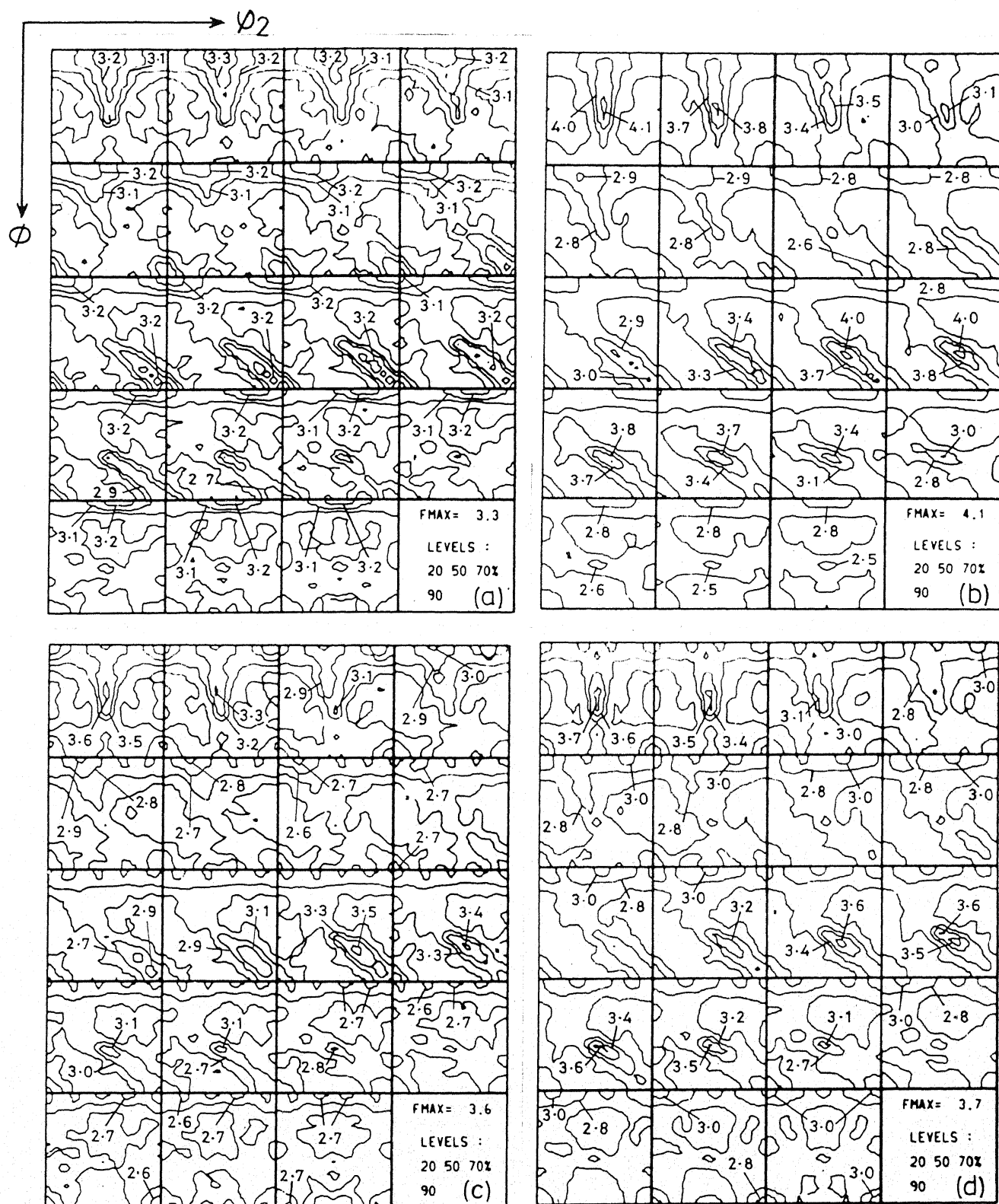


Fig.4.58 O.D.F's showing ϕ_1 sections for

- (a) A1/AC 750/WQ Rex 650/40 sec
- (b) A1/AC 750/WQ Rex 800/10 sec
- (c) A1/AC 810/WQ Rex 650/40 sec
- (d) A1/AC 810/WQ Rex 800/10 sec

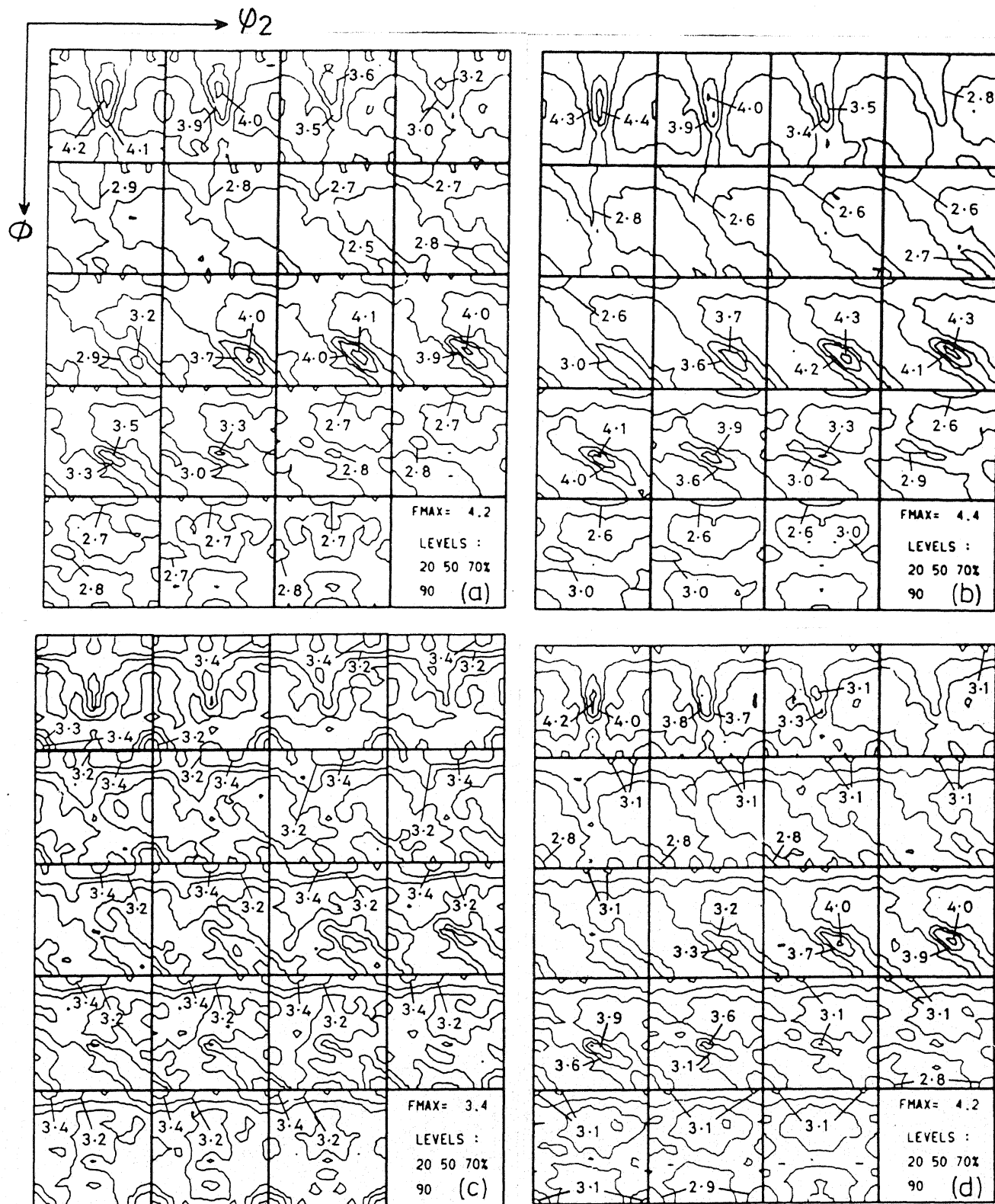


Fig.4.59 O.D.F.'s showing ϕ_1 sections for
 (a) A1/WQ 750/WQ Rex 650/40 sec
 (b) A1/WQ 750/WQ Rex 800/10 sec
 (c) A1/WQ 810/WQ Rex 650/40 sec
 (d) A1/WQ 810/WQ Rex 800/10 sec

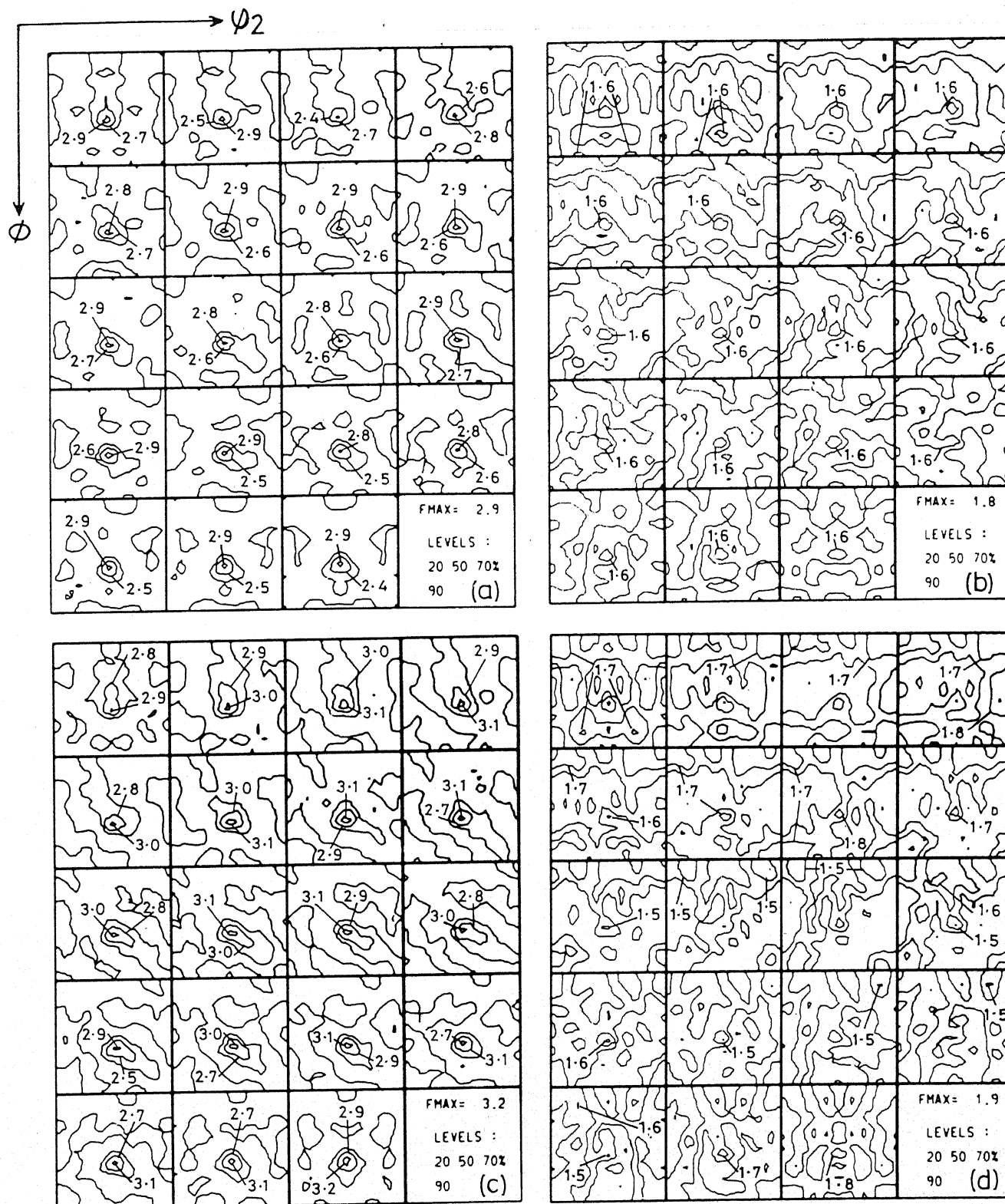


Fig.4-60 O.D.F's section ϕ_1 sections for

- (a) A4/AC 750/WQ Rex 650/60 sec
- (b) A4/AC 750/WQ Rex 800/10 sec
- (c) A4/AC 810/WQ Rex 650/60 sec
- (d) A4/AC 810/WQ Rex 800/10 sec

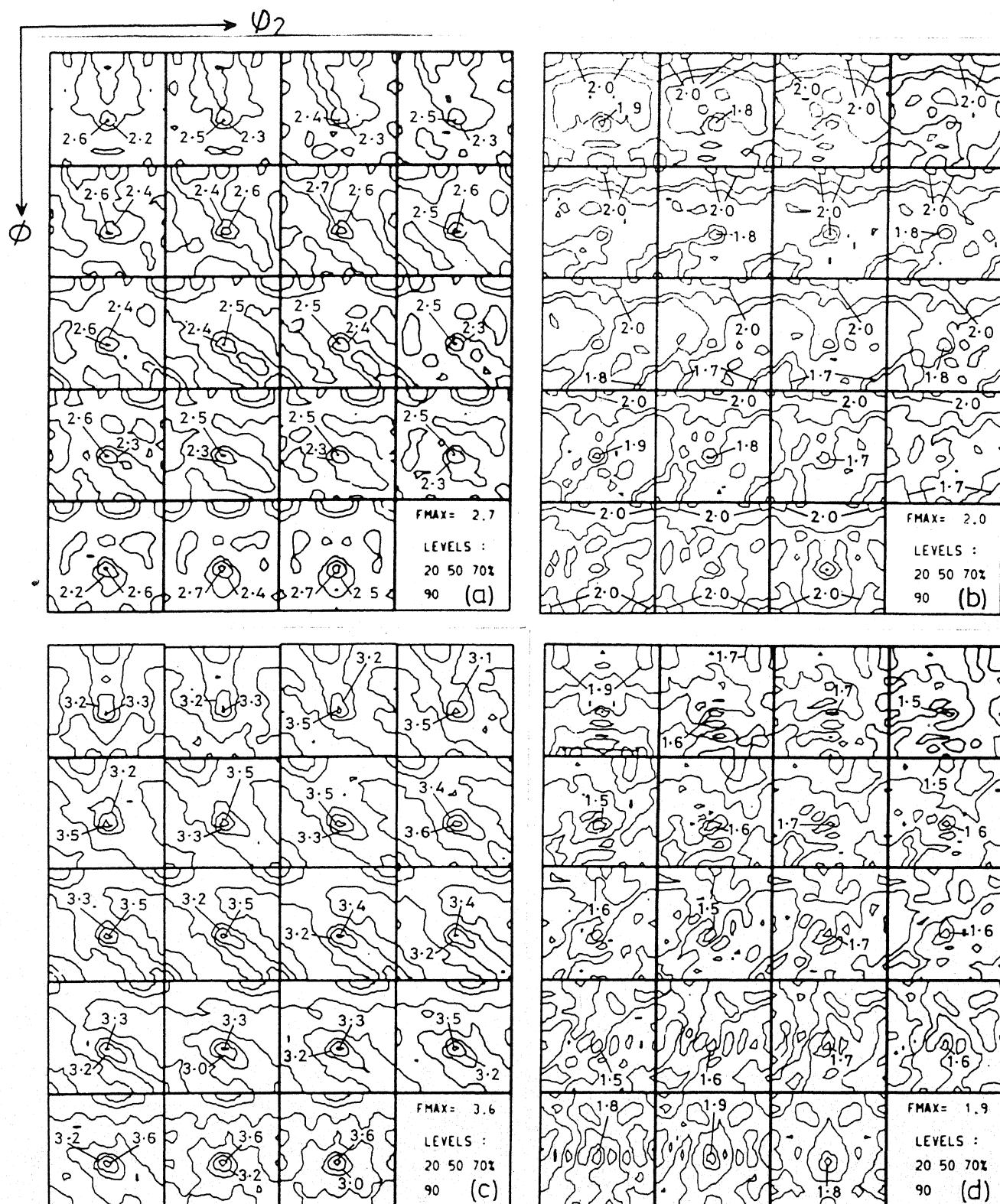


Fig.4.61 O.D.F.'s showing ϕ_1 sections for

- (a) A4/WQ 750/WQ Rex 650/60 sec
- (b) A4/WQ 750/WQ Rex 800/10 sec
- (c) A4/WQ 810/WQ Rex 650/60 sec
- (d) A4/WQ 810/WQ Rex 800/10 sec

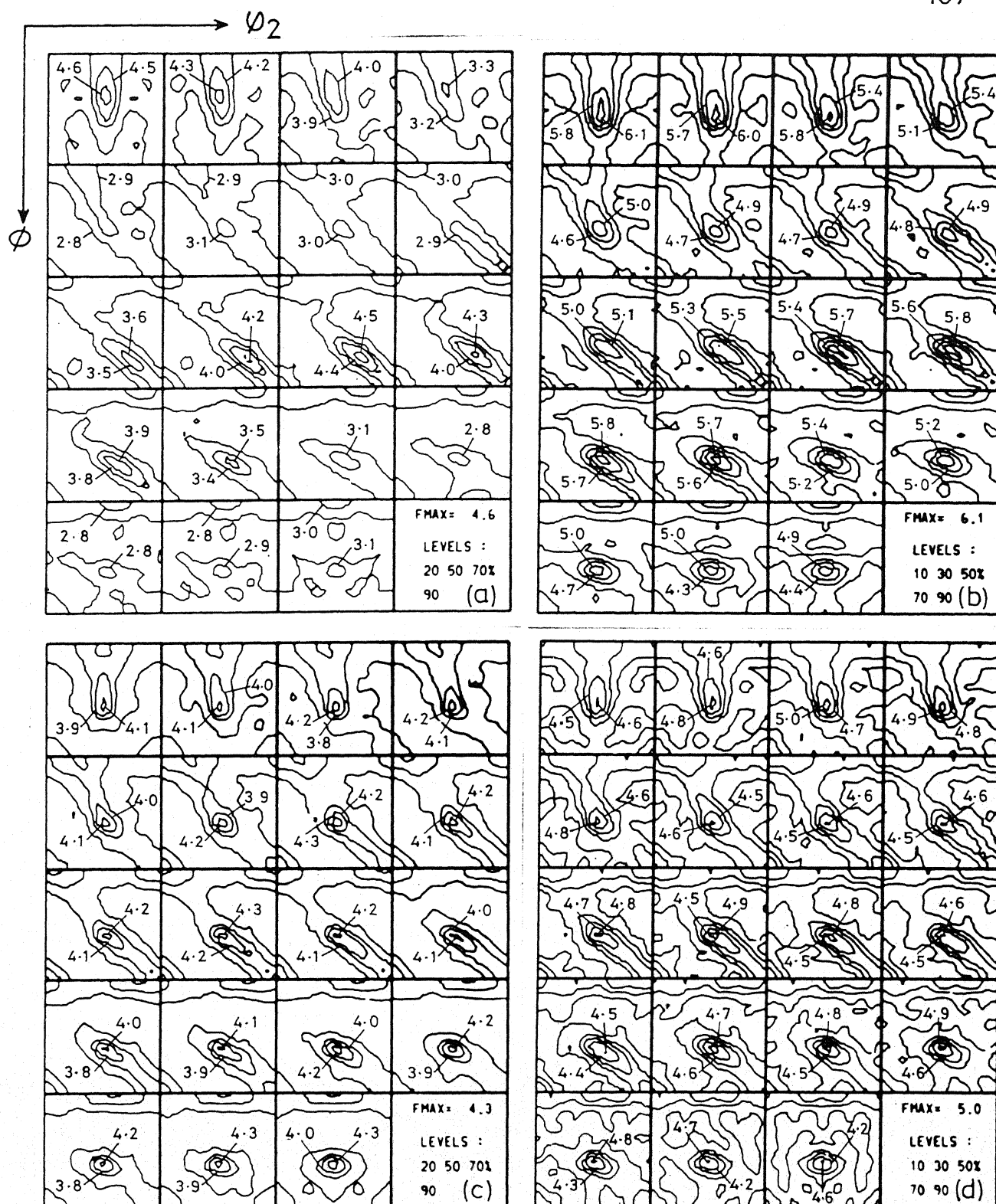


Fig.4.62 O.D.F.'s showing ϕ_1 sections for

- (a) A5 / AC 750 / WQ Rex 650/60 sec
- (b) A5 / AC 750 / WQ Rex 800/10 sec
- (c) A5 / AC 810 / WQ Rex 650/60 sec
- (d) A5 / AC 810 / WQ Rex 800/10 sec

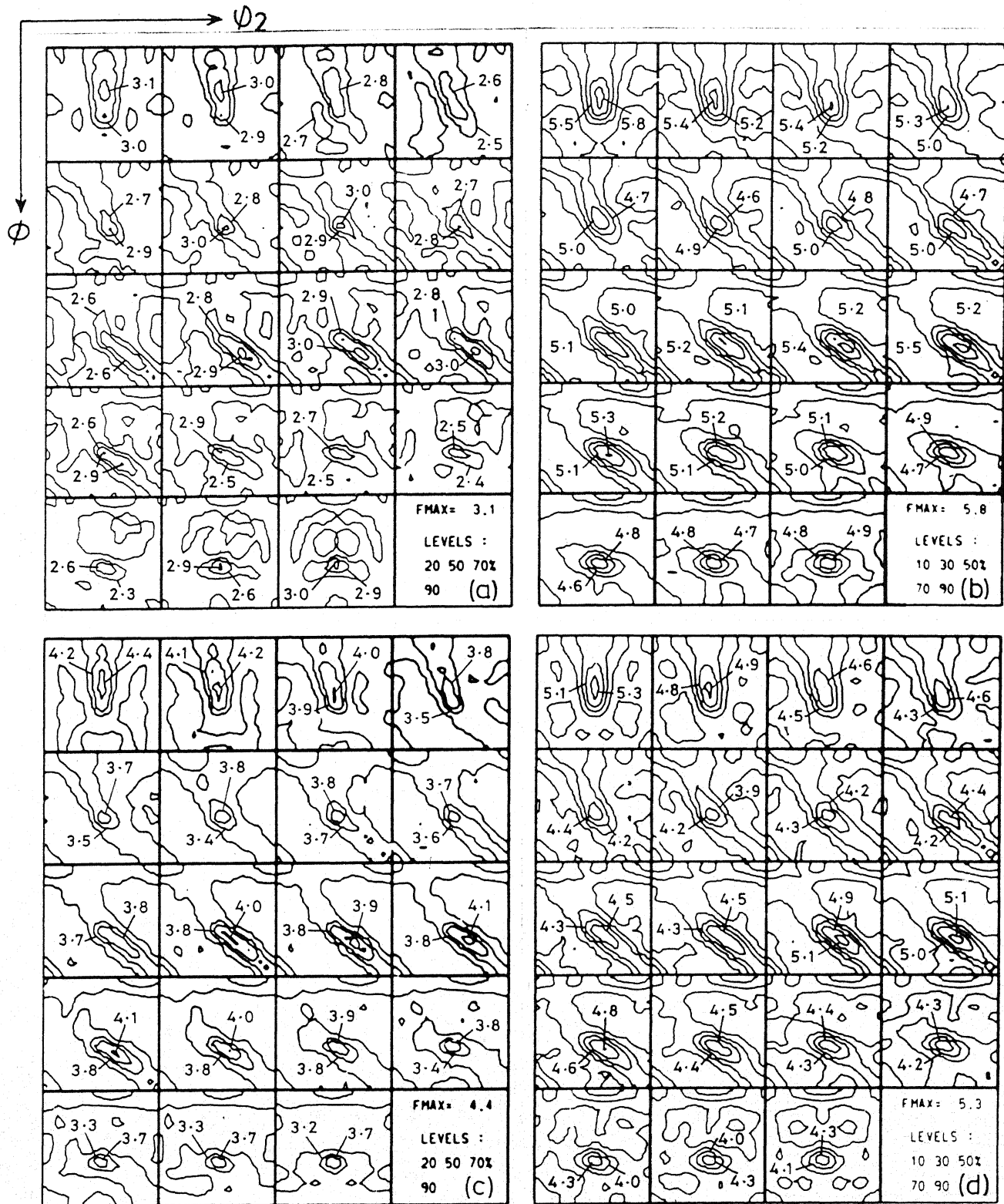


Fig.4.63 O.D.F's showing ϕ_1 sections for
 (a) A5/WQ 750/WQ Rex 650/60 sec
 (b) A5/WQ 750/WQ Rex 800/10 sec
 (c) A5/WQ 810/WQ Rex 650/60 sec
 (d) A5/WQ 810/WQ Rex 800/10 sec

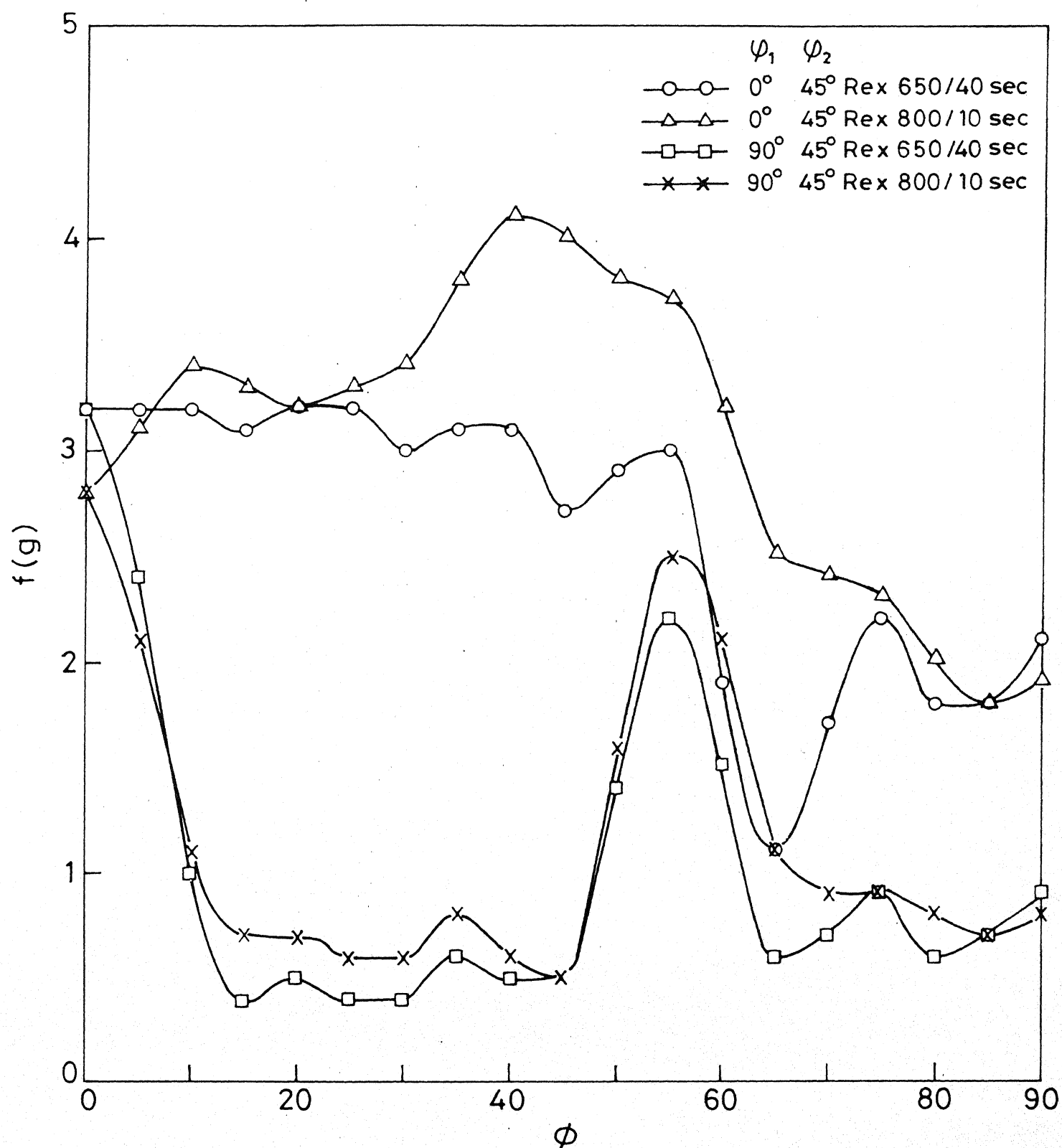


Fig.4.64 Variation of $f(g)$ with ϕ along different ϕ_1/ϕ_2 lines for A1/AC 750/WQ after recrystallisation.

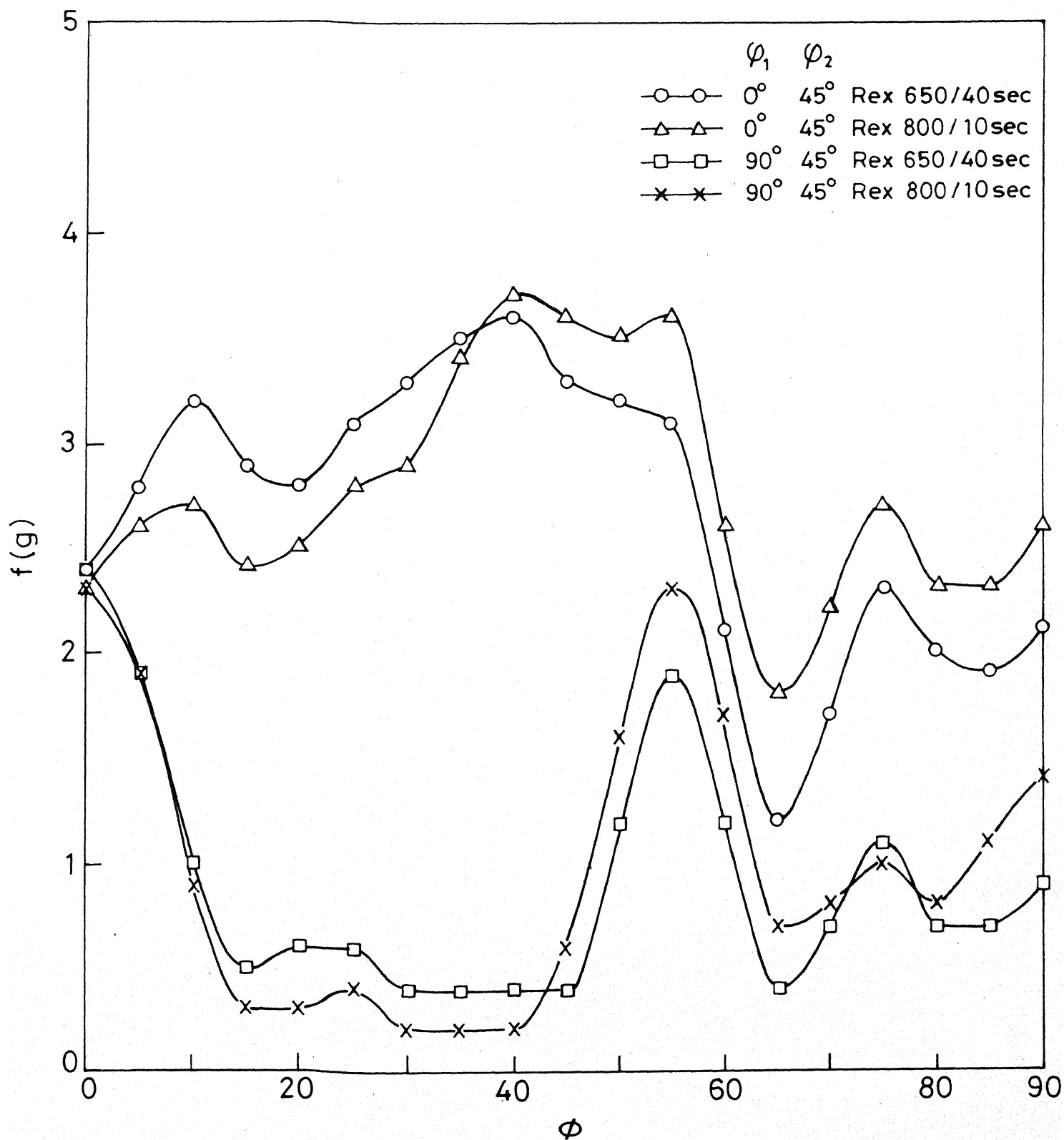


Fig.4.65 Variation of $f(g)$ with ϕ along different ϕ_1/ϕ_2 lines for A1/AC810/WQ after recrystallisation.

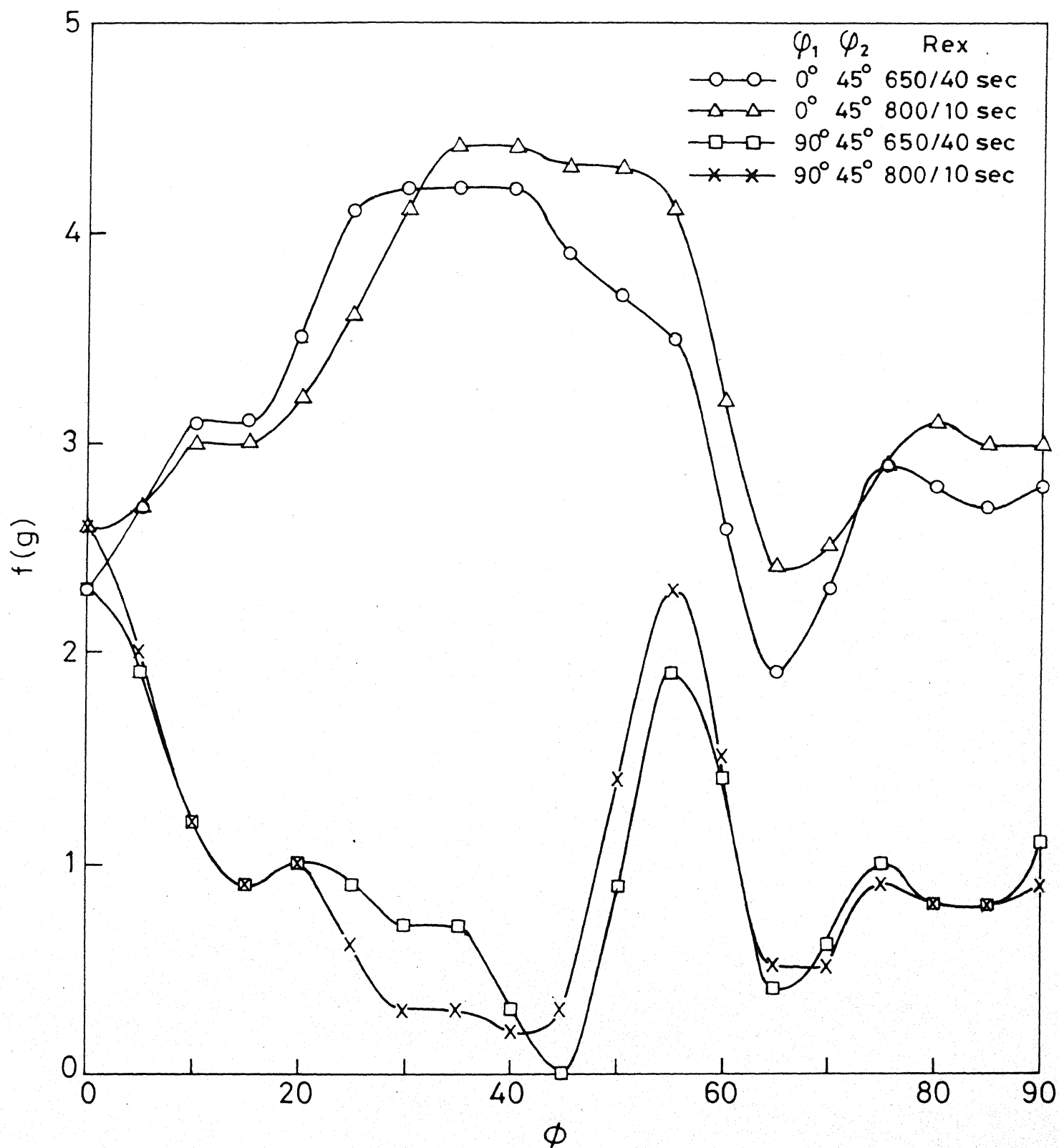


Fig.4.66 Variation of $f(g)$ with ϕ along different ϕ_1/ϕ_2 lines for A1/WQ 750/WQ after recrystallisation.

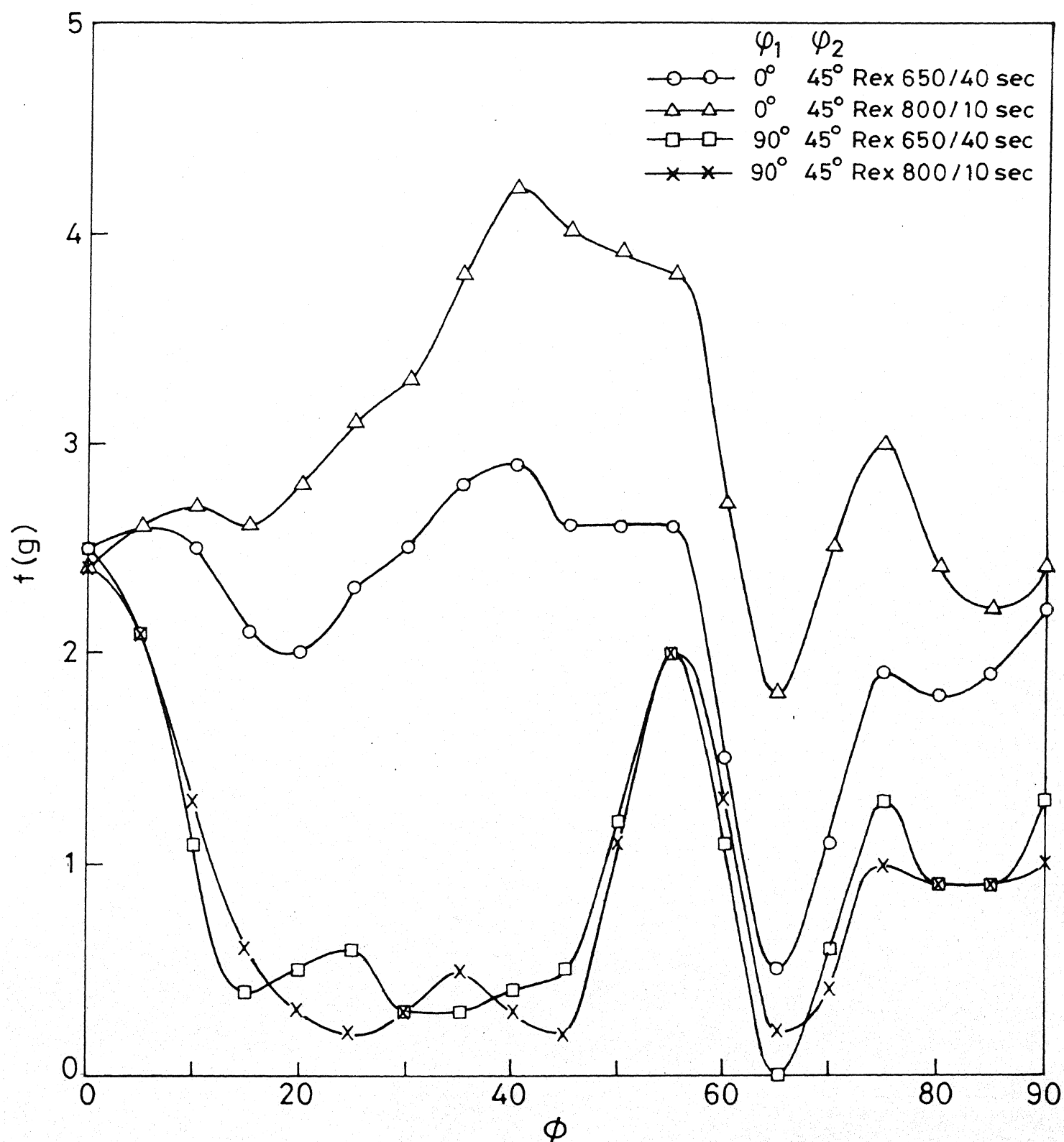


Fig.4.67 Variation of $f(g)$ with ϕ along different ϕ_1/ϕ_2 lines for A1/WQ 810/WQ after recrystallisation.

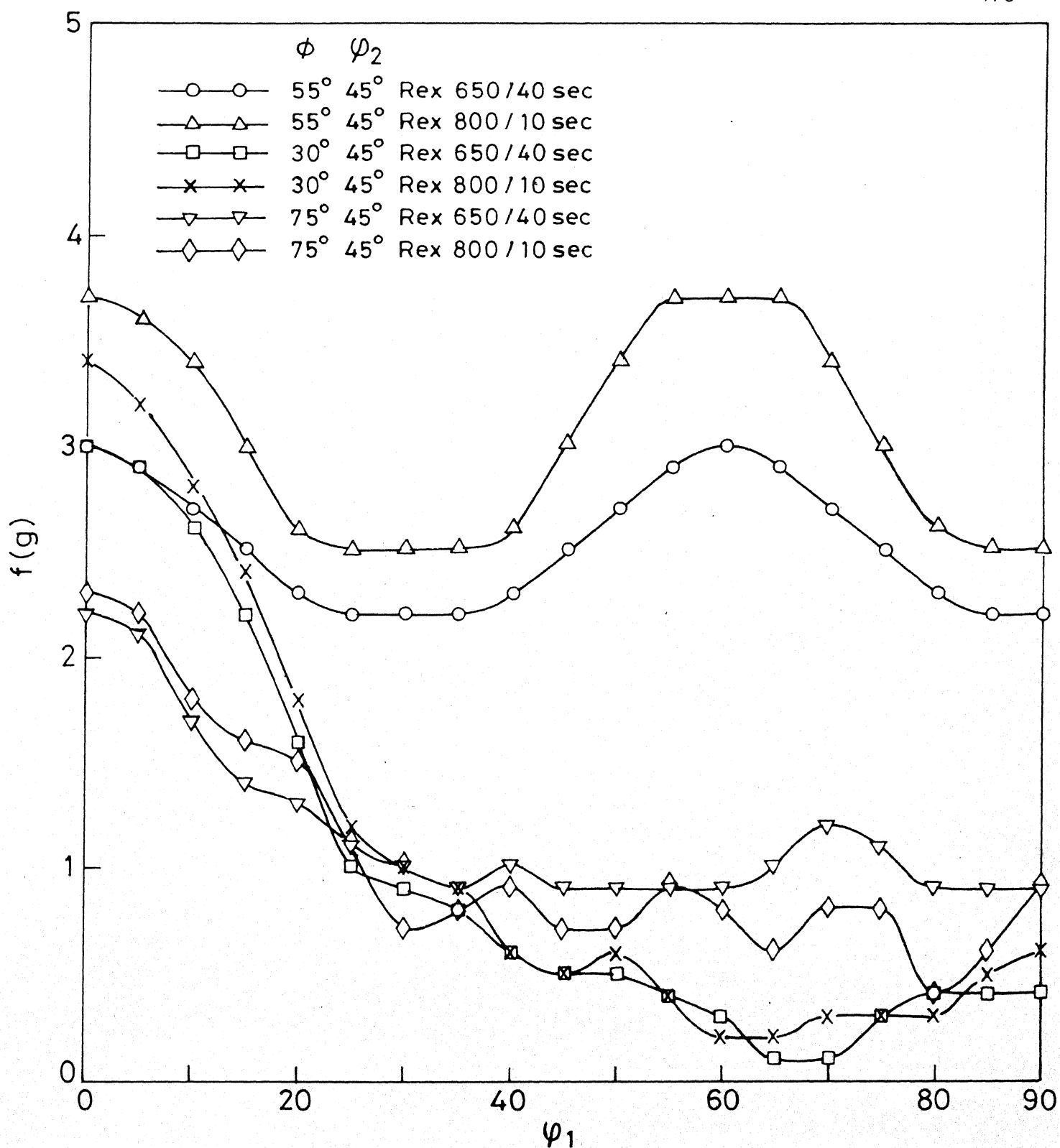


Fig.4.68 Variation of $f(g)$ with ϕ_1 along different ϕ/ϕ_2 lines for A1/AC750/WQ after recrystallisation.

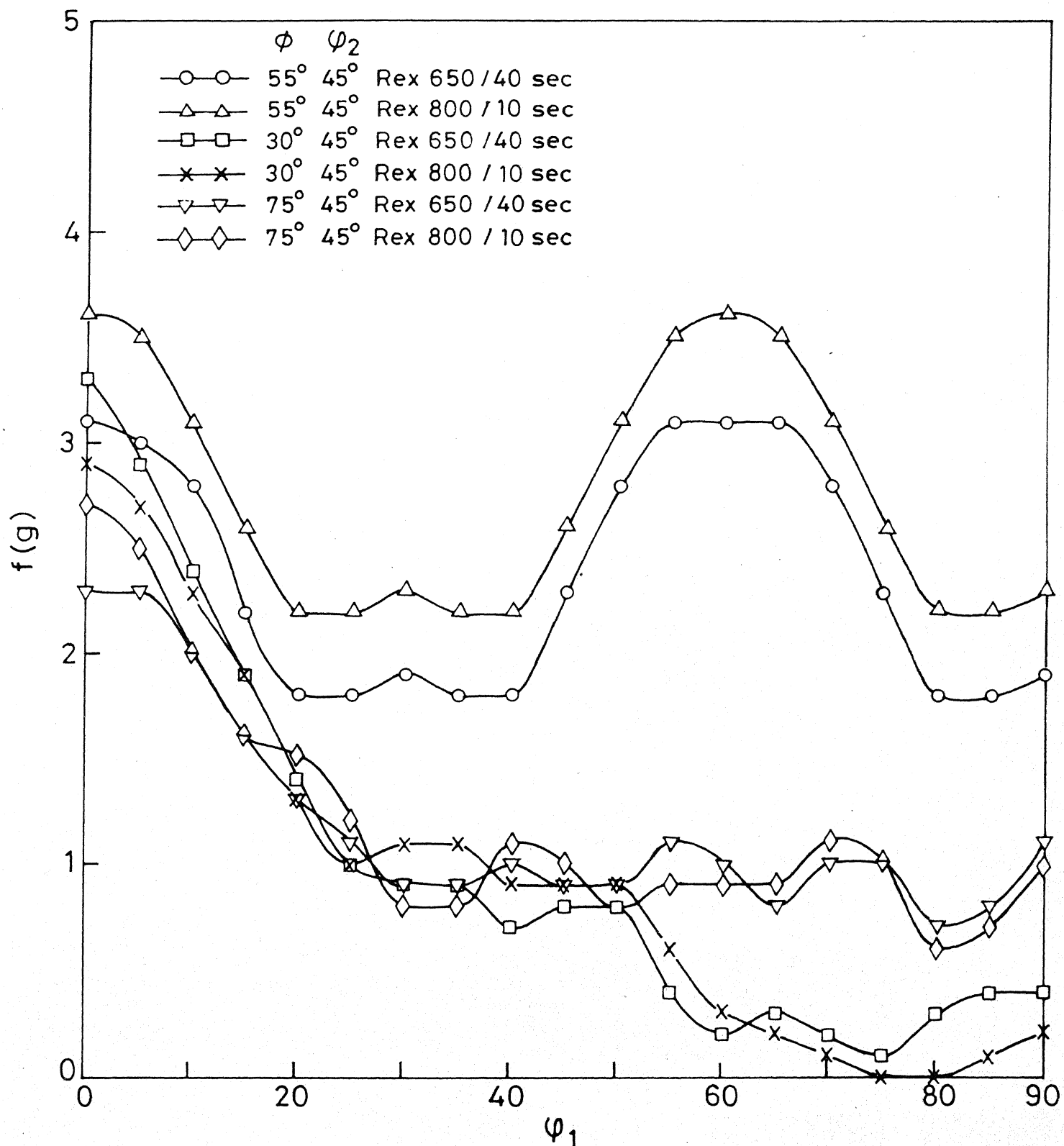


Fig. 4.69 Variation of $f(g)$ with ϕ_1 along different ϕ/ϕ_2 lines for A1/AC 810/WQ after recrystallisation.

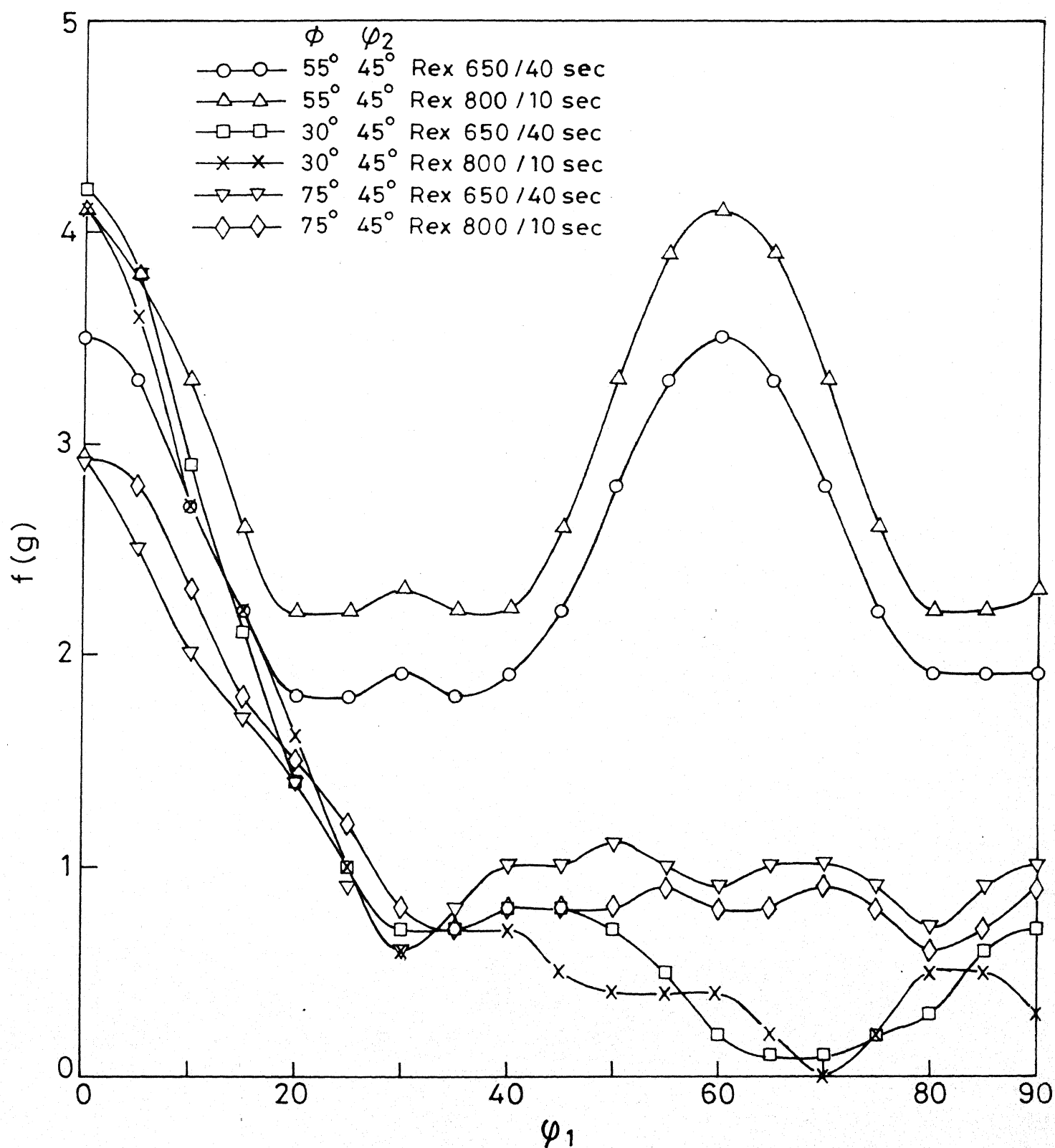


Fig.4.70 Variation of $f(g)$ with ϕ_1 along different ϕ/ϕ_2 lines for A1/WQ750/WQ after recrystallisation.

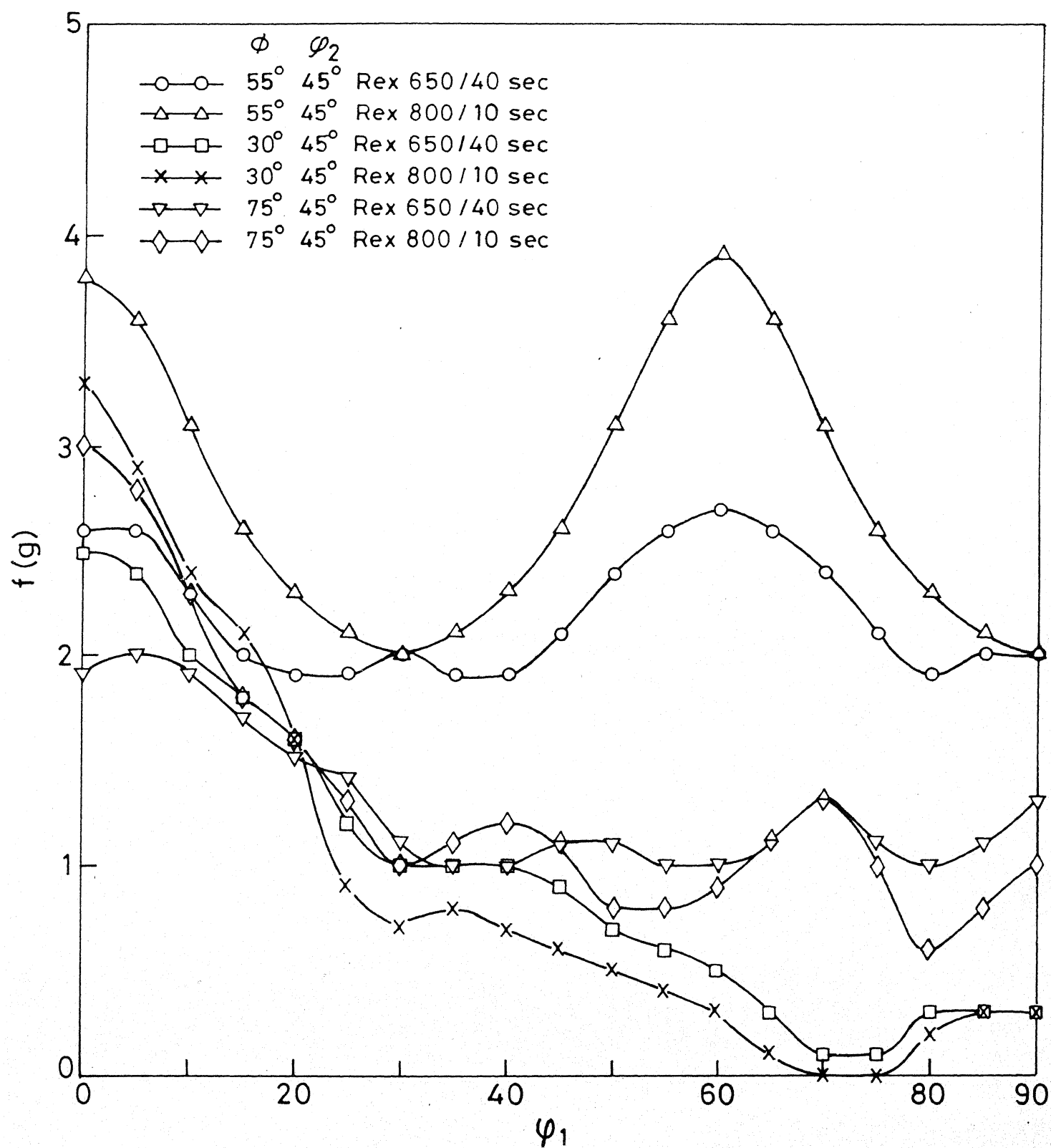


Fig.4.71 Variation of $f(g)$ with ϕ_1 along different ϕ/ϕ_2 lines for A1/WQ 810/WQ after recrystallisation.

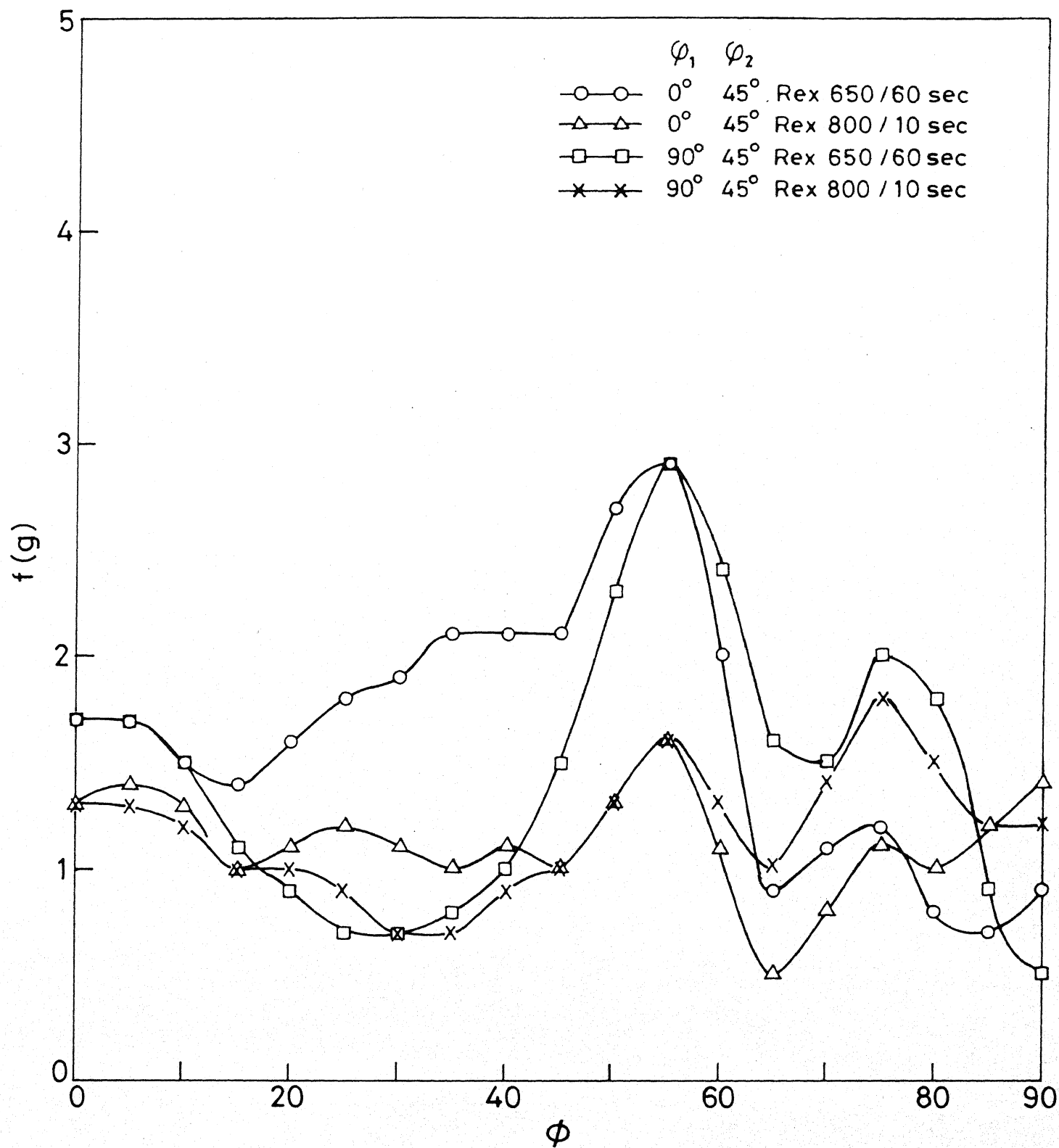


Fig.4.72 Variation of $f(g)$ with ϕ along different ϕ_1/ϕ_2 lines for A4/AC750/WQ after recrystallisation.

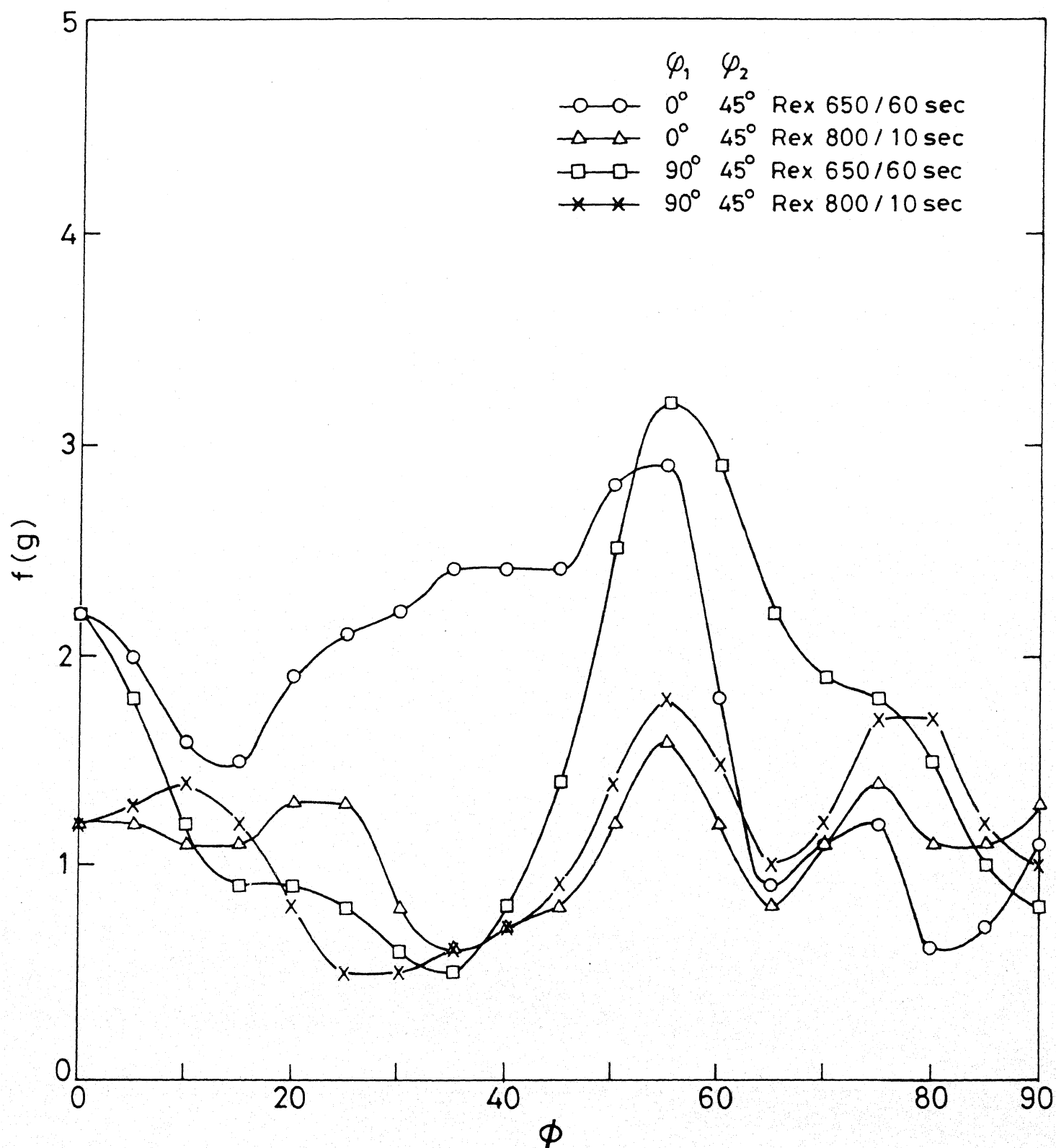


Fig.4.73 Variation of $f(g)$ with ϕ along different ϕ_1/ϕ_2 lines for A4/AC 810/WQ after recrystallisation.

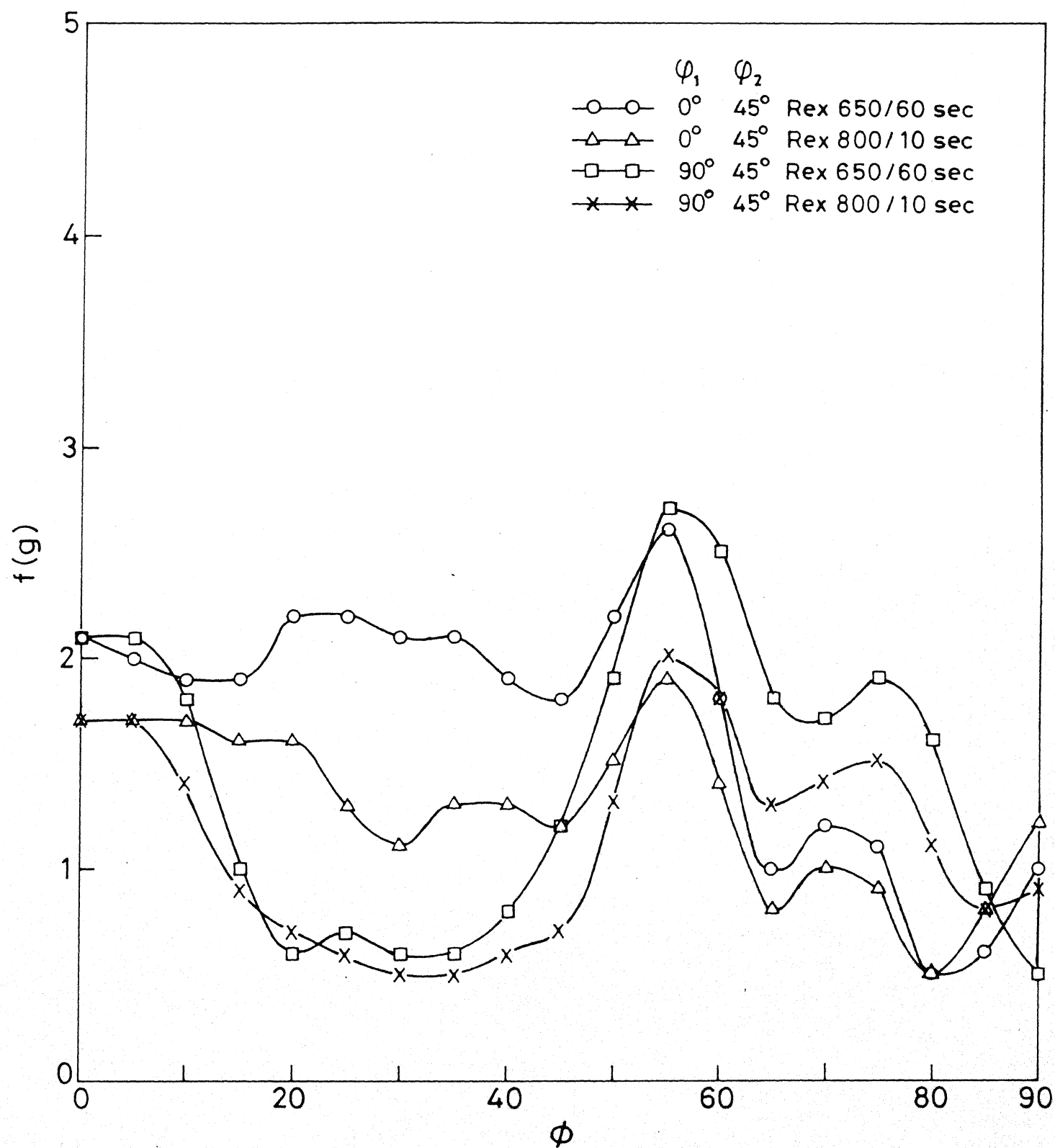


Fig.4.74 Variation of $f(g)$ with ϕ along different ϕ_1/ϕ_2 lines for A4/WQ 750/WQ after recrystallisation.

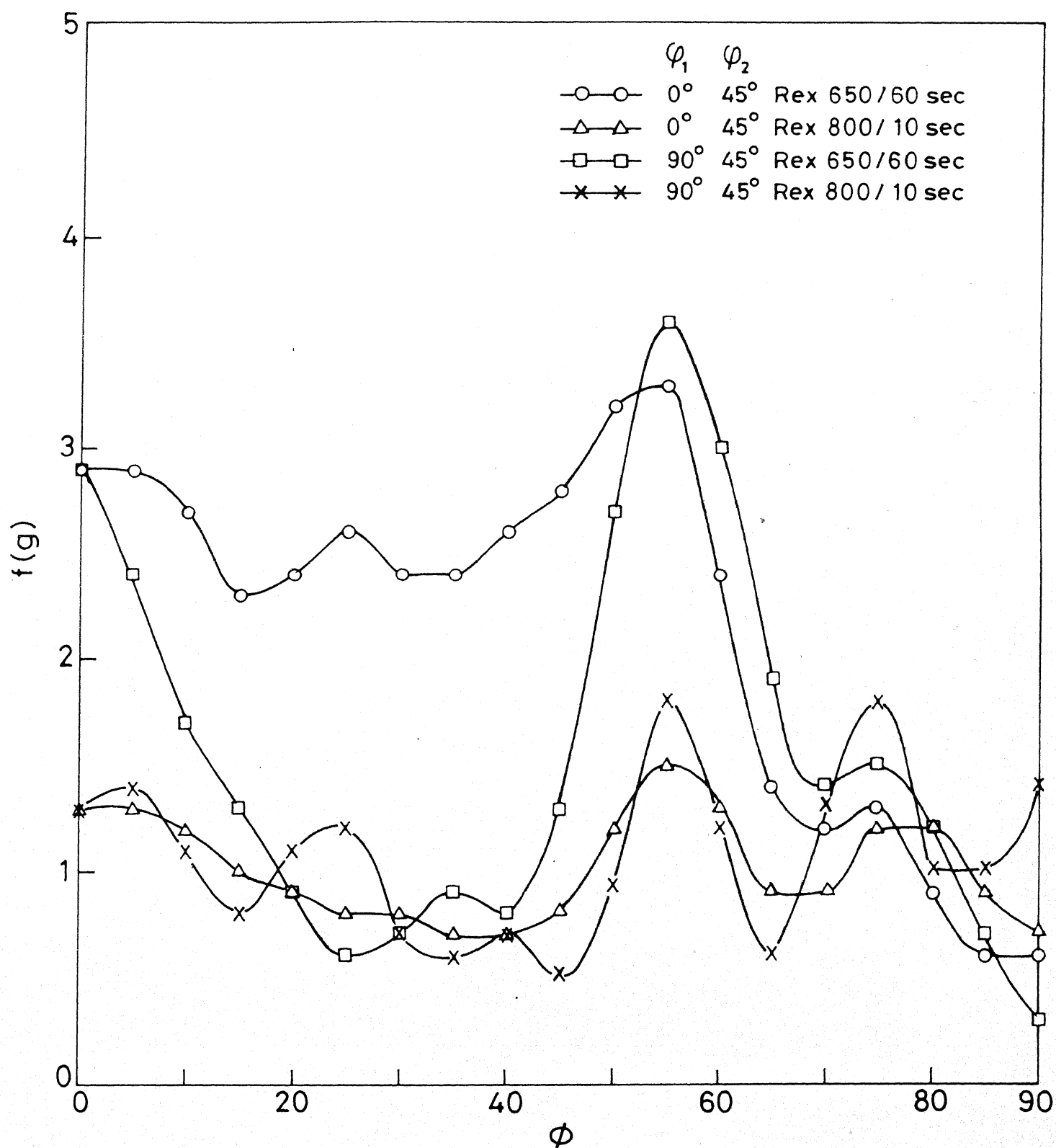


Fig. 4.75 Variation of $f(g)$ with ϕ along different ϕ_1/ϕ_2 lines for A4/WQ 810/WQ after recrystallisation.

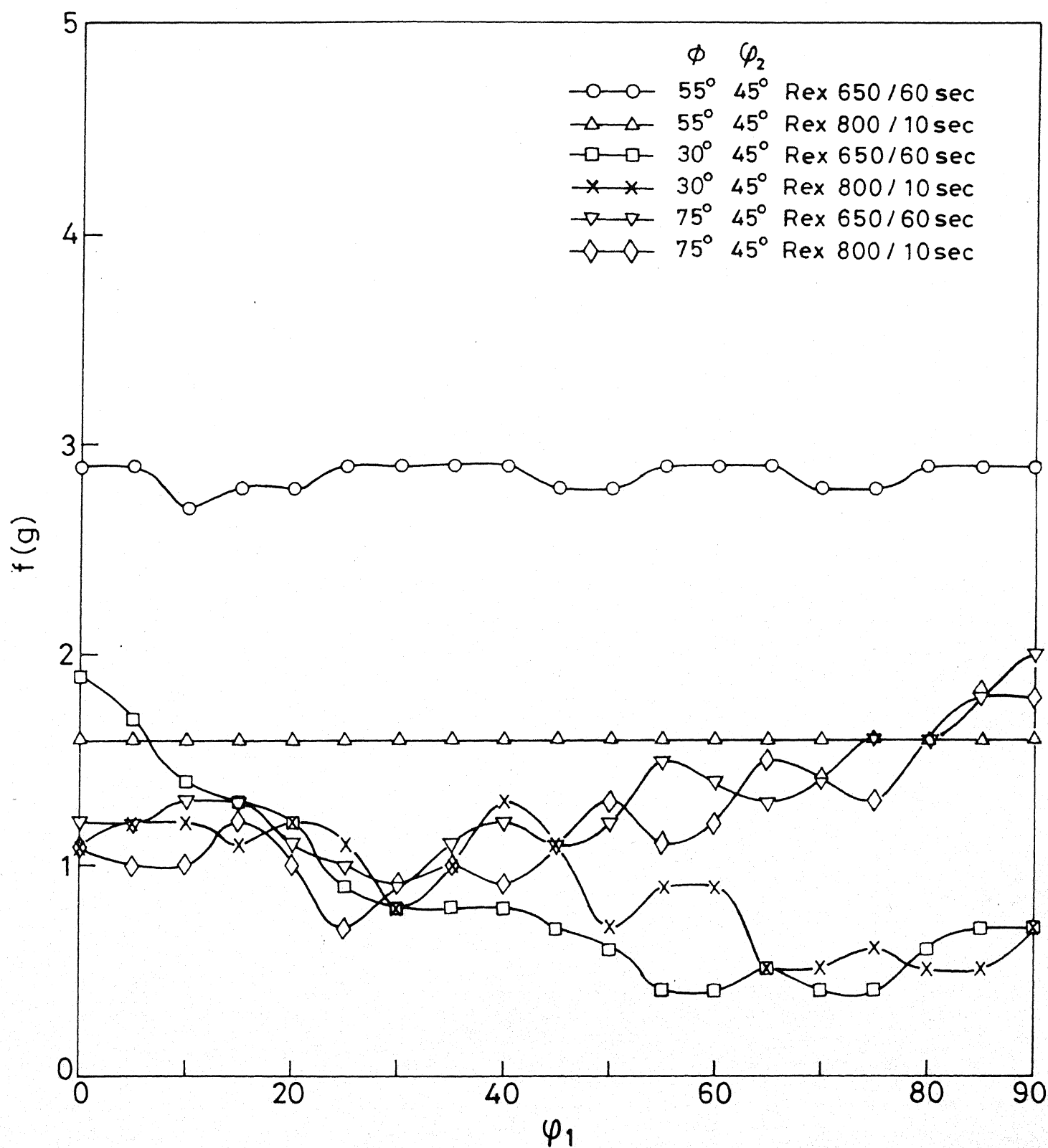


Fig.4.76 Variation of $f(g)$ with ϕ_1 along different ϕ/ϕ_2 lines for A4/AC750/WQ after recrystallisation.

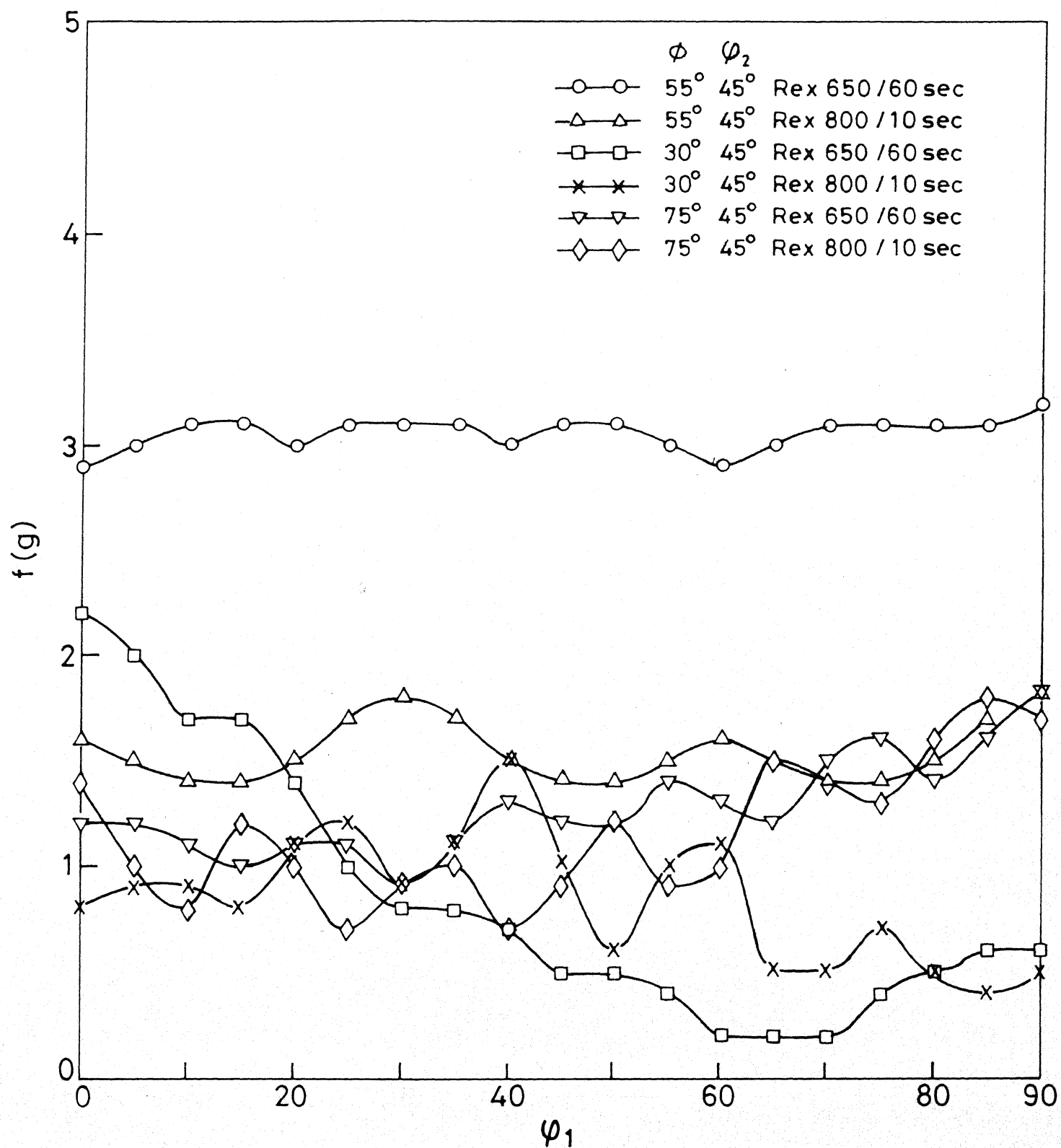


Fig.4.77 Variation of $f(g)$ with ϕ_1 along different ϕ/ϕ_2 lines for A4/AC810/WQ after recrystallisation.

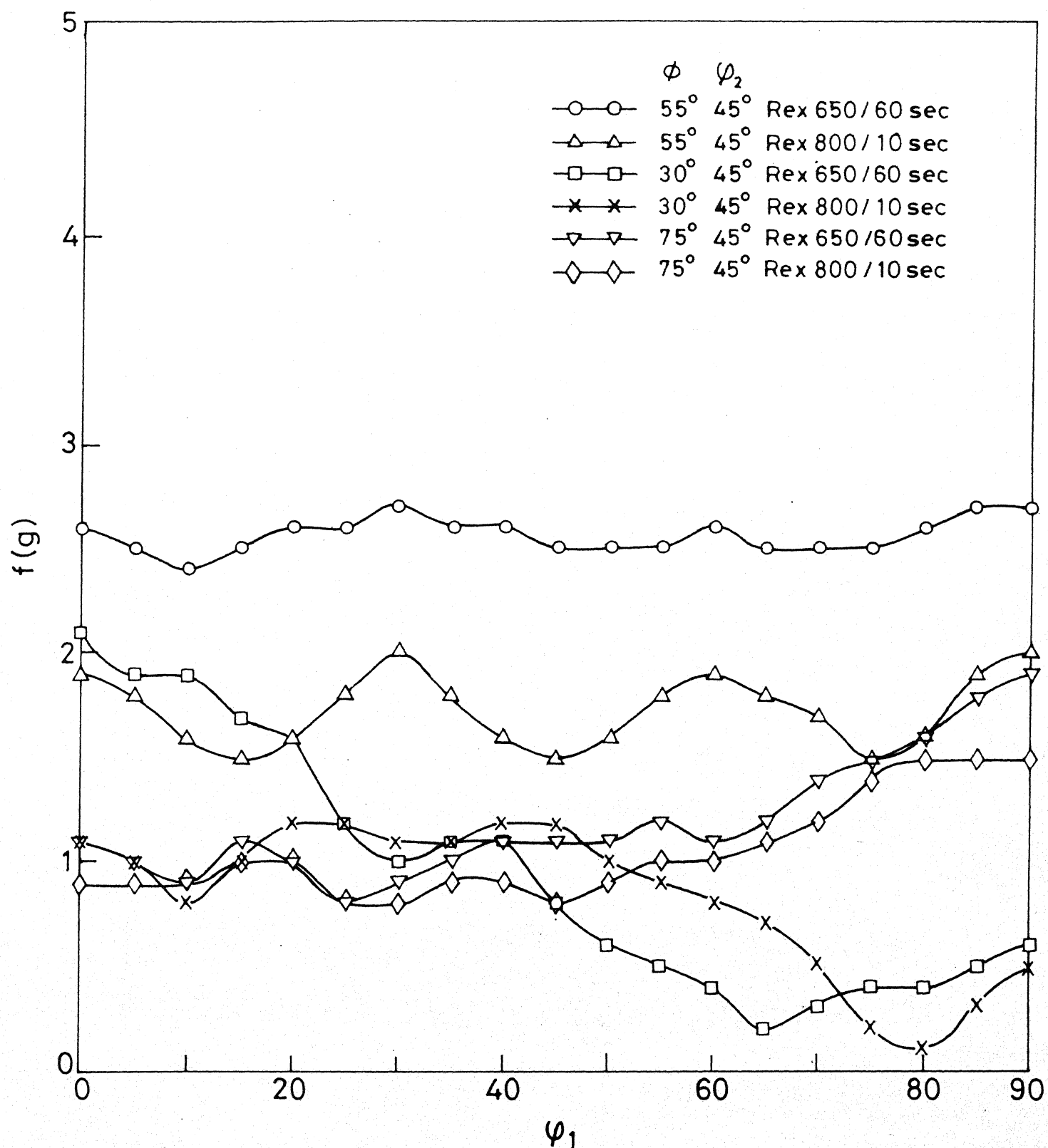


Fig.4.78 Variation of $f(g)$ with ϕ_1 along different ϕ/ϕ_2 lines for A4/WQ 750/WQ after recrystallisation.

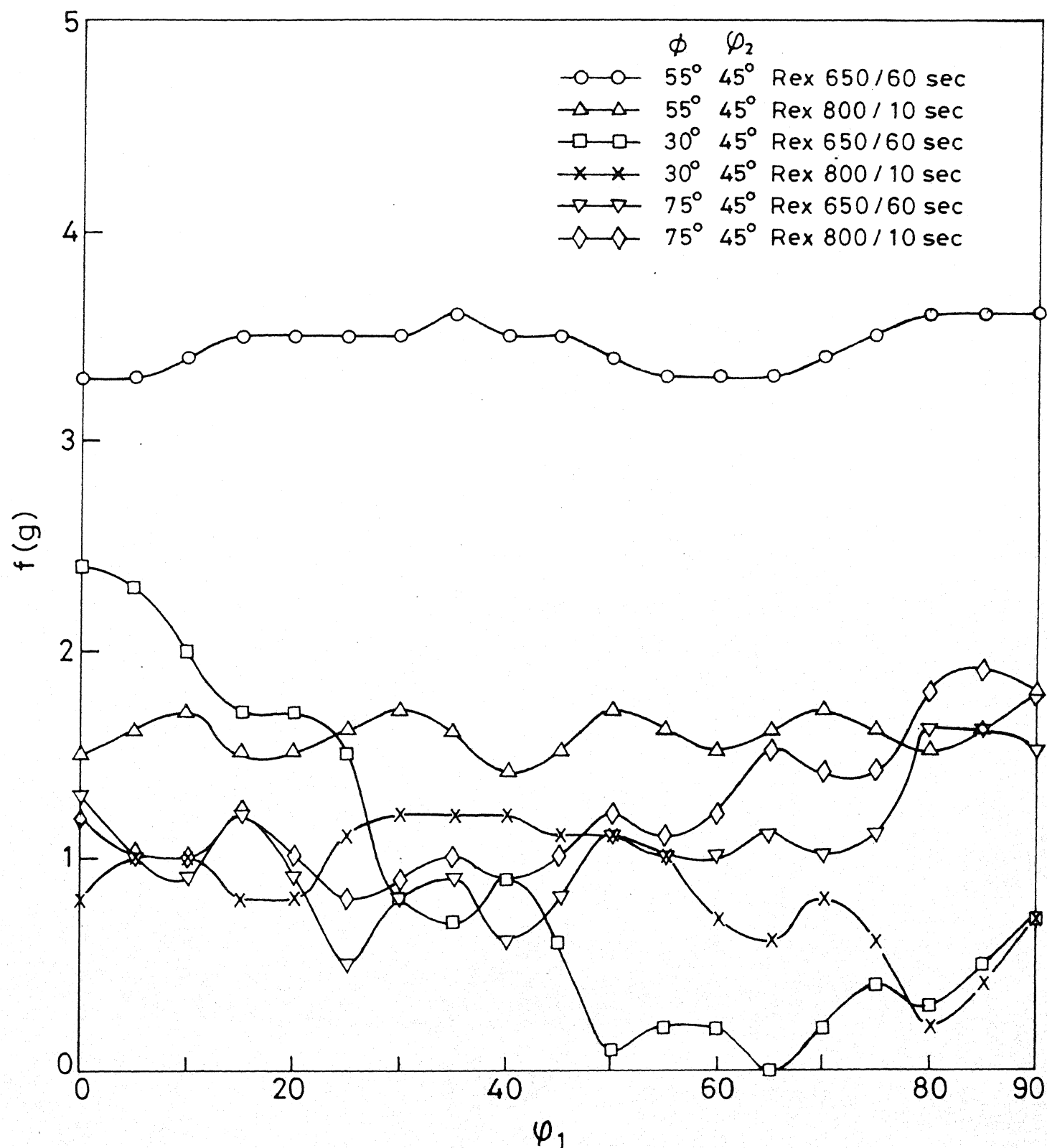


Fig. 4.79 Variation of $f(g)$ with ϕ_1 along different ϕ/ϕ_2 lines for A4/WQ 810/WQ after recrystallisation.

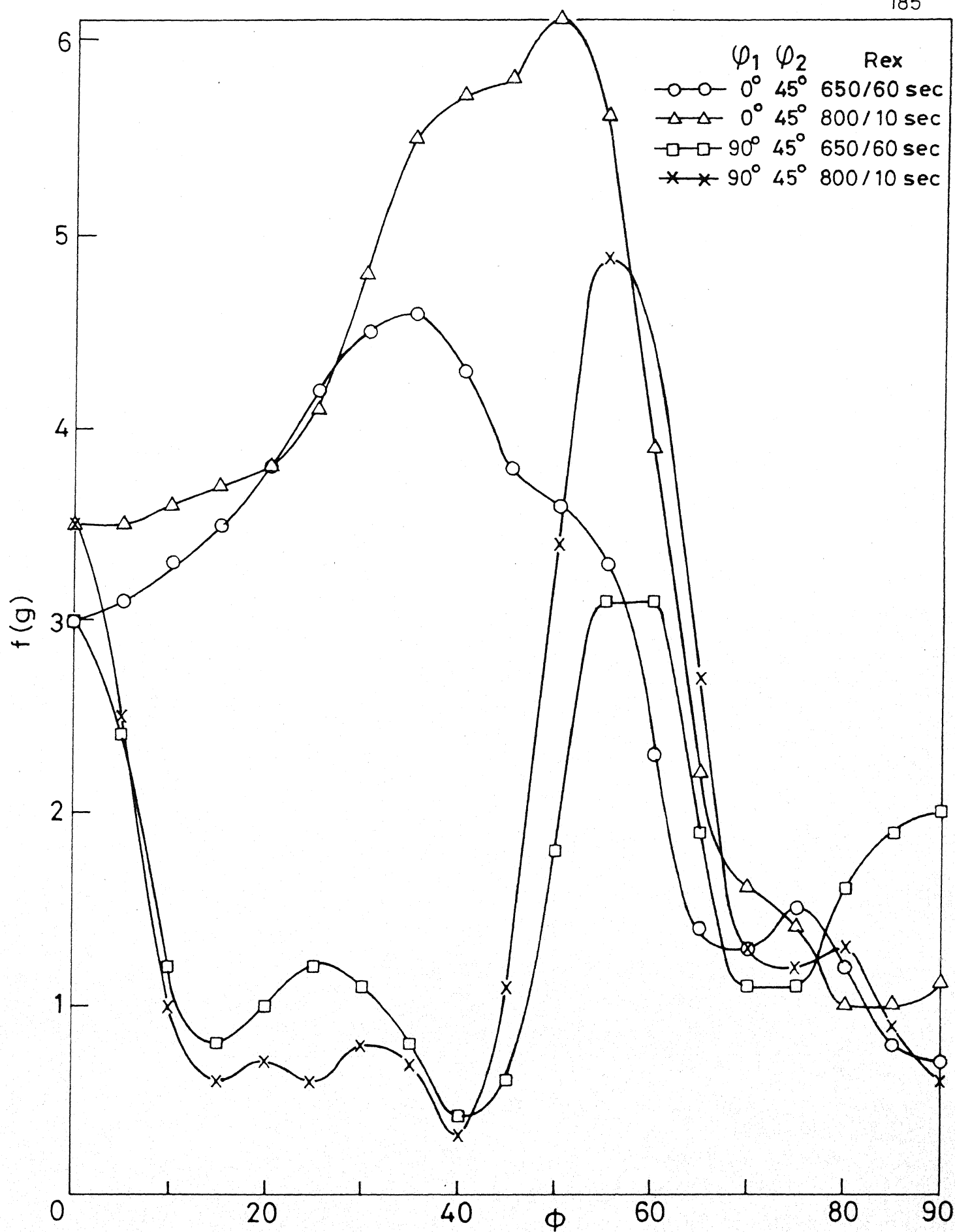


Fig.4.80 Variation of $f(g)$ with ϕ along different ϕ_1/ϕ_2 lines for A5/AC 750/WQ after recrystallisation.

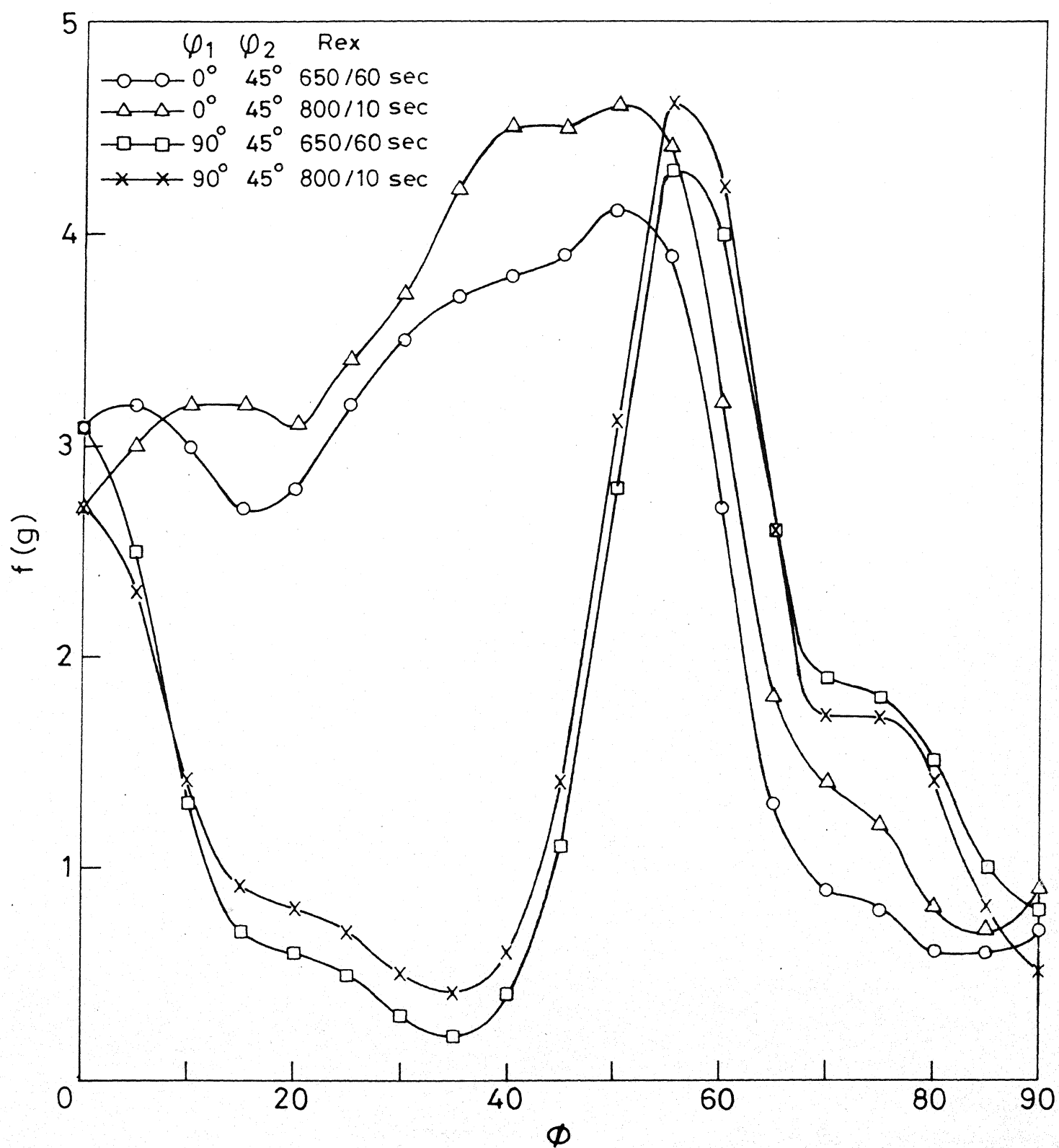


Fig.4.81 Variation of $f(g)$ with ϕ along different ϕ_1/ϕ_2 lines for A5/AC810/WQ after recrystallisation.

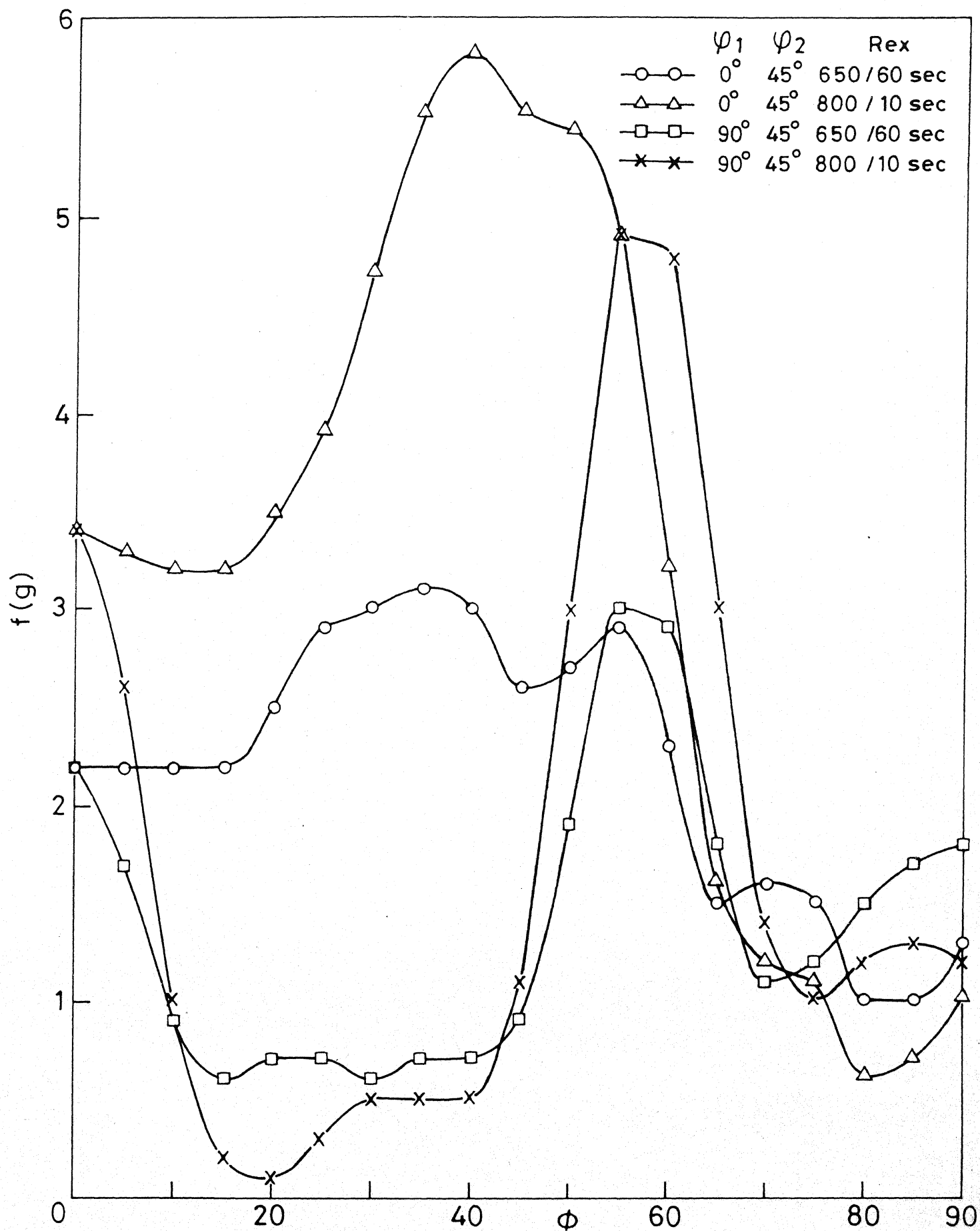


Fig.4.82 Variation of $f(g)$ with ϕ along different ϕ_1/ϕ_2 lines for A5/WQ 750/WQ after recrystallisation.

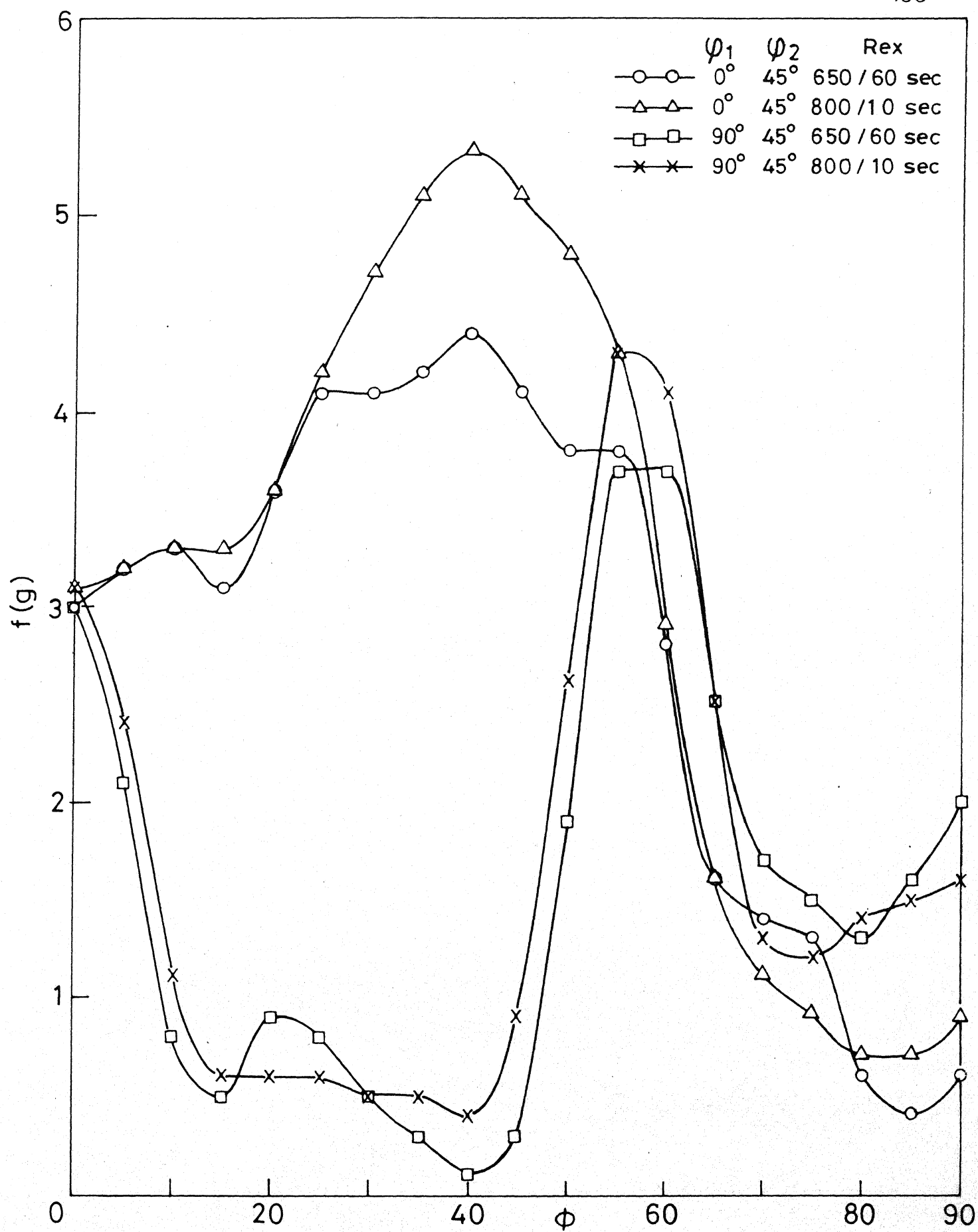


Fig.4.83 Variation of $f(g)$ with ϕ along different ϕ_1/ϕ_2 lines for A5/WQ 810/WQ after recrystallisation.

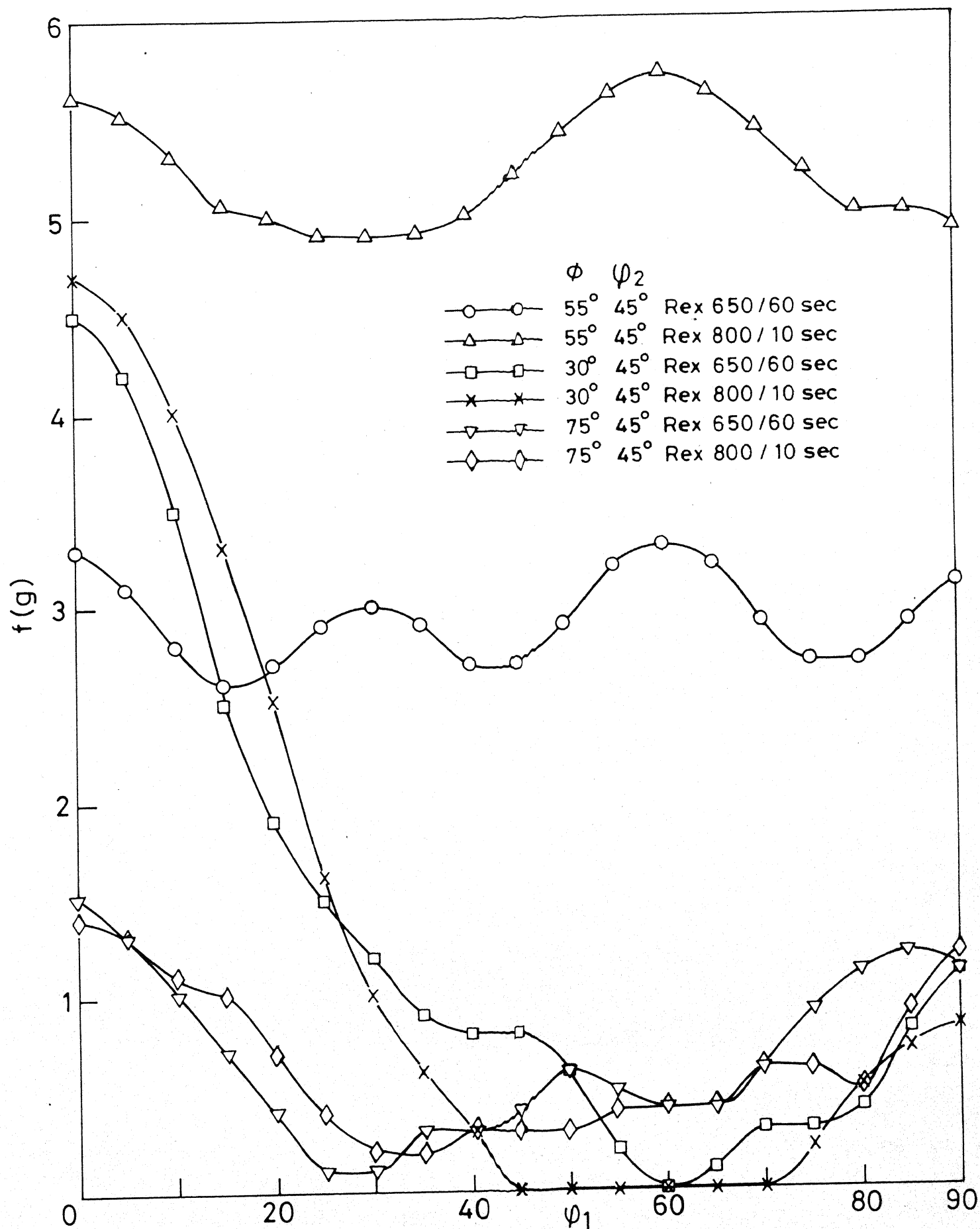


Fig.4.84 Variation of $f(g)$ with ϕ_1 along different ϕ/ψ_2 lines for A5/AC 750/WQ after recrystallisation.

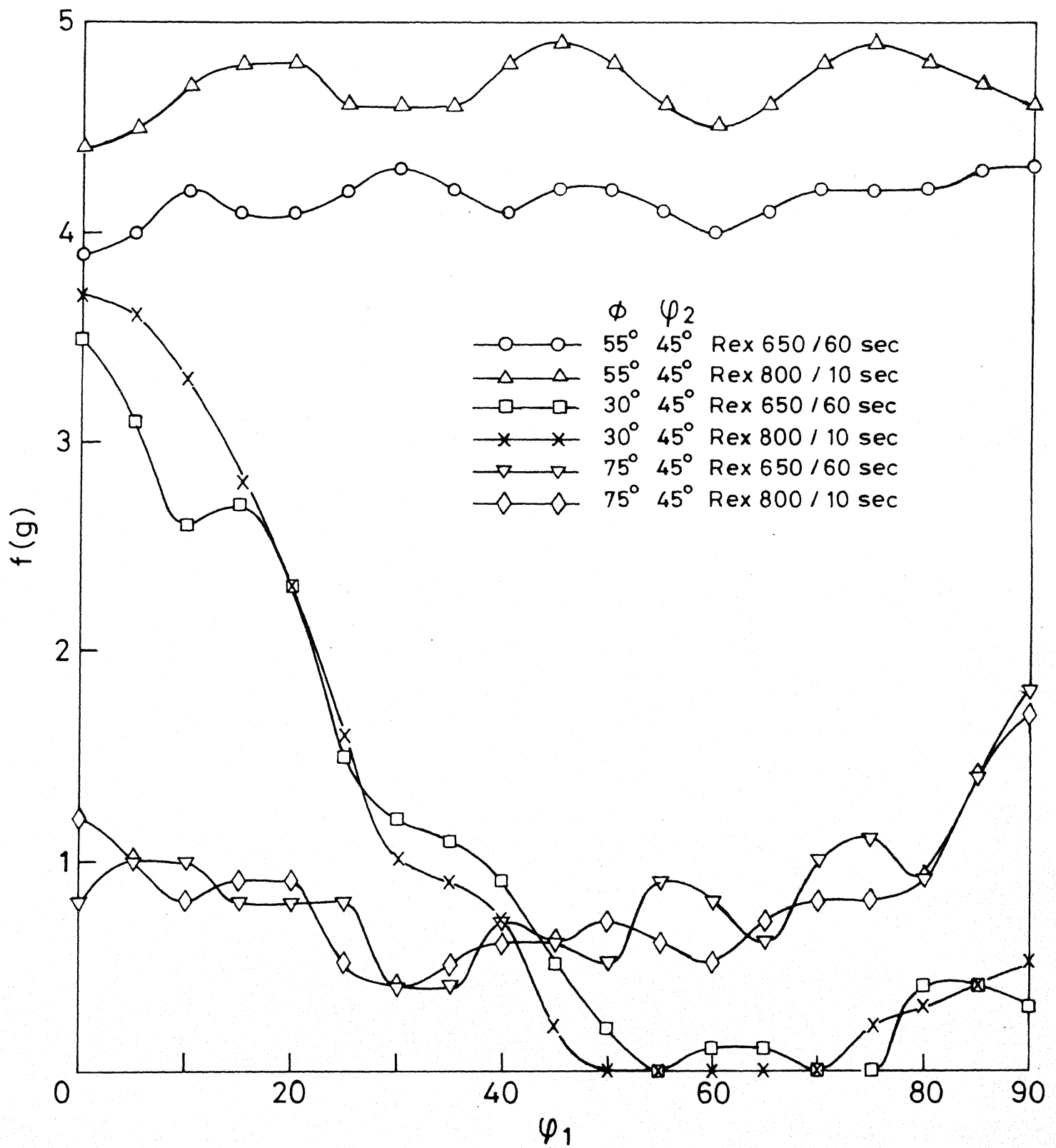


Fig.4.85 Variation of $f(g)$ with ψ_1 along different ϕ/ψ_2 lines for A5/AC810/WQ after recrystallisation.

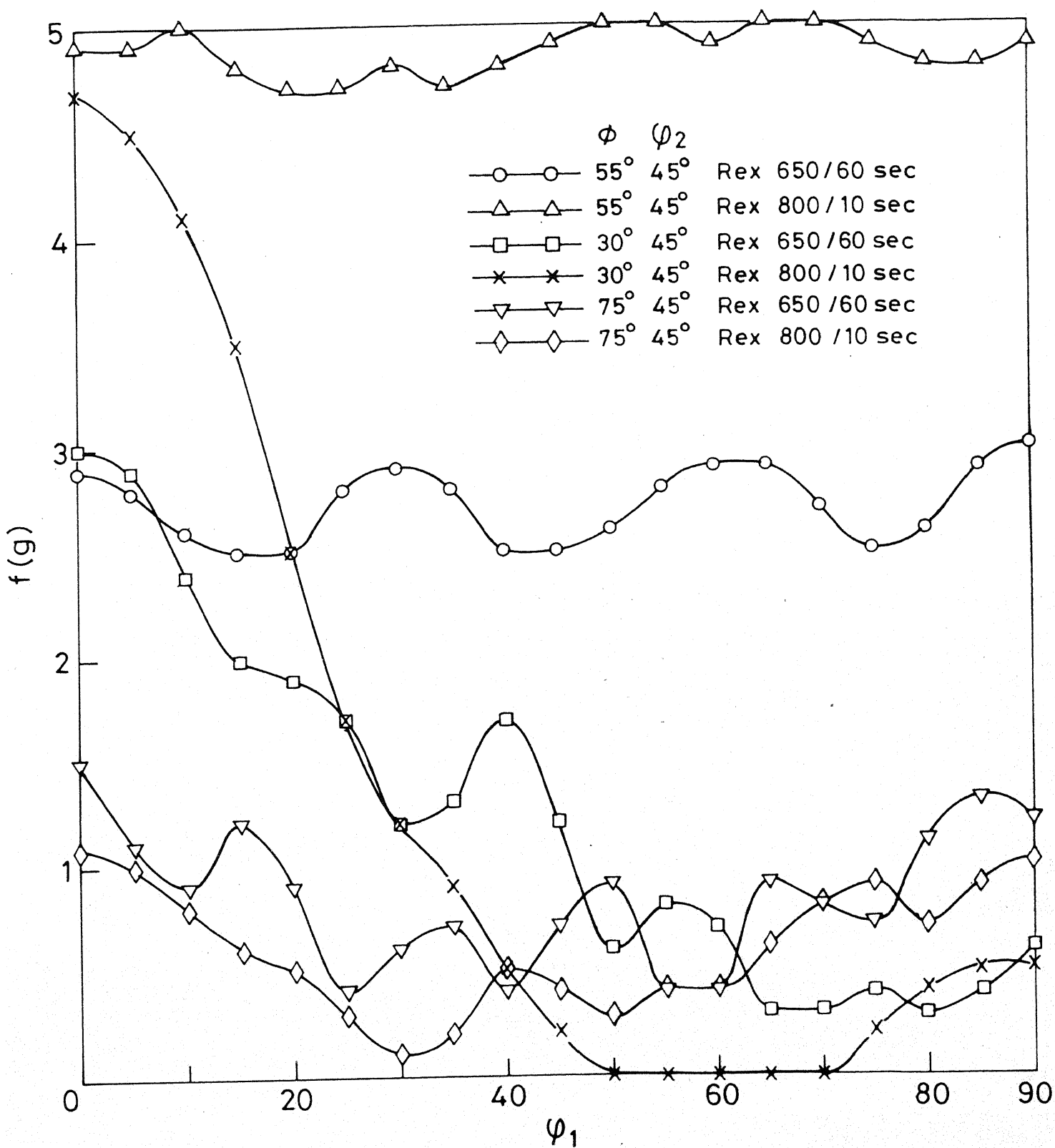


Fig.4.86 Variation of $f(g)$ with ϕ_1 along different ϕ/ϕ_2 lines for A5/WQ 750/WQ after recrystallisation.

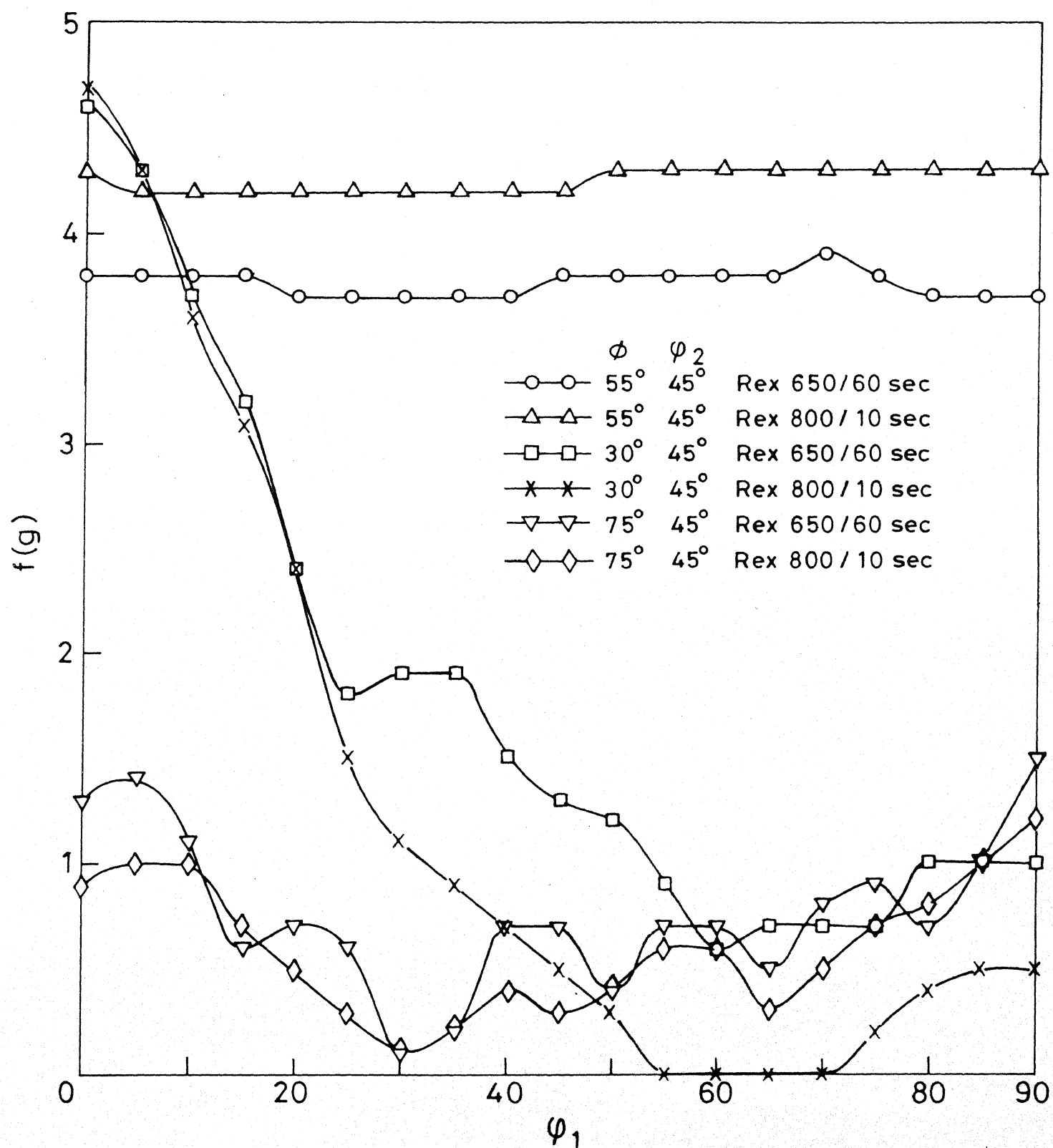


Fig.4.87 Variation of $f(g)$ with ϕ_1 along different ϕ/ϕ_2 lines for A5/WQ 810/WQ after recrystallisation.

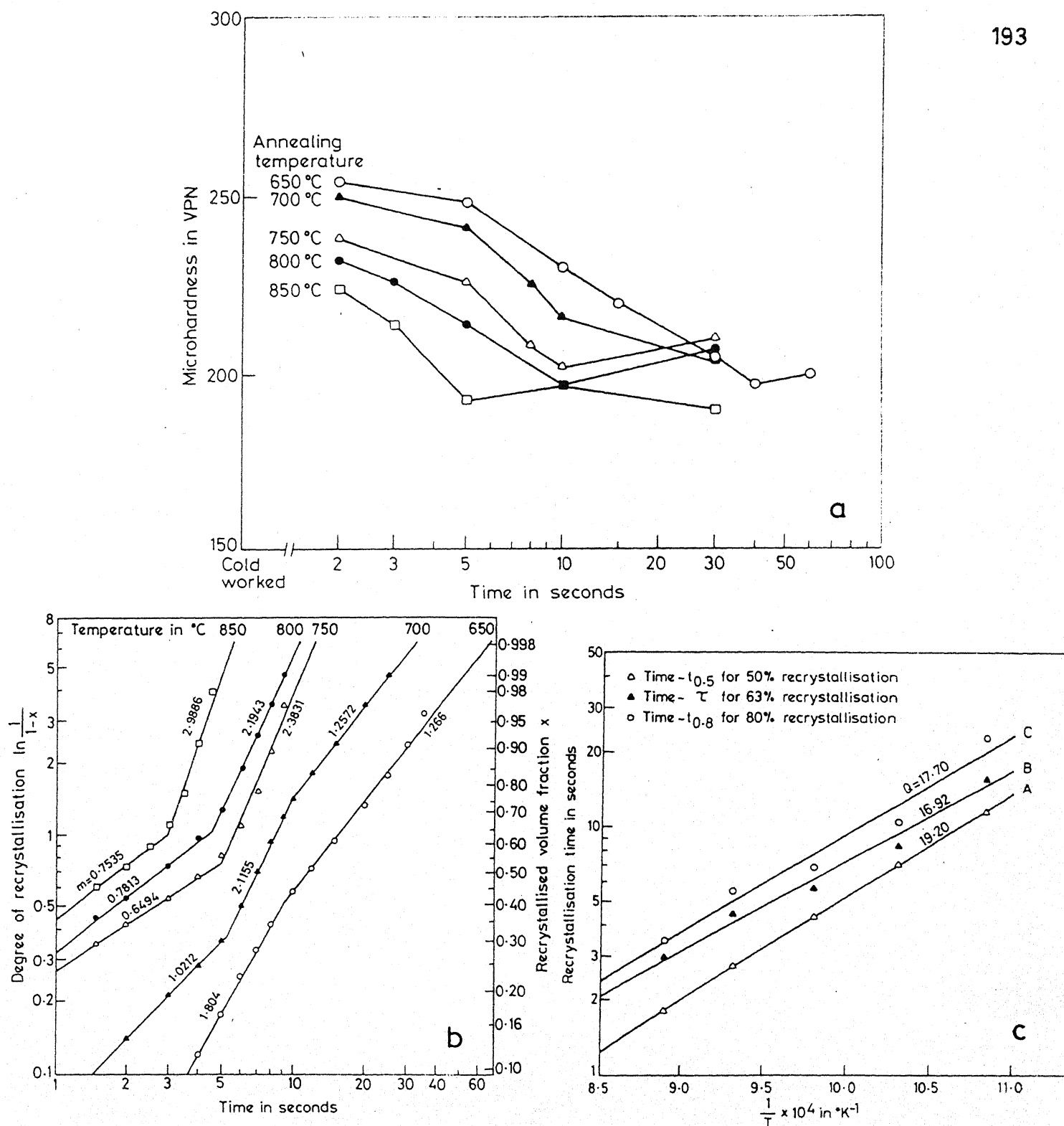


Fig.4.88 Results of recrystallisation kinetics studies for alloy A1 with initial heat treatment AC 750/WQ.

- (a) Variation of micro-hardness of ferrite with time at different annealing temperatures
- (b) Avrami-plots of recrystallised volume fractions estimated from micro-hardness values
- (c) Arrhenius-plot for measuring the 'Q'-values.

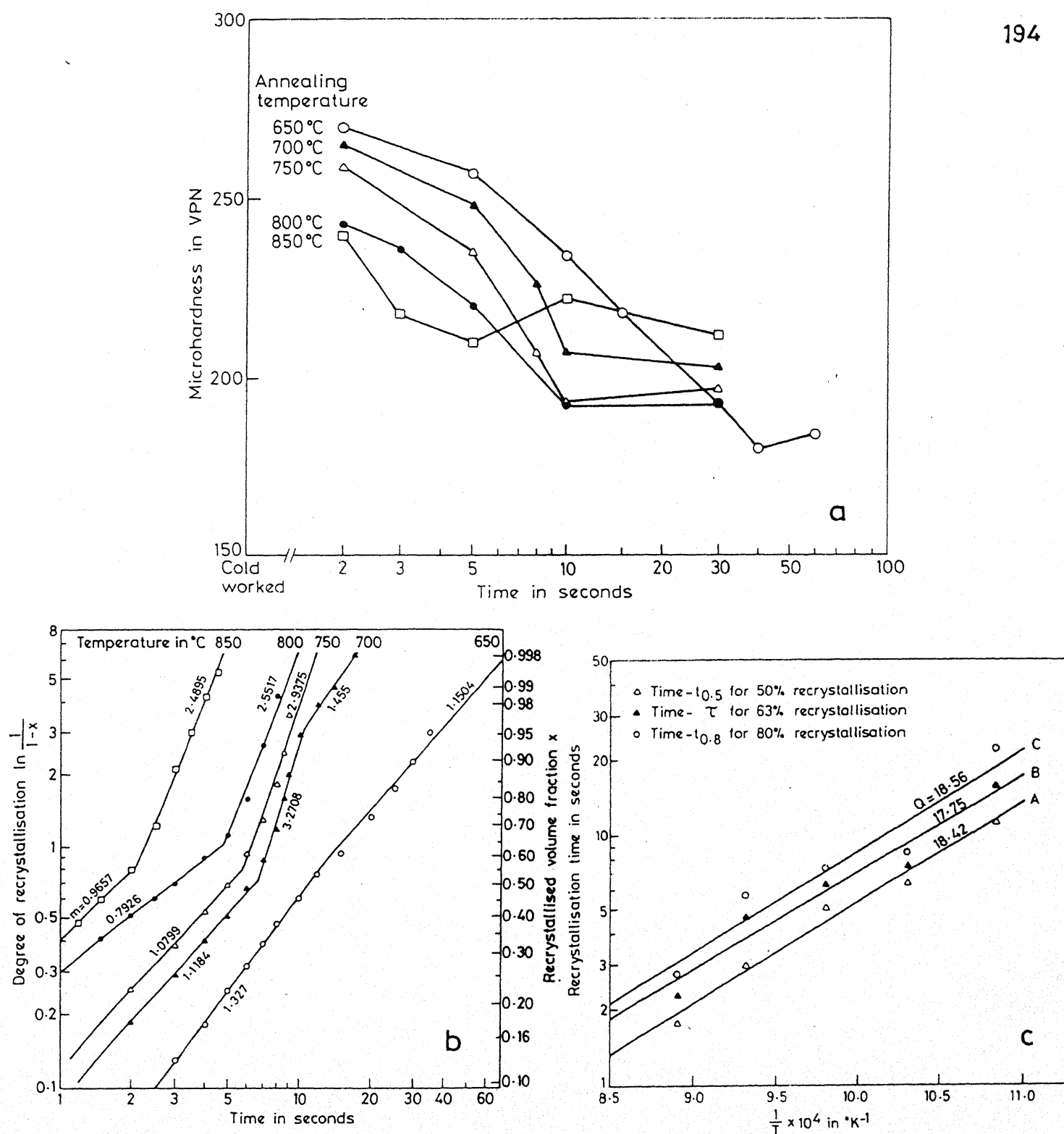


Fig.4.89 Results of recrystallisation kinetics studies for alloy A1 with initial heat treatment WQ 750/WQ

- (a) Variation of micro-hardness of ferrite with time at different annealing temperatures
- (b) Avrami-plots of recrystallised volume fractions estimated from micro-hardness values
- (c) Arrhenius-plot for measuring the 'Q'-values.

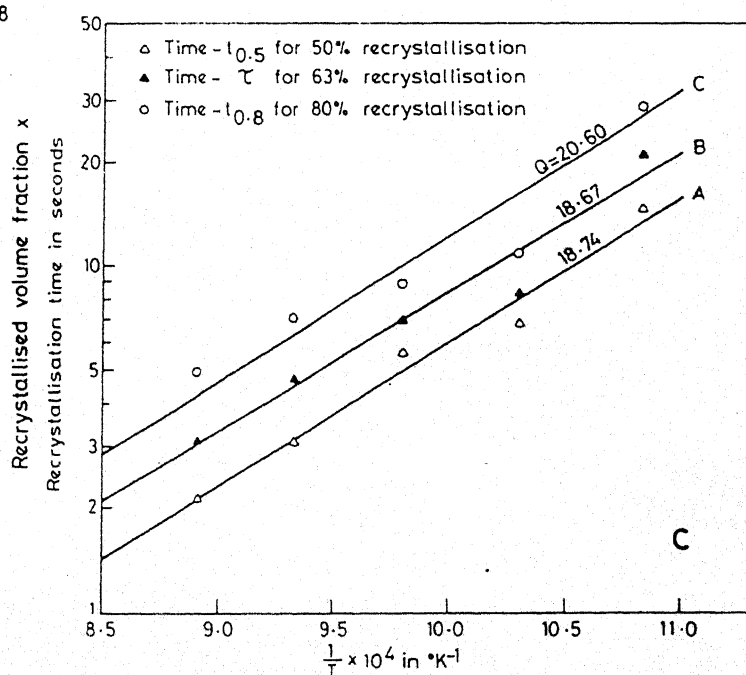
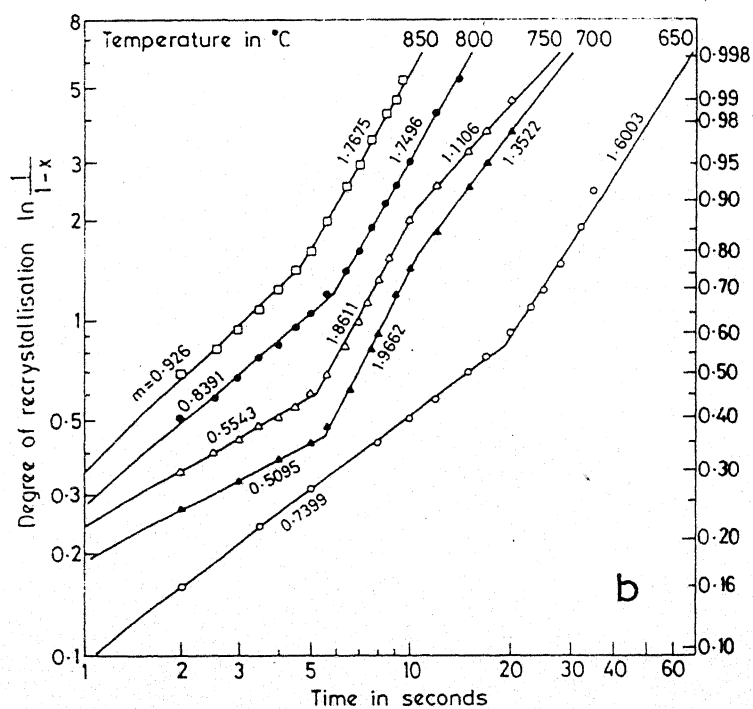
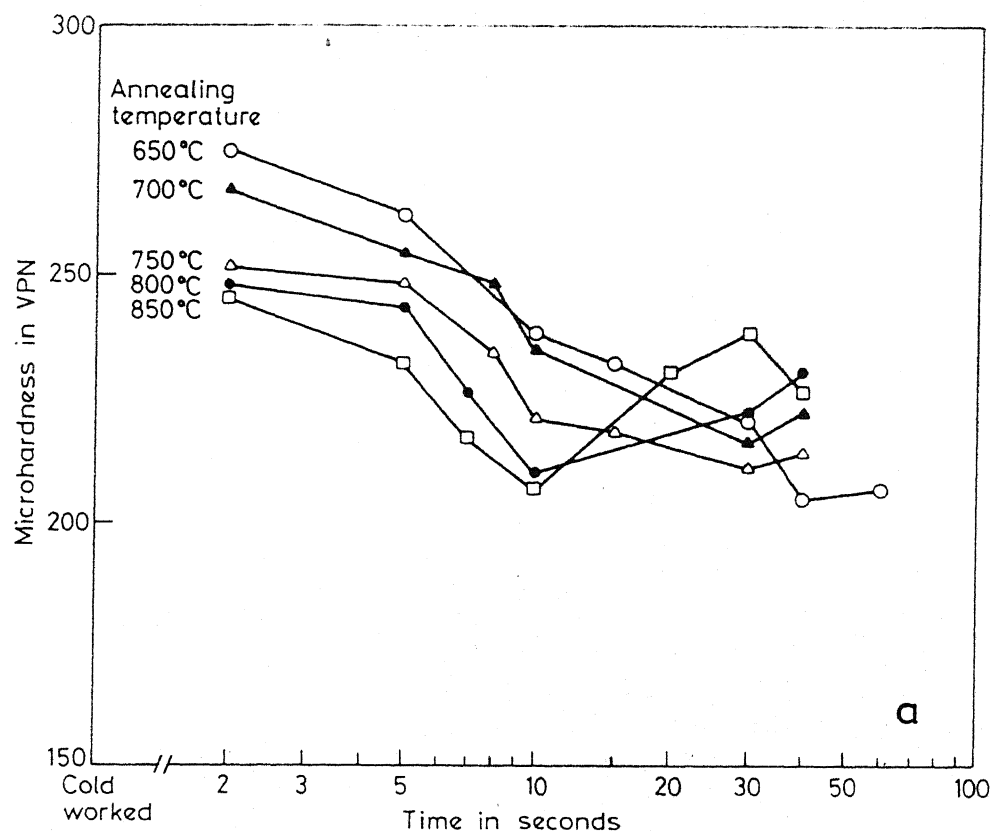


Fig.4.90 Results of recrystallisation kinetics studies for alloy A4 with initial heat treatment AC 750/WQ

- Variation of micro-hardness of ferrite with time at different annealing temperatures
- Avrami-plots of recrystallised volume fractions estimated from micro-hardness values
- Arrhenius-plot for measuring the 'Q'-values.

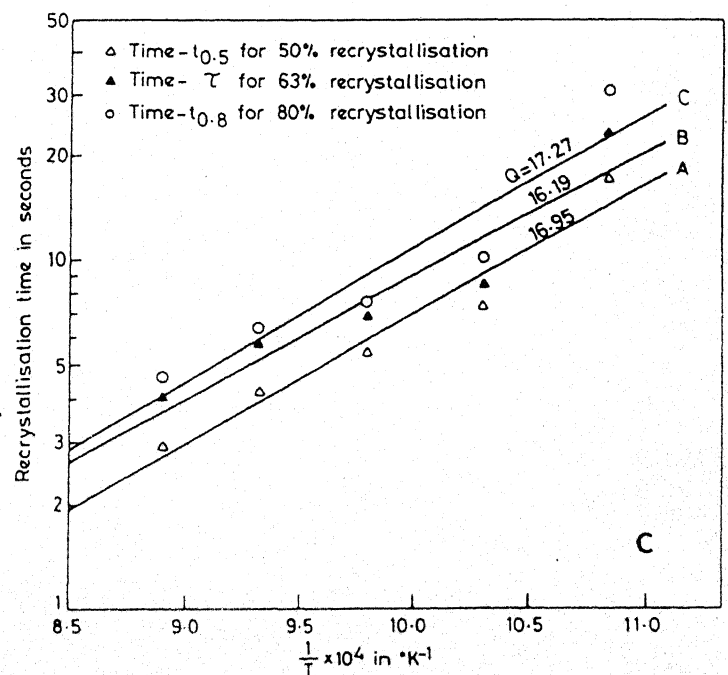
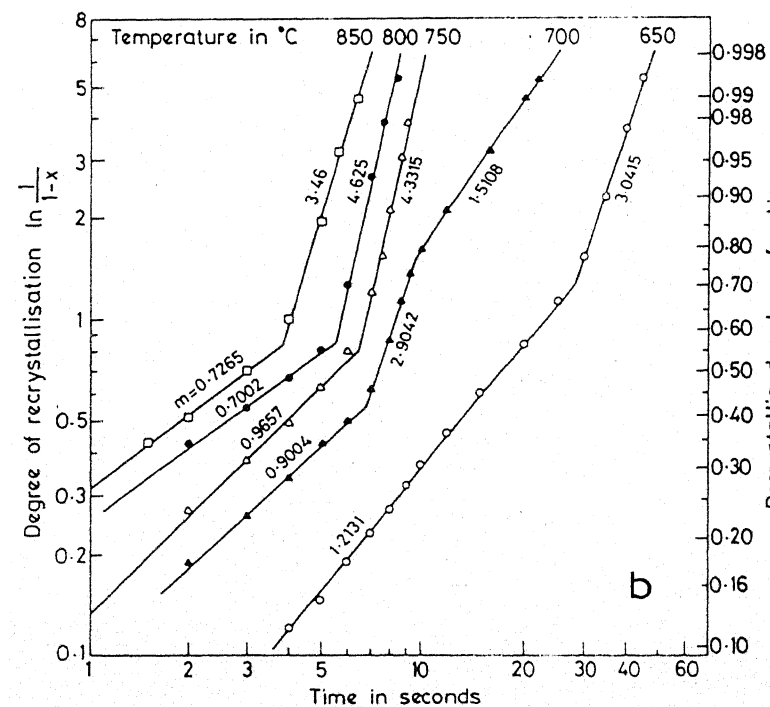
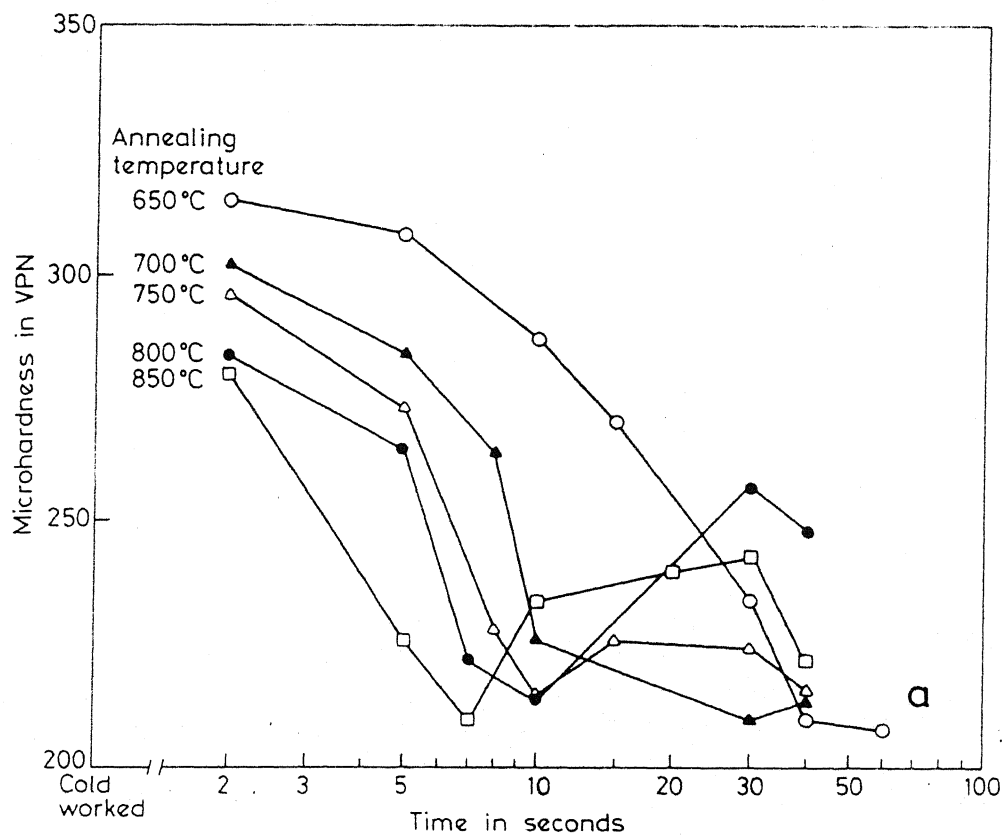


Fig.4.91 Results of recrystallisation kinetics studies for alloy A4 with initial heat treatment WQ750/WQ

- Variation of micro-hardness of ferrite with time at different annealing temperatures
- Avrami-plots of recrystallised volume fractions estimated from micro-hardness values
- Arrhenius-plot for measuring the 'Q'-values.

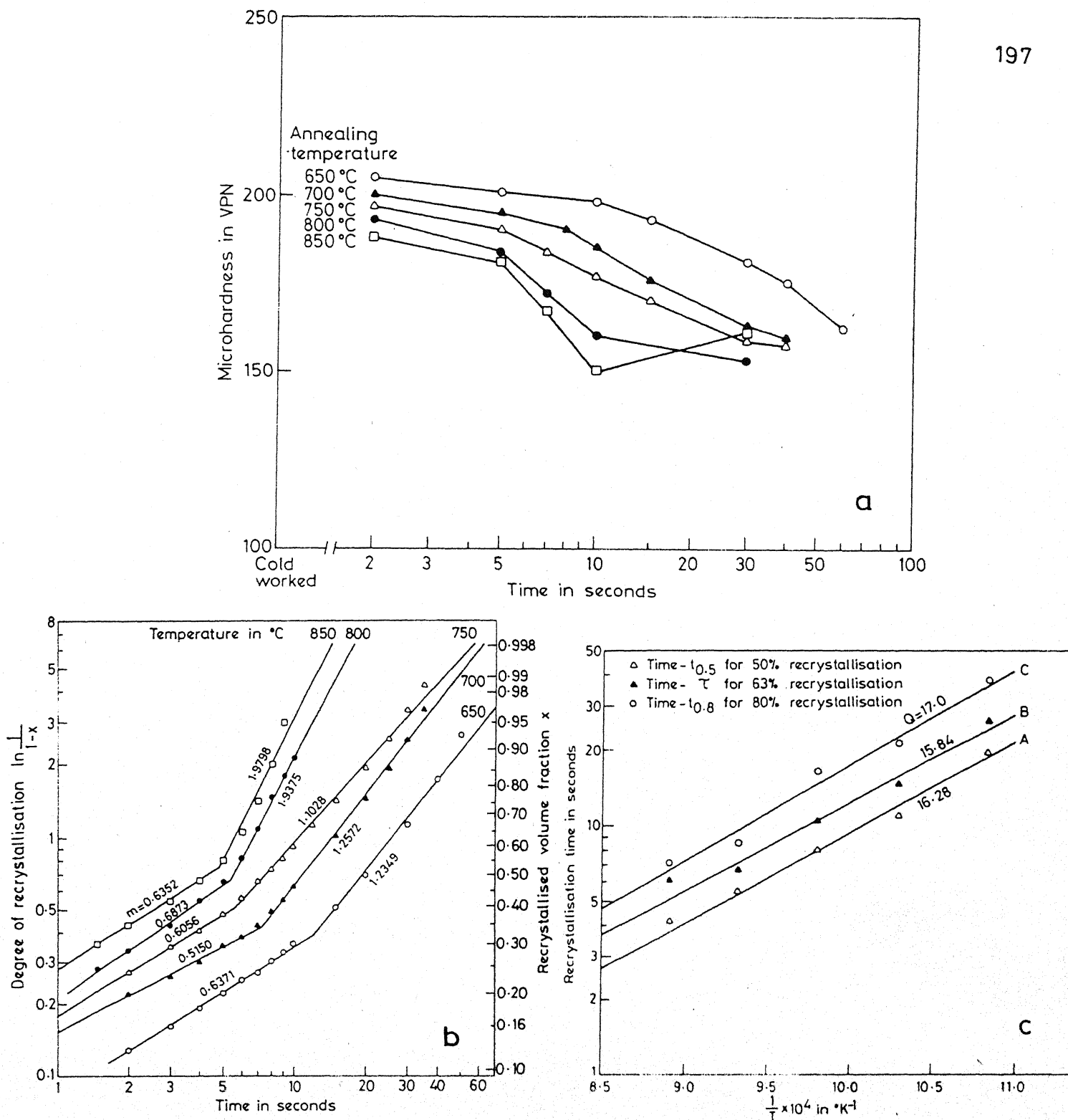
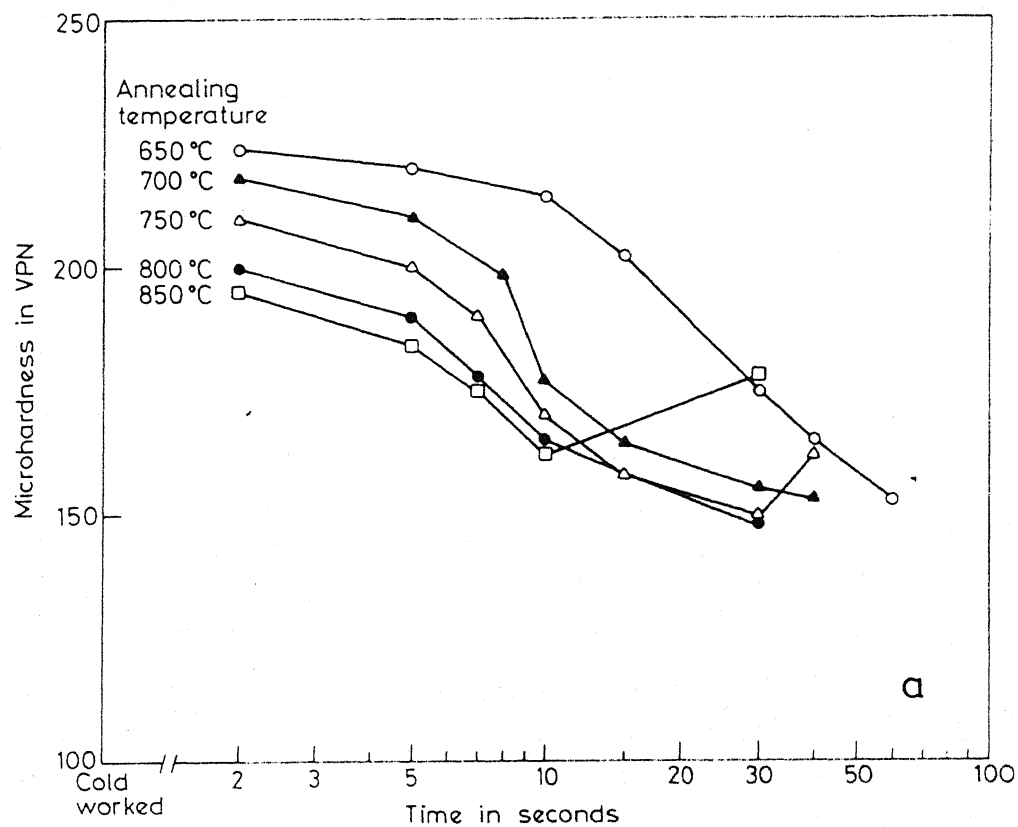
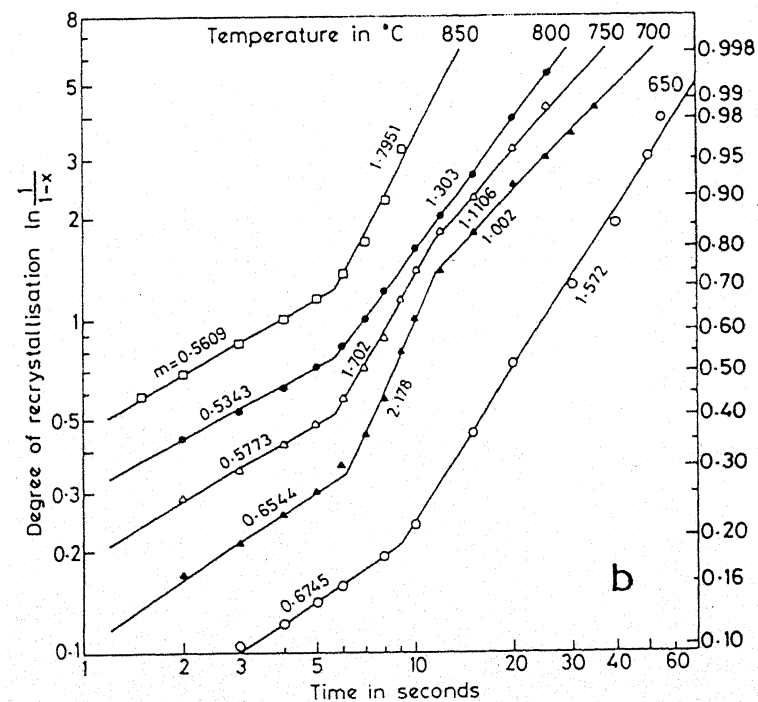


Fig.4.92 Results of recrystallisation kinetics studies for alloy A5 with initial heat treatment AC750/WQ

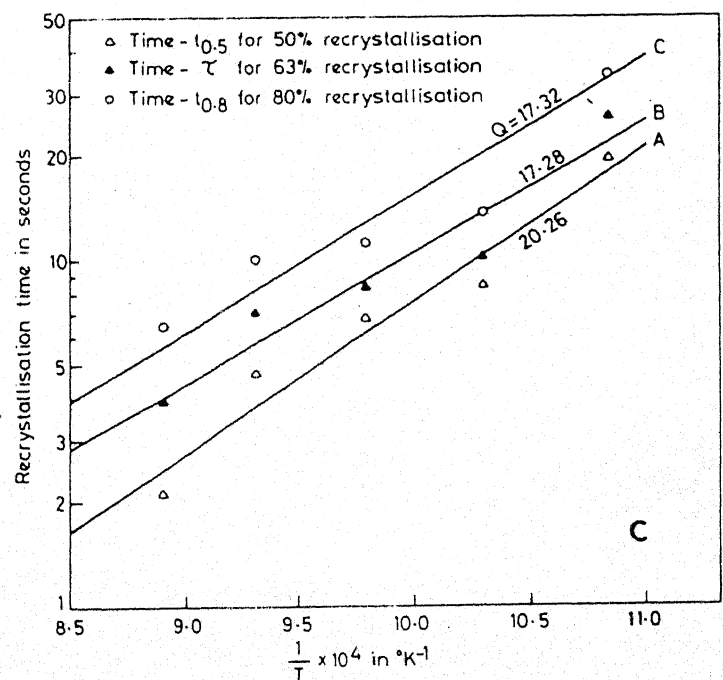
- (a) Variation of micro-hardness of ferrite with time at different annealing temperatures
- (b) Avrami-plots of recrystallised volume fractions estimated from micro-hardness values
- (c) Arrhenius-plot for measuring the 'Q'-values.



a



b



c

Fig.4.93 Results of recrystallisation kinetics studies for alloy A5 with initial heat treatment WQ 750/WQ

(a) Variation of micro-hardness of ferrite with time at different annealing temperatures

(b) Avrami-plots of recrystallised volume fractions estimated from micro-hardness values

(c) Arrhenius-plot for measuring the 'Q'-values.

4.4 Estimation of 'r'-Values

The variation of the theoretically calculated 'r' values with angle made with the rolling direction for the three alloys, A1, A4 and A5 in the cold-rolled condition, is shown graphically in Figures 4.94, 4.95 and 4.96 respectively. A high level of anisotropy in 'r' values is clearly apparent in all these diagrams. The values of r_0 , r_{45} , r_{90} and $\bar{r} = (r_0 + 2r_{45} + r_{90})/4$ have been taken from these diagrams and tabulated alloy-wise in Table 4.5. No clear-cut pattern of variation in \bar{r} -values, as a function either of alloy composition or heat-treatment, emerges from these results.

Table 4.5
r-values of Cold-worked Alloys

Alloy designation	r_0	r_{45}	r_{90}	\bar{r}	Δr
A1/AC 750/WQ	0.53	1.63	0.95	1.19	-0.89
A1/AC 810/WQ	0.70	0.86	1.40	0.96	0.19
A1/WQ 750/WQ	0.58	1.36	0.97	1.07	-0.59
A1/WQ 810/WQ	0.80	0.81	1.10	0.88	0.14
A4/AC 750/WQ	0.86	1.29	1.15	1.15	-0.29
A4/AC 810/WQ	0.61	0.84	1.01	0.82	-0.03
A4/WQ 750/WQ	0.82	1.30	1.14	1.14	-0.32
A4/WQ 810/WQ	0.77	1.27	1.11	1.11	-0.33
A5/AC 750/WQ	0.72	1.76	1.07	1.33	-0.87
A5/AC 810/WQ	0.73	1.36	1.14	1.15	-0.43
A5/WQ 750/WQ	0.65	1.19	1.08	1.03	-0.33
A5/WQ 810/WQ	0.61	1.12	1.12	0.99	-0.26

Figures 4.97 to 4.102 depict the variation of the theoretically calculated ' r '-values with angle made with the rolling direction for the three alloys in the fully recrystallised condition. The recrystallisation was accomplished at two different temperatures, namely, 650°C and 800°C. The results are also shown in a tabular form in Table 4.6.

Table 4.6
r-values of Recrystallised Alloys

Alloy designation	Recrystallised at 650°C					Recrystallised at 800°C				
	r_0	r_{45}	r_{90}	\bar{r}	Δr	r_0	r_{45}	r_{90}	\bar{r}	Δr
A1/AC 750/WQ	0.68	0.87	0.76	0.79	-0.15	0.82	1.12	0.82	0.97	-0.30
A1/AC 810/WQ	0.74	0.78	0.74	0.76	-0.04	0.96	0.82	0.90	0.88	0.11
A1/WQ 750/WQ	0.73	0.92	0.77	0.84	-0.17	0.91	1.08	0.80	0.96	-0.23
A1/WQ 810/WQ	0.75	0.67	0.77	0.71	0.09	0.81	0.84	0.76	0.82	-0.06
A4/AC 750/WQ	0.88	1.20	1.10	1.10	-0.21	1.07	0.83	0.88	0.90	0.15
A4/AC 810/WQ	0.86	1.29	1.13	1.15	-0.30	1.15	0.76	0.86	0.88	0.25
A4/WQ 750/WQ	0.76	1.05	1.06	0.98	-0.14	1.08	0.71	0.85	0.84	0.26
A4/WQ 810/WQ	0.72	1.19	1.03	1.03	-0.32	1.12	0.73	0.98	0.89	0.32
A5/AC 750/WQ	0.66	1.06	1.11	0.97	-0.18	0.69	1.69	1.03	1.27	-0.83
A5/AC 810/WQ	0.68	1.22	1.07	1.05	-0.35	0.66	1.31	1.06	1.08	-0.45
A4/WQ 750/WQ	0.94	0.91	1.34	1.02	0.23	0.66	1.50	1.08	1.19	-0.63
A5/WQ 810/WQ	0.77	1.10	1.23	1.05	-0.10	0.68	1.31	1.11	1.10	-0.42

The anisotropy behaviour in the ' r '-values, as observed for the cold-rolled materials, seems to persist even after recrystallisation. Out of the three alloys, alloy A1 possesses the minimum \bar{r} -values while alloys A4 and A5 have somewhat higher \bar{r} -values. There is also no significant variation of the ' r '-values as a function of recrystallisation temperature.

However, from a look at Table 4.6 this much can be said that alloy A5 has the highest and A1 the lowest set of 'r'-values whereas alloy A4 has intermediate values. Again, in alloy A5, the largest values of 'r' have been obtained for orientations making 45° with the rolling direction for the materials recrystallised at 800°C . Thus, it can be seen from Table 4.6 that r_{45} values as high as 1.69 and 1.50 have been obtained for A5/AC 750/WQ and A5/WQ 750/WQ respectively while a value of 1.31 has been found for both A5/AC 810/WQ and A5/WQ 810/WQ.

The values of the parameter $\Delta r = (r_0 + r_{90} - 2r_{45})/2$ have also been noted in Tables 4.5 and 4.6. Alloy A5 has been found to possess the largest set of Δr values while alloy A1 the smallest. The Δr values for alloy A4 have been found to lie in between these two extremes.

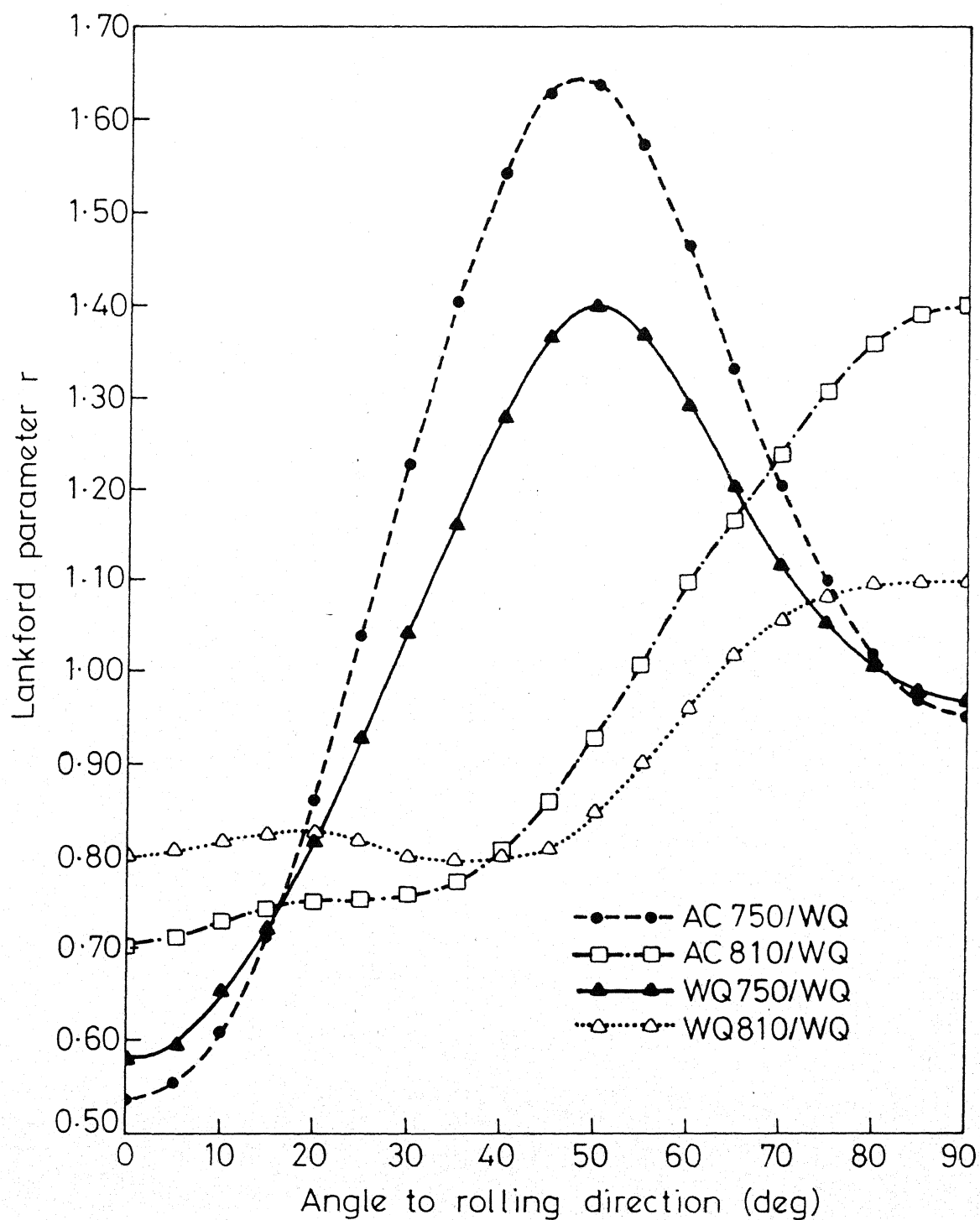


Fig.4.94 Variation in the Lankford strain ratio r with angle from the rolling direction for alloy A1, cold-rolled 60%.

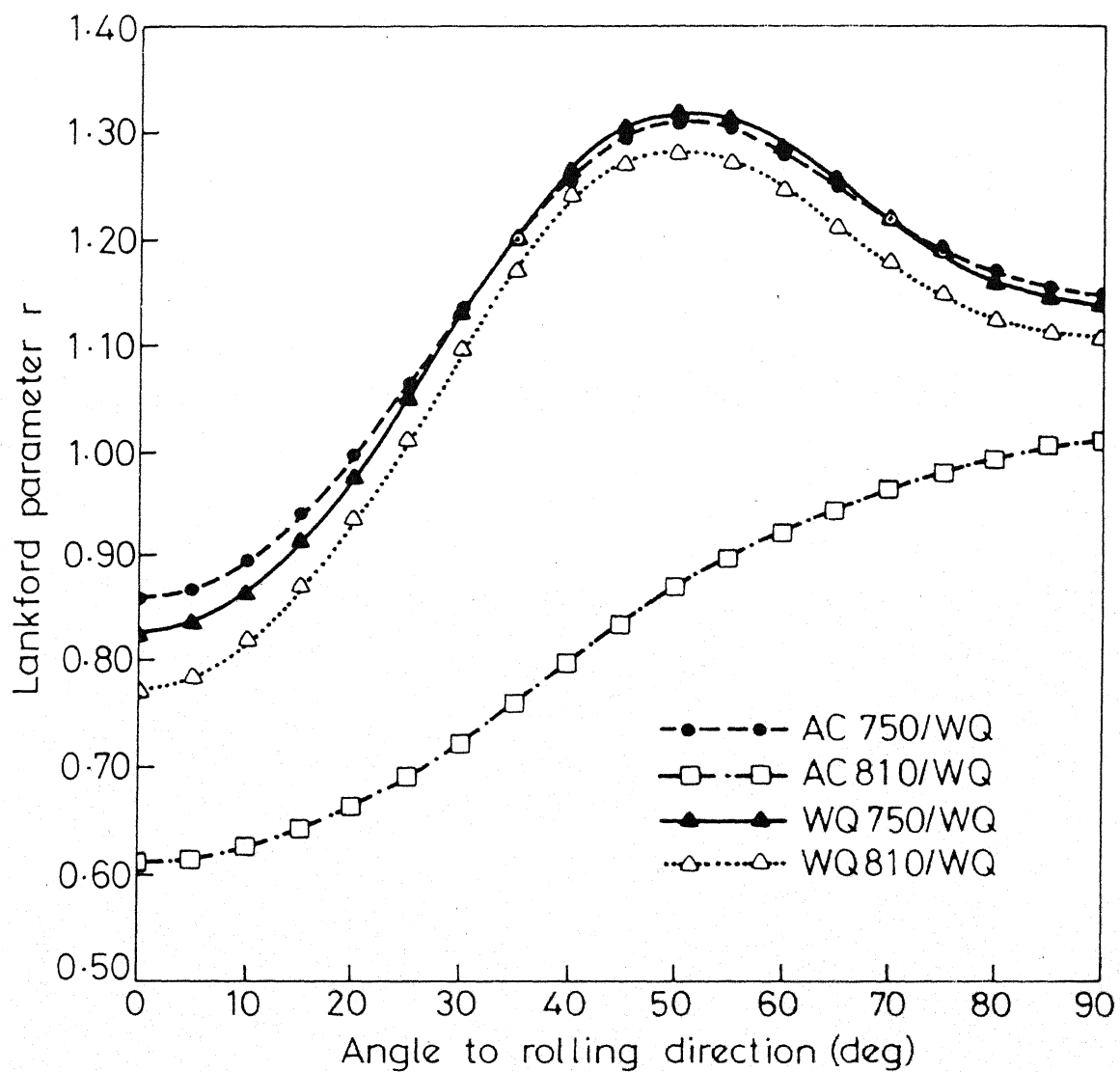


Fig.4.95 Variation in the Lankford strain ratio r with angle from the rolling direction for alloy A4, cold-rolled 60%.

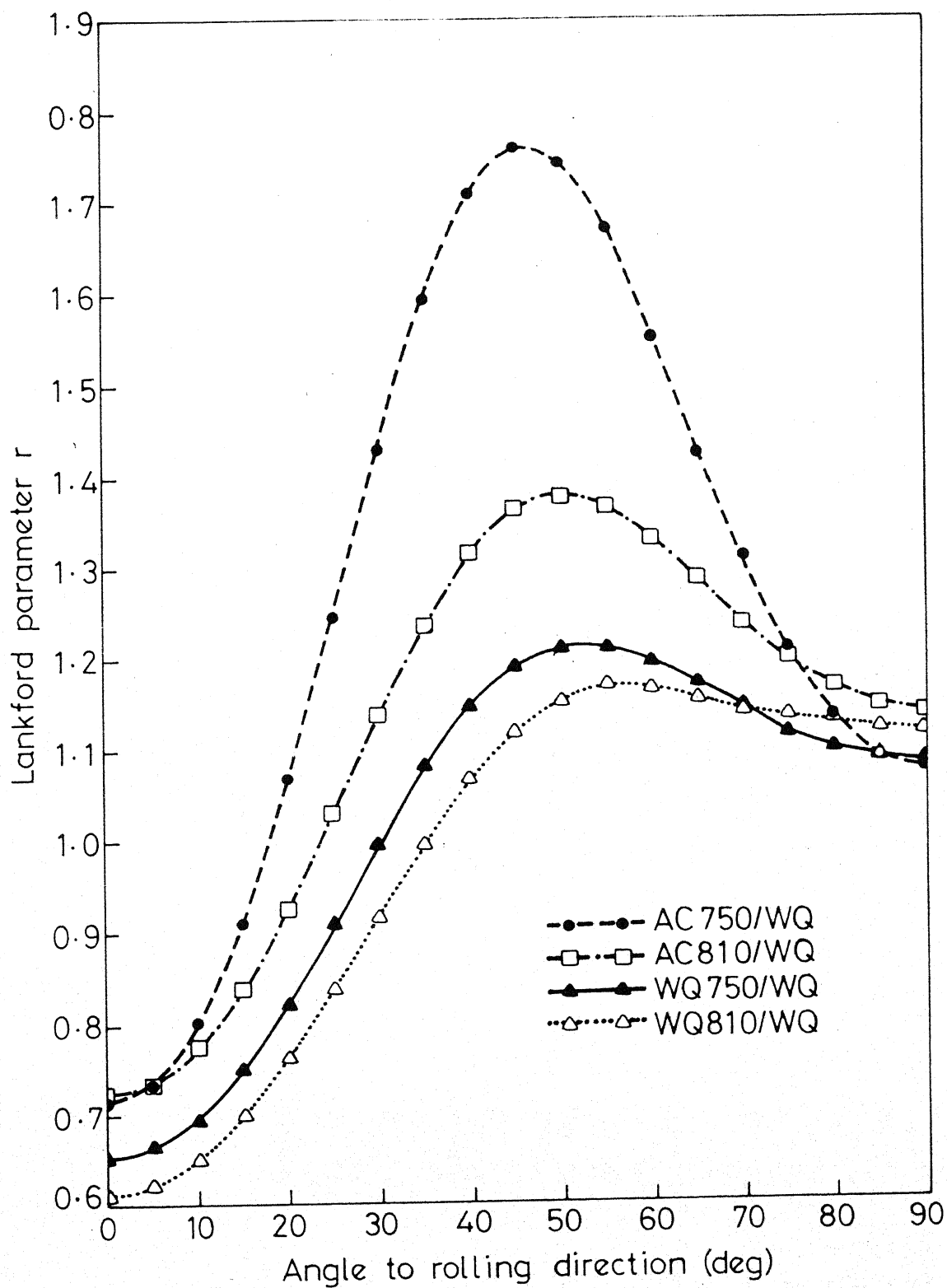


Fig.4.96 Variation in the Lankford strain ratio r with angle from the rolling direction for alloy A5, cold-rolled 60%.

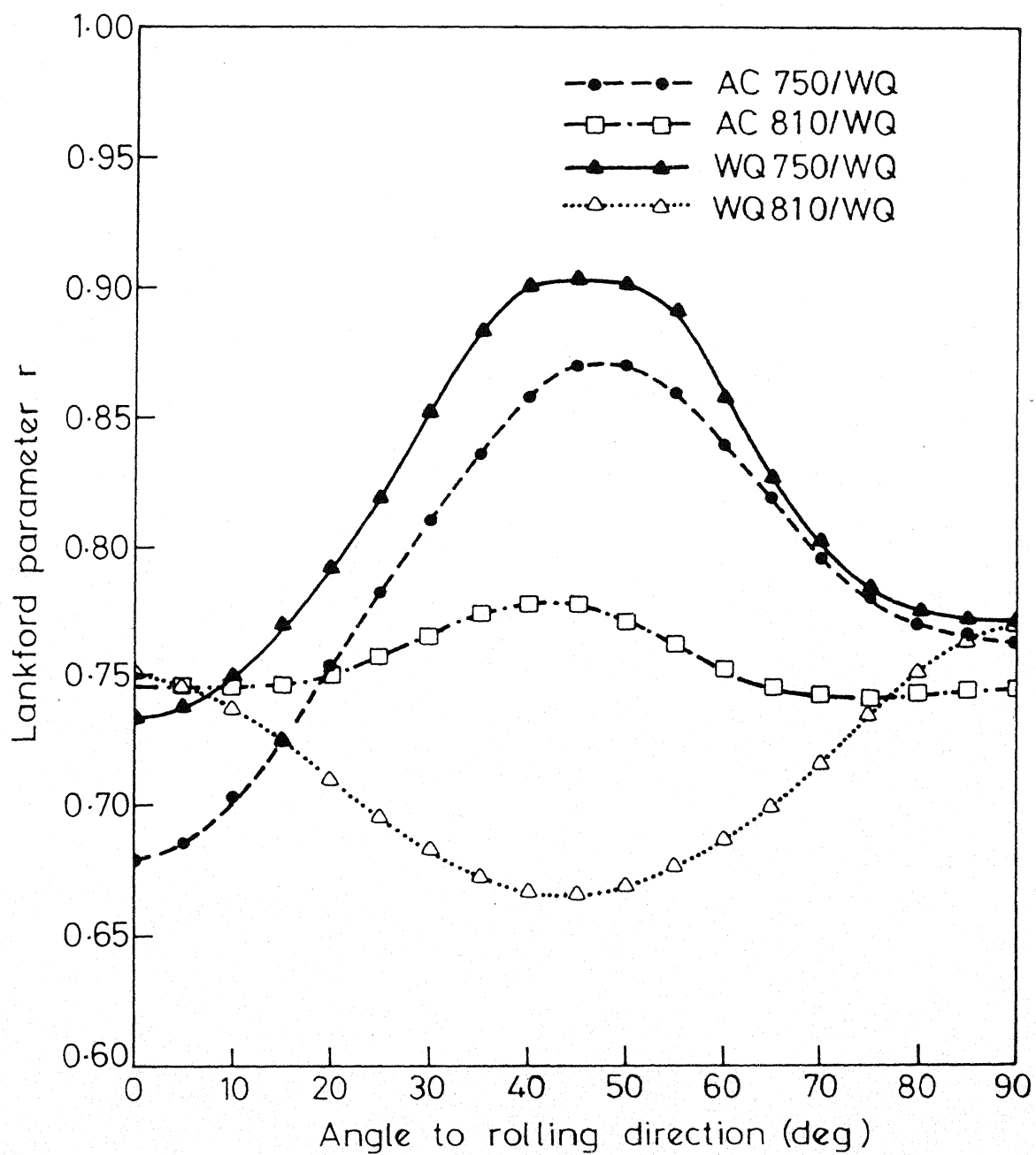


Fig.4.97 Variation in the Lankford strain ratio r with angle from the rolling direction for alloy A1, cold-rolled 60% and recrystallised at 650°C for 40 sec.

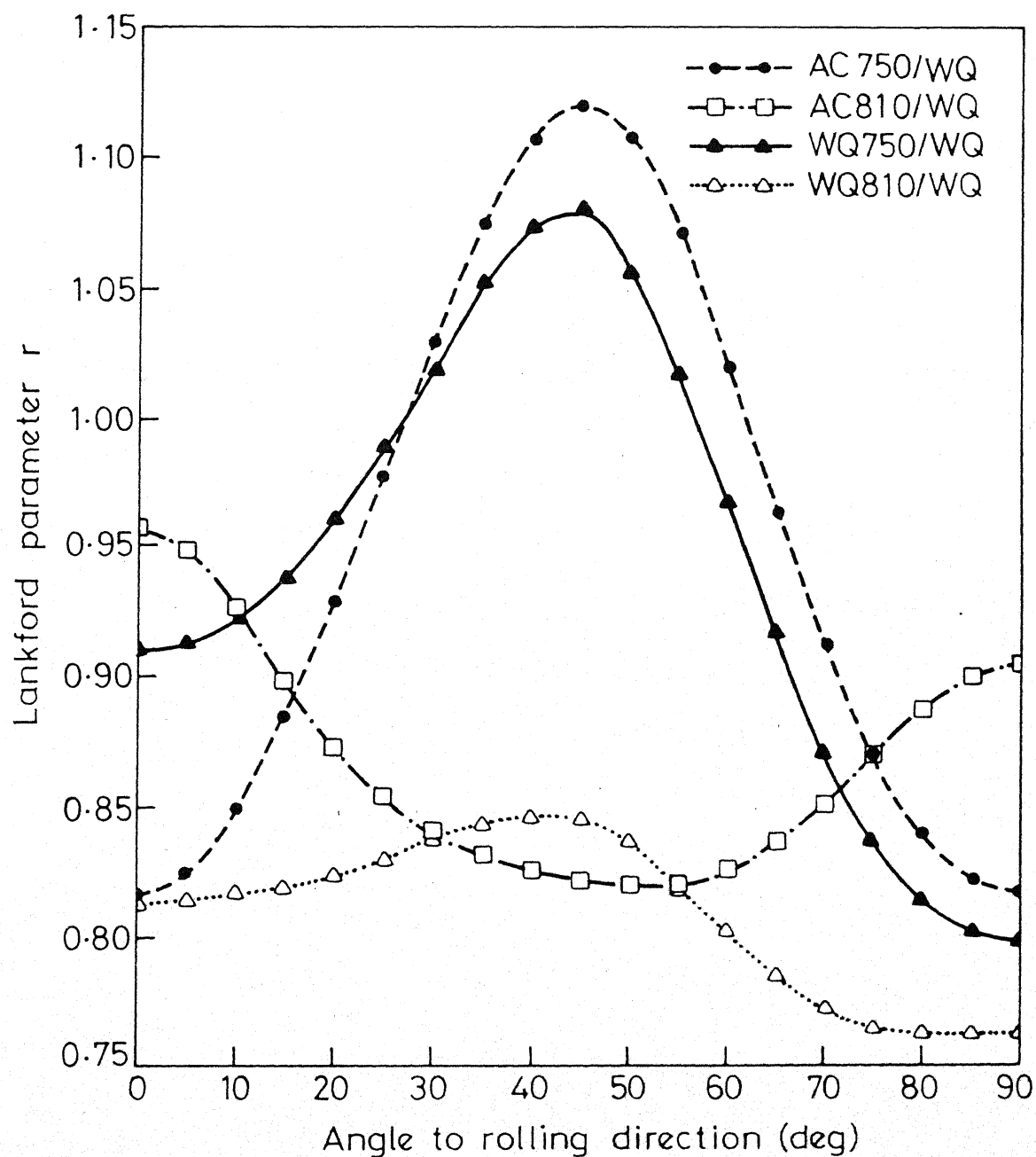


Fig.4.98 Variation in the Lankford strain ratio r with angle from the rolling direction for alloy A1, cold-rolled 60% and recrystallised at 800°C for 10 sec.

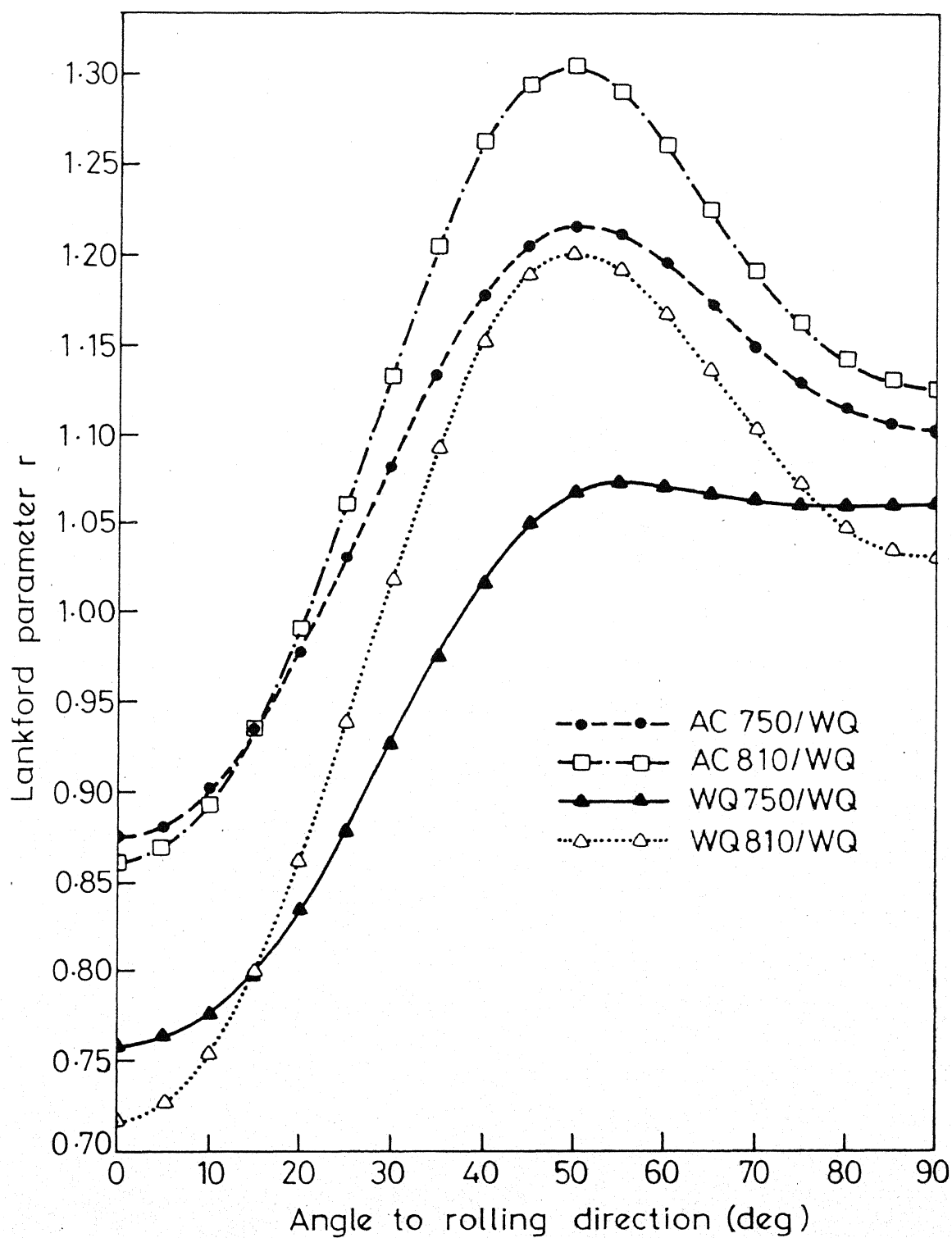


Fig.4.99 Variation in the Lankford strain ratio r with angle from the rolling direction for alloy A4, cold-rolled 60% and recrystallised at 650°C for 1 min.

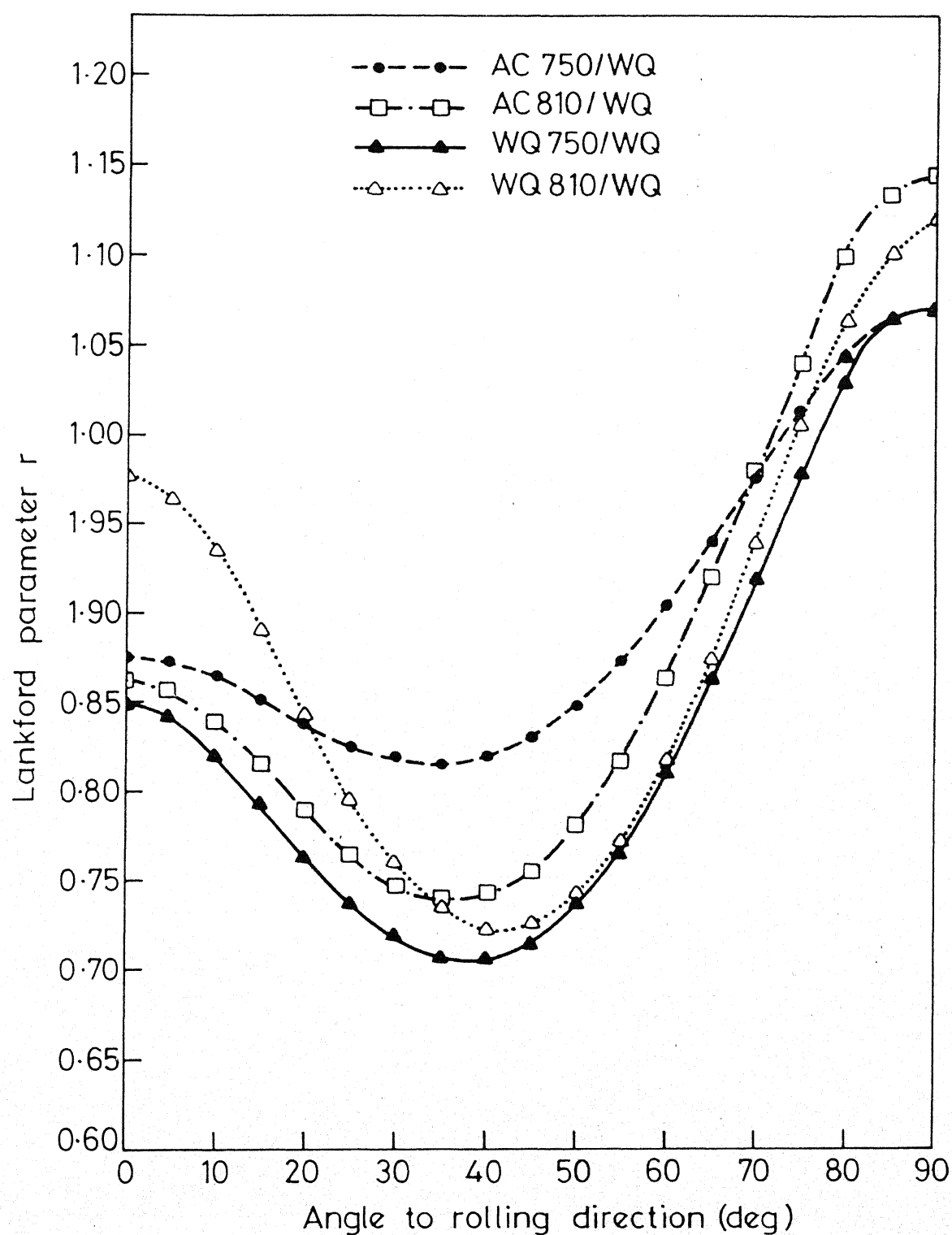


Fig.4.100 Variation in the Lankford strain ratio r with angle from the rolling direction for alloy A4, cold-rolled 60% and recrystallised at 800°C for 10 sec.

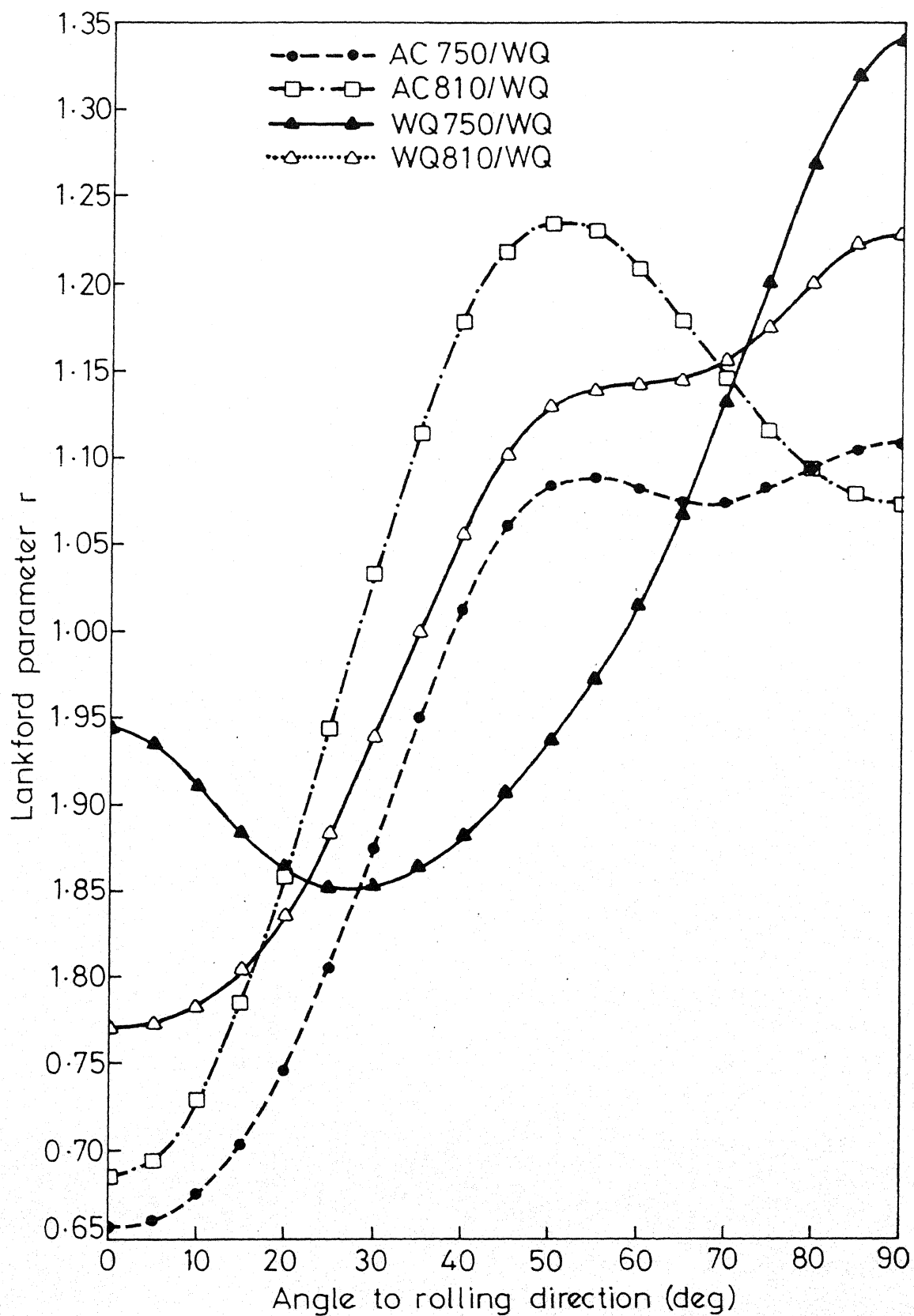


Fig.4.101 Variation in the Lankford strain ratio r with angle from the rolling direction for alloy A5, cold-rolled 60% and recrystallised at 650°C for 1 min.

Chapter V

Discussion

The foregoing pages deal with the experimental results of a systematic study of the recrystallisation behaviour and texture formation in three dual-phase steels, namely, A1, A4 and A5. The initial heat-treatments were so designed as to yield four different dual-phase structures in each alloy. Thus, for the three alloys, twelve such dual-phase distributions were arrived at, each one of which was then subjected to cold-rolling followed by recrystallisation treatments. The recrystallisation behaviour in each case was studied and the development of textures looked into in some detail. In this chapter the salient experimental observations are discussed critically.

5.1 Characterisation of the Starting Materials

The dual-phase steels, investigated in this study, consist essentially of ferrite and martensite. In alloy A5, the ferrite present is the one that existed during the intercritical holding and may be termed as "retained " or "old" ferrite. On the other hand, the total ferrite in alloys A1 and A4 is made up of both "old" ferrite and the ferrite which is formed during cooling from the intercritical temperatures, the "transformed" or "new" ferrite. The presence of new ferrite in alloys A1 and A4 and its absence in alloy A5 may be explained as follows. Table 3.1 shows that excepting carbon, whose amount is nearly the same in the three alloys, alloy A1 contains about 1.5% Si, alloy A4

contains about 1.5% Si and 1.5% Mn, whereas alloy A5 contains about 1.5% Mn as the dominant alloying elements. If sufficiently long intercritical annealing is allowed at a reasonably high temperature, manganese will tend to partition into the austenite phase, while silicon goes into the ferrite phase [194]. However, taking into consideration the intercritical annealing temperatures and times used in the present study, it may be argued that complete equilibrium will not be possible to attain, rather a paraequilibrium condition may be maintained. Thus, partitioning of the alloying elements may be limited to the austenite region adjacent to the old-ferrite/austenite interface, since the substitutional alloying elements are expected to diffuse rather slowly at these temperatures [43]. It is well-known that the addition of manganese makes the austenite more stable and slows down the reaction of austenite to form ferrite; on the other hand silicon makes the ferrite more stable and therefore accelerates this reaction.

When the rate of cooling is sufficiently high, as during quenching from the intercritical annealing temperature, the driving force for the austenite to "transformed" or "new" ferrite reaction will be large [195]. Depending on the composition of the alloy, this large driving force may or may not overwhelm the larger resistance for transformation to "new" ferrite of the austenite region near the "old" ferrite/austenite interface. Again, if lot of "old" ferrite is present by the end of the intercritical annealing, a large "old" ferrite/austenite interfacial area may help the process of growth of the "transformed" or "new" ferrite which possibly deposits epitaxially on the "old" ferrite without generating any large angle boundary between the two ferrite constituents. Optical micrographs

from the stained samples of alloy A1 (Figure 4.4) clearly support this idea. The volume percents of "new" ferrite likely to be formed in the three experimental alloys can now be rationalised on the basis of their chemical composition. Thus, alloy A1 which contains a large amount of Si but only a trace of manganese, will be expected to have a larger volume percent of "new" ferrite, for the same heat-treatment, as compared to alloy A4 which contains nearly the same amounts of silicon and manganese. For alloy A5 which contains a large amount of Mn but only a trace of silicon, the austenite is expected to be sufficiently stable not to transform into "new" ferrite during cooling from the intercritical annealing. The experimental results (Table 4.1) very well agree with these ideas.

Transmission electron microstructures taken from the three alloys, after different initial heat-treatments, did not reveal any basic difference in the structures of the constituent phases. The martensite in all cases was found to consist of dislocated laths while the ferrite was invariably found to contain a large density of very fine particles. A number of workers have reported the presence of very fine carbides (or carbonitrides) in the ferrite region of as-quenched dual-phase steels [38, 71, 196]. Fine particles ($\sim 20 \text{ \AA}$ wide, $\sim 100 \text{ \AA}$ long), presumably carbonitrides, have been observed in an as-quenched dual-phase steel having a composition similar to those of the three alloys under investigation [51]. It has been suggested that discontinuous precipitation of carbides results from the $\gamma \rightarrow \alpha + \text{carbide}$ reaction after the nucleation and growth stages of the "new" ferrite are complete upon quenching from the intercritical temperature. Figure 5.1 is a schematic

illustration of the sequence of interphase carbide precipitation in a quenched dual-phase steel. During quenching, the "new" ferrite nucleates epitaxially at the prior austenite/"old" ferrite interface and grows until the moving interface is saturated with respect to carbon (or vanadium, as in this case) to a critical level above which carbides nucleate along the moving interface [51]. Koo and Thomas [16] have reported that the particle size of the carbides will be coarser in the earlier stage of precipitation due to higher transformation temperature. If, on the other hand, the martensitic transformation proceeds before the nucleation of the interphase precipitation, the "new" ferrite will be sandwiched between martensite and "old" ferrite, leaving "precipitate free zones". The "old" ferrite also shows a very fine carbide precipitation inside.

The 0.2% Y.S. and the U.T.S. of the three alloys, after inter-critical annealing, are found to increase in the order: alloy A5 \rightarrow A1 \rightarrow A4 (Table 4.2). The highest strength properties of alloy A4 can be correlated to the presence of the maximum amount of martensite in this alloy. Although the volume percents of martensite in the alloys A1 and A5 are very nearly the same, the higher strength of A1 is very likely due to significant solid solution hardening of the ferrite phase due to silicon. High strength of ferrite also contributes to the total strengthening of the alloy A4. In fact, the microhardness values of the ferrite phase have been found to be significantly higher in alloys A1 and A4 as compared to alloy A5 (Table 4.3). The values for the strain-hardening parameter 'n' have been found to be the lowest for alloy A4 (Figure 4.12). For the other two alloys, namely A1 and A5, 'n' is found

to have rather low values for the AC 810/WQ material and substantially higher values for the AC 750/WQ material. In fact, it can be seen from Table 4.1 and Figure 4.12 that values of 'n' can be correlated quite well with the volume percents of martensite in the heat-treated dual-phase materials. In fact, higher the martensite volume fraction, lower is the 'n' value. Previous work [197] on the alloy A4 showed that it exhibits a strong Bauschinger effect over a range of tensile prestrain. The Bauschinger effect was found to increase with increasing martensite volume content upto about 20%, beyond which it showed a decrement. It was suggested that back stresses generated due to dislocations accumulated at martensite islands during tensile prestrain might be responsible for the large Bauschinger effect. However, when the martensite islands are situated too close, the groups of dislocations at the islands may result in lower magnitude of long range back stresses due to partial cancellation of back stresses through mutual interactions. The decrease in the magnitude of the Bauschinger effect when the martensite volume percent exceeded around 20% was suggested to be due to such a relaxation effect. There is little doubt that a similar explanation may be put forward in order to explain the variation of the strain-hardening parameters for the three alloys as a function of the corresponding martensite contents.

5.2 Microstructures and Textures of the Deformed Alloys

It has been found that, irrespective of the different initial heat-treatments, the microstructures in any of the cold-deformed alloys are remarkably similar. In all the cold-worked alloys, the original ferrite grains and, in most cases, even the martensitic regions have

been observed to be elongated along the direction of rolling. The structural features were found to be the finest in alloy A4, presumably due to the highest volume fraction and proximity of the martensite particles in that alloy. In all the alloys, the deformed ferrite grains were found to consist of a large number of nearly parallel cells with a high dislocation density. In contrast to the alloys A1 and A4, the ferrite cell-structure in many places in the cold-deformed alloy A5 showed distinct signs of recovery leading to the formation of subgrains. This difference is possibly due to the fact that the ferrite in alloy A5 is much softer as compared to the ferrites in the other two alloys (Table 4.3).

Distinct differences have been obtained in the deformation textures of the three alloys as described in detail in Chapter IV. Thus, the sharpest deformation textures were obtained for alloy A1 and the weakest for alloy A4 while intermediate values of texture intensities were found for alloy A5 (Figures 4.19-4.22). It is interesting to note that the experimentally determined values of the volume percents of martensite in the intercritically annealed microstructures of the three alloys are in the increasing order A1 \rightarrow A5 \rightarrow A4 (Table 4.1). Thus, it may be tempting to come to the conclusion that the intensity of the deformation texture increases in the order A4 \rightarrow A5 \rightarrow A1 as possibly because the available total volume of ferrite, which may undergo deformation during rolling, increases in the same order in the three alloys.

It can further be seen in Figures 4.19-4.22 that, in general, in any particular alloy, the cold-rolled texture of the material produced by the lower temperature (750°C) intercritical annealing is much sharper as compared to the texture of the material intercritically annealed at

higher temperature (810°C). This can again be related, in a manner similar to the above, to the differences in the martensite or ferrite contents of the materials produced by two different intercritical annealing temperatures. Evidently, martensite, being the harder phase, its presence in the microstructure is expected to inhibit easy plastic flow in the ferrite matrix. Thus, more the volume fraction of martensite in the alloy, more difficult it should be to systematically reorient the grains in the matrix (by plastic deformation) in order that a sharp texture may be produced. This coupled with the difference in the available ferrite content in the microstructure may explain the observed differences in the sharpness of the deformation textures.

The volume percent of martensite in the microstructure alone cannot determine the observed differences in the sharpness of the deformation texture. This will be clear if a comparison of the texture intensities is made, in the same alloy, for materials subjected to the AC/WQ treatment as well as the WQ/WQ treatment. Thus, in case of alloy Al (Figure 4.20), WQ 750/WQ and WQ 810/WQ materials have been found to possess a sharper texture as compared to the AC 750/WQ and AC 810/WQ materials, although the martensite contents of the former are marginally higher as compared to the latter. However, in the overall context, the present results clearly bring out the detrimental effect of martensite in producing a sharp deformation texture in the experimental alloys.

Detailed analysis of the O.D.F. results obtained from the cold-deformed alloy Al (Figures 4.23-4.30) indicates that although the intensities of individual components in $\{111\} \langle uvw \rangle$ texture may be very strong indeed, they do not comprise a fibre. On the other hand, reasonably strong

$\langle 111 \rangle$ || ND fibre textures have been observed in both the alloys A4 and A5 — the fibre in alloy A5 being much stronger in intensity as compared to the one in alloy A4 (Figures 4.31-4.46). The alloy A4 also shows two rather weak and incomplete fibres which may be described as $\{337\} \langle uvw \rangle$ and $\{11, 11, 4\} \langle uvw \rangle$ respectively. The former is not very well-developed in the alloys A1 and A5. The latter may be considered as a weak and incomplete fibre in alloy A1, whereas this is not so well-developed in alloy A5.

Hutchinson and Dillamore [198] have suggested that during cold-deformation of a polycrystalline metal, the crystals rotate towards the positions of stability which will ultimately constitute the deformation texture. Using the model proposed by Dillamore and Katoh [171], they have shown that the stable end-components of the rolling texture for a B.C.C. metal, like iron, will be $(112) [1\bar{1}0]$ and $(11, 11, 8) [\bar{4}, \bar{4}, 11]$. It is expected that the real texture will be spread around these stable ideal orientations. The orientation $(112) [1\bar{1}0]$ is only 4° away, in the Euler space, from the orientation $(337) [1\bar{1}0]$ which is one of the components of the weak $\langle 337 \rangle$ || ND fibre-texture found in the deformed alloy A4. The $(11, 11, 8) [\bar{4}, \bar{4}, 11]$ component, however, has not been found in the experimental deformation texture of any of the three alloys. This ideal orientation has the Euler angles $\psi_1 = 90^\circ$, $\phi = 63^\circ$ and $\psi_2 = 45^\circ$. The component $(11, 11, 4) [\bar{2}, \bar{2}, 11]$ which forms a part of the weak and incomplete $\{11, 11, 4\}$ -type of fibre texture in alloy A4, corresponds to the Euler angles $\psi_1 = 90^\circ$, $\phi = 76^\circ$ and $\psi_2 = 45^\circ$. The above two orientations are thus about 13° apart in the Euler space and hence the observed orientation $(11, 11, 4) [\bar{2}, \bar{2}, 11]$ may be considered to lie within the

spread around the theoretical ideal orientation, namely, $(11, 11, 8)$ $[\bar{4}, \bar{4}, 11]$.

The rolling texture components obtained for the three experimental alloys are not very different from typical rolling textures of iron and steels. For a 50% cold-rolled dual-phase steel, Bunge et al. [176] have observed that the texture in the as-rolled condition consists of two fibre texture components, namely, $A = \{111\} \langle uvw \rangle$ and $B = \{hkl\} \langle 110 \rangle$. For A there exists a rotational symmetry about a $\langle 111 \rangle$ direction which is parallel to the normal direction, whereas for the component B the rotation is about a $\langle 110 \rangle$ direction parallel to the rolling direction. Hu [161] has reported that for a deep-drawing quality phosphorus steel, the cold-rolling texture contains a very strong $(\bar{1}12) [\bar{1}\bar{1}0]$ component, a fairly strong $(001) [1\bar{1}0]$ component, and a prominent $\{111\} \parallel$ ND fibre texture in addition to another fibre of the type $\{hkl\} \langle 110 \rangle$ which extends from $(001) [1\bar{1}0]$ to slightly beyond $(331) [1\bar{1}0]$, this last orientation has the Euler angles, $\psi_1 = 0^\circ$, $\phi = 77^\circ$ and $\psi_2 = 45^\circ$, which is just 1° off from the orientation $(11, 11, 4) [1\bar{1}0]$ that forms a part of the weak and incomplete $\langle 11, 11, 4 \rangle \parallel$ ND fibre texture in alloy A4.

5.3 Microstructures and Textures of the Recrystallised Alloys

Textural results have shown that the deformation and recrystallisation textures in any of the experimental alloys are very similar, indicating that the recrystallised grains must have been formed in situ from cold-deformed regions having the same or nearly the same crystallographic orientation. This is also corroborated by the electron microscopy results from the partially recrystallised samples.

A look at the deformation texture plots (Figures 4.19-4.22) as well as the recrystallisation texture plots (Figures 4.55-4.63) clearly indicates that the intensity of texture is invariably weakened consequent upon recrystallisation in both the alloys Al and A4. Though the same is true for alloy A5 for the 650°C recrystallised materials, the texture definitely shows a noticeable sharpening after the 800°C anneal.

A comparison of the $f(g)$ versus ϕ curves for both deformed and recrystallised Al alloy (Figures 4.23-4.26 and 4.64-4.67) shows a consistently high value of $f(g)$ between $\phi = 0^\circ$ and 55° , in the section $\psi_1 = 0^\circ$, $\psi_2 = 45^\circ$, for the recrystallised materials. This indicates that reasonably large volume fraction of the recrystallised material must have acquired orientations starting from (001) $[1\bar{1}0]$, going through (113) $[1\bar{1}0]$, (337) $[1\bar{1}0]$ and (112) $[1\bar{1}0]$ to (111) $[1\bar{1}0]$. The near flat nature of these plots for the recrystallised materials also indicates that the chances of encountering grains of such diverse orientations are nearly equal. The same plots also show that there is a substantial intensity for the (11, 11, 4) $[1\bar{1}0]$ component and a moderate intensity for the (11, 11, 4) $[\bar{2}, \bar{2}, 11]$ component. Intensities of these orientations are noticeably sharper in the recrystallised materials as compared to the corresponding cold-deformed materials, indicating that nuclei of these orientations have grown during recrystallisation. The $\{111\}$ $\langle uvw \rangle$ orientations are found to have reasonably strong intensities, but they do not constitute a complete fibre texture. The plots of $f(g)$ versus ψ_1 for the alloy Al (Figures 4.68-4.71) also indicate that the intensity of the $\{111\}$ incomplete fibre always has a higher value for the material recrystallised at the higher temperature of 800°C as compared to the material recrystallised

at the lower temperature of 650°C . In general, a reverse trend is obtained for the components of the rather weak $\{11, 11, 4\}$ incomplete fibre. On the other hand, perceptible variation in intensity for the $\{337\} \langle uvw \rangle$ components as a function of the recrystallisation temperature could not be noticed. It may be recalled here that electron microstructures for the Al alloy, recrystallised at the lower temperature, invariably show the presence of some fine precipitates, whose identity could not be established, whereas the density of such precipitates is found to decrease very drastically when the alloy is recrystallised at the higher temperature (Figures 4.49b, 4.50d). Finely dispersed particles are normally known to reduce recrystallisation kinetics having a greater retarding influence on nucleation than on growth [116]. Out of the available orientations in the cold-rolled alloy, the $\{111\}$ texture components should nucleate rather early and therefore will have a long available time for growth before impingement occurs [86]. Since the volume fractions of crystallites in the deformed material having such orientations are also the largest, it is therefore no wonder that there will be a predominance of the $\{111\} \langle uvw \rangle$ components in the recrystallisation texture. The observed lower intensity of the $\{111\}$ texture components at the lower recrystallisation temperature of 650°C may be due to the presence of the fine particles in the deformed ferrite matrix that may hinder the growth of the $\{111\}$ recrystallised grains also. In the absence of such particles at the higher temperature of recrystallisation (800°C), the more numerous $\{111\}$ nuclei will have a more easy and uninterrupted growth giving rise to a sharper $\{111\}$ texture.

It may be recalled at this stage that in the previous chapter it was mentioned that the martensite content in an alloy after full recrystallisation (at and above the recrystallisation temperature of 750°C) was found to be invariably higher than the amount present in the original intercritically annealed condition. For comparison with the martensite contents of the three starting alloys (differently heat-treated) (Table 4.1), the volume fractions of martensite in the same materials after the recrystallisation anneal at 800°C were determined and are given in Table 5.1. A series of typical micrographs for the A4 alloy, recrystallised at 800°C , are also shown in Figure 5.2(a-d).

Table 5.1

Volume Percent Martensite in Fully Recrystallised (at 800°C) Alloys A1, A4 and A5

Alloy designation	Volume percent martensite
A1/AC 750/WQ	22.0
A1/AC 810/WQ	25.0
A1/WQ 750/WQ	26.0
A1/WQ 810/WQ	27.0
A4/AC 750/WQ	46.0
A4/AC 810/WQ	60.0
A4/WQ 750/WQ	58.0
A4/WQ 810/WQ	66.0
A5/AC 750/WQ	26.0
A5/AC 810/WQ	30.0
A5/WQ 750/WQ	35.0
A5/WQ 810/WQ	37.0

The amount of martensite present in the 650°C annealed material is expected to remain the same as for the intercritically annealed samples. Evidently, prior cold-work of dual-phase samples leads to a faster diffusion of the alloying elements, especially near the austenite-ferrite interfaces, in the $\alpha + \gamma$ region, and this may shorten the time to reach equilibrium volume fraction of austenite (martensite) at that temperature. The result will be an increase in the martensite content of the resulting dual-phase steel. This is expected to have a serious implication in that the volume of recrystallising ferrite at the higher temperature of 800°C will be less than its counterpart at the lower temperature of 650°C. Thus, whether the intensity of the $\{111\} \langle uvw \rangle$ components will increase or decrease at the higher recrystallisation temperature will depend on the relative strength of the two factors, namely, a decrease in the density of precipitate particles in ferrite allowing more rapid growth of the recrystallisation nuclei and an increase in the austenite (martensite) volume fraction at the recrystallisation temperature giving rise to a decrement in the recrystallising volume fraction of the ferrite constituent. In alloy A1 the former effect seems to be predominant, may be due to the fact that the volume percent of ferrite does not decrease significantly due to the 800°C anneal.

The observed higher intensity of the $\{111\} \langle uvw \rangle$ texture components after the 800°C anneal in alloy A5 may be explained in a similar manner. In this alloy too, the variation in the volume percents of recrystallising ferrite at the two annealing temperatures is not found to be large.

In contrast to these results, in alloy A4, the intensities of the $\{111\} \langle uvw \rangle$ components have been found to be consistently higher at the

lower temperature of recrystallisation, namely 650°C . A look at Tables 4.1 and 5.1 clearly shows that in this alloy there is a very significant increment in the volume percent of martensite in the material recrystallised at 800°C from the initial values. Already, in the intercritically annealed A4 alloy, the inter-martensite particle distance was nearly half the corresponding values for the A1 and A5 alloys. This distance narrowed down substantially during the cold-work and further narrowing down as a result of a larger volume fraction of martensite (austenite) due to the 800°C recrystallisation anneal, is expected to affect the growth of the $\{111\} \langle uvw \rangle$ nuclei substantially. This effect may be much stronger than the other effect due to a decrement of the density of precipitate particles in ferrite at 800°C .

A look at Figures 4.76-4.79 also indicates the presence of a weak and incomplete $\{11, 11, 4\} \langle uvw \rangle \parallel \text{ND}$ as well as a not so well-developed and weak $\{337\} \langle uvw \rangle \parallel \text{ND}$ fibres. In general, the intensities of the $\{337\} \langle uvw \rangle$ components are found to be higher as compared to the $\{11, 11, 4\} \langle uvw \rangle$ components till $\psi_1 \approx 50^{\circ}$, beyond which the intensities of the $\{11, 11, 4\} \langle uvw \rangle$ components become decidedly higher. Similar behaviour has also been observed in alloys A1 and A5 (Figures 4.68-4.71 and 4.84-4.87). A look at the plots for the corresponding deformation textures (Figures 4.27-4.30, 4.35-4.38 and 4.43-4.46) also reveals the same trend indicating that in situ recrystallisation occurs at both the annealing temperatures.

The results of the recrystallisation kinetics studies for the three alloys (Figures 4.88-4.93) clearly indicate that there may be two distinct stages during the process of recrystallisation. Roughly speaking

the change-over takes place at a recrystallised volume fraction (x) lying between 0.5 and 0.7 depending on the alloy and the recrystallisation temperature. The slope of any line, ' m ', in the Avrami plots, denotes a time exponent which is supposed to depend upon the geometrical character of the recrystallisation process itself as well as the time dependence of the nucleation rate, i.e., whether the recrystallisation is one, two or three dimensional [176]. A low value of ' m ' lying between approximately 0.5-1.0 has been found for the first stage and a higher ' m ' value between, on an average, 1.5 and 3.0 has been found for the second stage of recrystallisation. If, at the beginning of the recrystallisation, nucleation rate is high and then drops to zero, the value of the time exponent, ' m ' in the Avrami relationship should equal d , the dimensionality of the growth of the recrystallisation nuclei, whereas if the nucleation rate is constant during the entire process of recrystallisation, then $m = d + 1$ [176]. It is expected that the actual behaviour should lie in between these two limiting cases. Thus, the experimental values of ' m ' at the first stage (0.5-1.0) should indicate a dimensionality of about 1, at least in the early stages of the recrystallisation process. This will be followed by a 2 or 3-dimensional growth of the nuclei at the later stages. Transmission electron micrographs taken during various stages of recrystallisation (Chapter IV) indicated that, to start with, the elongated subgrains grow in a direction perpendicular to themselves and later on, when they have become sufficiently large, growth along two or all the three dimensions takes place.

Bunge et al. [176] have reported a single value of ' m ' (1.866) at all temperatures (between 680°C and 850°C) for the first half of the

recrystallisation process for their experimental alloy. The discrepancy between their results and the results of the present investigation may be due to the fact that Bunge et al. derived their recrystallisation kinetics from the changes in the overall hardness values of the dual-phase structures with the progress of recrystallisation. On the other hand, the present observations are based on precise microhardness values of the ferritic phase alone; and this is considered to be more relevant since it is the recrystallisation behaviour of the deformed ferrite that is being investigated.

Activation energies ranging approximately between 16.0 and 20.0 KCal $^{\circ}\text{mol}^{-1}$ have been obtained from the Arrhenius plots of $\ln t_{0.5}$, $\ln \tau$ or $\ln t_{0.8}$ versus $1/T$ as shown in Figures 4.88-4.93. These values are quite close to the value of 20.1 KCal $^{\circ}\text{mol}^{-1}$ for the diffusion of carbon in $\alpha\text{-Fe}$ [199]. Hence the present results imply that the kinetics of recrystallisation may be determined by the carbide particle coarsening. It has been reported that in Nb, Ti and V microalloyed steels, the activation energies for the recrystallisation process are equal to the activation energies for the diffusing microalloying elements in $\alpha\text{-Fe}$ [200, 201] which are much larger than for carbon. Thus, the present results signify that the fine particles seen in the microstructures of the present alloys may be predominantly of iron carbides and not vanadium carbonitrides as was expected previously. Similar results have also been reported by Bunge et al. [176] for their dual-phase steel containing, amongst other solutes, about 0.72% Cr. If that be the case, it is quite easy to understand that these carbide particles should go into solution when the cold-worked alloys are recrystallised at and

above 750°C, leaving the ferrite reasonably clean of the precipitate particles.

5.4 Formability Characteristics of the Alloys

A look at the \bar{r} values of the three alloys, in the recrystallised condition (Table 4.6), reveals that alloy A1 has $\bar{r} < 1$ for any of the initial heat-treatment conditions. Alloy A4 has $\bar{r} > 1$ for the 650°C recrystallised material, whereas alloy A5 has $\bar{r} > 1$ for the materials recrystallised both at 650°C and 800°C. The maximum value of \bar{r} (1.27) has been obtained for alloy A5/AC 750/WQ recrystallised at 800°C. Thus, out of the three alloys, A5 seems to have a slight edge over the other two in terms of deep-drawability. It may be recalled that, in general, the sharpest values for the intensity of the $\langle 111 \rangle \parallel$ ND fibre texture have been obtained for the A5 alloy recrystallised at 800°C. Figure 4.11 and Table 4.2 show that, out of three alloys, alloy A5 is of the lowest mechanical strength. Table 4.6 also shows that this alloy has a large planar anisotropy, as revealed by high values of Δr .

The minimum values of Δr have been obtained for the alloy A1. This alloy is mechanically stronger than alloy A5 but has the lowest set of \bar{r} values.

In terms of strength, \bar{r} and Δr values, alloy A4 may be considered to have the optimum properties out of the three alloys. Alloy A4 is the strongest of the three alloys and has a very good ductility (Table 4.2). After recrystallisation at 650°C, the highest \bar{r} value (1.15) has been obtained for the AC 810/WQ material. The Δr values have also been found to be reasonably low. The $f(g)$ value for the $\langle 111 \rangle \parallel$ ND fibre in this

material has been found to be about 3.0 (Figure 4.77). Figure 4.84 shows that the $f(g)$ value obtained for the $\langle 111 \rangle \parallel$ ND fibre in A5/AC 750/WQ material (showing the largest value of $\bar{r} = 1.27$) is slightly more than 5.5. Thus, the intensity of the $\{111\}$ fibre texture in alloy A4, although nearly half of the corresponding intensity in alloy A5, gives a somewhat comparable value of \bar{r} in the former as compared to the latter. These results suggested that it may be worthwhile to try to produce a sharper $\langle 111 \rangle \parallel$ ND fibre texture in alloy A4. With this idea in mind, samples of A4/AC 750/WQ materials were subjected to 80% cold-reduction by rolling. In this case AC 750/WQ samples were used instead of the AC 810/WQ samples (for which the highest value of \bar{r} was obtained in alloy A4) in order to keep the amount of the deleterious martensite content to the minimum. The cold-rolled samples were then recrystallised at a temperature of 700°C , the temperature being intentionally kept below the $\alpha + \gamma$ range. Grain-growth after primary recrystallisation is known to sharpen the $\{111\}$ fibre texture in steels [125]. Keeping this in view, the cold-rolled samples were recrystallised at 700°C for prolonged periods of 24 hours and 100 hours. The relevant texture plots for the cold-rolled and recrystallised materials are shown in Figures 5.3 to 5.5. It is interesting to note from these figures that a partial $\langle 111 \rangle \parallel$ ND fibre with an $f(g)_{\text{max}}$ value of nearly 6.0 is obtained for the 80% cold-rolled material, and this is more than 1.5 times the intensity value of the same fibre in the 60% cold-rolled material. The recrystallised materials also exhibit a nearly perfect $\{111\}$ fibre texture with $f(g)$ values lying around 5.0-5.5. The material recrystallised for 24 hours shows a little bit sharper intensity as compared to the one recrystallised for 100 hours.

The intensity of the fibre in these recrystallised samples is about 1.5-2.0 times the intensity of the same fibre obtained in the previously recrystallised samples of alloy A4 after 60% cold-reduction. If the sharpness of the $\langle 111 \rangle \parallel$ ND fibre were the only criterion for achieving a large value of \bar{r} , then these samples should possess much larger values of \bar{r} as compared to their counterparts mentioned previously. However, a look at Figure 5.6 clearly shows that the \bar{r} values of these latter samples are less than unity, i.e., even worse as compared to the samples cold-rolled 60% and then recrystallised.

Thus, it is clear that in dual-phase steels sharpness of the $\{111\}$ fibre texture is not the sole criterion for achieving a large \bar{r} value.

Kurihara et al. [82] showed that, in dual-phase steels, the degradation of the \bar{r} value depended on the volume fraction and proximity of the martensite islands and the hardness ratio for the martensite and ferrite constituents. They suggested that \bar{r} value should decrease as each of these factors increases. In the course of the present investigation, it was not possible to measure the microhardness values for the martensitic phase, although the microhardnesses of the ferrite phase in the twelve initial structures were accurately measured. These values are given in a tabular form in Table 4.3. This table shows clearly that the microhardness of ferrite increases in the order A5 \rightarrow A4 \rightarrow A1. In fact, the larger values of microhardnesses of ferrite in alloys A1 and A4 are quite comparable and may be assigned to the solid solution hardening of ferrite by the large amount of silicon in these two alloys. The alloy A5, with a trace of silicon only, should give rise to a softer ferrite which has been obtained in practice. Even without going into the actual

hardnesses of the martensitic phase in the twelve initial structures, and making the reasonable assumption that for all the three alloys, for a particular type of heat-treatment (like AC 750/WQ, AC 810/WQ etc.) the martensite in the dual-phase structures will have comparable hardness values, it can be readily visualised, from Table 4.3, that the ratio of the hardnesses of martensite and ferrite should be substantially higher for alloy A5 as compared to those of A1 and A4. According to Kurihara et al. \bar{r} should be higher for A1 and A4 as compared to A5, which is exactly opposite to the results obtained in the present investigation. Again, the volume fraction of martensite and proximity of the martensite islands is much more in alloy A4 as compared to the alloy A1, with possibly not much different martensite/ferrite hardness ratios in them. But the \bar{r} -value has been found to be somewhat better in the A4 alloy. The above clearly shows that the reasons for the attainment of rather poor \bar{r} -values in dual-phase steels are far from clear.

Hutchinson [84] has made a theoretical analysis of the deep-drawing characteristics of dual-phase steels. His work clearly showed that relative to comparable ferritic steels, dual-phase steels have a lower normal anisotropy. According to him, this decrease in anisotropy is not due to any dilution of the ferritic texture by the presence of the hard martensitic phase. The martensite particles are supposed to produce an increment of isotropic strengthening, whose magnitude is a function of the volume fraction, dispersion and hardness of the martensite constituent. According to Hutchinson's analysis, the \bar{r} -value of dual-phase steels is a function of the quantity $\Delta\sigma/\sigma^*$ where, σ^* is the yield stress of the ferritic matrix and $\Delta\sigma$ is the increment of isotropic hardening due to the

martensitic constituent. In fact, this analysis predicts that \bar{r} should decrease with increase in the value of $\Delta\sigma/\sigma^*$. It would be interesting to see how this prediction compares with the present experimental results. The martensite volume fraction and its distribution in the alloys A1 and A5 have not been found to be significantly different in the intercritically annealed condition. The strengths of the martensitic phase in both the alloys are also supposed to be comparable since both are basically composed of dislocated laths. Hence, as a rough approximation, $\Delta\sigma$ value can be taken as nearly the same for both the alloys. Although the yield stress values of the ferritic phase are not available, the microhardness of ferrite in alloy A1 has been found to be ~ 1.5 times the microhardness of ferrite in alloy A5. Hence σ^* value for alloy A5 should be sufficiently low as compared to the σ^* value for alloy A1. It all boils down to the conclusion that $\Delta\sigma/\sigma^*$ is expected to be much higher in alloy A5 as compared to alloy A1. According to Hutchinson's analysis, this should lead to a lower value of \bar{r} for alloy A5 as compared to alloy A1. However, this is exactly the opposite to what has been obtained experimentally in the present work. It should be noted here that, in the present case, to test Hutchinson's hypothesis, comparison between two different steels (having different chemical composition) have been made. The predictions, however, seemed to tally quite well with his own experimental results on one particular steel composition that was given various heat-treatments to produce a variety of martensite dispersion and amount. It should also be taken into account that the maximum amount of martensite produced in the steel used by Hutchinson was limited to about 20%, whereas, in general, for all the different heat-treatments, the present series of

alloys contain more than that amount of martensite. Therefore, it may not be very proper to try to test Hutchinson's hypothesis on the basis of the data obtained in the present investigation. Nevertheless, the present work seems to emphasize that careful experimentation on a much larger number of dual-phase steel compositions with proper control of the various parameters may be beneficial to have a more basic understanding of the problem of achieving satisfactory deep-drawability in dual-phase steels.

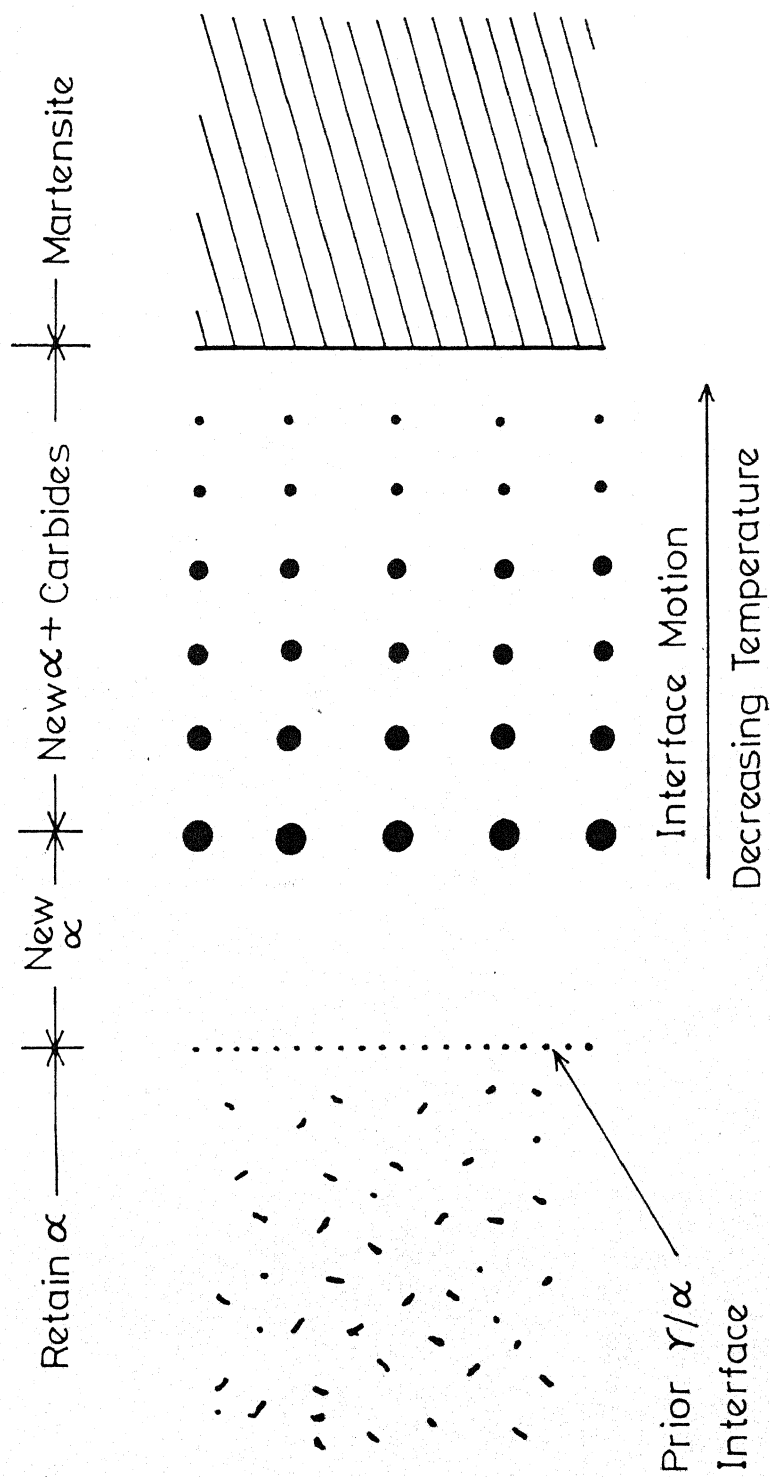


Fig.5.1 Schematic illustration of the sequence of interphase carbide precipitation in a quenched dual-phase steel.[51]

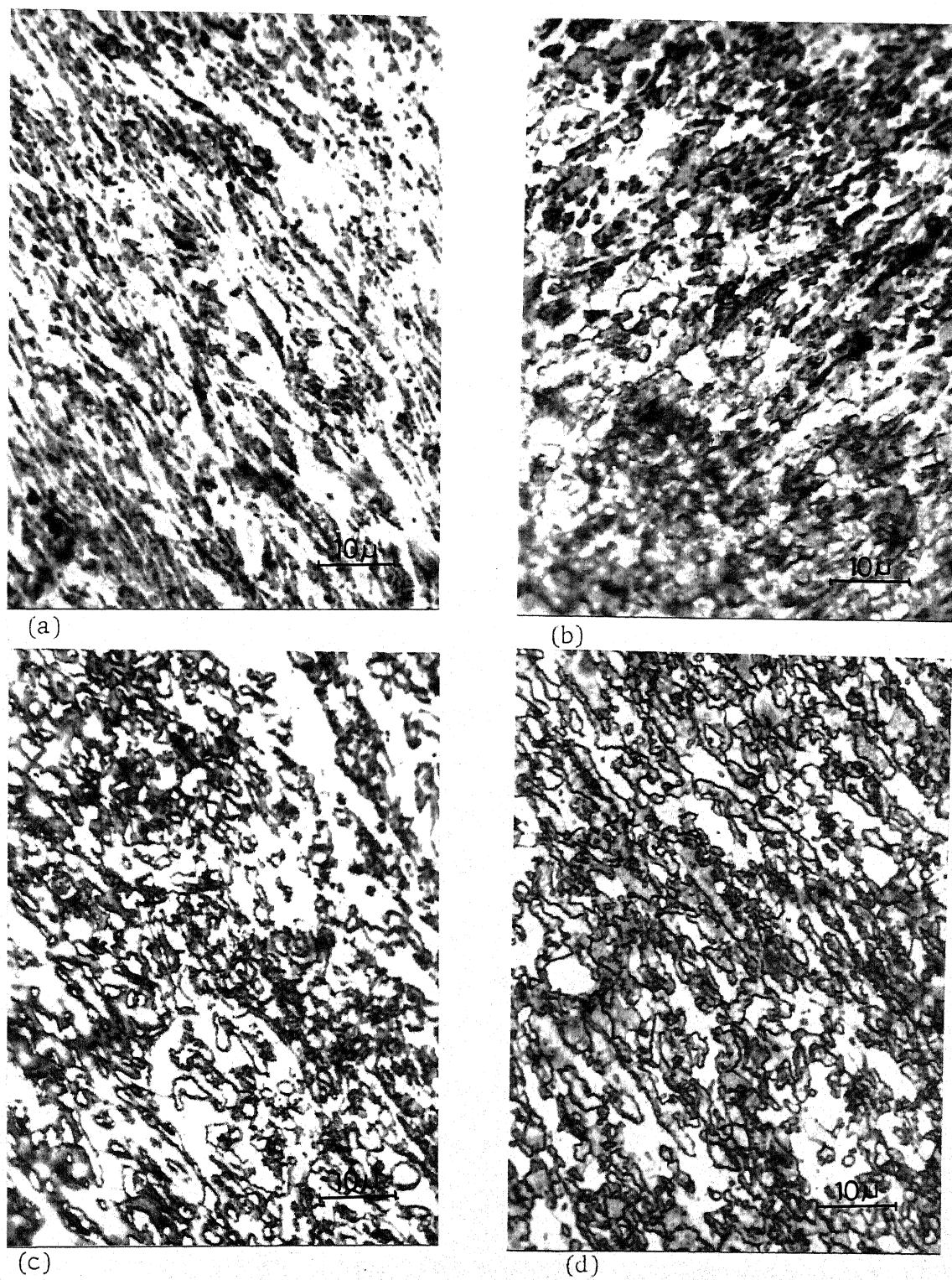


Fig. 5.2 A series of typical micrographs for the alloy A4, recrystallised at 800°C

(a) WQ 810/2 sec	(b) WQ 810/5 sec
(c) WQ 810/7 sec	(d) WQ 810/10 sec.

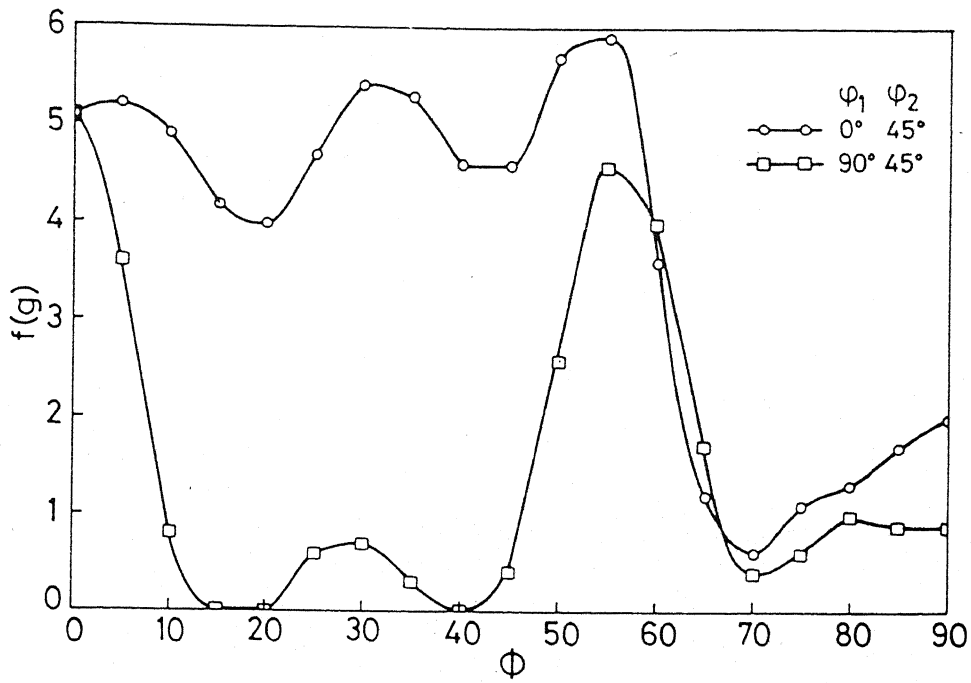


Fig.5.3a Variation of $f(g)$ with Φ along different Φ_1/Φ_2 lines for A4/AC 750/WQ after 80pct.cold-rolling.

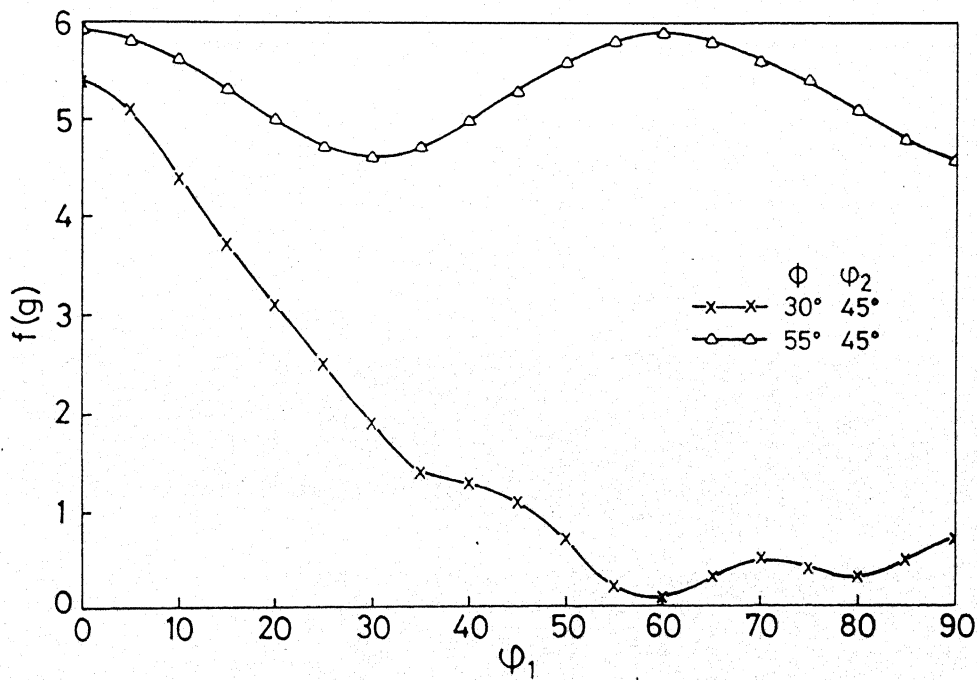


Fig.5.3b Variation of $f(g)$ with Φ_1 along different Φ/Φ_2 lines for A4/AC 750/WQ after 80pct.cold-rolling.

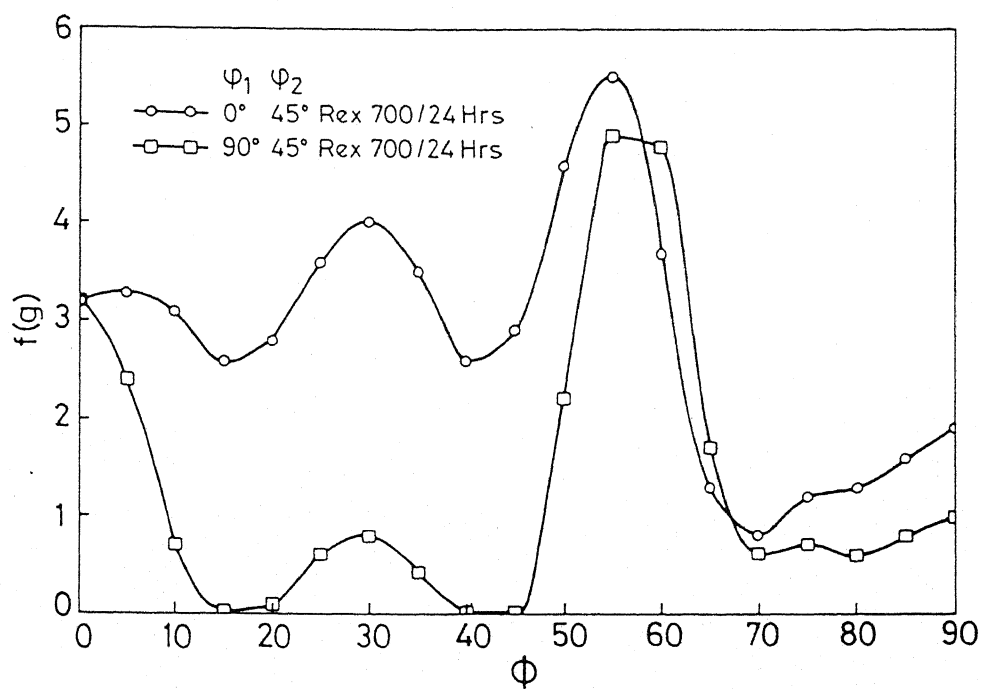


Fig. 5.4a Variation of $f(g)$ with Φ along different Φ_1/Φ_2 lines for A4/AC750/WQ after recrystallisation.

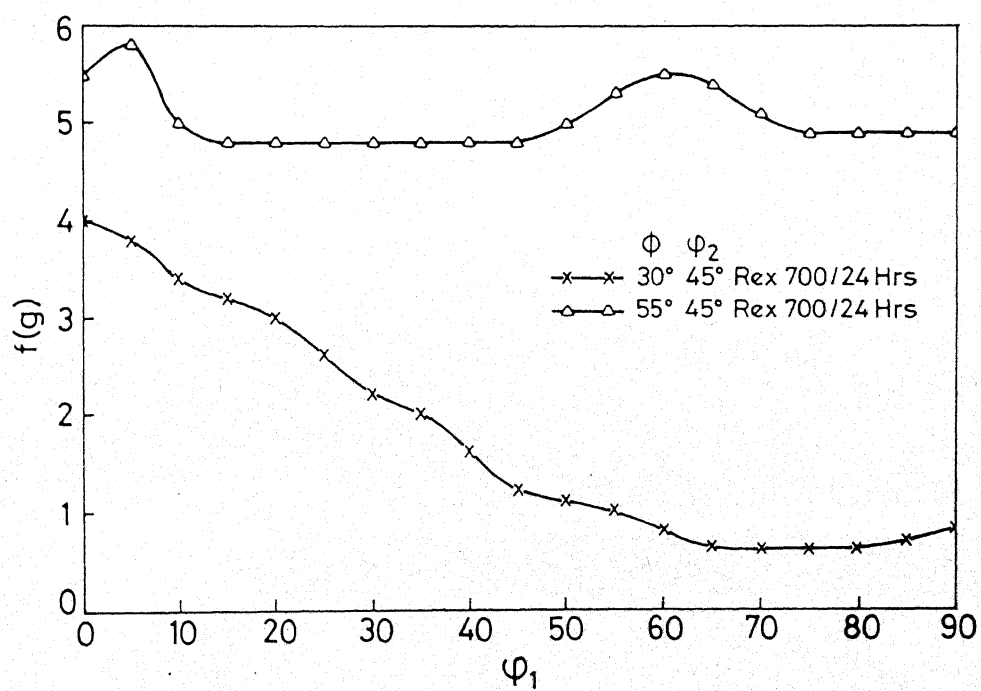


Fig. 5.4b Variation of $f(g)$ with Φ_1 along different Φ/Φ_2 lines for A4/AC750/WQ after recrystallisation.

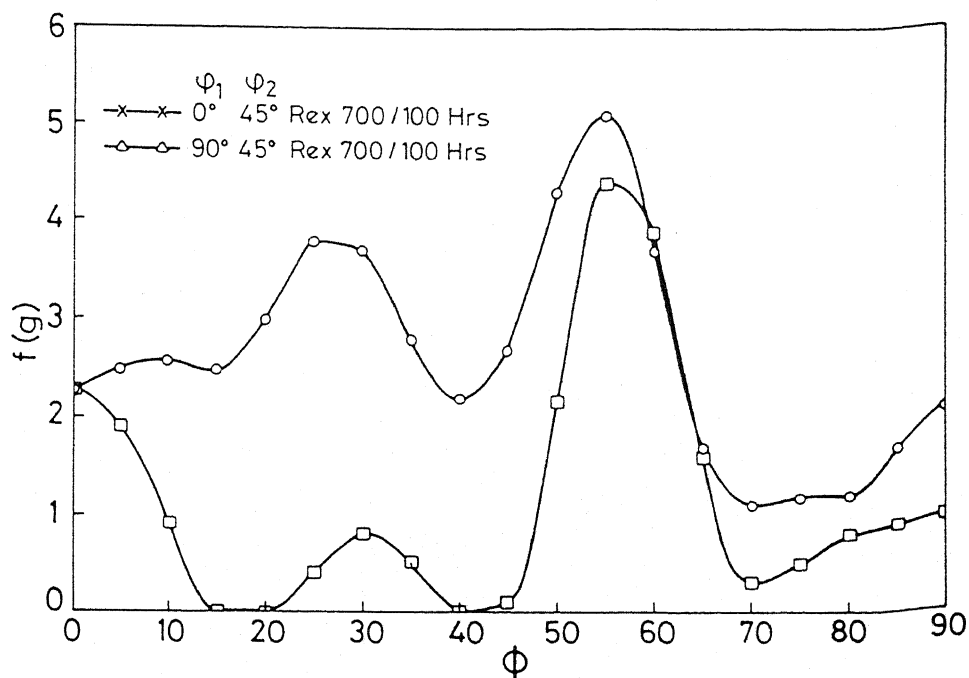


Fig. 5.5a Variation of $f(g)$ with Φ along different Φ_1/Φ_2 lines for A4/AC 750/WQ after recrystallisation.

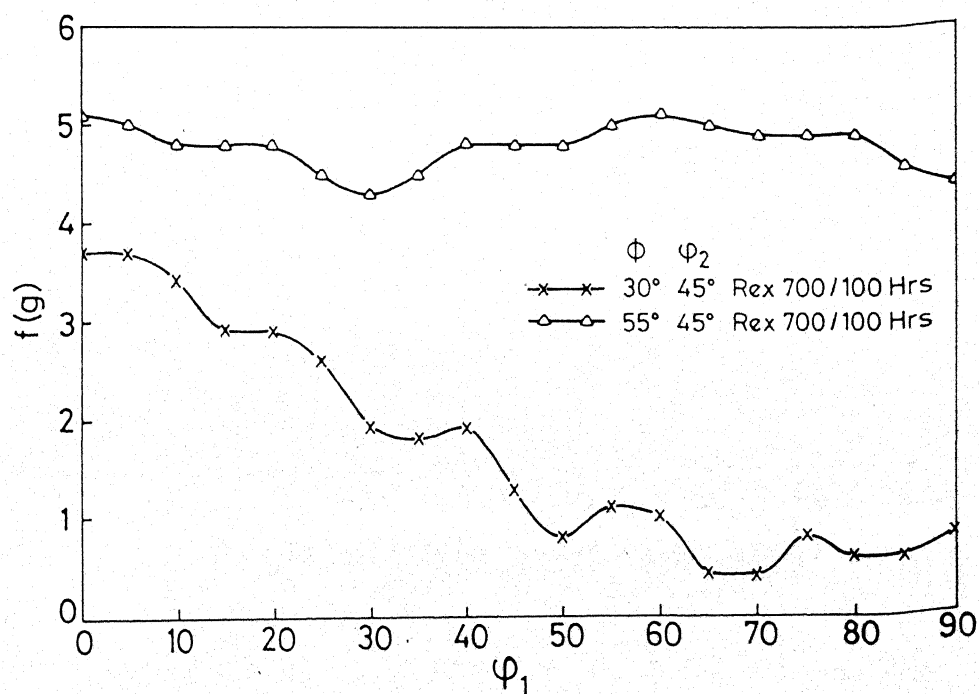


Fig. 5.5b Variation of $f(g)$ with Φ_1 along different Φ/Φ_2 lines for A4/AC 750/WQ after recrystallisation.

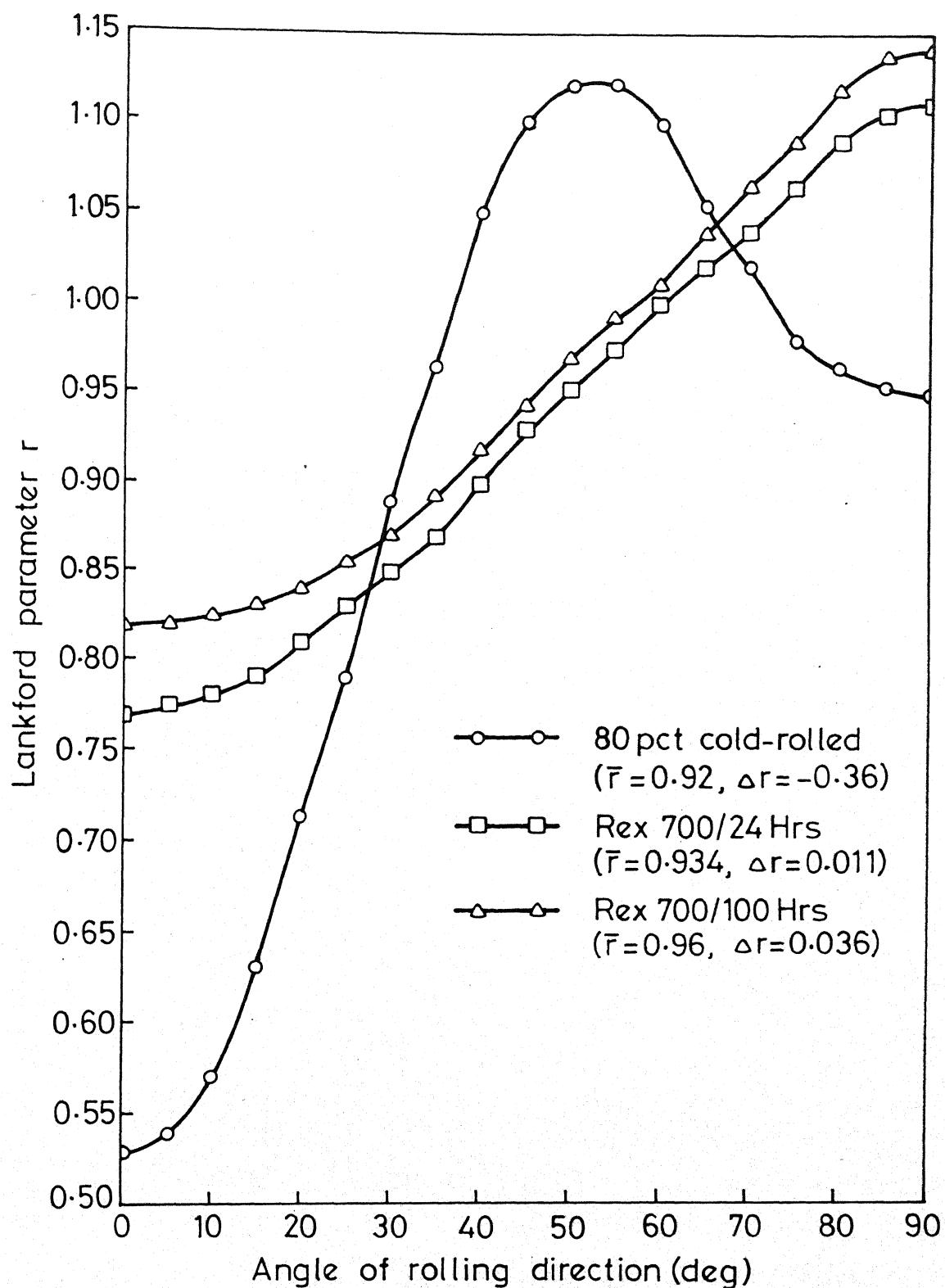


Fig.5.6 Variation in the Lankford strain ratio r with angle from the rolling direction for alloy A4.

Chapter VI

Conclusions

1. Different distributions of ferrite-martensite structures can be produced in the three experimental dual-phase steels, namely, A1, A4 and A5 by following the two different kinds of heat-treatment cycles, AC/WQ and WQ/WQ, and by intercritical annealing at two different temperatures, 750°C and 810°C. However, the differences in these microstructures are not found to be significant.
2. In general, alloy A4 contains the maximum and alloy A1 the minimum volume fraction of martensite, with alloy A5 coming in between. However, the 0.2% Y.S. and U.T.S. of the three alloys are found to vary in the order A4 (highest) → A1 → A5 (lowest). The ferrite phases in alloys A1 and A4 have comparable microhardness values and these are much stronger than the ferrite in alloy A5.
3. The ferrite phases present in the alloys A1 and A4 are supposed to form in two different ways : (i) before and/or during the intercritical annealing ('old' ferrite) and (ii) during the cooling of the alloys from the intercritical annealing temperatures (transformed or 'new' ferrite). The amount of new ferrite is found to be larger in alloy A1 as compared to alloy A4. Alloy A5 does not show any measurable amount of new ferrite.
4. Optical as well as electron microstructures obtained from the cold-deformed materials are found to be practically the same irrespective

of the different initial heat-treatments. The structural features are found to be the coarsest for the alloy A1, rather coarse for alloy A5 and finest in alloy A4. In contrast to the alloys A1 and A4, many areas in a number of thin foils from the cold-worked alloy A5 show distinct signs of recovery at places leading to the formation of subgrains.

5. During recrystallisation anneal of all the three alloys at the lower temperature of 650°C , the cold-worked ferritic areas start recrystallising, whereas at the higher temperature of 800°C re-austenitisation of martensite and recrystallisation of cold-worked ferrite take place simultaneously. The end-product, in both cases, consist of islands of martensite embedded in a recrystallised ferrite matrix.

6. In any of the alloys, during recrystallisation, no perceptible difference in the microstructure as a function of the initial dual-phase heat-treatment can be observed. The recrystallised ferrite grains nucleate at or near cold-worked regions of the same or nearly the same orientation by an in situ process.

7. Recrystallisation kinetics results indicate that two distinct processes must be occurring during recrystallisation. The activation energies measured from the Arrhenius plots range between 16.0 to 20.0 KCal/ $^{\circ}\text{mole}$. On the basis of these values the kinetics of recrystallisation is supposed to be controlled by diffusion of carbon in $\alpha\text{-Fe}$.

8. In all the three alloys, in the cold-deformed condition, the major texture components are found to be $\{111\} \langle 112 \rangle$ and $\{111\} \langle 110 \rangle$ while the minor components are of the type $\{337\} \langle 110 \rangle$, $\{337\} \langle 776 \rangle$, $\{112\} \langle 111 \rangle$ and $\{112\} \langle 110 \rangle$. In addition, low intensity texture

components like $\{110\} \langle 001 \rangle$, $\{001\} \langle 110 \rangle$, $\{110\} \langle 110 \rangle$ and $\{310\} \langle 001 \rangle$ are also found.

9. Detailed analysis shows that a reasonably strong $\langle 111 \rangle ||$ ND fibre texture is present in both the cold-deformed alloys A4 and A5, whereas alloy A1 does not show such a fibre. Again a weak $\langle 11, 11, 4 \rangle ||$ ND fibre is observed in alloy A4 which is not so well-developed in alloy A5, while the same may be treated as weak and incomplete in case of alloy A1. A rather weak and incomplete $\langle 337 \rangle ||$ ND fibre texture is found in alloy A4, although $\{337\} \langle uvw \rangle$ orientations do not comprise a fibre in either alloy A1 or A5.

10. In any of the three alloys, the textures in the recrystallised condition are found to be basically similar to the ones for the corresponding cold-deformed materials, with the difference that the orientation densities are somewhat weaker in the former. A major difference between the recrystallisation textures of alloys A1 and A5 on the one hand and alloy A4 on the other is that whereas the intensities of the $\{111\} \langle uvw \rangle$ components are found to be stronger in the former after the 800°C recrystallisation anneal, for the latter, intensities for the same components are found to be more at the lower temperature of recrystallisation at 650°C .

11. The intensities of the $\{111\} \langle uvw \rangle$ components at different recrystallisation temperatures are supposed to be controlled by two factors, namely, (i) presence of a fine precipitation, predominantly of iron carbide, in the ferrite and (ii) the total available ferrite content at any particular recrystallisation temperature.

12. The theoretically determined \bar{r} -values for the three recrystallised alloys show that while alloy A1 has \bar{r} -values <1.0 , the corresponding values for alloys A4 and A5 are >1.0 . Out of the three alloys, the alloy A5 seems to have a distinct edge over the other two so far as the \bar{r} -values are concerned. However, on the basis of high strength, high \bar{r} -value and low Δr value, alloy A4 seems to have the optimum properties.

13. The deep-drawing characteristics of the three experimental dual-phase steels are evaluated in terms of their \bar{r} -values. These results are also compared with those reported by others for similar materials, as well as those predicted from theory. Attempts are made to explain the differences in the results obtained in the present investigation with those reported by others and the need for more research in this area is emphasized.

References

1. M.S. Rashid : SAE Paper 760206 (1976) and General Motors Research Publications Nos. GMR 2044, 2326, 2413, 2647.
2. S. Hayami and T. Furukawa : Microalloying '75, 1, 78 (1977) New York, Union Carbide Corp.
3. F.B. Pickering : Microalloying '75, 1 (1977) 3.
4. T. Gladman, O. David and I.D. McIvor : Microalloying '75, 1 (1977) 25.
5. W.S. Owen : Metall. Ital., 75 (1977) 293.
6. D.J. Bailey : 2nd Int. Conf. 'Mechanical Behaviour of Materials', Preprint, Boston, Mass. (1976) 1722.
7. D.J. Bailey : Soc. of Automotive Engineers, Preprint (1976).
8. D.J. Bailey and R. Stevenson : Metall. Trans. A, 10A (1979) 47.
9. R. Stevenson, D.J. Bailey and G. Thomas : ibid, 57.
10. M.S. Rashid : SAE Preprint 770211 (1977).
11. J.W. Morrow, A.P. Coldren and G. Tither : Climax Molybdenum Co., Reports L-176-165, L-176-166 (1976).
12. G. Tither, A.P. Coldren and J.W. Morrow : Proc. 20th Mech. Working Conf., Chicago, III (1978).
13. J.W. Morrow and G. Tither : J. Met., 12 (1978) 20.
14. T. Matsouka and K. Yamamori : Metall. Trans., 6A (1975) 1613.
15. R.A. Grange : Metall. Trans., 2 (1971) 65.
16. J.Y. Koo and G. Thomas : Mat. Sci. and Engg., 24 (1976) 187.
17. J.Y. Koo and G. Thomas : Metall. Trans. A, 8A (1977) 525.
18. J.Y. Koo and G. Thomas : Scripta Met., 13 (1979) 1141.
19. R.G. Davies : Metall. Trans. A, 9A (1978) 41.
20. R.G. Davies : Metall. Trans. A, 9A (1978) 451.
21. R.G. Davies : Metall. Trans. A, 9A (1978) 671.

22. R.G. Davies : Metall. Trans. A, 10A (1979) 113.
23. R.G. Davies : Metall. Trans. A, 10A (1979) 1549.
24. A.P. Coldren and G. Tither : J. Met., 4 (1978) 6.
25. T. Furukawa, H. Morikawa, H. Takechi and Koyama : 'Process Factors for Highly Ductile Dual-Phase Sheet Steels', Report from Research Lab., Nippon Steel Corp., Kawasaki, Japan.
26. E.C. Bain and H.W. Paxton : 'Alloying Elements in Steels', 2nd Ed., ASM, Ohio (1966).
27. P.R. Mould and C.C. Skena : 'Formable HSLA and Dual-Phase Steels' (A.T. Davenport, Ed.) AIME, New York (1977) 181.
28. R.G. Davies : ibid, 25.
29. G.F. Bolling and R.H. Richman : Canadian J. Phys., 45 (1967) 541.
30. H. Masui and H. Takechi : Trans. ISIJ, 16 (1976) 69.
31. P.M. Kelly and J. Nutting : JISI, 197 (1961) 199.
32. G.R. Speich and R.C. Miller : 'Structure and Properties of Dual-Phase Steels' (R.A. Kot and J.W. Morris, Eds.), AIME, New York (1979) 145.
33. J.H. Bucher and E.G. Hamburg : SAE Paper 770164 (1977).
34. T. Tanaka, M. Nishida, K. Hashiguchi and T. Kato : 'Structure and Properties of Dual-Phase Steels' (R.A. Kot and J.W. Morris, Eds.), AIME, New York (1979) 221.
35. W.C. Leslie : Metall. Trans. A, 3 (1973) 5.
36. S. Takeuchi, T. Taoka and H. Yoshida : Trans. ISIJ, 9 (1969) 105.
37. K.W. Andrews : J. Iron Steel Inst., London, 203 (1965) 721.
38. M.O. Geib, D.K. Matlock and G. Krauss : Metall. Trans. A, 11A (1980) 1683.
39. M.A. Grossman and E.C. Bain : 'Principle of Heat-Treatment', 5th Ed., ASM, Metals Park, Ohio (1964).
40. C.A. Siebert, D.V. Doane and D.H. Breen : 'The Hardenability of Steels', ASM, Metals Park, Ohio (1977).
41. G.S. Huppi, D.K. Matlock and G. Krauss : Scripta Met., 14 (1980) 1239.

42. G.R. Speich and R.L. Miller : 'Structure and Properties of Dual-Phase Steels' (R.A. Kot and J.W. Morris, Eds.), AIME, New York (1979) 145.
43. G.R. Speich, V.A. Demarest and R.L. Miller : Metall. Trans. A, 12A (1981) 1419.
44. C.I. Garcia and A.J. Deardo : 'Structure and Properties of Dual-Phase Steels' (R.A. Kot and J.W. Morris, Eds.), AIME, New York (1979) 40.
45. G.R. Speich, A. Szirmai and M.J. Richards : Trans., TMS-AIME, 245 (1969) 1063.
46. M. Hillert, K. Nilsson and L.B. Torndahl : JISI, London, 209 (1971) 49.
47. N.J. Kim and G. Thomas : Metall. Trans. A, 12A (1981) 483.
48. J.M. Rigsbee and P.J. Van der Arend : 'Formable HSLA and Dual-Phase Steels' (A.T. Davenport, Ed.), AIME, New York (1977) 56.
49. J.M. Rigsbee, J.W. Pickens, A.T. Davenport, J.E. Franklin and J.K. Abraham : 'Structure and Properties of Dual-Phase Steels' (R.A. Kot and J.W. Morris, Eds.), AIME, New York (1979) 304.
50. W.R. Cribb and J.M. Rigsbee : ibid, 91.
51. A. Nakagawa, J.Y. Koo and G. Thomas : Metall. Trans. A, 12A (1981) 1965.
52. G. Tither, A.P. Coldren and J.W. Morrow : Climax Molybdenum Co., Report L-176-163 (1976).
53. A.P. Coldren, G. Tither, A. Conford and J.R. Hiam : 'Formable HSLA and Dual-Phase Steels' (A.T. Davenport, Ed.), AIME, New York (1977) 205.
54. A.R. Marder : ibid, 87.
55. K. Araki, S. Fukunaka and K. Uchida : Trans. ISIJ, 17 (1977) 701.
56. J.Y. Koo and G. Thomas : 'Formable HSLA and Dual-Phase Steels' (A.T. Davenport, Ed.), AIME, New York (1977) 40.
57. J.H. Hollomon : Trans. AIME, 162 (1945) 268.
58. M.S. Rashid : 'Formable HSLA and Dual-Phase Steels' (A.T. Davenport, Ed.), AIME, New York (1977) 1.

59. I.L. Dillamore, K.I. Nam and M.B.O.O. Shitta : 3rd Congresso Brasileiro de Engenharia e Ciência dos Materials, Dec. (1978).
60. D.A. Kozakwa, R.D. Lawson, D.K. Matlock and G. Krauss : Scripta Met., 14 (1980) 1023.
61. C. Crussard : Rev. Met., Paris, France, 10 (1953) 697.
62. B. Jaoult : J. Mech. and Phys. Solids, 5 (1957) 95.
63. P. Ludwik : Elements der Technologischem Mechanik, Julius Springer, Berlin (1909) 32.
64. R.G. Davies and C.L. Magee : 'Structure and Properties of Dual-Phase Steels' (R.A. Kot and J.W. Morris, Eds.), AIME, New York (1979) 1.
65. R.G. Davies and C.L. Magee : Vanitec Seminar on Vanadium Cold Pressing and Dual-Phase Steels, Oct. (1978) W. Berlin, Germany.
66. S.T. Mileiko : J. Mat. Sci., 4 (1969) 974.
67. G. Garmon and R.B. Thompson : Metall. Trans. A, 4A (1973) 863.
68. R. Priestner and C.L. Aw : Scripta Met., 18 (1984) 133.
69. A.R. Marder : Metall. Trans. A, 13A (1982) 85.
70. R.G. Davies and C.L. Magee : Unpublished research.
71. G. Thomas and J.Y. Koo : 'Structure and Properties of Dual-Phase Steels' (R.A. Kot and J.W. Morris, Eds.), AIME, New York (1979) 183.
72. P. Öström and I. Lindgren : Swedish Inst. for Metals Research, IM-1308, Aug. (1978).
73. P. Öström : Metall. Trans. A, 12A (1981) 355.
74. H. Fischmeister and B. Karlsson : Z. Metallk., 68 (1977) 311.
75. P. Uggowitzer and H.P. Stuwe : Mat. Sci. and Engg., 55 (1982) 181.
76. Y. Tomota, H. Yoshino and K. Kuroki : Scripta Met., 11 (1977) 853.
77. R.K. Ray : Scripta Met., 18 (1984) 1205.
78. W.T. Lankford : Trans. ASM, 42 (1950) 1197.
79. R.L. Whiteley : Trans. ASM, 52 (1960) 154.
80. R.L. Whiteley, D.E. Wise and D.J. Blickwede : Sheet Met. Ind., 38 (1961) 349.

81. M.B.O.O. Shitta : Ph.D. thesis, Univ. of Aston, Birmingham (1981).
82. K. Kurihara, Y. Hosoya and K. Nakaoka : Proc. 6th Int. Conf. 'Texture of Materials', Tokyo (1981).
83. H. Hu : Metall. Trans. A, 13A (1982) 1257.
84. W.B. Hutchinson : Sheet. Met. Ind. (1983) 502.
85. R.K. Ray, M.B.O.O. Shitta, W.B. Hutchinson and I.L. Dillamore : Univ. of Aston, Birmingham, Unpublished work.
86. W.B. Hutchinson : Met. Sci., 8 (1974) 185.
87. P.A. Beck : Adv. Phys., 3, 11 (1954) 245.
88. R.W. Cahn : 'Recrystallisation, Grain Growth and Textures' (H. Margolin, Ed.), Metals Park, Ohio, ASM (1966) 99.
89. R.D. Doherty and R.W. Cahn : J. Less-Common Metals, 28 (1972) 279.
90. R.D. Doherty : Met. Sci. J., 8 (1974) 132.
91. J.G. Byrne : 'Recovery, Recrystallisation and Grain Growth', Macmillan, London (1965).
92. P. Cotterill and P.R. Mould : 'Recrystallisation and Grain Growth in Metals', Surrey Univ. Press, 450 Edgware Rd., London (1976).
93. J.W. Martin and R.D. Doherty : 'The Stability of Microstructure in Metals', Cambridge Univ. Press, Cambridge (1976).
94. H. Hu : 'Recovery and Recrystallisation of Metals' (L. Himmel, John Wiley and Sons, Eds.), New York, 63 (1963) 311.
95. J.L. Walter and E.F. Koch : Acta Met., 11 (1963) 923.
96. R.K. Ray, W.B. Hutchinson and B.J. Duggan : Acta Met., 23 (1975) 831.
97. R.K. Ray, W.B. Hutchinson, F.M.C. Besag and R.E. Smallman : J. Microscopy, 97 (1973) 217.
98. M. Schweizer and W. Form : J. Inst. Metals, 101 (1973) 924.
99. P.A. Compere and W. Form : Z. Metallk., 67 (1976) 158.
100. G.L. Ferran, R.D. Doherty and R.W. Cahn : Acta Met., 19 (1971) 1019.
101. J.R. Teodosia and G.L. Ferran : Texture Conf., Cambridge Univ. (1975) to be published in Met. Sci.

102. S.P. Bellier and R.D. Doherty : Acta Met., 25 (1977) 521.
103. K. Detert : 'Recrystallisation of Metallic Material' (F. Haessner, Ed.), (1978) 97.
104. A. Kreisler and R.D. Doherty : Submitted to Met. Sci.
105. H. Fujita : J. Phys. Soc., Japan, 16 (1961) 397.
106. R.C. Koo and H.G. Sell : 'Recrystallisation, Grain Growth and Textures' (H. Margolin, Ed.), Metals Park, Ohio, ASM (1966) 97.
107. R.H. Goodenow : Trans. Quart. ASM, 59 (1966) 804.
108. B. Bay : J. Mat. Sci., 5 (1970) 617.
109. J.C.M. Li : J. Appl. Phys., 33 (1962) 2958.
110. C.J.E. Smith and I.L. Dillamore : Met. Sci., 4 (1970) 161.
111. I.L. Dillamore, P.L. Morris, C.J.E. Smith and W.B. Hutchinson : Proc. Roy. Soc. London, 329A (1972) 405.
112. I.L. Dillamore, C.J.E. Smith and T.W. Watson : Met. Sci., 1 (1967) 49.
113. R.L. Whiteley and D.E. Wise : 'Flat Products III', AIME, New York (1962).
114. G.I. Taylor : J. Inst. Metals, 62 (1938) 307.
115. P.R. Mould and P. Cotterill : J. Mat. Sci., 2 (1967) 241.
116. R.D. Doherty and J.W. Martin : Trans. Am. Soc. Metals, 57 (1964) 874.
117. P.R. Mould and J.M. Gray : Metall. Trans. A, 3A (1972) 3121.
118. R.H. Goodenow and J.F. Held : ibid, 1 (1970) 2507.
119. W.C. Leslie, R.L. Rickett, C.L. Dotson and C.S. Walton : Trans. Am. Soc. Metals, 46 (1954) 1470.
120. B.J. Duggan : Ph.D. thesis, Univ. Birmingham (1972).
121. W.B. Hutchinson : Ph.D. thesis, Univ. Birmingham (1969).
122. H. Hu and S.R. Goodman : Metall. Trans. A, 1A (1970) 3057.
123. I.F. Hughes and E.W. Page : ibid, 24 (1971) 2067.

124. R. Giles, D.T. Gawne and W.B. Hutchinson : Unpublished work.
125. W.B. Hutchinson, T.W. Watson and I.L. Dillamore : J. Iron Steel Inst., 207 (1969) 1479.
126. S.T. Higgins : Met. Sci., 8 (1974) 143.
127. M. Hillert : Acta Met., 13 (1965) 227.
- 127A. M. Hatherly and W.B. Hutchinson : 'An Introduction to Textures in Metals', The Inst. of Metallurgists, Mon. No. 5 (1979) 6.
128. B.F. Decker, E.T. Asp and D. Harker : J. Appl. Phys., 19 (1948) 388.
129. L.G. Schulz : J. Appl. Phys., 20 (1949) 1030.
130. R.O. Williams : Trans. Met. Soc., AIME, 242 (1968) 105.
131. R.J. Roe : J. Appl. Phys., 6 (1965) 2024.
132. H.J. Bunge : Mathematische Methoden der Texturanalyse, Akademie-
verlag, Berlin (1969).
- 132A. J. Hansen, J. Pospiech and K. Lücke : Tables for Texture Analysis
of Cubic Crystals, Springer Verlag (1978).
133. H. Hu : 'Textures of Materials' (G. Gottstein and K. Lücke, Eds.),
Berlin, Springer-Verlag, 2 (1978).
134. U. Lotter, W. Müschenborn and R. Knorr : ibid, 285.
135. K. Matsudo and T. Shimomura : Trans. ISIJ, 10 (1970) 448.
136. P.R.V. Evans, J.C. Bitcon and I.F. Hughes : J. Iron Steel Inst.,
207 (1969) 331.
137. H. Kubotera et al. : J. Iron Steel Inst. Japan, 72 (1976) 846.
138. K. Matsudo, T. Shimomura and O. Nozoe : Texture, 3 (1978) 53.
139. M. Matsuo, H. Hayakawa and S. Hayami : 'Textures of Materials',
(G. Gottstein and K. Lücke, Eds.), Berlin, Springer-Verlag, 2
(1978) 275.
140. K. Toda et al. : Trans. ISIJ, 15 (1975) 305.
141. A. Okamoto and M. Takahashi : 'Textures of Materials', Proc. 6th
Int. Conf., Tokyo, ISIJ (1981) 739.
142. S. Ono, O. Nozoe, T. Shimomura and K. Matsudo : 'Metallurgy of
Continuous Annealed Sheet Steel' (B.L. Bramfitt and P.L.
Mangonon, Eds.), TMS/AIME (1982) 99.

143. I.S. Brammar, T.R. Thomson and R.M. Hobbs : J. Aust. Inst. Met., 17 (1972) 147.
144. M. Shimizu, K. Matsukura, N. Takahashi and Y. Shinagawa : J. Iron Steel Inst. Japan, 50 (1964) 2094.
145. Yawata Iron and Steel Co., Japan : U.K. Patent 1170950 (1966) 69, cf. Ref. 14.
146. B.G. Duggan and W.B. Hutchinson : 'Texture and the Properties of Materials' (G.J. Davies et al., Eds.), London, TMS (1976) 292.
147. M. Shimizu et al. : French Patent 1511529 (1967); U.S. Patent 3522110 (1970).
148. D.A. Karlyn, R.W. Vieth and J.L. Forand : 'Mechanical Working and Steel Processing VII', New York, AIME (1969) 127.
149. J.A. Elias and R.E. Hook : 'Mechanical Working and Steel Processing IX', New York, AIME (1971) 348.
150. N. Fukuda and M. Shimizu : Socei-to-Kakou, 13 (1972) 841.
151. P. Messien and T. Greday : 'Texture and the Properties of Materials' (G.J. Davies et al., Eds.), London, TMS (1976) 266.
152. R. Gillanders, C. Dasarathy and R.C. Hudd : ibid, 245.
153. Y. Meyzaud, P. Parnière, B.J. Thomas and R. Tixier : 'Texture of Materials' (G. Gottstein and K. Lücke, Eds.), Berlin, Springer-Verlag, 2 (1978) 243.
154. S.R. Goodman and H. Hu : U.S. Patent 3709744 (1973).
155. N. Ohashi, M. Konishi and Y. Arima : Kawasaki Steel Tech. Rep., 5 (1973) 164.
156. H. Hu : Texture Cryst. Solids, 2 (1976) 113.
157. H. Hu : Metall. Trans. A, 8A (1977) 1567.
158. H. Hu : Texture Cryst. Solids, 3 (1979) 215.
159. H. Hu : 'Formable HSLA and Dual-Phase Steels' (A.T. Davenport, Ed.), AIME, New York (1977) 109.
160. J.T. Michalak and H. Hu : Proc. Symp. 'Recovery, Recryst. and Grain Growth in Materials', Chicago, AIME (1977).
161. H. Hu : Texture Cryst. Solids, 4 (1980) 13.
162. K. Matsudo et al. : 'Textures of Materials', Proc. 6th Int. Conf., Tokyo, ISIJ (1981) 759.

163. P. Wacquez and R. Van Daeale : Sheet Met. Ind., 44 (1967) 21.
164. S. Teshima and M. Shimizu : 'Mechanical Working of Steel II', New York, AIME (1964) 279.
165. S.R. Goodman and H. Hu : Metall. Trans. A, 6A (1970) 1629.
166. S.D. Bhole, W.T. Roberts and D.V. Wilson : Met. Sci., 8 (1974) 277.
167. S. Satoh, T. Irie and O. Hashimoto : Trans. ISIJ, 21 (1981) B283.
168. H. Takechi, H. Kato and S. Nagashima : Trans. AIME, 242 (1968) 56.
169. A.J. Heckler and W.G. Granzow : Metall. Trans. A, 1A (1970) 2089.
170. H.J. Bunge, D. Schleusener and D. Schläfer : Met. Sci., 8 (1974) 413.
171. I.L. Dillamore and H. Kato : Met. Sci., 8 (1974) 21.
172. P.L. Antonucci and R. Ricci Bitti : 'Textures of Materials', Proc. 6th Int. Conf., Tokyo, ISIJ (1981) 759.
173. J.L. Lebrun, G. Maeder and P. Parniere : ibid, 787.
174. D.J. Blickwede : Trans. ASM, 61 (1968) 653.
175. R.K. Ray : Scripta Met., 11 (1984) 1211.
176. H.J. Bunge, C.M. Vlad and H. Kopp : Archiv für Eisenhüttenwesen, 55 (1984) 163.
177. S. Mandziej, C.A. Verbrack, J. Beyer and B.H. Kolster : 'Texture', Proc. 7th Int. Conf., Netherlands (1983) 421.
178. R.K. Ray : J. Mat. Sci. Lett., 4 (1985) 67.
179. R.K. Ray : Proc. 13th Biennial Cong. of I.D.D.R.G., Melbourne (1984) 263.
180. R.K. Ray : Proc. 14th Biennial Cong. of I.D.D.R.G., Köln (1986) 383.
181. H. Hu : Metall. Trans. A, 13A (1982) 1257.
182. R.L. Lawson, D.K. Matlock and G. Krauss : Metallography, 13 (1980) 71.
183. W.R. Cribb : Scripta Met., 12 (1978) 893.

184. B.D. Cullity : 'Elements of X-ray Diffraction', 2nd Ed., Addison-Wesley Pub. Co., Inc. (1978) 308.
185. R. Alam, H.D. Mengelberg and K. Lücke : Z. Metallk., 58 (1967) 867.
186. U. Kobbe and H. Schuon : Siemens Z., 47 (1973) 119.
187. R.J. Roe : J. Appl. Phys., 37 (1966) 2069.
188. H.J. Bunge : Z. Metallk., 56 (1965) 872.
189. J. Pospiech and J. Jura : Z. Metallk., 65 (1974) 324.
190. J. Jura and J. Pospiech : Texture Cryst. Solids, 2 (1976) 81.
191. C.M. Vlad and H.J. Bunge : 'Texture of Materials', Proc. 6th Int. Conf., Tokyo, ISIJ (1981) 649.
192. S. Mishra, C. Därmann and K. Lücke : Metall. Trans. A, 14A (1983) 11.
193. R.K. Ray : Mat. Sci. and Engg., 77 (1986) 169.
194. P.A. Wycliffe, G.R. Purdy and J.D. Embury : 'Fundamentals of Dual-Phase Steels' (R.A. Kot and B.L. Bramfitt, Eds.), AIME, Wa, Pa (1981) 59.
195. W.C. Jeong and C.H. Kim : Scripta Met., 19 (1985) 37.
196. T. O'Neill : M.S. thesis, Univ. of California, Berkeley, CA, LBL-9047 (1979).
197. A. Goel, R.K. Ray and G.S. Murty : Scripta Met., 17 (1983) 375.
198. W.B. Hutchinson and I.L. Dillamore : Metalurgia, 5 (1979) 257.
199. H.J. Eckstein : Wärmebehandlung von Stahl: VEB Deutscher Verlag Für Grundstoffindustrie, Leipzig (1970).
200. C.M. Vlad and K. Klimpel : Proc. 8th Biennial Cong. Int. Deep-Drawing Research Group, Gothenburg (1974) 163.
201. U. Lotter, W. Müschenborn and E. Tiemann : 'Metallurgy and Materials Science', Proc. 1st Risø Int. Symp., Risø National Laboratory (1980).

7